Investigation of seismic performance of elastomeric isolation bearings using low-temperature hybrid simulation technique

TAN YUQING

2022

Investigation of seismic performance of elastomeric isolation bearings using low-temperature hybrid simulation technique

TAN YUQING

Department of Urban Management

Graduate School of Engineering

Kyoto University, Japan

This dissertation is submitted for the degree of Doctor of Engineering

2022

Abstract

In the application of High Damping Rubber (HDR) bearing and spring confined Pb high damping rubber bearing (SPR-S bearing) as seismic isolation for bridges in cold regions, there are concerns about the low-temperature effect on the hysteresis performance of HDR bearing and SPR-S bearing and the resulting deterioration in bridge performance under strong ground motions. The stiffness and damping ratio of the HDR bearing and SPR-S bearing significantly increase at lower ambient temperatures, and the stiffness reduces as the inner temperature of the bearing increases due to the self-heating of rubber material and lead plugs under repeated cyclic loading, resulting in a complicated thermo-mechanical coupled hysteresis behavior which is not expressed by the currently available restoring force models of HDR bearing and SPR-S bearing.

The aim of this study is to investigate the low-temperature effect on the seismic performance of the HDR bearing and SPR-S bearing, and this research consists of three parts.

In part I, the quasi-static cyclic loading tests and pseudo dynamic hybrid simulation of HDR bearings are conducted at three different ambient temperatures (−20℃, 0℃, 23℃) to investigate the low-temperature effect on the seismic performance of this type of seismic isolation bearing. The initial loading effect on the seismic performance of HDR bearing is studied by comparing the hybrid simulation results using the HDR bearings that have not been loaded and the HDR bearings that have been loaded. A simple formula is developed to estimate the inner temperature of the HDR bearing based on the dissipated energy calculated by the area of displacement-force hysteresis loops of the bearing and the energy loss from the bearing to the loading machine, and the calculated inner temperature of the bearing is compared with the measured temperature. The hysteresis behavior depending on the inner temperature and strain amplitude are also investigated based on the calculated inner temperature. Meanwhile, the seismic response analysis of a bridge isolated with the HDR bearings is conducted using the bilinear model for the bearing to investigate the applicability of the conventional bilinear model for the HDR bearings at low temperatures.

Moreover, the quasi-static cyclic loading tests and pseudo dynamic hybrid simulation of SPR-S bearings are also conducted at three different ambient temperatures (−20℃, 0℃, 23℃) to investigate the low-temperature effect on the seismic performance of this new type of seismic isolation bearing possessing both the characteristics of lead rubber bearing and HDR bearing. The comparison of seismic responses between the SPR-S bearing and HDR bearing shows that the SPR-S bearing is less affected by the low-temperature effect than the HDR bearing. The hysteresis behavior of SPR-S bearings depending on the inner temperature and strain amplitude are investigated based on the successfully measured inner temperature. Meanwhile, the seismic response analysis of a bridge isolated with the SPR-S bearings is conducted using the bilinear model for the bearing to investigate the applicability of the conventional bilinear model for the SPR-S bearing at low temperatures.

In part II, the real-time hybrid simulation is carried out to investigate the loading rate dependence on the seismic response of HDR bearings at low temperatures. The real-time hybrid simulation results are compared with those obtained in the pseudo dynamic hybrid simulation with a slower loading rate in terms of the hysteresis loops of the HDR bearing, bearing strain, pier top displacement, pier acceleration, the inner temperature of the bearing and energy dissipation. 10 thermocouples are installed in the HDR bearing in the real-time hybrid simulation to better understand the temperature distribution of the bearing.

In part III, two simplified thermo-mechanical coupled hysteretic restoring force models of HDR bearing are newly developed based on the temperature-independent bilinear model and modified Park-Wen model. The model parameters are identified from the shear strain-stress curves of HDR bearing in quasi-static cyclic loading tests at three different ambient temperatures. Accuracy of the improved models is verified by comparing the numerical result of seismic response analysis of a bridge model using the proposed HDR restoring force models with the result of hybrid simulation of the same bridge model including the HDR bearing loading test under low-temperature conditions.

In addition, a micro-scaled physical model (called Mullins TMC MPW model) is also proposed based on the developed thermo-mechanical coupled modified Park-Wen model for the HDR bearing, the phenomenon of sharply decreased stiffness after the first cycle at a certain strain amplitude called the Mullins effect can be described by this proposed model. The parameters of Mullins TMC MPW model are firstly identified by the hysteresis loops of the HDR bearing obtained from the cyclic shear loading tests, and the hysteresis loops of HDR bearing using the Mullins TMC MPW model with identified model parameters are compared with those using TMC MPW model and the experimental hysteresis loops of HDR bearing obtained from the cyclic shear loading tests. Then the model parameters are also directly identified from the hybrid simulation results considering the different loading conditions between the cyclic loading tests and ground motion. The seismic response analysis of HDR bearings isolated bridge is conducted using the Mullins TMC MPW model, and the accuracy of the advanced model is verified by comparing the analytical results with the hybrid simulation results. Finally, the verified Mullins TMC MPW model is used to conduct seismic response analysis of the HDR bearings isolated bridge under 18 types of earthquake to investigate the low-temperature effect on the seismic performance of HDR bearing under different ground motions.

Contents

List of figures

List of tables

Chapter 1 Introduction

1.1 Background

Seismic isolation has been proved to be a very excellent method to protect structures from being destroyed under severe earthquakes [1-2]. Among some means of seismic isolation for bridges, the application of rubber bearings is recognized as one of the effective techniques. The rubber bearings have been widely used for bridges since the Great Hanshin-Awaji Earthquake of 1995 (Kobe, Japan). The seismic response of bridges can be reduced with increased natural period and added damping capacity by using the rubber bearings, as shown in Fig 1.1. Specifically, the resonance can be prevented as the natural period of bridge is increased away from the natural period of the ground.

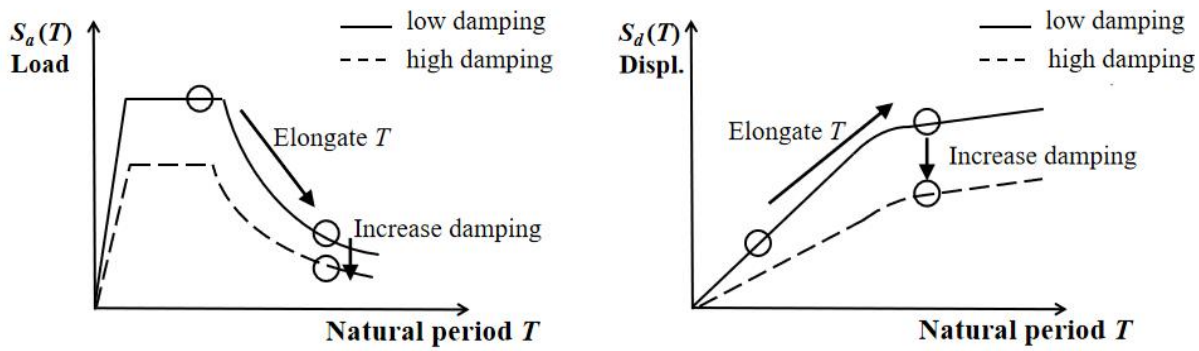

Figure 1.1 Seismic response of isolated bridges using rubber bearings

Natural rubber (NR) bearings [3-4], high-damping rubber (HDR) bearings [5] and lead rubber bearings (LRB) [6] are currently three typical types of isolated rubber bearings for bridges in Japan. The rubber bearings have the good deformation capability in the horizontal direction and the sufficient rigidity in the vertical direction by alternating rubber layers and steel plates in a single unit. The natural rubbers are applied in the NR bearings and LRB, while the high-damping rubbers with enhanced damping capability are used in the HDR bearings to increase the seismic performance, and the energy dissipation capacity of the LRB is enhanced by the plastic deformation of the lead plugs. The NR bearings are often used with dampers to increase the energy dissipation capability of this type of bearings, while the HDR bearing or LRB with high damping capability can be used as a single unit.

High-damping rubber layers and steel layers are laminated and vulcanized in the HDR bearings as shown in Fig. 1.2, the cover rubber is used to protect the inner steel plates and the high damping rubber. The seismic energy can be absorbed by the dissipation performance of the HDR bearings by the viscous and frictional resistance of the high damping rubber.

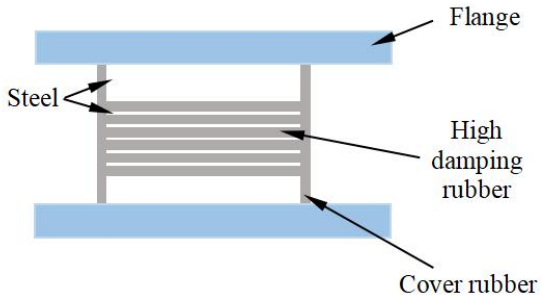

Figure 1.2 High damping rubber bearing

The spring confined Pb high damping rubber bearing (SPR-S bearing) [7] shown in Fig. 1.3 consists of laminated high damping rubber and lead plugs wrapped around by steel springs for confinement. As a new type of isolation bearings possessing both the characteristics of LRB and HDR bearings, the conventionally separately used lead plugs and high damping rubber are combined and installed in a single device to further improve the damping performance of the SPR-S bearing. The energy dissipation performance of the SPR-S bearing is provided by both the viscous and frictional resistance of the high damping rubber and plastic deformation of the lead plugs.

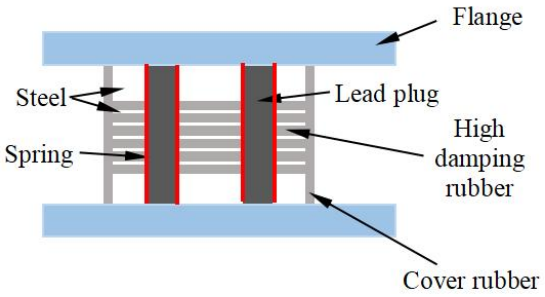

Figure 1.3 Spring confined Pb high damping rubber bearing

The HDR bearings and SPR-S bearings are the two types of bearings investigated in this study. Many experiments have been conducted in the past studies to obtain better understanding of the mechanical behaviors of laminated rubber bearings [8-12]. Since the essential properties of those bearings for effective seismic isolation are low stiffness and enhanced damping, the equivalent stiffness and equivalent damping ratio expressed as their strain amplitude dependence play important roles in the seismic performance evaluation of bridges in the design practice. It has been found that the mechanical characteristics of bearings is affected by many factors such as the temperature effect [13], Mullins effect [14], loading rate dependence [15], vertical axial force [16], bidirectional loading [17] and so on. In this study, the temperature effect, Mullins effect and rate dependence are investigated.

1.2 Conditional effects on the mechanical characteristics of isolated rubber bearings

1.2.1 Low-temperature effect

In the application of HDR bearings as seismic isolation devices for bridges in cold regions, there are concerns about the low-temperature effect on the hysteresis performance of these bearings and the resulting deterioration in bridge performance under strong ground motions. The stiffness and characteristic strength of the HDR bearing in the initial loading cycle significantly increase at lower ambient temperatures, as shown in Fig. 1.4. In the past, the mechanical characteristics of HDR bearings have been considered to be affected by the ambient temperature. However, it has been proved that the mechanical characteristics of the HDR bearing are inner temperature dependent rather than the ambient temperature dependent, the stiffness reduces as the inner temperature of the bearing increases due to the self-heating of rubber materials under repeated cyclic loading [18], and the changed stiffness can further affect the rate of inner temperature rise which is theoretically related to the amount of energy dissipation represented by the area of the hysteresis loops, resulting in a complicated thermo-mechanical coupled hysteresis behavior which is not expressed by the currently available restoring force models of HDR bearings.

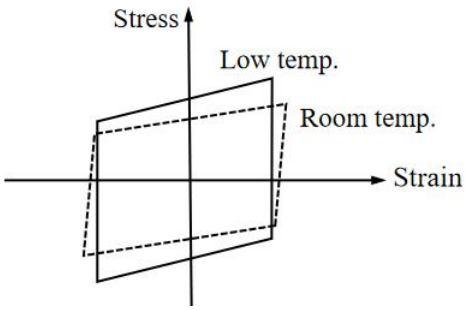

Figure 1.4 Hysteresis loops of the bearing at room and low inner temperatures

The temperature dependence of the bearing has been extensively investigated in previous studies. Okui et al. [18] found that the mechanical behavior of HDR bearings is inner temperature dependent and proposed a simple formula to calculate the inner temperature of the bearing. Takaoka et al. [19] investigated the effects of increased temperature on the mechanical behavior of bearings under large shear cyclic loading. Cardone and Gesualdi [20] investigated the sensitivity of the cyclic behavior of elastomeric materials to different ambient temperatures. Mendez-Galindo et al. [21] presented the mechanical characteristics of LRB at room and low temperatures. However, these studies only focused on the mechanical characteristics such as the characteristic strength, effective stiffness, damping ratio and energy dissipation of bearings under cyclic loading, the seismic performance of bearings as well as the resulting seismic response of the entire isolate bridge under low-temperature condition are still not available. Moreover, in the currently used design standards such as ISO 22762-2 [22], JRA Bearing Handbook [23] for example, the standard temperature for

determining the properties of elastomeric isolators is specified as 23°C or 27°C; although test results carried out at a different temperature shall be corrected to the value of the property at the standard temperature by an appropriate method, even the ambient temperature dependence is not considered in the hysteretic restoring force for nonlinear time-history analysis for design assessment.

1.2.2 Mullins effect

The phenomenon of sharply decreased stiffness after the first cycle at a certain strain amplitude that has not been experienced is usually called the Mullins effect, as shown in Fig. 1.5, and the stress-strain behavior of the bearing at the strain amplitude that has not been experienced will not be influenced by the Mullins effect [24]. In general, the phenomenon of gradually decreased stiffness with the increased number of cyclic loops is assumed to be caused by both the Mullins effect and self-heating effect, in which the maximum stress softening effect occurs after the first cycle is considered to be mainly caused by the Mullins effect, and the stress softening effect occurs after the second cycle and the subsequent cycles is considered to be mainly caused by the inner temperature effect. Moreover, the Mullins effect is more obvious observed at lower temperatures, as shown in Fig. 1.6. In summary, the hysteretic restoring force characteristics associated with the low-temperature and Mullins effect include the following effects: (1) ambient temperature dependence of the stiffness and damping during the initial stage (2) Mullins effect and its inner temperature dependence (3) reduction of stiffness and damping with the progress of loading. The performance of lengthening the period of the isolated bridge degrades as the stiffness of bearing increases in the initial stage at a lower ambient temperature, resulting a larger demand on the piers. The reduction of stiffness with the progress of cyclic loading may cause a larger deformation of bearings than allowed in design practice. However, the currently available models are not able to describe these behaviors for the HDR bearings.

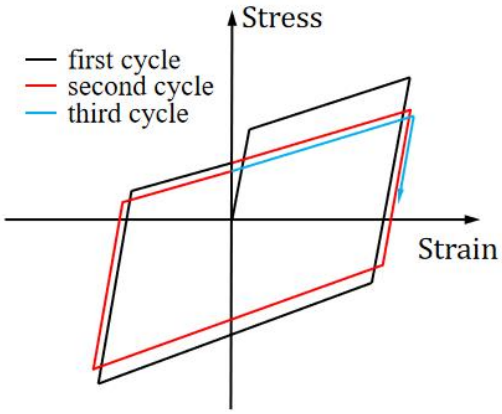

Figure 1.5 Schematic of strain-stress relationship of the HDR bearing at different cycles under cyclic loading

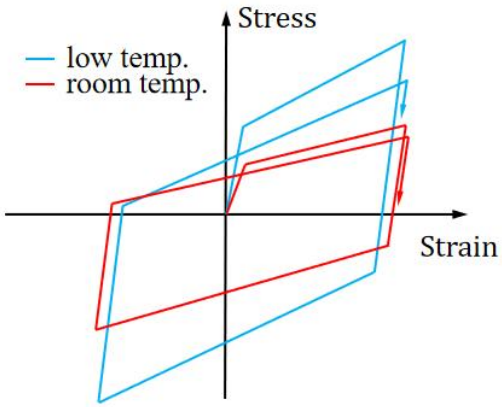

Figure 1.6 Schematic of difference of strain-stress relationship of the HDR bearing under cyclic loading at room temperature and that under a low ambient temperature condition

In the 2018 Hokkaido Eastern Iburi Earthquake, the ground motion with seismic magnitude of 7 was observed in Hokkaido for the first time, hence, the large earthquakes with the same level of seismic magnitude as the 1995 Hyogoken Nanbu Earthquake and the 2016 Kumamoto Earthquake are likely to occur in cold regions. The recorded minimum temperature distribution in Hokkaido [25] is shown in Fig. 1.7. It can be seen that there are many regions where the temperature is below −30°C, to introduce the HDR bearings in cold regions like the Hokkaido in the future, it is urgently needed to investigate the seismic performance of bearings under low temperatures.

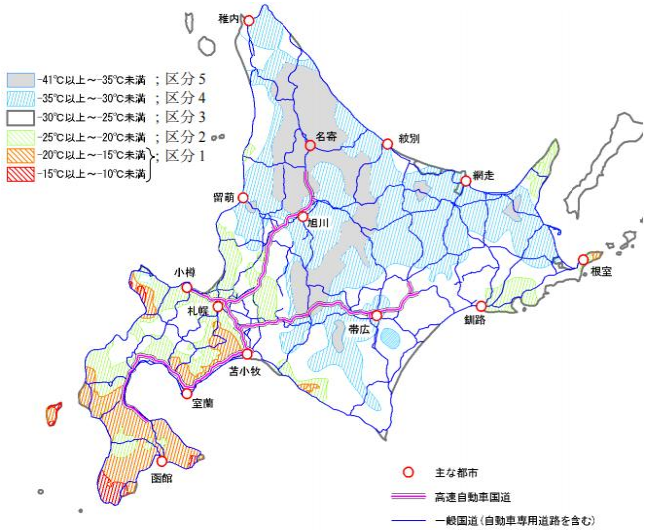

Figure 1.7 Recorded minimum temperature distribution in Hokkaido [25]

Experimental studies have found that the stiffness of the rubber can recover to its initial value after a very short time, this recovery speed is very fast for the first phase and then gradually slows down, and is considered to be affected by the elapsed time from the initial load, temperature and material compositions [26]. Since the time interval between two strong ground motions in the real environment is long enough for the stiffness recovery of bearings, the recovery dependence is usually not considered in the seismic response analysis.

1.2.3 Rate-dependence

The mechanical behavior of HDR bearings is found to be loading rate dependent caused by the viscosity of high damping rubber materials and other performance of the bearing. Gyeong and Ohtori [27] verified that the slower loading rates result in smaller stiffness and lower hysteresis damping for HDR bearings. Imai et al. [28] conducted shear cyclic loading tests using HDR bearings, NR bearings and LRB under different strain rates and found that the shear stress is larger at higher strain rate for all of these three types of bearings, and the rate dependence is more obviously observed for the HDR bearings than the other bearings. However, these experiments were conducted under room temperature. Zhang and Li [29] carried out a series of cyclic shear tests, simple relaxation tests and multi-step relaxation tests under −30℃, −10℃ and 20℃ using high-performance rubber bearing (HPRB) to investigate the rate dependence and temperature effect of this newly developed bearing, it is found that the equivalent stiffness of the HPRB increases at higher loading rate even at lower temperatures, then they proposed a fractional derivative three-element model to describe the loading rate dependent behaviors of the HPRB at different ambient temperatures, however, the seismic response of the whole isolated structure under low temperatures and arbitrary earthquakes is still unknown. Other scholars developed rate-dependent models to better describe the hysteresis behaviors of bearings [30-33]. All these researches prove the non-negligible loading rate dependence for rubber bearings.

1.3 Hybrid simulation

Since the loading condition of rubber bearings under regular cyclic loading with progressively changed strain amplitudes in the cyclic loading test is different from that under the real random earthquake ground motions, and the complicated thermo-mechanical coupled hysteresis behavior of the HDR bearings and SPR-S bearings is not able to be expressed by the currently available restoring force models, it is necessary to obtain reliable experimental information regarding the seismic response of the bridge isolated with the seismic isolation bearings at low temperatures. Moreover, the measured inner temperature history of seismic isolation bearings obtained in tests is an important information in investigating the hysteresis behavior of bearings and the development of hysteretic restoring force models. To do these, hybrid simulation [34-35] is considered to be an effective method for obtaining more reliable data regarding the seismic response of an isolated bridge. The hybrid simulation was invented by Takanashi et al. [36] and was investigated by many researches in the past [37-40]. As shown in Fig. 1.8, the hybrid simulation is a test that combines the experimental and analytical part, only the rubber bearing which the hysteretic behavior is difficult to be modeled is loaded as the experimental part in the horizontal direction, and the seismic response of the entire bridge is calculated by a computer.

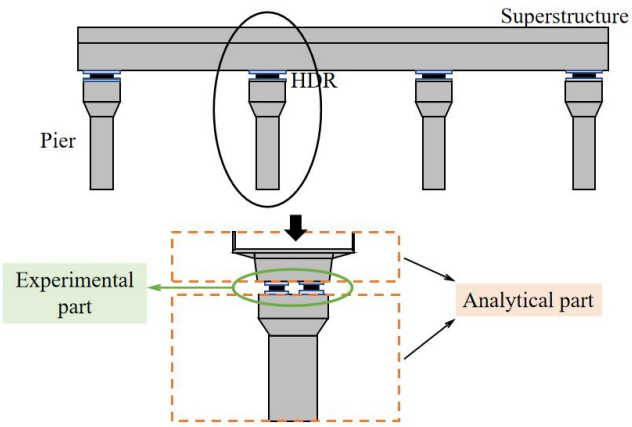

Figure 1.8 Hybrid simulation combines experimentss and analyses

The flowchart of hybrid simulation in this study is shown in Fig. 1.9, the calculation of the seismic response of the whole isolated bridge and the loading of the isolated rubber bearing are conducted simultaneously, only the bearing specimen is loaded step by step during the hybrid simulation, and the measured restoring force of the bearing at each time step is used to correct the seismic response of isolated bridge for the next time step. Many integration algorithms have been developed in the past [41-45] in the hybrid simulation, and the Newmark's β method is applied in this study. The seismic response of the whole isolated structure can be obtained in hybrid simulation with high accuracy without the need to conduct the shaking table tests with high cost.

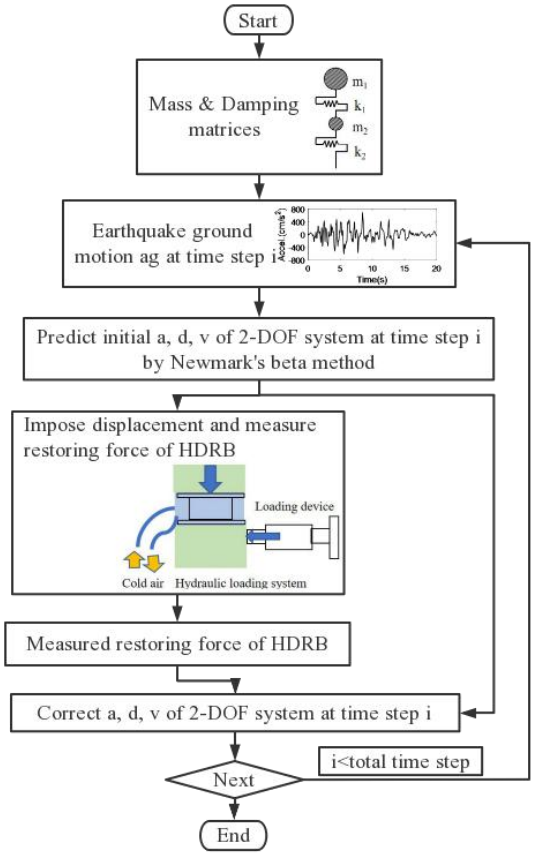

Figure 1.9 Flowchart of hybrid simulation

As the mechanical behavior of HDR bearings is rate-dependent, it is necessary to conduct the real-time hybrid simulation [46-48] to investigate the seismic performance of HDR bearings under realistic experimental condition, the real-time hybrid simulation can be treated as an extension of the conventional pseudo-dynamic hybrid simulation. The real-time hybrid simulation with higher loading speed is more difficult to be conducted compared with the conventional pseudo-dynamic hybrid simulation with a smaller loading speed. In the real-time hybrid simulation, it is required that the displacement commanded on the substructure imposed by the actuator is same with the calculated displacement in real-time, and the actuator delay [49-51] caused by the servo-hydraulic dynamics may lead to the fail of the experiment. To avoid this fail, many researchers investigated the actuator delay compensation methods [52-56]. Moreover, there is a concern that the bearing force may reach the maximum force of the loading system as the maximum force of the loading system is smaller at higher loading speed under the condition of constant oil flow for the oil pressure control machine. Hence, the pseudo-dynamic hybrid simulation with constant loading speed is firstly conducted considering about the safety, then the real-time hybrid simulation with higher loading speed is carried out in this study.

1.4 Hysteretic restoring force models of rubber bearings

The temperature dependence of the bearing performance has been extensively investigated in previous studies. However, these previous studies focused on the mechanical characteristics such as the characteristic strength, effective stiffness, damping ratio and energy dissipation of bearings under cyclic loading. The detailed behavior of HDR bearings under arbitrary loading and the resulting seismic response of the entire isolated bridge under low temperatures need to be clarified. Since the currently available restoring force models of HDR bearings for seismic performance assessment do not allow the representation of the complicated behavior that can be a potential source of unconservative assessment of the seismic performance of the bridge, the development of reliable hysteretic restoring force models expressing the temperature dependence of hysteresis behavior of HDR bearings is urgently needed to introduce the HDR bearings to bridges in cold earthquake-prone regions.

Numerous temperature-independent models have been proposed for bearings in the past researches. Yuan et al. [32] developed a constitutive model that is capable to represent the rate-dependence of HDR bearings under shear deformation. Kikuchi et al. [11] proposed a model to predict the mechanical properties of the elastomeric bearing at large strain amplitudes. Wen and Park et al. [57-58] developed the Park-Wen model for the seismic response analysis of a structure under bi-directional earthquake ground motions. On the basis of the Park-Wen model, Dang et al. [59] proposed a modified Park-Wen model that allows to capture the stiffening behaviour of HDR bearings at higher strain levels. Yoshida et al. [60] developed a constitutive model which is composed by the elastoplastic part and hyperelastic part for HDR materials. Bhuiyan et al. [61] developed an elasto-viscoplastic rheology model to describe the rate dependent behavior for the HDR bearings. These models take into account the factors that affect the hysteresis behavior of rubber bearings, such as

rate-dependence, experienced shear strain level, bidirectional loading and so on. However, they are developed at room temperature and are not able to capture the variations of mechanical properties of bearings at low temperatures.

Several temperature-dependent hysteretic restoring force models have been proposed for LRB. Kalpakidis and Constantinou et al. [62-63] proposed a thermo-mechanical coupled model that accounts for lead core heating effect for lead-rubber bearings, and the characteristic strength of lead-rubber bearings was incorporated due to the lead core heating. Kondo et al. [64] developed a response analysis method with consideration of heat-mechanical interaction behavior of lead rubber bearings, and the difference method was used in the heat conduction analysis.

Several temperature-dependent hysteretic restoring force models have been proposed for HDR bearings. Hwang et al. [65] presented an analytical model that accounts for the temperature effects, scragging, frequency dependence and Mullins effect for HDR bearings. Nguyen et al. [66] proposed a rheology model to represent the rate-dependent hysteresis behavior of HDR bearings at subzero and room ambient temperatures. Hwang and Hsu [67] improved the fractional derivative Kelvin model with consideration of the ambient temperature effect, and the beginning ambient temperature was incorporated into this model. However, these temperature-dependent models only considered the ambient temperature effect. Although Kikuchi and Ishii [68] developed a thermo-mechanical coupled hysteretic model for HDR bearings, lead-rubber bearings and tin-rubber bearings employing a finite volume method in the thermal conductivity simulation, the evaluation of the inner temperature with consideration of self-heating effect requires intensive computing resource, which may limit applicability of the thermo-mechanical coupled model to the seismic response analysis for isolated bridges.

Many models have been developed to explain the Mullins effect in the past researches. Hwang et al. [65] described the cyclic softening behaviour of HDR bearings by introducing load history-dependent parameters in a mathematical model. Naito et al. [69] developed a model to describe the softening effect occurs in the first cycle. Dall'Asta and Ragni [70] took the Mullins effect into account by using damage parameters that update with the progressed strain history in the model for high damping rubber dissipating devices. Tubaldi et al. [71] advanced the model in [70] by accounting the negative and positive direction dependence of the Mullins effect, and investigated the stress softening effect on the seismic responses of isolated structures. However, these models only considered the stress softening behavior of bearings at room temperature, the more intense Mullins effect at lower temperatures has not been investigated.

Therefore, to predict the seismic response of bridges isolated with HDR bearings in cold earthquake-prone regions with more accuracy, it is necessary to propose a nonlinear hysteretic restoring force model of HDR bearings with consideration of the thermo-mechanical coupled effect and Mullins effect.

1.5 Contents

The purpose of this study is to investigate the seismic performance of the HDR bearings and SPR-S bearings at low temperatures and develop hysteretic restoring force models with consideration of thermo-mechanical coupled effect and Mullins effect. The dissertation consists of seven chapters, and the organization of this study is shown in Fig. 1.10.

In Chapter 2, the quasi-static cyclic loading tests and hybrid simulation of HDR bearings are conducted at there different ambient temperatures (−20℃, 0℃, 23℃) to investigate the low-temperature effect on the seismic performance of this type of seismic isolation bearings. The testing equipment is modified to enable low-temperature shear loading tests under constant axial load by putting the HDR bearing specimen in an insulation chamber. The initial loading effect on the seismic performance of the HDR bearing is investigated by conducting the hybrid simulation using the HDR bearings that has not been loaded and the HDR bearings that has been loaded, respectively. A formula is proposed to calculate the inner temperature of the HDR bearing, and the analytical inner temperature is compared with the measured inner temperature of bearing. Meanwhile, the seismic response analysis of a bridge isolated with the HDR bearings is conducted using the bilinear model to investigate the applicability of the conventional bilinear model for the HDR bearings at low temperatures.

In Chapter 3, the quasi-static cyclic loading tests and hybrid simulation of SPR-S bearings are conducted at there different ambient temperatures (−20℃, 0℃, 23℃) to investigate the low-temperature effect on the seismic performance of this type of seismic isolation bearings. The seismic response of the SPR-S bearings is compared with that of the HDR bearings in terms of the bearing hysteresis loops, bearing strain, pier top displacement and energy dissipation. Moreover, the seismic response analysis of a bridge isolated with the SPR-S bearings is conducted using the bilinear model to investigate the applicability of the conventional bilinear model for the SPR-S bearings at low temperatures.

In Chapter 4, the real-time hybrid simulation of HDR bearings are conducted at there different ambient temperatures (−20℃, 0℃, 23℃) to investigate the loading rate dependence of the seismic performance of this type of seismic isolation bearings under low temperatures. The quasi-static cyclic loading tests in which there is an interval time about 1 hour between the loading with different strain amplitudes are carried out to investigate the mechanical characteristics of the HDR bearings. Meanwhile, the seismic response of the HDR bearings in the real-time hybrid simulation is compared with the pseudo dynamic hybrid simulation described in chapter 2. Ten thermocouples are installed in the HDR bearing in the real-time hybrid simulation and quasi-static cyclic loading tests to better understand the temperature distribution of the HDR bearing.

In Chapter 5, two simplified thermo-mechanical coupled hysteretic restoring force models of HDR bearings are developed. The two hysteretic restoring force models are based on the existing temperature-independent bilinear model and the modified Park-Wen model with consideration of thermo-mechanical coupled effect at different temperatures. The model parameters are identified from the shear strain-stress curves of HDR bearings obtained by

cyclic loading tests at ambient temperatures of −20°C, 0°C and 23°C described in chapter 2, and the accuracy of the proposed models is discussed by comparing the results of seismic response analysis of a HDR bearings isolated bridge model using the proposed models with the experimental results in hybrid simulation at room and low temperatures.

In Chapter 6, a hysteretic restoring force model (called the Mullins TMC MPW) with consideration of the Mullins effect based on a previously proposed thermo-mechanical coupled modified Park-Wen (TMC MPW) model in chapter 5 is developed for HDR bearings at low temperatures. The model parameters are firstly identified by the hysteresis loops of the HDR bearings obtained in the cyclic shear loading tests, then the parameters are also directly identified from the hybrid simulation results considering the different loading conditions between the cyclic loading tests and ground motions. Moreover, the seismic response analysis of a HDR bearings isolated bridge simplified as 2-degree-of-freedom system model is conducted using the advanced model, and the accuracy of the model is verified by comparing the analytical results with the hybrid simulation results. Finally, the verified Mullins TMC MPW model is used to conduct seismic response analysis of a HDR bearings isolated bridge under 18 types of earthquake to investigate the low-temperature effect on the seismic performance of HDR bearings under different ground motions.

In chapter 7, the conclusions of this study are summarized and the possible future research topics are recommended.

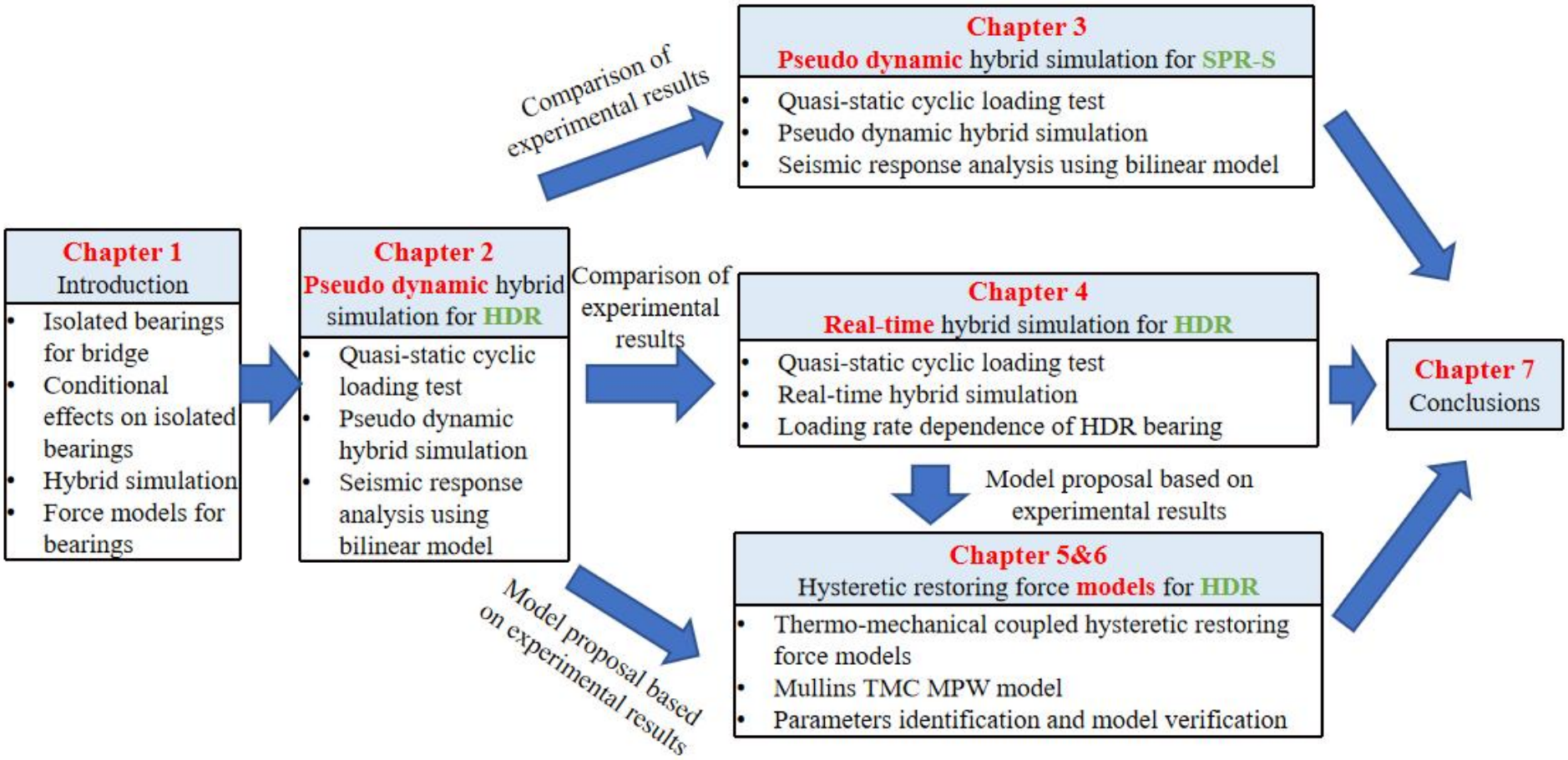

Figure 1.10 Organization of chapters

Chapter 2 Hybrid simulation for seismic performance assessment of HDR bearings at low temperatures

2.1 General

High damping rubber bearing (HDR bearing) is one of the widely used seismic isolated bearing in bridge in Japan, however, it has not been extensively applied at clod regions such as Hokkaido considering about the temperature dependence of the HDR bearing. The mechanical characteristics of HDR bearing are highly dependent on the temperature, with the stiffness increasing as the ambient temperature decreases. Meanwhile, the stiffness decreases due to the self-heating of rubber materials under cyclic loading. As a result, the seismic performance of HDR bearings can be strongly influenced by both the ambient temperature and inner temperature.

To introduce HDR bearings in cold earthquake-prone regions in the future, reliable information is needed regarding the seismic response of bridges isolated with HDR bearings at low temperatures. Although there are many hysteresis restoring force models proposed for the HDR bearings in the past, most of these models are developed without the consideration of temperature dependence or the inner temperature of the bearing is not considered, and the numerical method is yet to be verified. Meanwhile, the loading condition of bearings during cyclic reversals is different from those under the earthquake ground motions. Hence, it is necessary to quantitatively obtain the seismic response of a bridge isolated with HDR bearings at low temperatures from tests. For this purpose, hybrid simulation is considered to be an effective method for directly obtaining more credible seismic responses of a bearings isolated bridge.

In this chapter, hybrid simulation for HDR bearings' seismic isolation effectiveness assessment in cold regions is conducted. The testing equipment for HDR bearing specimens is modified to enable low-temperature shear loading tests under axial load. Firstly, the experimental program and test facilities are described, the cyclic loading test is conducted to investigate the mechanical characteristics of HDR bearings at there different ambient temperatures (23^{o}C, 0^{o}C or −20^{o}C). Then the hybrid simulation results are discussed in terms of HDR bearing hysteresis loops, bearing strain, pier responses, super-structure responses, measured temperature and energy dissipation of bearings, the response mode shape of the entire bridge is also investigated according to the measured pier responses and super-structure responses. The initial loading effect on the seismic performance of HDR bearings is studied by comparing the hybrid simulation results using the bearing specimens that have not been

loaded and the bearing specimens that have been loaded. Next, a formula is proposed to calculate the inner temperature of HDR bearings based on the method proposed in [18], the method in [18] is extended by including the energy loss caused by the heat radiation and conduction from the bearing contact surfaces. Then the hysteresis behavior of the bearing is investigated, and an empirical formula is proposed to calculate the shear modulus and equivalent damping ratio of HDR bearings based on the strain amplitude and calculated inner temperature. Finally, analytical seismic response of a HDR bearings isolated bridge is conducted by using the bilinear model, and the analytical results are compared with the experimental results in terms of the bearing hysteresis loops, bearing strain, pier top displacement and pier acceleration.

2.2 Experimental program and test facilities

2.2.1 HDR bearing specimen

The HDR-S bearing (one type of HDR bearings) which has enhanced damping capacity compared with the conventional HDR bearing was used in this study. The HDR bearing specimen and thermocouple layout are shown in Fig. 2.1. The specimen was a 1/6-scaled HDR bearing with dimensions of 240 × 240 mm. The rubber layer thickness is 5 mm and the total rubber thickness is 30 mm, the steel plate thickness is 3.2 mm and the total steel thickness is 16 mm, and the shear modulus is 1.2 N/mm^2. Four thermocouples were installed for each HDR bearing specimen to measure the temperature of the bearing: two were installed in the central location at the fourth layer of rubber (P1 and P2). These two thermocouples were installed at the same location, since the thermocouples are susceptible to failure during loading tests. Two additional thermocouples were installed on the outside surface of the rubber at the location of 1/2 (S1) and 3/4 (S2) of the total height.

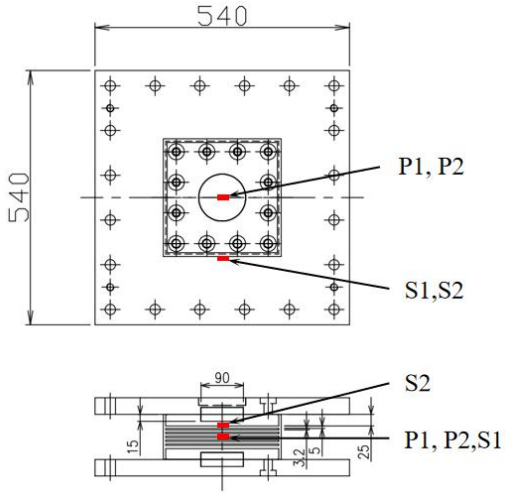

Figure 2.1 HDR bearing specimen and thermocouple layout

The dimensions and material properties of the HDR bearing specimen are given in Table 2.1.

Table 2.1 Dimensions and material properties of the HDR bearing specimen

Parameters	Specification
Cross-section (mm^2)	240 × 240
Number of rubber layers	6
Number of steel plates	5
Thickness of one rubber layer (mm)	5
Total rubber thickness (mm)	30
Thickness of one steel plate (mm)	3.2
Cover rubber thickness (mm)	5
Shear modulus (MPa)	1.2
First shape factor	12
Second shape factor	8

2.2.2 loading system

The loading system is shown in Fig. 2.2. In the horizontal direction, the HDR bearing specimen was controlled by displacement, and the maximum horizontal force and displacement capacity of the loading system were ±400kN and ±200mm, respectively. The maximum vertical force and displacement capacity of the loading system were −2000/+1000kN and ±150mm, respectively. During the test, the specimen was loaded by a constant axial stress of 6 MPa.

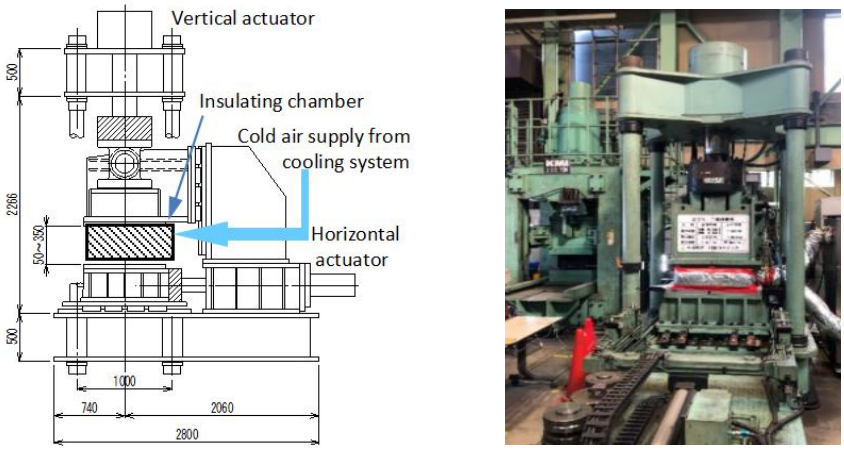

Figure 2.2 loading system

The capacity of the loading machine is given in Table 2.2.

Table 2.2 The capacity of the loading machine

Parameters	Vertical direction	Horizontal direction
Maximum force	−2000kN/+1000kN	± 400kN
Maximum stroke	±150mm	±200mm
Maximum speed	7mm/s	630mm/s

2.2.3 Temperature condition

The ambient temperature of the HDR bearing specimen was set to be 23°C, 0°C or −20°C for both the cyclic loading tests and hybrid simulation, in which the 23°C represents the room temperature, and the temperature of −20°C was selected considering the capacity of the loading system. The specimen was placed within an insulation chamber during the tests, as shown in Fig. 2.3, and the temperature in the chamber was controlled by delivering a continuous flow of cold air through the cooling system, as shown in Fig. 2.4. A sufficient space was provided between the insulation chamber and the specimen so that loading of the specimen was not affected by the insulation chamber during the test. As shown in Fig. 2.5, the cold air to maintain the ambient temperature of the bearing specimen to an expected value was provided to the chamber through one of the pipes connected to the cooling system and circulated around the specimen, and the circulated air was returned to the cooling system through the other pipe. Before each test, the specimen was placed within the chamber and cooled by the cooling system for at least one day until the temperature of the specimen reached the expected value. The measured temperature of the specimen was recorded in a data logger connected with the thermocouples.

Figure 2.3 Bearing specimen placed in the insulation chamber

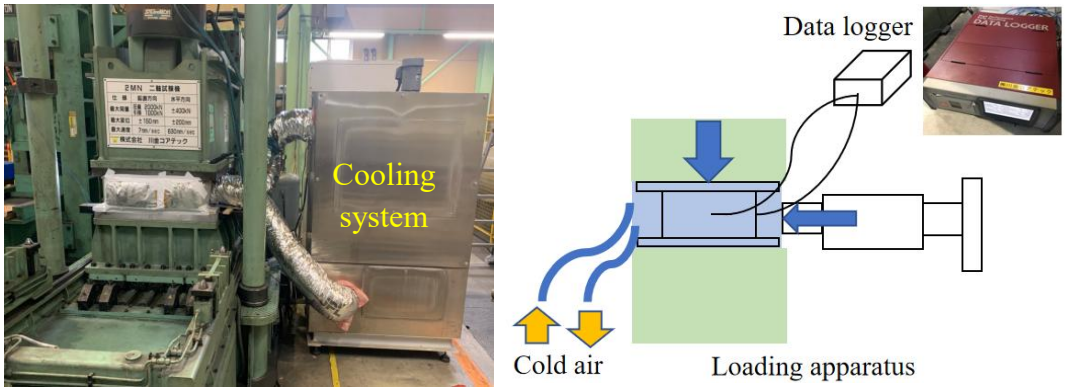

Figure 2.4 Cooling system

Figure 2.5 Detail of pipes for providing cool air to the chamber

Furthermore, two high-strength cement-based heat insulating plates were installed on and under the bearing specimen to prevent heat transfer from the specimen to the loading system. The insulating plate installed on the specimen is shown in Fig. 2.6. The heat transfer from the specimen to the loading system is limited to that through the shear key which was installed at the upper center of the specimen for the shear force transmission.

Figure 2.6 Heat insulating plate installed on the top loading interface

K-type thermocouples were used, the working range is −50°C～400°C and the resolution is ±2.5°C. The used thermocouple and the capacity of the thermocouple are shown in Fig. 2.7 and Table 2.3, respectively.

Figure 2.7 Thermocouple used in the test

Table 2.3 The capacity of the thermocouple

Temperature range	−50℃～400℃
Resolution	±2.5℃
Response speed	8 sec

2.2.4 Test cases and test sequence

The restoring force of the HDR bearing generates in the first cycle is larger than that in the second and subsequent cycles under repeated loading in the case of initial loading. Since the effect of such initial loading is considered to be an important factor affects the seismic response of bridges isolated with HDR bearings, hybrid simulation is conducted twice at each ambient temperature in which one is using the bearing specimens that have not been previously loaded and the other one is using the bearing specimens that have been loaded, the same specimens are loaded again after some recovery days.

The test cases for the cyclic loading tests and hybrid simulation are listed in Table 2.4. Four HDR bearing test specimens (No.1, No. 2, No. 3, No. 4) were used for the cyclic loading tests C1, C2, C3 and six hybrid simulation tests H1, H2, H3, H4, H5, H6 at three different air temperatures (23℃, 0℃ and −20℃). The tests H1, H2, H3 were conducted using previously unloaded specimens No.2, No.3 and No.4, and then those specimens were used in the tests C1, C2, H4, H5, respectively. A preliminary cyclic loading test at strain amplitude 175% under 23℃ was conducted using the specimen No.1 to measure the initial stiffness of HDR bearing, then this specimen was used in the tests C3 and H6. An interval between the hybrid simulation case and the cyclic loading case for each specimen was more than seven days except for the test H6.

Table 2.4 Test cases

Case No.	Test	Temperature (℃)	Specimen No.	Date	Initial loading	Recovery days
C1	Cyclic loading	−20	2	2019/12/24	No	7
H1	Hybrid simulation	−20	2	2019/12/17	Yes	Initial loading
H4	Hybrid simulation	−20	2	2020/01/30	No	43
C2	Cyclic loading	0	3	2020/01/28	No	12
H2	Hybrid simulation	0	3	2020/01/16	Yes	Initial loading
H5	Hybrid simulation	0	3	2020/02/04	No	18
C3	Cyclic loading	23	1	2019/11/13	No	-
H3	Hybrid simulation	23	4	2020/01/24	Yes	Initial loading
H6	Hybrid simulation	23	1	2019/11/14	No	1

2.3 Quasi-static cyclic loading test

2.3.1 Loading history

The cyclic shear loading tests were conducted with a constant axial stress of 6 MPa. The displacement pattern of sinusoidal function with a frequency of 0.25 Hz, shear strain amplitudes of 50%, 100%, 150%, 200% and 250%, progressed from 50% to 250% with 5

cycles were repeated at each shear strain amplitude, as shown in Fig. 2.8. Although it is not indicated in the figure, one cycle with taper amplitude was loaded after the 5th cycle in each strain amplitude to avoid abrupt stop of the loading system. Also, the cyclic loading is halted during interval times of approximately 3 minutes before the start of loading cycles with different strain amplitudes.

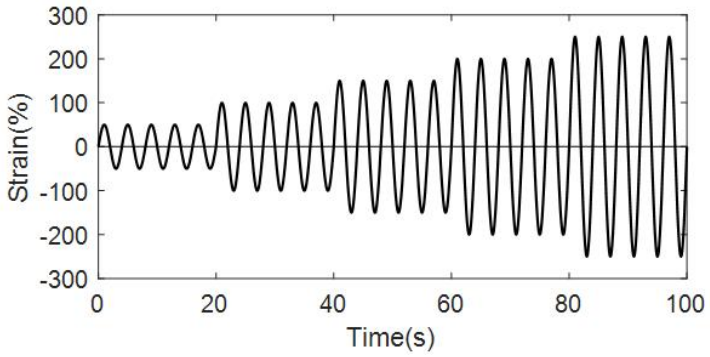

Figure 2.8 Loading pattern applied in cyclic loading test

The loading condition in cyclic loading test is specified in Table 2.5.

Table 2.5 Loading condition in cyclic loading test

Axial stress (MPa)	6				
Strain amplitude (%)	50	100	150	200	250
Horizontal displacement (mm)	15	30	45	60	75
Frequency (Hz)	0.25	0.25	0.25	0.25	0.25
Period (sec)	4	4	4	4	4
Maximum velocity (mm/s)	23.55	47.1	70.65	94.2	117.75
Number of cycle	5				
Ambient temperature (°C)	23, 0, −20				

2.3.2 Cyclic behavior of the HDR bearing at different temperatures

The shear stress–strain relationships of the HDR bearing specimens obtained in the cyclic loading tests C1, C2 and C3 are shown in Fig. 2.9. The strain is calculated as the relative displacement of the specimen divided by the total rubber thickness, and the stress is calculated as the load divided by the cross-sectional area of the rubber layer. Those test results shows the features of the restoring force characteristics of HDR bearings as described in Section 1.2, so that the stiffness of the HDR bearing increases as the ambient temperature decreases, and the stiffness decreases with the progress of the loading cycle at the same strain level. In particular, the drop of the maximum load between the first and second cycles as the consequence of the Mullins effect becomes more visible at lower ambient temperatures.

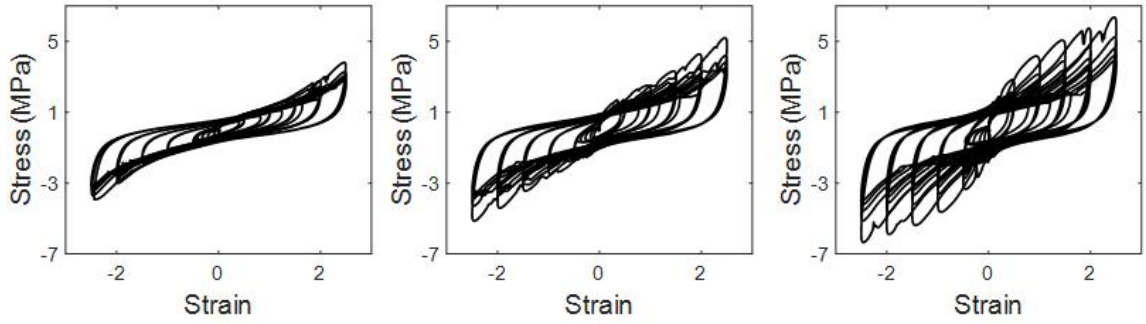

(a) 23℃ (b) 0℃ (c) −20℃

Figure 2.9 Shear stress–strain relationships of the HDR bearings at different temperatures

2.3.3 Mechanical characteristics of the HDR bearing

Based on the hysteresis loops of HDR bearings in the cyclic loading tests, the shear modulus and equivalent damping ratio of the bearing are calculated.

According to the design manual [72], the equivalent shear modulus G_e is calculated by

$$G_e = \frac{t_r}{A}\frac{f_m^+ - f_m^-}{d_m^+ - d_m^-} \tag{2.1}$$

where t_r is the total thickness of the rubber layers, A is the cross-sectional area of the bearing, f_m^+ and f_m^- are the maximum and minimum forces of the bearing, respectively, d_m^+ and d_m^- are the maximum and minimum displacements of the bearing, respectively in one cycle obtained in cyclic loading tests.

The equivalent damping ratio h_{eq} is defined by

$$h_{\mathrm{eq}} = \frac{E}{2\pi W} \tag{2.2}$$

where E is the energy loss per cycle and can be calculated as the area of one displacement-force hysteresis loop, W is the elastic strain energy. The energy loss E and elastic strain energy W are shown in Fig. 2.10.

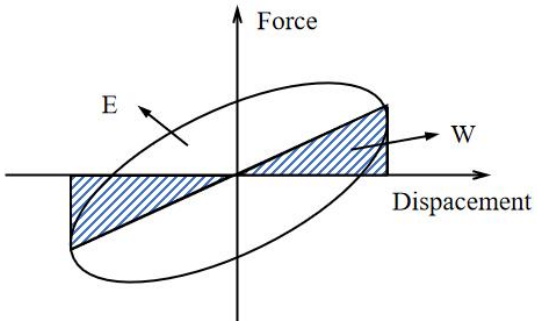

Figure 2.10 Energy loss and elastic strain energy

Bilinear model is a simple non-linear hysteretic restoring force model with only three

parameters: the elastic stiffness K_1, the characteristic strength q, and the post-yield stiffness ratio α calculated as the post-yield stiffness K_2 divided by K_1. Additional parameters shown in Fig. 2.11 are the yield force F_0 and the yield displacement d_0. More details about the bilinear model is described in section 2.8.1.

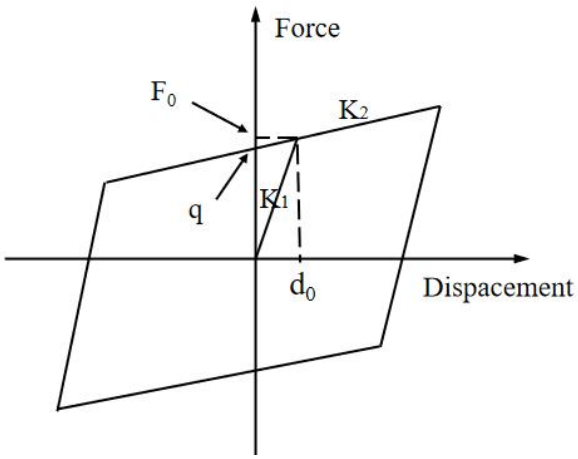

Figure 2.11 Bilinear model

The shear modulus G_1 and G_2 are defined by

$$G_1 = \frac{K_1 \times t_r}{A} \tag{2.3}$$

$$G_2 = \frac{K_2 \times t_r}{A} \tag{2.4}$$

where K_1 and K_2 are the bilinear model parameters shown in Fig 2.11, and are identified by the hysteresis loops obtained in the cyclic loading tests.

The plot of the shear modulus and equivalent damping ratio of the bearing versus the strain amplitude obtained by the cyclic loading tests C1, C2 and C3 are shown in Fig. 2.12. The results calculated by the first cycle and the fifth cycles are shown in the plot. Not only the increase of the shear modulus but also the increase of the equivalent damping ratio for the lower ambient temperatures are observed. Although the difference in the shear modulus between the first and fifth cycles becomes greater for lower temperatures, no significant change of the equivalent damping ratios between the first and fifth cycles is observed at each temperature. The shear modulus and equivalent damping ratio calculated by the empirical polynomial functions of the shear strain specified in the design manual [72] are also shown in Fig. 2.12 for comparison. The design manual provides the values close to the results of the cyclic loading tests at 23℃.

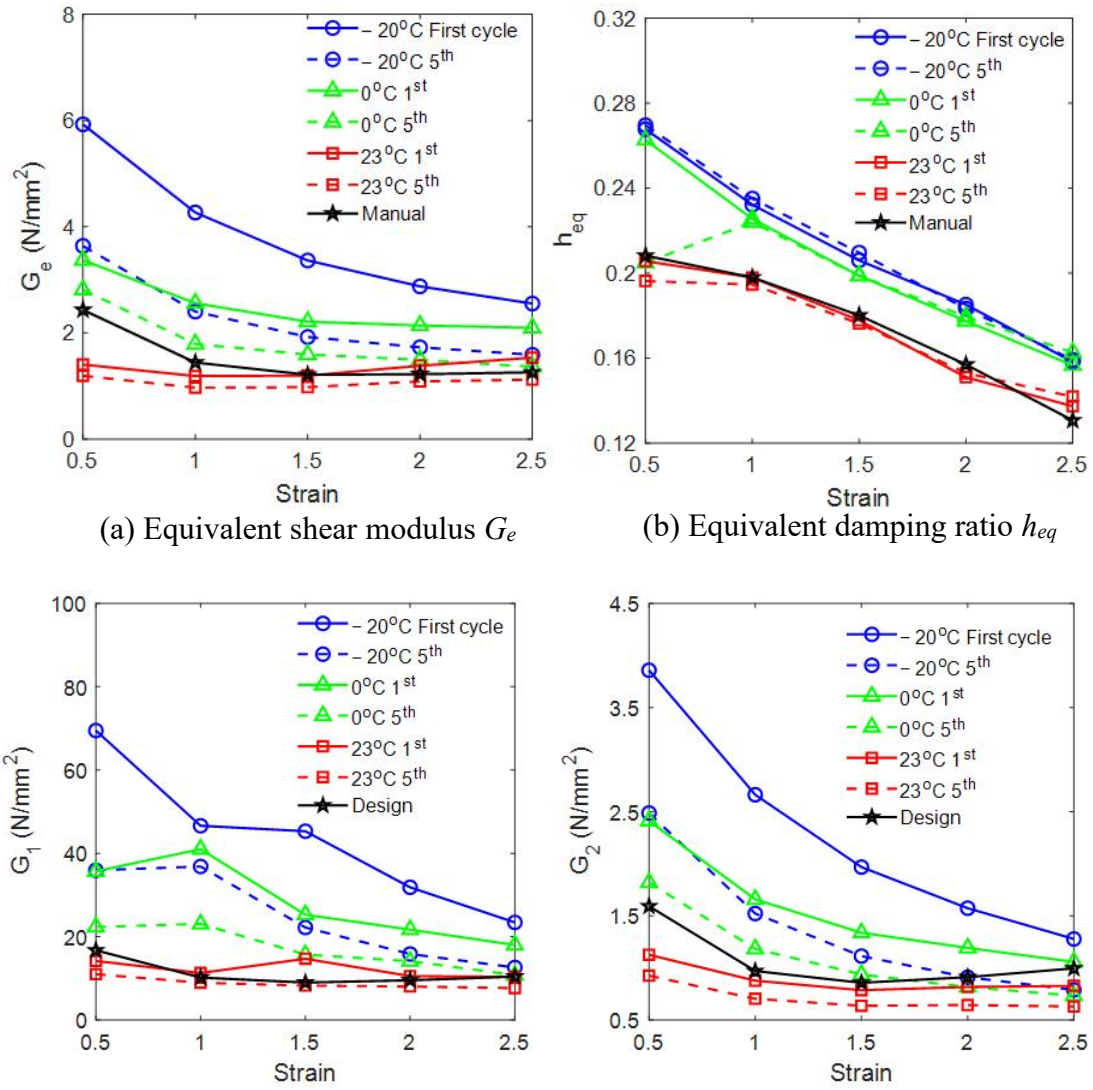

(a) Equivalent shear modulus G_e (b) Equivalent damping ratio h_{eq}

(c) Shear modulus G_1 (d) Shear modulus G_2

Figure 2.12 Shear modulus and equivalent damping ratio of the HDR bearing

Consequently, the mechanical characteristics of HDR bearings should be described according to the inner temperature of the bearing, which is dependent on both the initial ambient temperature and self-heating under cyclic loading. Because the loading condition of the bearing is different under cyclic loading and ground motions, it is challenging to use the hysteresis loops of cyclic loading to investigate the seismic performance of the HDR bearing. Hence, the hybrid simulation is conducted to investigate the seismic performance of the HDR bearings at room and low temperatures in the following section.

2.4 Hybrid simulation description

2.4.1 Simulation model

For the loading tests of the HDR bearing specimens using hybrid simulation, application of HDR bearings installed in a hypothetical 3-span continuous girder bridge is assumed as shown in Fig. 2.13. The isolated bridge is modeled as a two degree-of-freedom system in the longitudinal direction for the dynamic response, in which the four piers and eight HDR bearings that support the superstructure behave identically. Displacements of the lumped masses m_1 and m_2 represent the response of the superstructure and the pier top, respectively. The pier is assumed to be a linear elastic element with stiffness k_2 for simplicity.

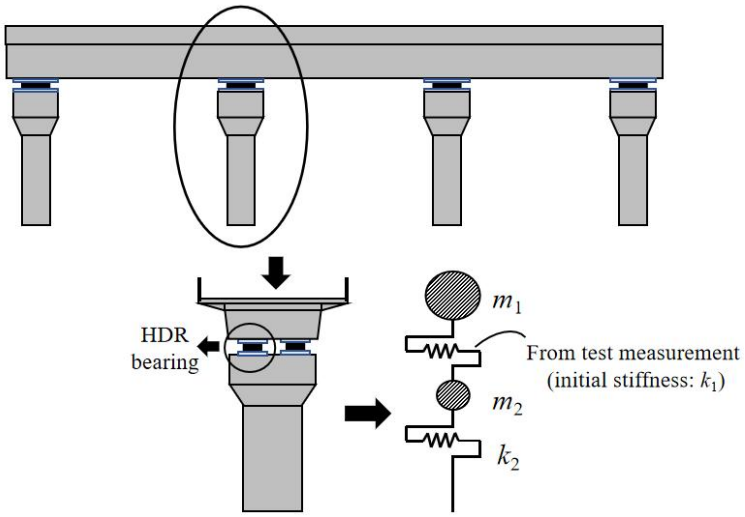

Figure 2.13 Assumed bridge and dynamic model

The characteristic values of the 2-DOF model are shown in Table 2.6. The natural period of the bridge model is calculated based on the initial stiffness of the bearing measured obtained in a preliminary cyclic loading test with a strain amplitude of 175% at room temperature. The shown natural period, 1.3 sec, is slightly shorter than normal values for usual seismic isolation bridges determined with 1/3 of the initial stiffness of the bearing according to the seismic design practice. In this study, the initial stiffness is used for the HDR bearings to avoid the overshooting at the loading steps.

Table 2.6 Characteristic values of 2-DOF model

Super-structure mass, m_1	10156 (ton)
Pier mass, m_2	3385 (ton)
Initial stiffness of bearing, k_1	955 (kN/mm)
Stiffness of pier, k_2	400 (kN/mm)
Damping ratio	0.05
Natural period	1.3 (sec)

2.4.2 Experimental framework

The framework of the test system for hybrid simulation is shown in Fig. 2.14. The numerical time integration of the equations of motion and the command signal processing were conducted in a DSP unit implementing Texas Instruments OMAP-L137 EVM processor. A Windows-based test control PC was used to control and monitor the code execution in the DSP unit. The measurement data was displayed and recorded in a PC for measurement. The velocity of the imposed displacement by the loading system was limited to 10 mm/s. A similitude law was used in the hybrid simulation as shown in Table 2.7, it is based on the same strain and stress between the bearing with real size and the 1/6 scaled bearing specimen in the test, hence, the scale factor is 6, implying that the plan dimensions of the prototype HDR bearing are assumed to be 1440 × 1440 mm, and the total rubber thickness is 180mm. At each time step, the numerical time integration of the equations of motion using the Newmark's β (β=1/6) method was conducted in the DSP (Digital Signal Processor) at a quick speed, and the calculated numerical bearing's displacement was divided by 6 and sent to the control panel through the terminal block, then the specimen was loaded by the loading system according to the signal obtained from the control panel, next, the measured restoring force of the specimen was multiplied by 36 and send to the DSP for correction of the seismic response of isolated bridge [73-74]. This procedure was repeated until the end of hybrid simulation. The C language is used to develop the program in the DSP and visual C++ language is used to develop the program in the test control PC. The details about the algorithm for hybrid simulation in this study can be found in Appendix A.

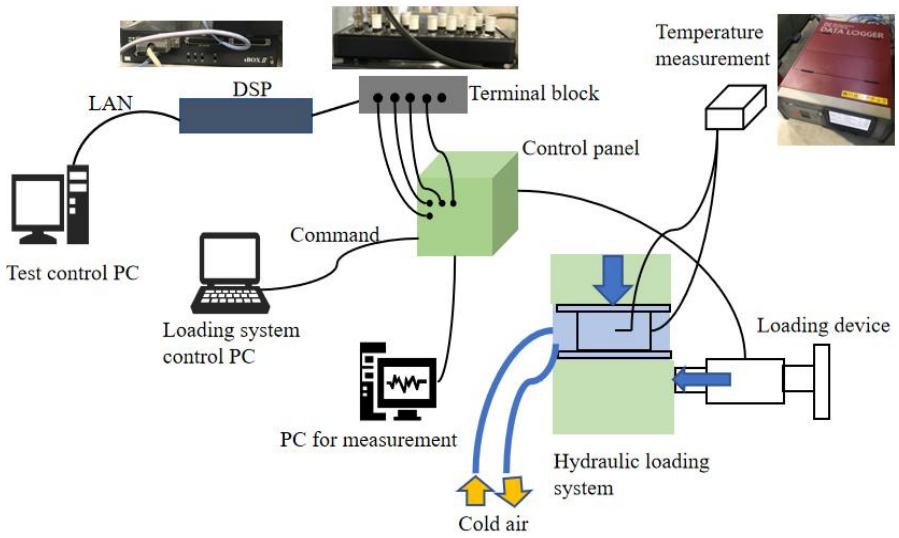

Figure 2.14 Overview of the hybrid simulation system

Table 2.7 Similitude law for hybrid simulation

Physical parameter	Unit	Scale factor
Length	m	S
Area	m^2	S^2
Volume	m^3	S^3
Strain	1	1
Stress	N/m^2	1
Displacement	m	S
Force	N	S^2
Stiffness	N/m	S
Acceleration	m/s^2	S^{-1}
Mass	kg	S^3
Velocity	m/s	1
Time	sec	S

2.4.3 Input ground motion

Level-2 type II ground type-II accelerogram 1 (II-II-1) specified in the Design Specification of Highway Bridges (Japan Road Association, 2017) shown in Fig. 2.15 was used as the input ground motion.

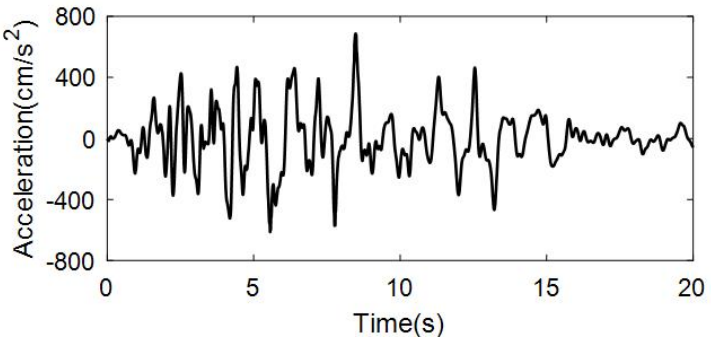

Figure 2.15 Input ground motion

2.5 Hybrid simulation results

The results from section 2.5.1 to 2.5.4 are obtained in hybrid simulation H1, H2 and H3, and the comparison of initial loading effect is discussed in section 2.5.5.

2.5.1 Seimic response of HDR bearings isolated bridge

The load-displacement hysteresis loops and shear strain time history of the HDR bearings

obtained in Tests H1, H2 and H3 are shown in terms of stress-strain relationship in Fig. 2.16. The tendency of higher stiffness and peak loads for lower ambient temperatures can also be seen in the simulated seismic response. The maximum strain of the bearing is reduced by a factor of 0.55 at −20°C compared with the result at 23°C in the negative direction of the strain. However, the increased restoring force of the HDR bearing in lower temperatures results in increased maximum displacement in the positive side of the bearing displacement in these seismic loading cases.

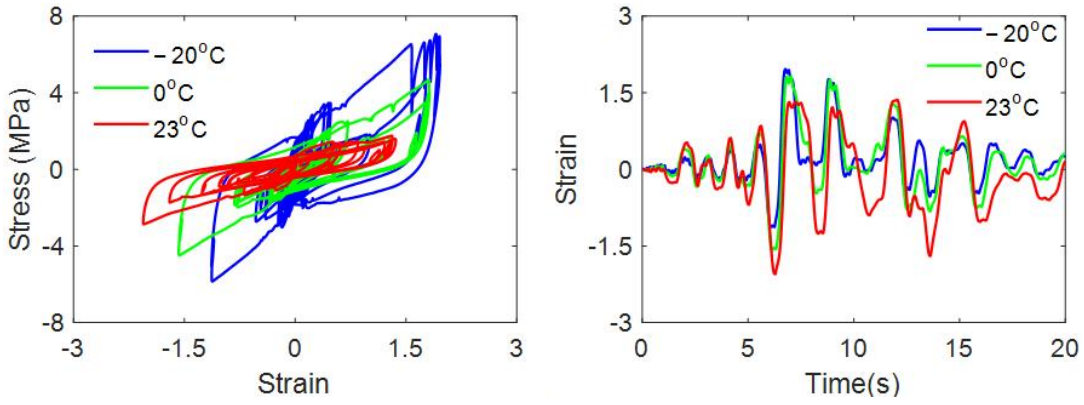

(a) Hysteresis loop (b) Time history

Figure 2.16 Test results of HDR bearing responses

The pier top displacement, velocity and acceleration simulated in Tests H1, H2, H3 are shown in Fig. 2.17. The pier top responses at lower temperatures are greater than those at 23°C, and the maximum pier top displacement is increased by a factor of 2.82 at −20°C compared with that at 23°C. It is presumably cause by the increased restoring force of the bearing at lower temperatures, and the force transmitted to the pier consequently becomes larger. These test results can be a quantitative demonstration of low temperature effect on the mechanical characteristics and the anticipated increase in seismic demand of piers due to a low temperature. The increased load and stiffness of the HDR bearings in lower temperatures appear to be reflected in the increase of the pier top acceleration amplitude as indicated by Fig. 17(c).

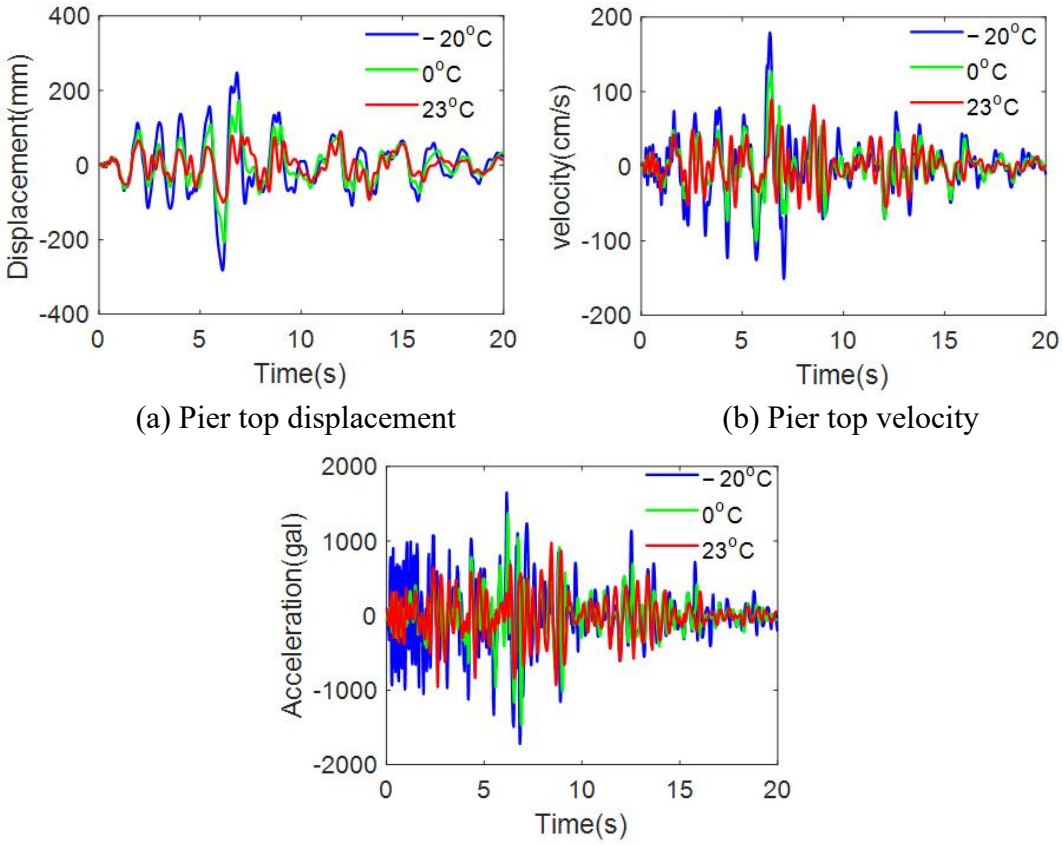

(a) Pier top displacement (b) Pier top velocity

(c) Pier top acceleration

Figure 2.17 Pier top responses

The super-structure response in Tests H1, H2, H3 is shown in Fig. 2.18, and it can be concluded that the super-structure response at lower temperature is greater than those for 23°C, implying the quantitative increase of seismic demand of super-structure due to a low temperature.

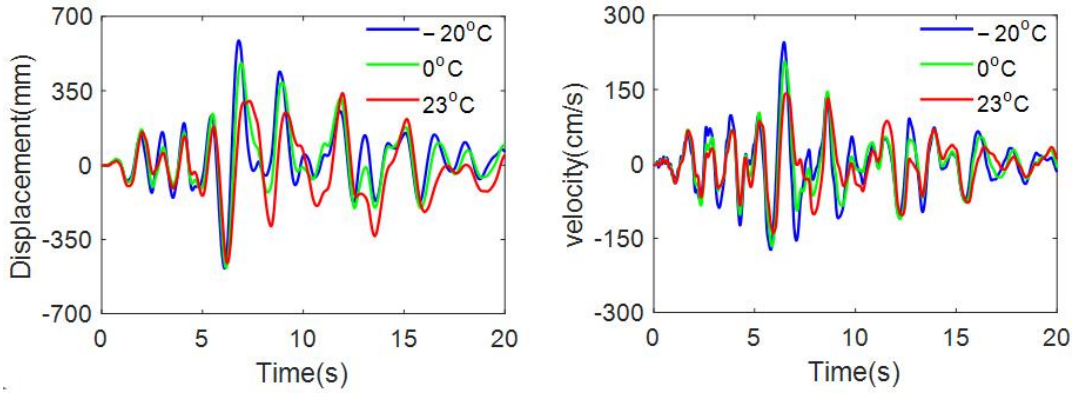

(a) Super-structure displacement (b) Super-structure velocity

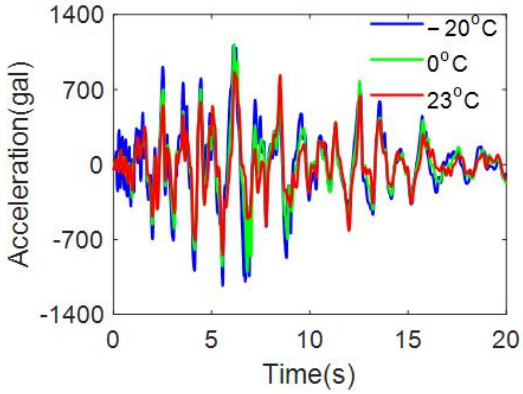

(c) Super-structure acceleration

Figure 2.18 Super-structure response

The seismic response amplification factor of HDR bearings isolated bridge due to low temperatures is shown in Table 2.8, the amplification factor is calculated as the maximum response at 0°C/−20°C divided by the maximum response at 23°C in the positive or negative direction, m_1 and m_2 represent the super-structure and pier, respectively. The maximum pier top displacement is increased by a factor of 2.82 at −20°C and 2.06 at 0°C compared with the result at 23°C, implying the quantitative increase of seismic demand of piers due to a low temperature.

Table 2.8 Seismic response amplification factor due to low temperatures

Temperature case	Bearing strain	Bearing stress	m_1 disp.	m_1 vel.	m_1 accle.	m_2 disp.	m_2 vel.	m_2 accle.
0ºC	0.77	2.66	1.42	1.46	1.30	2.06	1.64	1.54
−20ºC	0.55	3.96	1.73	1.73	1.34	2.82	2.47	1.80

2.5.2 Ratio of maximum response to earthquake motion

The ratios of the maximum absolute acceleration and displacement between the super-structure or pier and the earthquake ground motion were obtained from Eqs. 2.5 and 2.6, respectively, in which $a_{pier/super}$ is the maximum absolute acceleration of the pier or super-structure, $d_{pier/super}$ is the maximum absolute displacement of the pier or super-structure, and a_e and d_e are the maximum acceleration and displacement of the earthquake ground motion, respectively.

$$R_a = \frac{a_{pier/super} + a_e}{a_e} \tag{2.5}$$

$$R_d = \frac{d_{pier/super} + d_e}{d_e} \tag{2.6}$$

To observe changes in the response mode shape of the entire bridge, the maximum responses of the acceleration and displacement for the 2-DOF system model, corresponding to the super-structure and the top of the pier, are shown in Fig. 2.19, normalized by the maximum ground motion value. Here the horizontal axis shows the response ratio for each DOF at each ambient temperature. It can be seen that the maximum acceleration of the pier is larger than that of the super-structure at lower temperatures. The maximum displacement of the pier is smaller than that of the super-structure at 23 ℃ and similar to that of the super-structure at 0 ℃; however, at −20 ℃, the maximum displacement of the pier is larger than that of the super-structure. Thus, the deformation primarily occurs at the pier at low temperatures, which may arise from a changed structural modal shape caused by hardening of the rubber bearings at low temperatures.

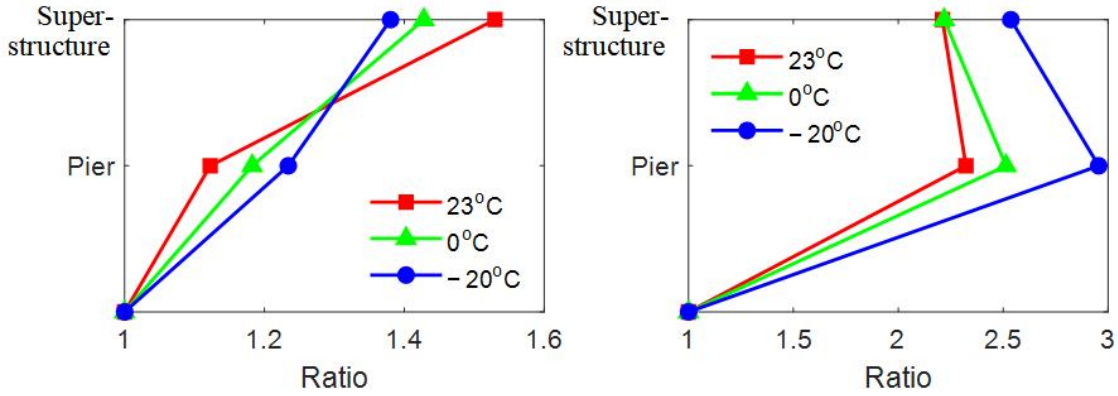

(a) Ratio of displacement (b) Ratio of acceleration

Figure 2.19 Ratio of the maximum response between the super-structure or pier and the earthquake motion

2.5.3 Measured Temperature

The plot of the measured temperature of the HDR bearings is shown in Fig. 2.20. The simulated seismic loading was performed within the time range marked by solid lines and arrows in the plot. The plot shows the temperature data measured by the thermocouples that successfully survived from the beginning until the end of the simulated seismic loading. In all ambient temperature cases, while the rise of the surface temperatures (S1 and S2) of the bearing from the ambient temperature throughout the simulated seismic loading is observed to be limited, the variation of the inner temperature (P1 and P2) is shown to be significant, particularly in Test H1 (−20℃). After the rise of the temperature during the loading, the temperature decay after the end of loading can be seen in all cases. However, the decay of the temperature does not seem to be simply an exponential function converging to the ambient temperature with constant decay rates. It may be explained by the assumption that the process of the temperature change involves not only the heat transfer with the loading interfaces through the base plates and shear keys, but also heat conduction within the bearing rubber material and steel plates.

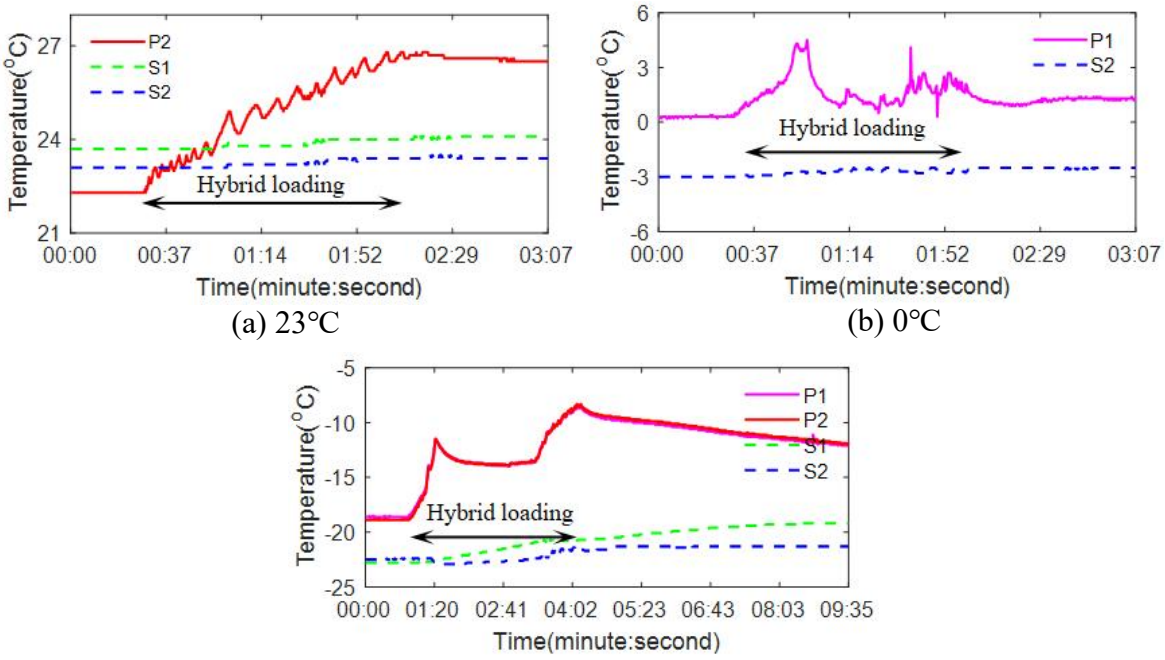

(a) 23°C (b) 0°C

(c) −20°C

Figure 2.20 Measure temperature of HDR bearings at different temperatures

2.5.4 Energy dissipation

The dissipated energy E_n at each time step n is determined by

$$E_n = \sum_{k=1}^{n} \frac{(d_k - d_{k-1}) \times (f_k + f_{k-1})}{2} \tag{2.7}$$

where d is the displacement and f is the force of the bearing specimen, respectively, which are obtained in hybrid simulation.

The calculated dissipated energy at three ambient temperature cases is shown in Fig. 2.21. The energy dissipation capacity increases due to the exposure to lower ambient temperatures, which is favorable under ground motions, as the energy will be mainly absorbed by the HDR bearings rather than by the piers. A sharp increase in the dissipated energy is observed at approximately 6 sec, and is caused by the sharp increased deformation of the HDR bearing.

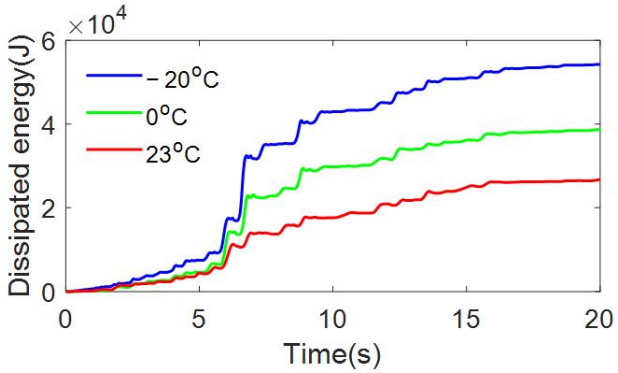

Figure 2.21 Dissipated energy

2.5.5 Initial loading effect on seismic response

The shear strain stress hysteresis loops of the HDR bearing under initial (Tests H1, H2, H3) and non-initial (Tests H4, H5, H6) loading are shown in Fig. 2.22 at three ambient temperatures. For the cases of 23°C and −20°C, there was no significant difference in the hysteresis curves, although the stress was slightly larger under initial loading. At 0°C, there was a slight difference between the two situations, which arose because the two internal thermocouples were damaged prior to the Test H5. Thus, the initial inner bearing temperature was unknown, and the Test H5 was started when the surface temperature was −3°C. In this case, the actual internal temperature of the bearing specimen was unknown (in the Test H2, the surface temperature of the bearing was −3°C, and the internal temperature was 0°C).

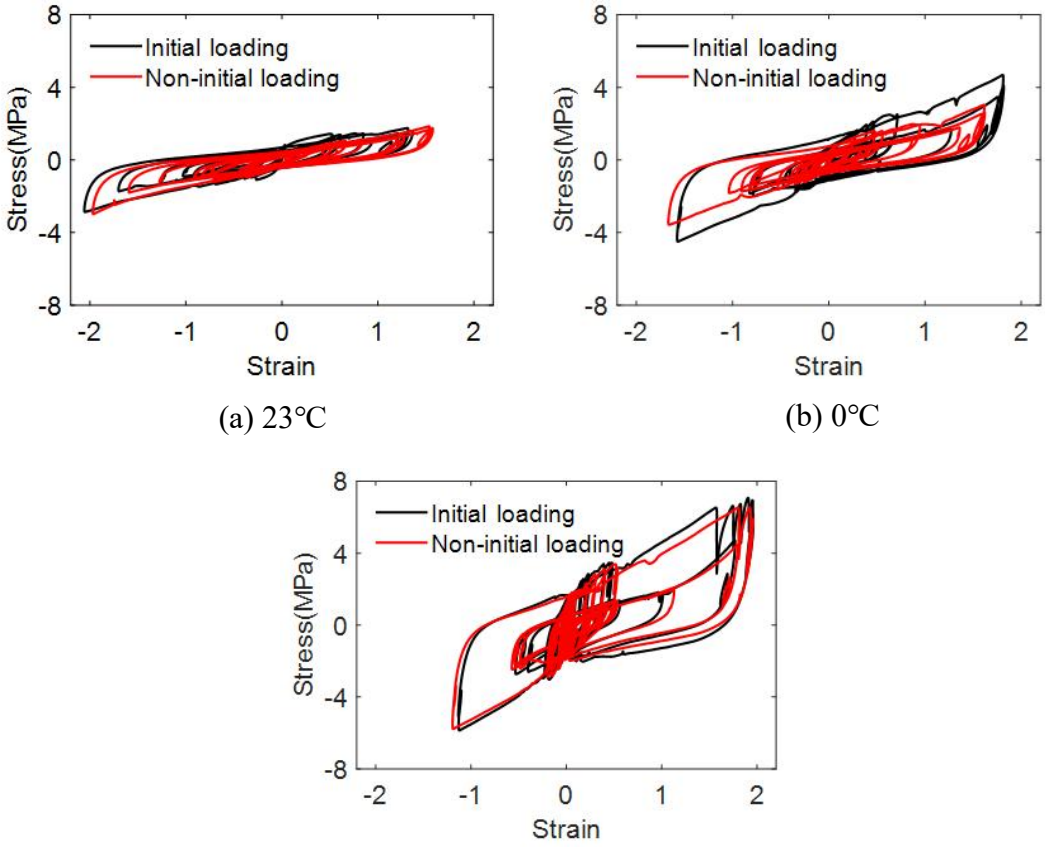

(a) 23°C (b) 0°C

(c) −20°C

Figure 2.22 Shear strain stress hysteresis loops of the HDR bearing under initial and non-initial loading

The shear strain of the HDR bearing under initial (Tests H1, H2, H3) and non-initial (Tests H4, H5, H6) loading is shown in Fig. 2.23 for the three ambient temperature cases, and it can also be seen that there was no significant difference in the bearing strain for each ambient temperature case. Thus, the initial loading effect appears to have little influence on the seismic performance of HDR bearings, however, the assertion from these limited experiments may not be valid. In addition, the dependence on the internal temperature is easier to be predicted than the effect of the initial loading effect on the seismic performance of the bearing, and it is more appropriate to consider these two effects respectively.

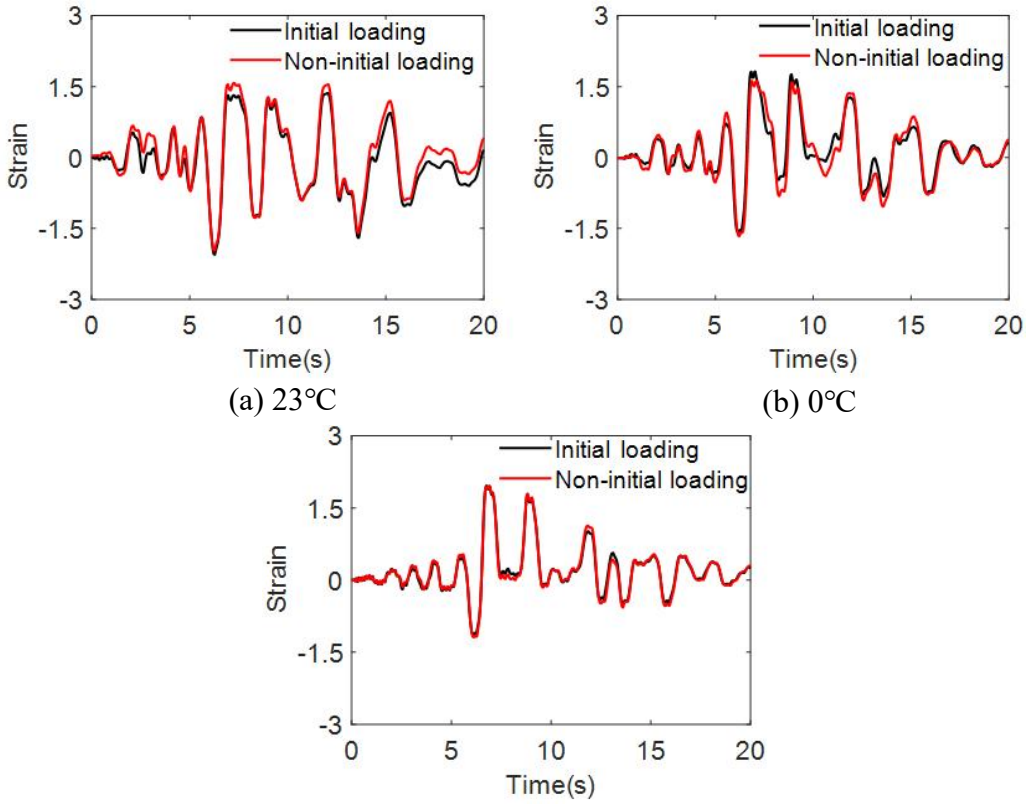

(a) 23℃ (b) 0℃

(c) −20℃

Figure 2.23 Shear strain time history of the HDR bearing under initial and non-initial loading

2.6 Comparison of numerical and experimental inner temperature

2.6.1 Inner temperature evaluation method

The inner temperature of the bearing is increased as the HDR bearing with hysteretic damping absorbs the energy produced under cyclic loading and converts it into heat energy. Okui et al. [9] developed a simple formula to calculate the inner temperature of the HDR bearing. Although the temperature inside the HDR bearing is not uniformly distributed because of the temperature diffusion, the inner temperature is assumed to be uniformly distributed over the volume of bearing for simplicity of calculation in [9], as expressed by

$$\dot{T} = \dot{E}\lambda \tag{2.8}$$

where T is the inner temperature of the HDR bearing, E is the dissipated energy due to the hysteretic force-displacement response of the bearing under cyclic loading, and the dot symbol denotes the time derivative. The dissipated energy E is expressed as

$$E(t) = \int_0^t F(\tau)\dot{d}(\tau)d\tau \tag{2.9}$$

in which $F(t)$ and $d(t)$ are the shear force and displacement of bearing at time t, respectively. In the case of cyclic loading, increase of E per cycle corresponds to the area of one hysteresis loop. The constant λ is determined by

$$\lambda = \frac{1}{m_r C_{\mathrm{pr}} + m_s C_{ps}} \tag{2.10}$$

where m_r and C_{pr} are the mass and specific heat capacity of rubber layers, respectively, m_s and C_{ps} are the mass and specific heat capacity of steel layers, respectively.

In this study, the Eq. 2.8 is extended by including the energy loss caused by the heat radiation and conduction from the bearing contact surfaces for higher precision, as expressed by

$$\dot{T} = \left(\dot{\mathrm{E}} - \dot{Q}\right)\lambda \tag{2.11}$$

where the energy loss Q is expressed by

$$\dot{Q} = Ah\left(T - T_a\right) \tag{2.12}$$

in which A is the side area of the shear key, as the energy loss is considered to be the energy of heat transfer from the bearing to the base plates through the shear key. In the natural environment, A is assumed to be the sum of upper and lower surface areas of the HDR bearing which is larger than the side area of the shear key in the test. The parameter h is the convective heat transfer coefficient given by $W/(m^2 \cdot K)$, where W, m, K are the convective heat, length and temperature, respectively, and T_a is the ambient temperature, which is set to be 23°C, 0°C or −20°C, respectively for each ambient temperature case of test in this study. The density and thermal property of rubber and steel are presented in Table 2.9, and the material parameters are presented in Table 2.10. The details of calculation method for parameters A and λ can be found in Appendix B.

Table 2.9 Density and thermal property of rubber and steel

Material	Density(kg/m^3)	Specific heat capacity(J/(kg·K))
Rubber	1146	1732
Steel	7740	432

Table 2.10 Material parameters

A (m^2)	h ($W/(m^2 \cdot K)$)	$\lambda(K/J)$
0.0042	300	1.536e-4

2.6.2 Comparison of numerical and experimental inner temperature of bearing in cyclic loading test

In this section, the analytical inner temperature is compared with the experimental temperature measured in cyclic loading tests C1, C2, C3. There are three different analytical cases of the inner temperature, as shown in Table 2.11. To investigate the effect of energy loss, a comparison between case 1 and case 2 is conducted, the Eq. 2.8 and Eq. 2.11 are used in case 1 and 2, respectively. And a comparison between case 2 and case 3 is also conducted to investigate the effect of the bearing contact surface area A for the energy loss calculation. The A of case 2 is the cross sectional area of the shear key in hybrid simulation considering about the insulation measures, and the A of case 3 is the sum of upper and lower surface area of the bearing considering about the actual environment for isolated bearings. The details of calculation for parameter A can be found in appendix B.

Table 2.11 Analytical cases of inner temperature

Case 1	Eq. 2.8
Case 2	Eq. 2.11 A=0.0042m^2
Case 3	Eq. 2.11 A=0.1152m^2

The calculated inner temperature is compared with those measured by the thermocouples (P1 or P2) installed in the central section of HDR bearings in cyclic loading tests C1, C2, C3, as shown in Fig. 2.24. Only the inner temperature of shear strain amplitudes 50%, 100%, 150% at ambient temperature −20°C and 50%, 100% at 0°C was successfully measured, as the thermocouples were broken by the cyclic loading at larger strain levels, and the thermocouples were broken by the cyclic loading in the beginning at ambient temperature 23°C. Furthermore, there was a pause between the adjacent different shear strain amplitudes in order to input test control parameters for the next cyclic loading of higher strain amplitude. It is observed that the experimental temperature is higher than case1 or case2 at the loading phase for each strain amplitude, as the measured inner temperature is higher than the uniform temperature, then the experimental temperature tends to be same with the case1 or case2 because of the temperature diffusion. The temperature in case 2 is smaller than case 1 as the energy loss is considered in case 2, but there is not obvious difference between case 1 and case 2 because of the good insulation measures in the test. The analytical temperature in case 3 gradually decreases to the ambient temperature and the temperature drop rate is higher than the case 2, as the energy loss is greater in case 2.

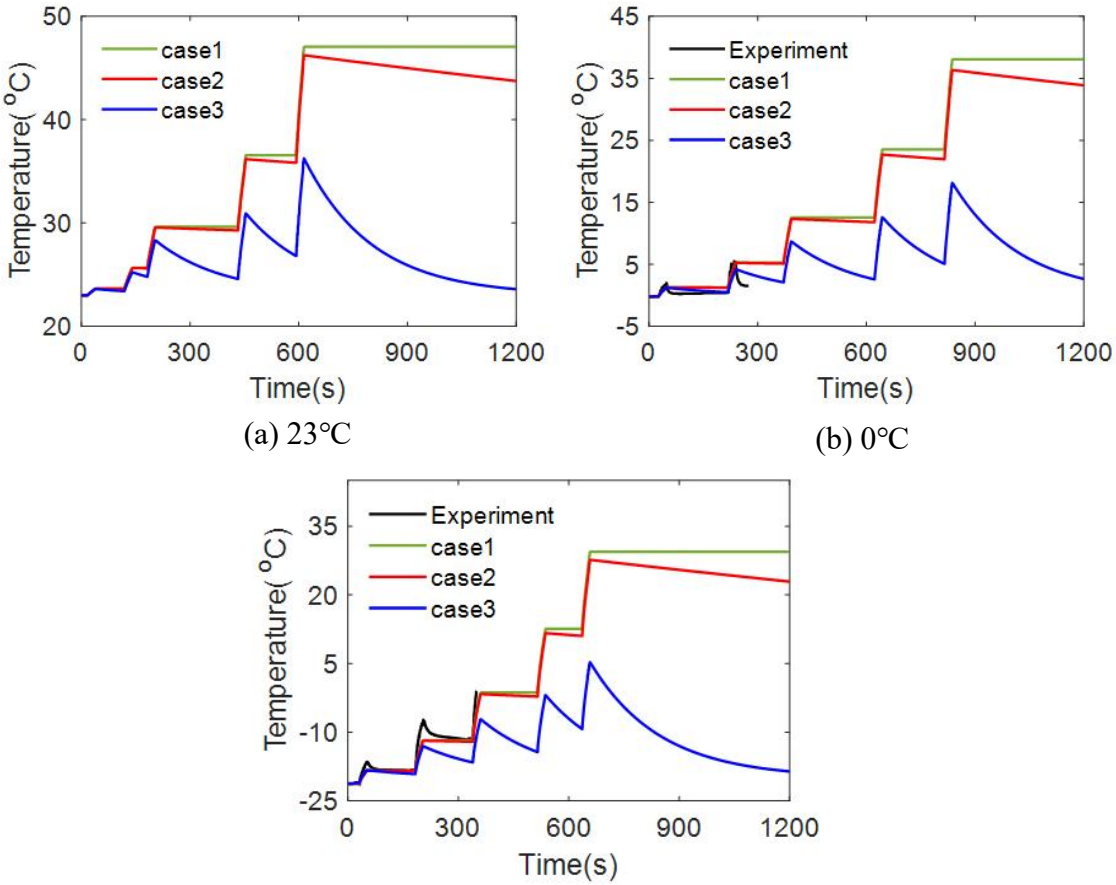

Figure 2.24 Comparison between experimental and numerical inner temperature of HDR bearings in cyclic loading

2.6.3 Comparison of numerical and experimental inner temperature of the bearing in hybrid simulation

Comparison between the numerical inner temperatures using hysteresis loops of bearings directly obtained in Tests H1, H2, H3, H4 and those measured by thermocouples (P1 and P2) installed in the central location of bearings in Tests H1, H2, H3, H4 is shown in Fig. 2.25. The difference between the numerical and experimental inner temperature is considered to be caused by the nonuniform distribution of the actual inner temperature over the volume of bearings, as opposed to the assumption of uniformly distributed inner temperature in Eq. 2.8 and Eq. 2.11. The momentary temperature decrease is caused by the decreased area of hysteretic force-displacement loop of HDR bearing in unloading phase. The tendency of the time variation of the inner temperature is found to be similar between the analytical value and that measured during the test except for the case of 0℃. The discrepancy for Test H2 (0℃ case) is due to the failure and malfunction of the thermocouples.

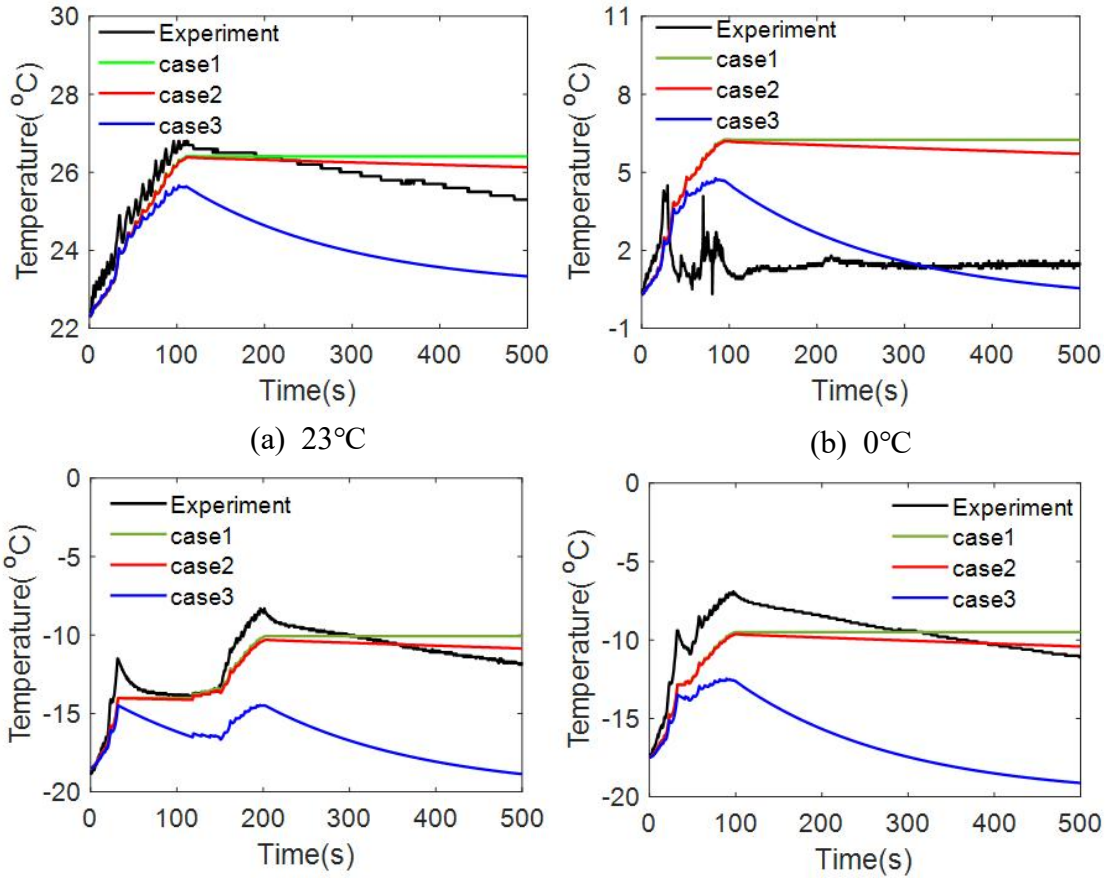

(a) 23℃ (b) 0℃

(c) −20℃ (Test H1) (d) −20℃ (Test H4)

Figure 2.25 Comparison between experimental and numerical inner temperature of HDR bearings in hybrid simulation

2.7 Hysteresis behavior depending on inner temperature and strain amplitude

The shear modulus and equivalent damping ratio of HDR bearings are plotted against calculated inner temperature by Eq. 2.11 at different strain amplitude levels, as shown in Fig. 2.26. For each strain level, the first to the fifth data points are calculated from the five hysteresis loops of the bearing obtained in cyclic loading test at ambient temperature −20°C, the sixth to the tenth data points are calculated from the five hysteresis loops at 0°C, and the eleventh to the fifteenth data points are calculated from the five hysteresis loops at 23°C. It can be seen that the variations of shear modulus and equivalent damping ratio are discontinuous for different ambient temperatures at the same strain level, especially at low strain levels, this may be caused by the heat conduction over the volume of the bearing, as the actual temperature distribution is not uniform over the volume of the bearing.

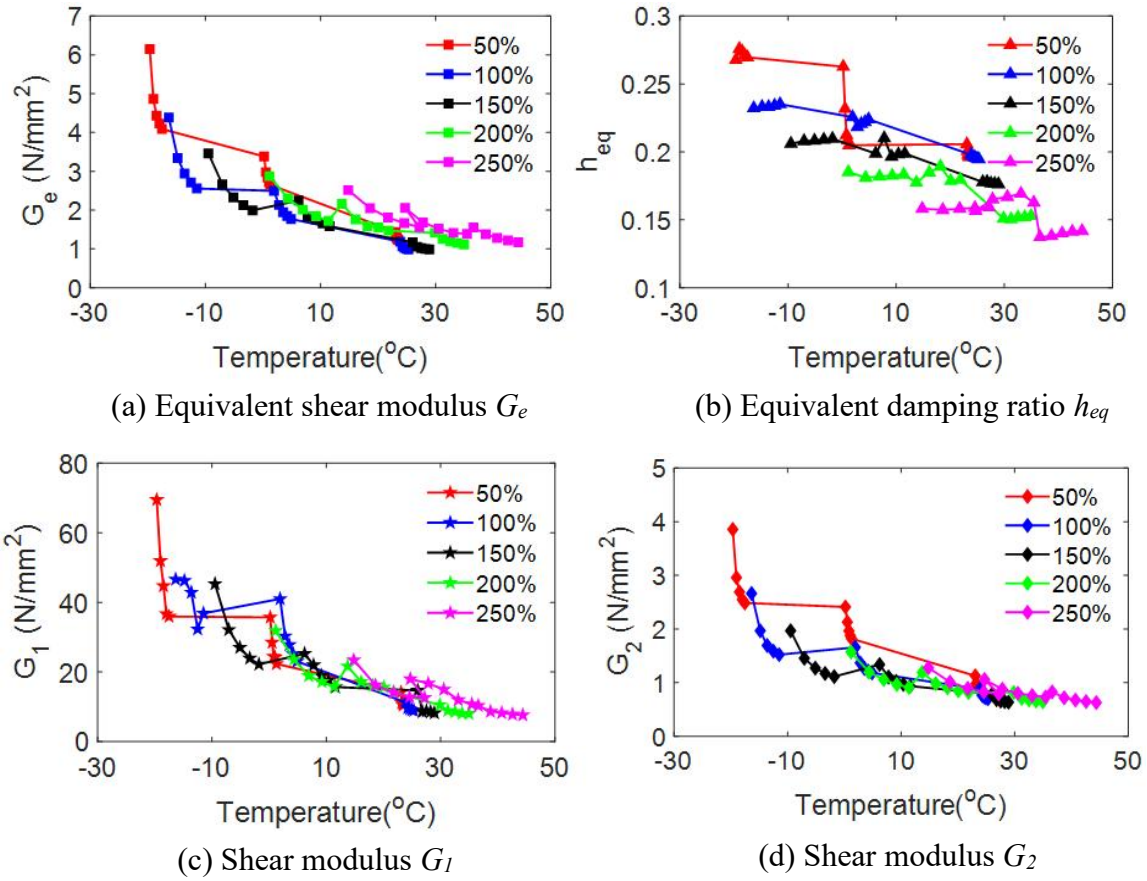

(a) Equivalent shear modulus G_e (b) Equivalent damping ratio h_{eq}

(c) Shear modulus G_1 (d) Shear modulus G_2

Figure 2.26 Shear modulus and equivalent damping ratio vs. inner temperature in cyclic loading

The equivalent shear modulus G_e and equivalent damping ratio h_{eq}, shear modulus G_1 and shear modulus G_2 are expressed by the predicted inner temperature T and the shear strain level ε, as expressed in the following 14 different equations. Only the polynomials are used from Eq. 2.13.a to Eq. 2.13.d, and the exponential formulas are used in other equations, Eq. 2.13.f to Eq. 2.13.n are simplified from the Eq. 2.13.e.

$$G_e / h_{eq} / G_1 / G_2 = a_1 + a_2 \times (T-23) + a_3 \times \varepsilon \tag{2.13.a}$$

$$G_e / h_{eq} / G_1 / G_2 = a_1 + a_2 \times (T-23) + a_3 \times (T-23)^2 + a_4 \times \varepsilon \tag{2.13.b}$$

$$G_e / h_{eq} / G_1 / G_2 = a_1 + a_2 \times (T-23) + a_3 \times \varepsilon + a_4 \times \varepsilon^2 \tag{2.13.c}$$

$$G_e / h_{eq} / G_1 / G_2 = a_1 + a_2 \times (T-23) + a_3 \times (T-23)^2 + a_4 \times \varepsilon + a_5 \times \varepsilon^2 \tag{2.13.d}$$

$$G_e / h_{eq} / G_1 / G_2 = a_1 \times (T-23) + a_2 \times e^{a_3 \times (T-23)} + a_4 \times \varepsilon + a_5 \times e^{a_6 \times \varepsilon} \tag{2.13.e}$$

$$G_e / h_{eq} / G_1 / G_2 = a_1 \times e^{a_2 \times (T-23)} + a_3 \times e^{a_4 \times \varepsilon} \tag{2.13.f}$$

$$G_e / h_{eq} / G_1 / G_2 = a_1 \times (T-23) + a_2 \times e^{a_3 \times (T-23)} + a_4 \times e^{a_5 \times \varepsilon} \tag{2.13.g}$$

$$G_e / h_{eq} / G_1 / G_2 = a_1 \times e^{a_2 \times (T-23)} + a_3 \times \varepsilon + a_4 \times e^{a_5 \times \varepsilon} \quad (2.13.h)$$

$$G_e / h_{eq} / G_1 / G_2 = a_1 \times (T-23) + a_2 \times e^{a_3 \times (T-23)} \quad (2.13.i)$$

$$G_e / h_{eq} / G_1 / G_2 = a_1 \times \varepsilon + a_2 \times e^{a_3 \times \varepsilon} \quad (2.13.j)$$

$$G_e / h_{eq} / G_1 / G_2 = a_1 \times (T-23) + a_2 \times e^{a_3 \times (T-23)} + a_4 \times \varepsilon \quad (2.13.k)$$

$$G_e / h_{eq} / G_1 / G_2 = a_1 \times (T-23) + a_2 \times \varepsilon + a_3 \times e^{a_4 \times \varepsilon} \quad (2.13.l)$$

$$G_e / h_{eq} / G_1 / G_2 = a_1 \times (T-23) + a_2 \times e^{a_3 \times \varepsilon} \quad (2.13.m)$$

$$G_e / h_{eq} / G_1 / G_2 = a_1 \times e^{a_2 \times (T-23)} + a_3 \times \varepsilon \quad (2.13.n)$$

From the comparison of these equations, the most suitable equation that fits the experimental data is chosen. The similarity of the analytical result comparing to the experimental result is defined by the contribution rate *R*, as expressed by

$$R = 1 - \frac{\sum_{i=1}^{N} (V_{an,i} - V_{ex,i})^2}{\sum_{i=1}^{N} (\overline{V_{ex}} - V_{ex,i})^2} \quad (2.14)$$

where the $V_{an,i}$ is the analytical result at time step *i*, $V_{ex,i}$ is the experimental result, and $\overline{V}_{ex}$ is the average of $V_{ex,i}$. In this section, the V is the shear modulus or equivalent damping ratio. The analytical result is closer to the experimental result when the *R* is closer to 1.

An optimum calculation method [59] is used to determine the formula parameters and corresponding contribution rate, and the details can be found in Appendix C, the calibrated contribution rate is summarized in Table 2.12. Although the contribution rate of Eq. 2.13.e is the largest, there is a modal overfitting by this formula. Hence, the Eq. 2.13.h with relatively smaller contribution rate and fewer parameters is chosen as the best formula, the contribution rates of shear modulus and equivalent damping ratio using Eq. 2.13.h are above 0.87, which shows a good agreement between the analytical and experimental results.

Table 2.12 Contribution rate of equivalent shear modulus and equivalent damping ratio

	6.a	6.b	6.c	6.d	6.e	6.f	6.g	6.h	6.i	6.j	6.k	6.l	6.m	6.n
G_e	0.733	0.837	0.857	0.900	0.937	0.856	0.900	0.912	0.842	0.240	0.849	0.854	0.736	0.841
h_{eq}	0.913	0.920	0.917	0.921	0.922	0.920	0.920	0.922	0.769	0.686	0.920	0.916	0.915	0.917
G_1	0.820	0.870	0.843	0.875	0.877	0.874	0.878	0.870	0.866	0.224	0.872	0.836	0.821	0.870
G_2	0.726	0.814	0.850	0.882	0.918	0.831	0.882	0.894	0.807	0.410	0.821	0.852	0.731	0.794

Hence, the shear modulus and equivalent damping ratio are expressed by Eq. 2.13.h, and the identified parameters of shear modulus and equivalent damping ratio are summarized in Table 2.13.

$$G_e / h_{eq} / G_1 / G_2 = a_1 \times e^{a_2 \times (T-23)} + a_3 \times \varepsilon + a_4 \times e^{a_5 \times \varepsilon} \quad (2.13.h)$$

Table 2.13 Identified parameters of shear modulus and equivalent damping ratio

	a_1	a_2	a_3	a_4	a_5
G_e	0.588	-0.044	0.448	39.130	-7.716
h_{eq}	0.041	-0.021	-0.007	0.178	-0.111
G_1	11.597	-0.034	1.031	0.495	-2.925
G_2	0.413	-0.039	0.199	4.264	-3.521

The best fit 3D plots for the relationship between shear modulus/equivalent damping ratio, inner temperature and shear strain are shown in Fig. 2.27. The scatter points are the experimental results, and the surface is fitted by Eq. 2.13.h. It is observed that the equivalent damping ratio is less affected by inner temperature compared to the shear modulus.

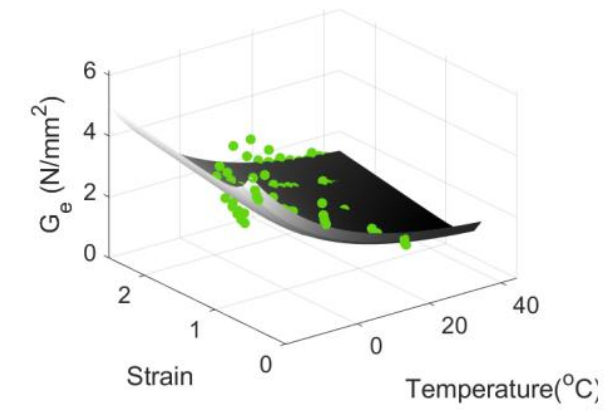

(a) Equivalent shear modulus G_e

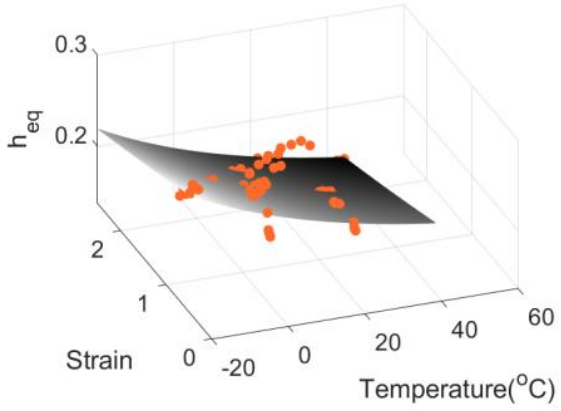

(b) Equivalent damping ratio h_{eq}

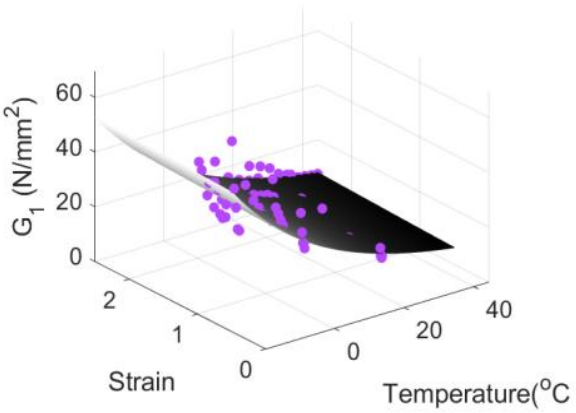

(c) Shear modulus G_1

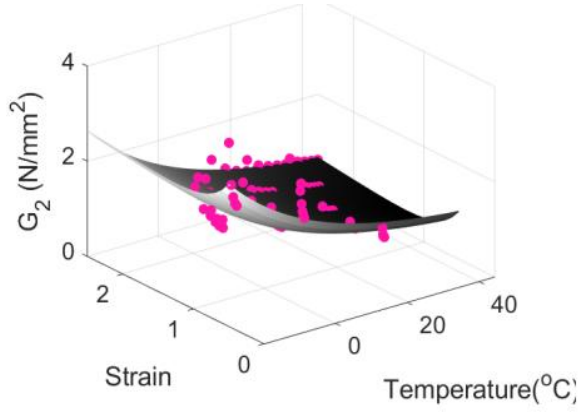

(d) Shear modulus G_2

Figure 2.27 Shear strain/equivalent damping ratio, inner temperature and shear strain relationship

2.8 Comparison of numerical and experimental seismic response by bilinear model

2.8.1 Bilinear model

The restoring force F of the bilinear model can be expressed by the sum of the elastic restoring force F_e and elasto-plastic force F_{ep} for easier calculation in the code, as shown in Fig 2.28 and Eq. 2.15.

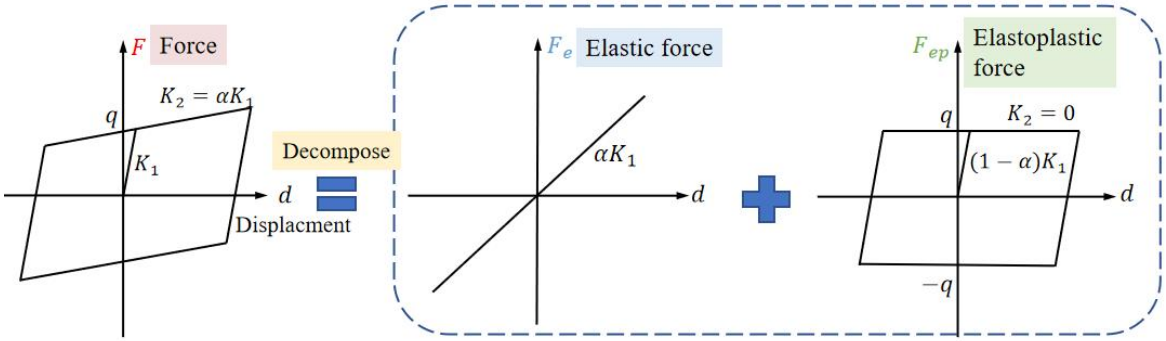

Figure 2.28 Elastic and elastoplastic force in bilinear model

$$F = F_{\mathrm{e}} + F_{\mathrm{ep}} \tag{2.15}$$

F_e at time $n+1$ can be simply expressed by

$$F_{\mathrm{e,n+1}} = F_{\mathrm{e,n}} + \alpha K_1 \Delta d \tag{2.16}$$

which has only one elastic stiffness and is easy to be calculated, Δd is the horizontal displacement increment of the bearing at each time step increment.

F_{ep} at time $n+1$ is expressed by

$$F_{\mathrm{ep,n+1}} = F_{\mathrm{ep,n}} + (1-\alpha) K_1 \Delta d \tag{2.17}$$

The maximum absolute value of $F_{ep,n+1}$ is determined by

$$\left| F_{ep,n+1} \right| \le q \tag{2.18}$$

$F_{ep,n+1}$ is set to be $+q$ or $-q$ if the absolute value of $F_{ep,n+1}$ exceeds characteristic strength q. q is calculated by

$$q = (1-\alpha) K_1 d_0 \tag{2.19}$$

2.8.2 Model parameters identification by cyclic loading tests

Then the bilinear model parameters are identified from the hysteresis loops of bearings obtained in the cyclic loading tests C1, C2, C3, the identified parameters and contribution rates are shown in Table 2.14. The contribution rate is determined by Eq. 2.14, and the V is the force of HDR bearing in this section. The model parameters are identified respectively in each ambient temperature cases, hence, there are three sets of model parameters for different temperatures. It can be seen that the stiffness and characteristic strength are larger at lower ambient temperature, and the contribution rate at room temperature is higher than that at the lower temperature.

Table 2.14 Identified parameters and contribution rates using the bilinear model

Temperature case	K_1 (KN/mm)	α	q (KN)	Contribution rate R
23°C	3.69	0.35	26.46	0.86
0°C	6.01	0.28	42.31	0.85
−20°C	8.84	0.22	65.57	0.81

The comparison of the experimental and numerical hysteresis loops computed by the bilinear model in cyclic loading tests is shown in Fig. 2.29. It can be seen that the bilinear model can only describe the hysteresis behavior of HDR bearings at small strain amplitudes and room temperature, the phenomenon of increased stiffness caused by the increased strain amplitude and decreased temperature are not able to be captured by the conventional bilinear model.

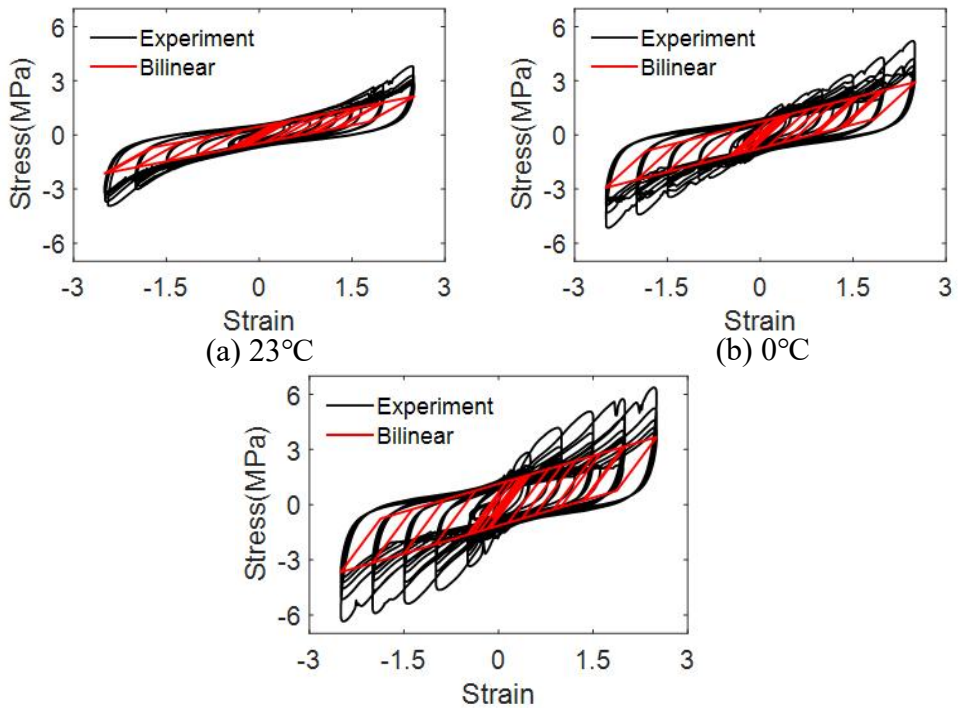

(a) 23℃ (b) 0℃

(c) −20℃

Figure 2.29 Comparison of the experimental and numerical hysteresis loops computed by the bilinear model in cyclic loading tests

2.8.3 Comparison of numerical and experimental seismic response

The identified model parameters are used to calculate the seismic response of the HDR bearings isolated bridge at each ambient temperature. The experimental (Tests H1, H2, H3) and analytical bearing hysteresis loops are compared in Fig. 2.30 at different ambient temperatures. At 23°C, although the maximum stress is well described, the maximum strain is overestimated by the bilinear model. The bilinear model parameters are identified form all the hysteresis loops of bearing from the strain amplitude 50% to 250%, hence, the identified stiffness is smaller than that identified from the hysteresis loops at small strain amplitude. Moreover, a substantial difference is observed at lower ambient temperatures, especially at −20°C, demonstrating that the bilinear model cannot accurately represent the hysteresis behavior of HDR bearings at low temperatures. Thus, it is necessary to propose a new constitutive model in which the self-heating effect and temperature dependence are considered to more accurately simulate the seismic performance of the HDR bearing at low temperatures.

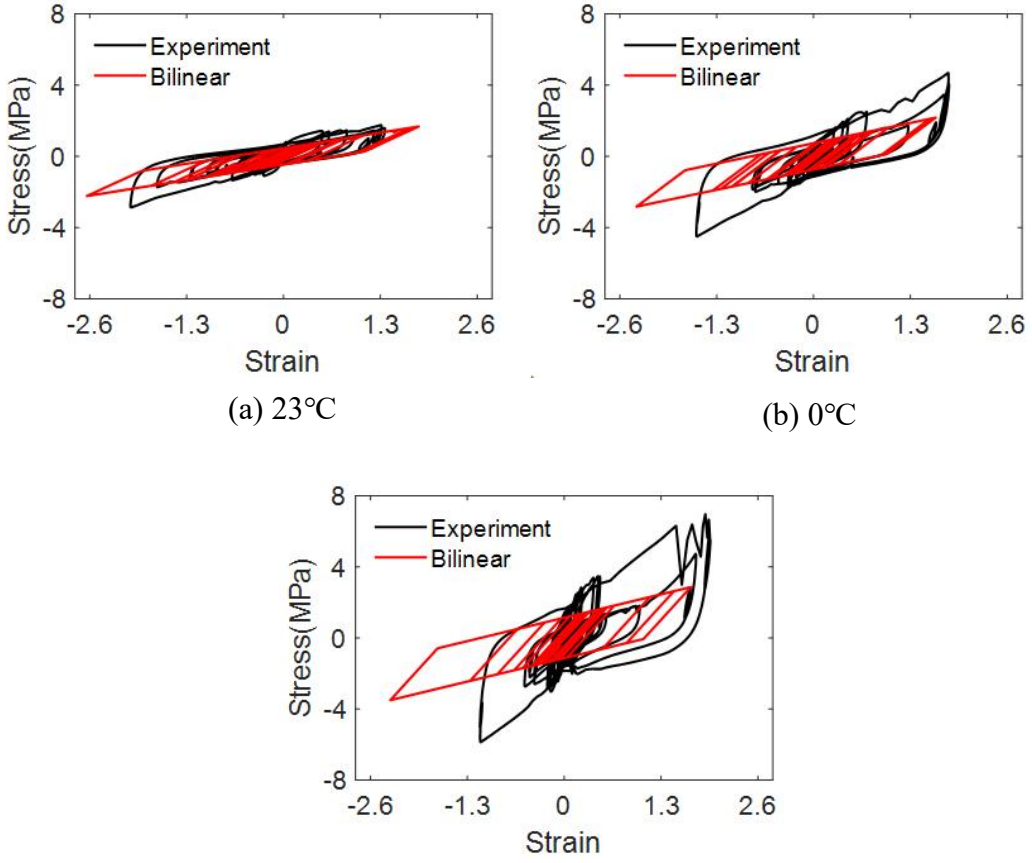

(a) 23℃ (b) 0℃

(c) −20℃

Figure 2.30 Comparison between experimental and analytical HDR bearings hysteresis loops at different ambient temperatures

The experimental and analytical bearing strain are compared in Fig. 2.31 for different ambient temperatures. It can be seen that the maximum strain is overestimated by the bilinear model, especially at −20°C.

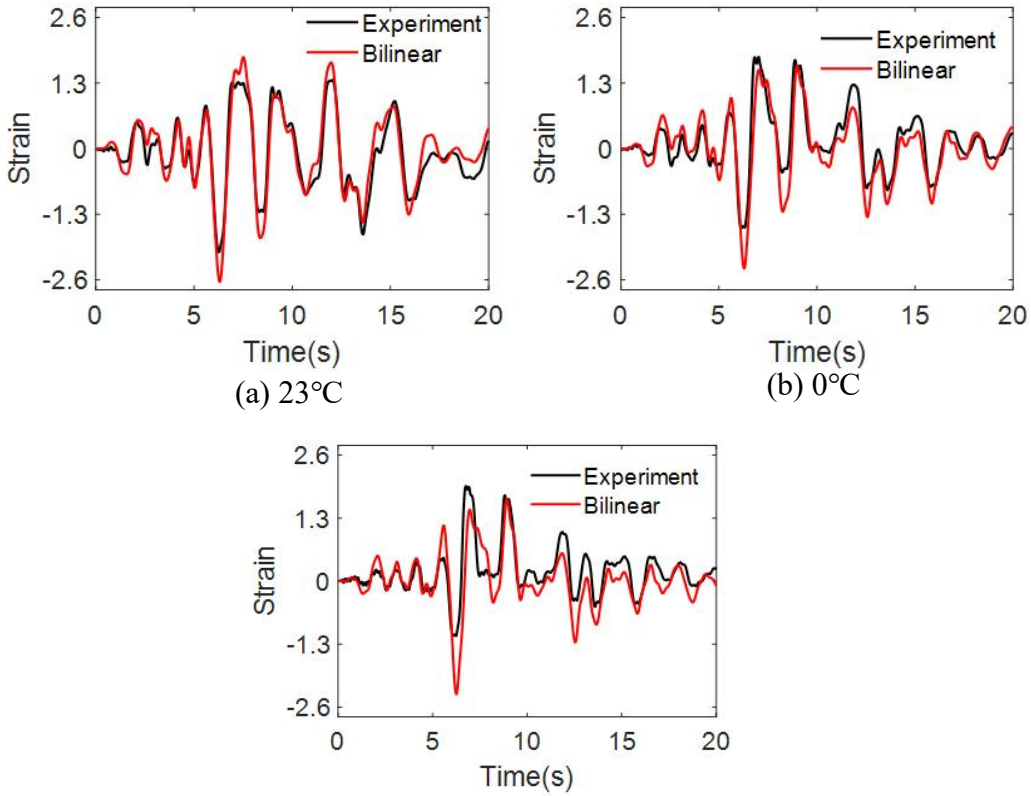

(a) 23℃ (b) 0℃

(c) −20℃

Figure 2.31 Comparison between experimental and analytical HDR bearing strain at different ambient temperatures

The experimental and analytical results in terms of the pier top displacement and acceleration at the three ambient temperatures are compared in Fig. 2.32 and Fig. 2.33, respectively. The analytical results show relatively good agreement with the experimental results for 23℃, while a notable difference is observed at lower temperatures, especially for the case of −20℃.

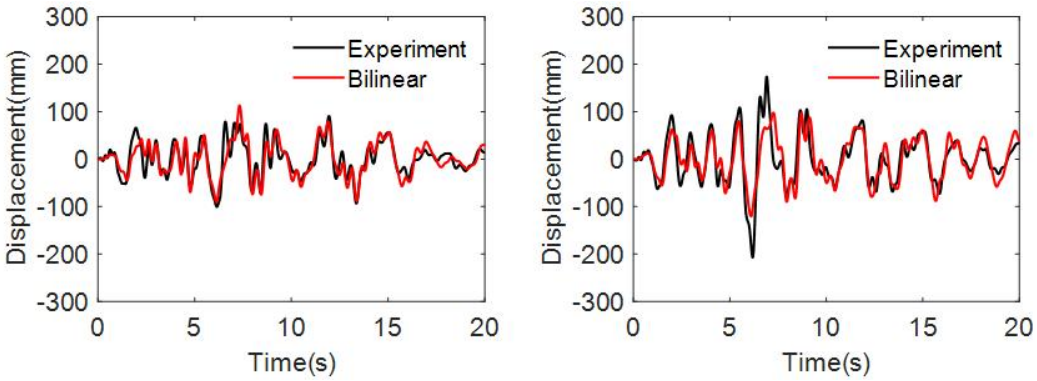

(a) 23℃ (b) 0℃

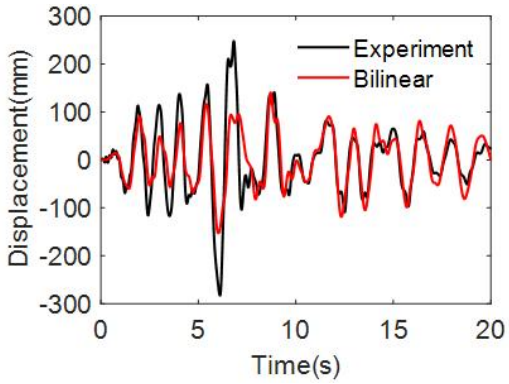

(c) −20℃

Figure 2.32 Comparison between experimental and analytical pier top displacement at different ambient temperatures

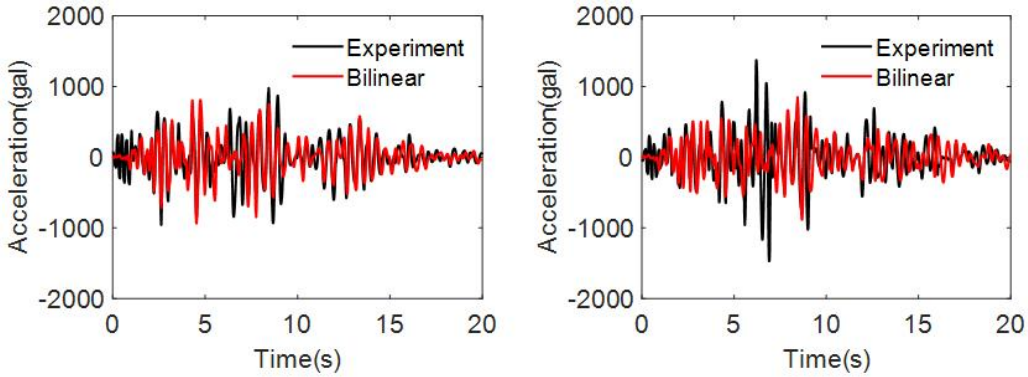

(a) 23℃ (b) 0℃

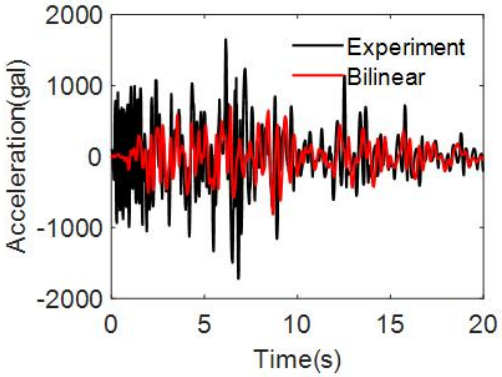

(c) −20℃

Figure 2.33 Comparison between experimental and analytical pier top acceleration at different ambient temperatures

2.9 Summary

In this chapter, the quasi-static cyclic loading tests and hybrid simulation of HDR bearings are conducted at there different ambient temperatures (−20℃, 0℃, 23℃) to investigate the

seismic performance of this type of seismic isolation bearing. A formula to calculate the inner temperature of the HDR bearing is developed, and the analytical inner temperature is compared with the measured temperature obtained in cyclic loading tests and hybrid simulation. The hysteresis behavior depending on the inner temperature and strain amplitudes are investigated based on the calculated inner temperature. Moreover, the bilinear model is applied to conduct the seismic response analysis of a HDR bearings isolated bridge, and the analytical results are compared with the experimental results in terms of the bearing hysteresis loops, bearing strain, pier top displacement and pier top acceleration. Based on the experimental and analytical results, the following main conclusions can be drawn.

(1) Under cyclic loading, the shear modulus and damping ratio of the bearing increase as the ambient temperature decreases. The differences in stiffness at different temperatures become smaller at larger strain amplitudes which is considered to be caused by the self-heating of rubber materials.

(2) In the hybrid simulation, the stiffness and peak stress of the HDR bearings increase, as well as the pier top displacement, for lower ambient temperature cases. The maximum strain of the bearing is reduced by a factor of 0.77 at 0°C and 0.55 at −20°C compared with the result at 23°C, the maximum pier top displacement is increased by a factor of 2.06 at 0°C and 2.82 at −20°C compared with the result at 23°C. This test result is a clear quantitative demonstration of the anticipated increase in seismic demand on the piers at low temperatures.

(3) The maximum deformation primarily occurs on the pier at low temperatures, which may arise from the changed structural modal shape in the response due to hardening of the rubber bearings at low temperatures.

(4) The actual inner temperature change of HDR bearings due to the self-heating effect is obtained successfully under random loading in hybrid simulation, this is considered to be important data for evaluating the hysteretic restoring force characteristics of HDR bearings under low-temperature environment. Moreover, a lower initial ambient temperature corresponds to a larger temperature rise of bearings under ground motions.

(5) The equivalent damping ratio is less affected by the inner temperature compared to the shear modulus at low temperatures.

(6) Regarding the effect of initial loading, there is no significant difference in seismic response between initial loading and non-initial loading at 23°C and −20°C.

(7) A comparison between experimental and analytical results shows that the bilinear model can only be used at room temperature. Thus, a new constitutive model is needed to more accurately simulate the seismic performance of HDR bearings at low temperatures.

Chapter 3 Hybrid simulation for seismic performance evaluation of SPR-S bearings at low temperatures

3.1 General

As a new type of elastomeric bearing, the seismic performance of the spring confined Pb high damping rubber bearing (SPR-S bearing) is enhanced by combining lead plug and high damping rubber in a single device. However, this new type of bearings exhibits a same problem with the conventional Lead Rubber Bearings (LRB) and HDR bearings under low-temperature condition, the strength of the SPR-S bearing is increased at lower temperatures and is reduced under cyclic deformation caused by the self-heating of lead plugs and high damping rubber, resulting a consequent detrimental effect on the dynamic response of the SPR-S bearings isolated structure. Meanwhile, the complicated thermal-mechanical behavior of the SPR-S bearing is difficult to be modeled and the results of the numerical method have yet to be verified by the tests.

In this chapter, the hybrid simulation is conducted at ambient temperatures of 23^{o}C, 0^{o}C and −20^{o}C aimed at quantitatively evaluating the seismic performance degradation of a SPR-S bearing isolated bridge in terms of the hysteresis loops of the SPR-S bearing, bearing strain, pier response and super-structure response at lower temperatures. The hybrid simulation result of the SPR-S bearing isolated bridge is compared with the that of the HDR bearing isolated bridge. The cyclic shear loading tests at ambient temperature 23^{o}C, 0^{o}C and −20^{o}C are also carried out to investigate the mechanical characteristics variation of the SPR-S bearing due to a low temperature, the inner temperature of the SPR-S bearing is successfully measured in cyclic loading tests as the thermocouples are installed perpendicular to the shear loading direction. The method proposed in chapter 2 to calculate the inner temperature of HDR bearing is improved and used to calculate the inner temperature of the SPR-S bearing. Meanwhile, the hysteresis behavior of the SPR-S bearing depending on the inner temperature is investigated, different from the chapter 2, the inner temperature is measured from the cyclic loading rather than calculated by the proposed formula. Finally, the seismic non-linear dynamic analyse of a SPR-S bearings isolated bridge model using the bilinear model is conducted and compared with the hybrid simulation results.

3.2 Experimental program

The loading conditions for the SPR-S bearing are same with those of the HDR bearing in cyclic loading tests and hybrid simulation as described in chapter 2.

3.2.1 SPR-S bearing specimen

The 1/6 scaled SPR-S bearing specimen is shown in Fig. 3.1. Four lead plugs with a diameter of 34.5 mm are distributed on the four corners of the SPR-S bearing specimen, respectively, the proportion of lead plugs to the total cross section area is 6.5%. Same with the HDR bearing, the effective dimensions of SPR-S bearing specimen are 240×240 mm, one rubber layer thickness is 5mm and the total rubber thickness is 30 mm, one steel plate thickness is 3.2 mm and the total steel thickness is 19.2 mm, the shear modulus of the high damping rubber material is 1.2 N/mm^2.

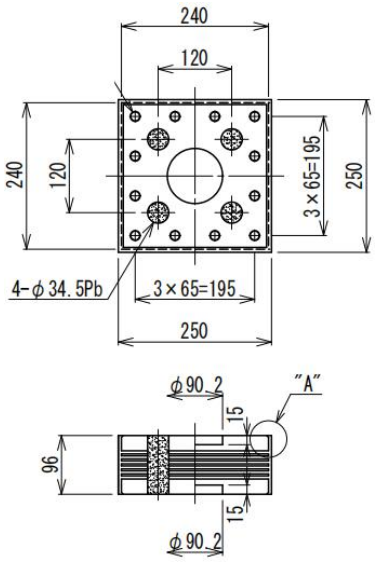

Figure 3.1 SPR-S bearing specimen

The thermocouple layout of SPR-S bearing specimen is shown in Fig. 3.2. The temperature of high damping rubber was measured by four thermocouples: two installed within the center of the third rubber layer at the same position (called the rubber1 and rubber2), and two installed on the outer surface of the cover rubber at the fourth and first rubber layers (called the out1 and out2, respectively). The temperature of lead plug was measured by three thermocouples: one inserted on the side surface center of lead plug with a depth of 50 millimeter, one attached to the upper surface center of the lead plug, and one inserted into the inner center of lead plug with a depth of 50 millimeter (called the lead1, lead2 and lead3, respectively). The thermocouples were inserted in a perpendicular direction to the horizontal shear load in order to protect the thermocouples from damage as much as possible.

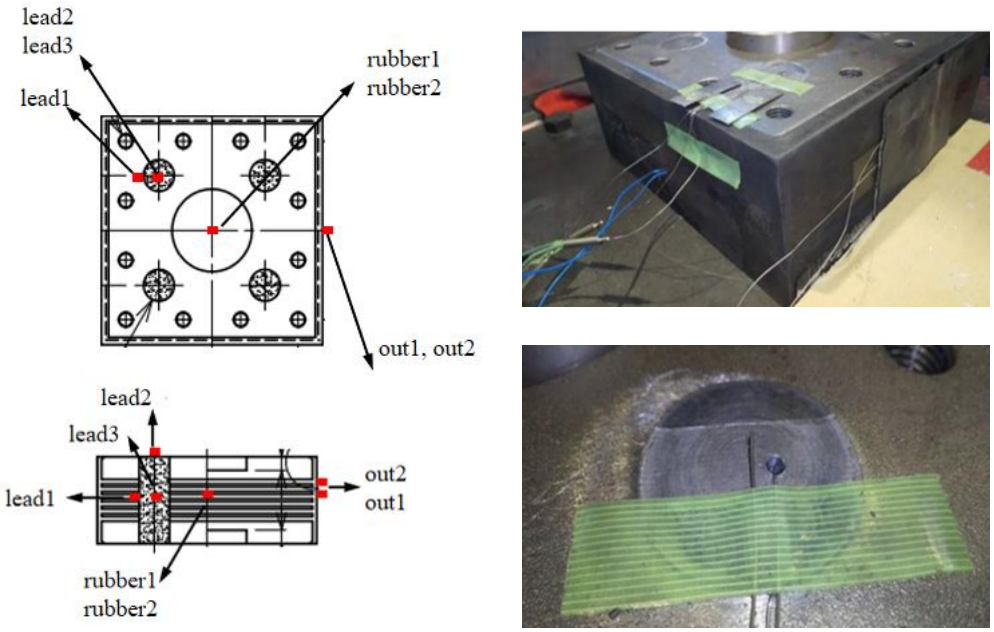

Figure 3.2 Thermocouple layout of SPR-S bearing specimen

3.2.2 Test cases and test sequence

The test cases for the cyclic loading tests and hybrid simulation are listed in Table 3.1. Three SPR-S bearing test specimens (No. 5, No. 6, No. 7) were used for the cyclic loading tests SC1, SC2, SC3 and three hybrid simulation tests SH1, SH2, SH3 at three different air temperatures (23℃, 0℃ and −20℃). The tests SC1, SC2, SC3 were conducted using previously unloaded specimens No. 5, No. 6 and No. 7, and then those specimens were used in the tests SH1, SH2 and SH3, respectively.

Table 3.1 Test cases

Case No.	Test	Temperature (℃)	Specimen No.	Date	Initial loading	Recovery days
SC1	Cyclic loading	−20	5	2020/12/17	Yes	Initial loading
SH1	Hybrid simulation	−20	5	2020/12/22	No	5
SC2	Cyclic loading	0	6	2021/1/6	Yes	Initial loading
SH2	Hybrid simulation	0	6	2021/1/8	No	2
SC3	Cyclic loading	23	7	2021/1/13	Yes	Initial loading
SH3	Hybrid simulation	23	7	2021/1/15	No	2

3.3 Quasi-static cyclic loading test

3.3.1 Cyclic behavior of the SPR-S bearing at different temperatures

The hysteresis shear strain-stress loops of the SPR-S bearing at different ambient temperatures in the cyclic loading tests SC1, SC2, SC3 are shown in Fig. 3.3. The shear strain is defined as the ratio of the relative horizontal displacement of the specimen to the total rubber thickness, and the shear stress is defined as the ratio of the horizontal force to the effective area of the specimen. It is evident that the stiffness is larger at lower ambient temperatures and smaller strain levels, and the stress of SPR-S bearing for the first loop is obviously bigger than that of the next four loops called the Mullins effect. The cyclic behavior of the SPR-S bearing at 23℃ and 0℃ is similar, while the cyclic behavior at −20℃ shows a significant difference with the results at 23℃ and 0℃, as the stiffness hardening and higher energy dissipation are more obviously observed at −20℃.

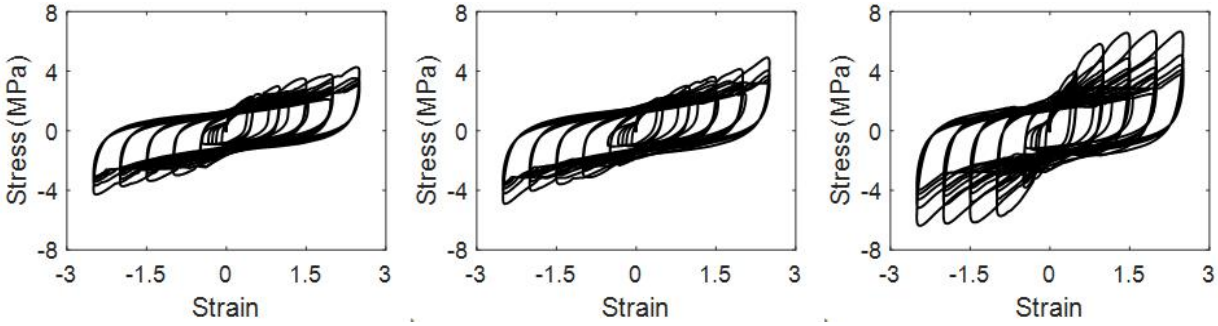

(a) 23℃ (b) 0℃ (c) −20℃

Figure 3.3 Hysteresis shear strain-stress loops of the SPR-S bearing in cyclic loading tests

3.3.2 Mechanical characteristics of the SPR-S bearing

The mechanical characteristics of SPR-S bearings in terms of shear modulus and equivalent damping ratio at different temperatures and shear strain amplitudes calculated from the first and fifth cycles of hysteresis loops obtained in Tests SC1, SC2 and SC3 are shown in Fig. 3.4. The calculation method is same with that described in section 2.3.3. It is observed that the shear modulus and equivalent damping ratio of the SPR-S bearing decrease as the shear strain increases for each ambient temperature case. The shear modulus of the first cycle at −20°C is distinctly higher than that of the other cases, while the equivalent damping ratio of the first cycle at −20°C is distinctly lower than that of the other cases, indicating that the Mullins effect is more intense at lower temperatures. Furthermore, the difference of mechanical characteristics of SPR-S bearings at different temperatures decrease as the cyclic loading progresses to larger shear strain amplitudes, which is considered to be caused by the self-heating of high damping rubber and lead plugs. The equivalent damping ratio of the SPR-S bearing is obviously higher than that of the HDR bearing shown in Fig. 2.12.

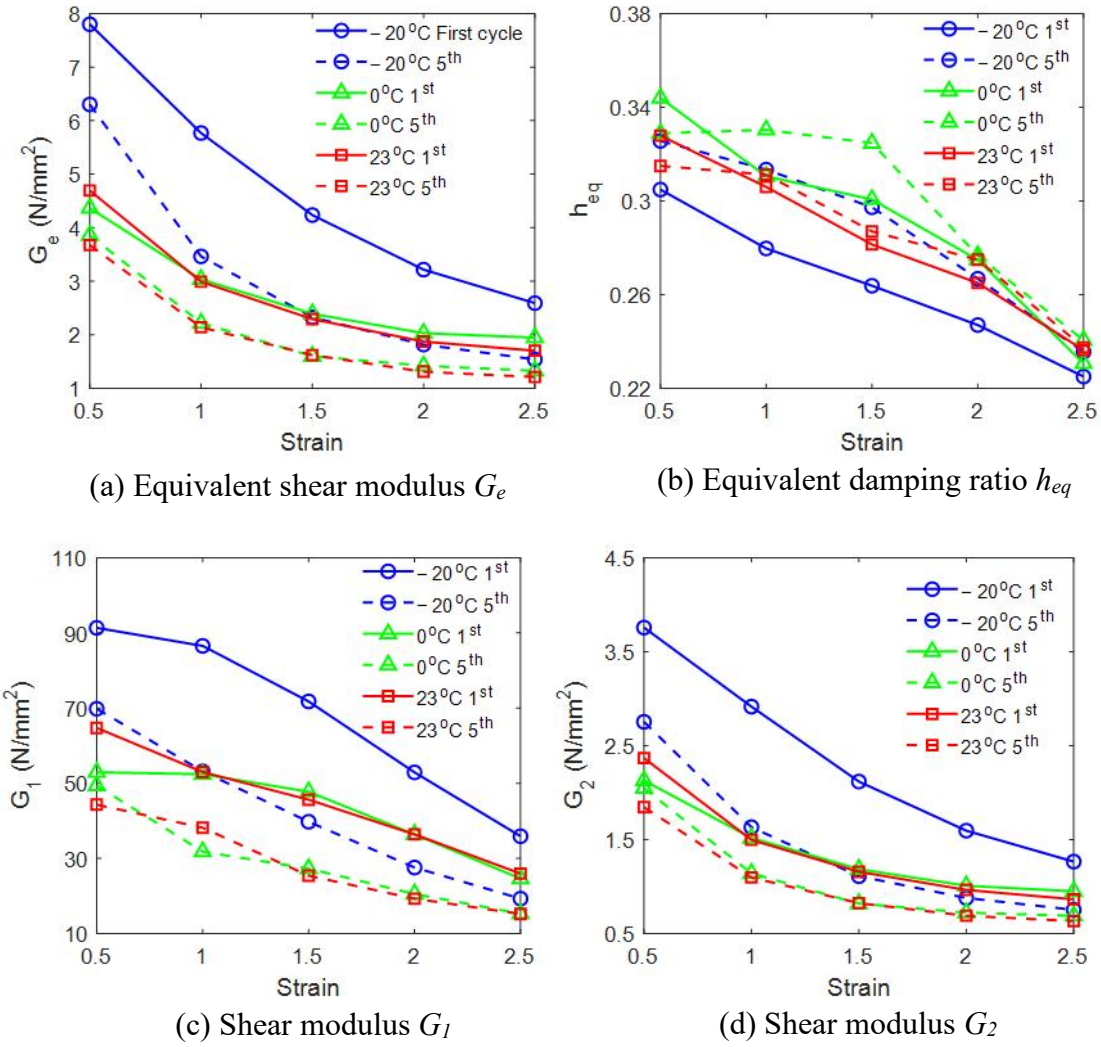

(a) Equivalent shear modulus G_e (b) Equivalent damping ratio h_{eq}

(c) Shear modulus G_1 (d) Shear modulus G_2

Figure 3.4 Mechanical characteristics of the SPR-S bearing

3.3.2 Comparison of mechanical characteristics between the SPR-S bearing and the HDR bearing

The comparison of mechanical characteristics between the SPR-S bearings and HDR bearings is shown in Fig. 3.5. All of the mechanical characteristics are calculated from the fifth cycles of hysteresis loops of bearings. It is observed that the equivalent shear modulus, equivalent damping ratio and shear modulus G_1 of the SPR-S bearing are higher than those of the HDR bearing, and the difference of equivalent shear modulus, shear modulus G_1 and shear modulus G_2 between the SPR-S bearing and HDR bearing decreases as the strain amplitude increases. However, the difference of equivalent damping ratio between the SPR-S bearing and HDR bearing is less affected by the strain amplitude and temperature. The SPR-S bearings show better damping performance than the HDR bearings, and the SPR-S bearings are less affected by the temperatures than the HDR bearings.

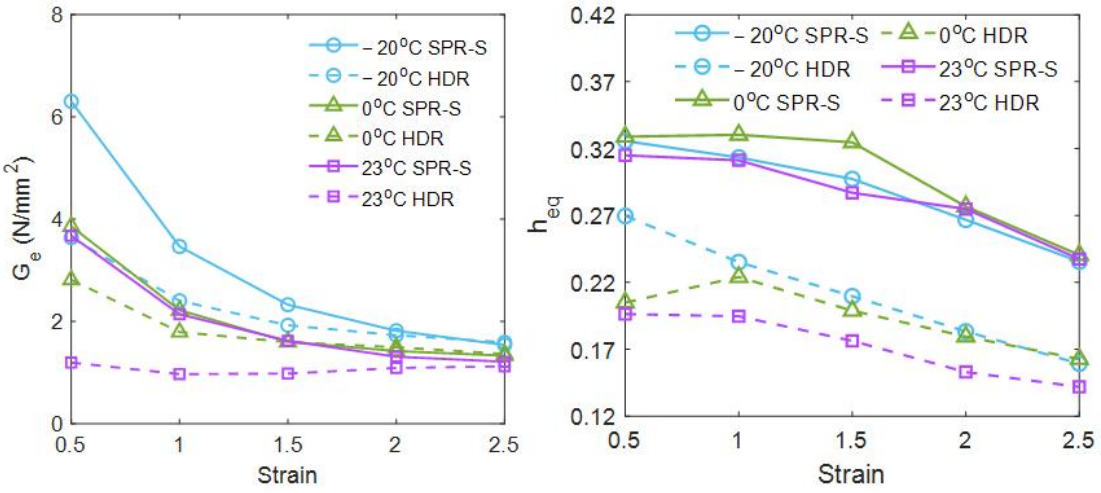

(a) Equivalent shear modulus G_e (b) Equivalent damping ratio h_{eq}

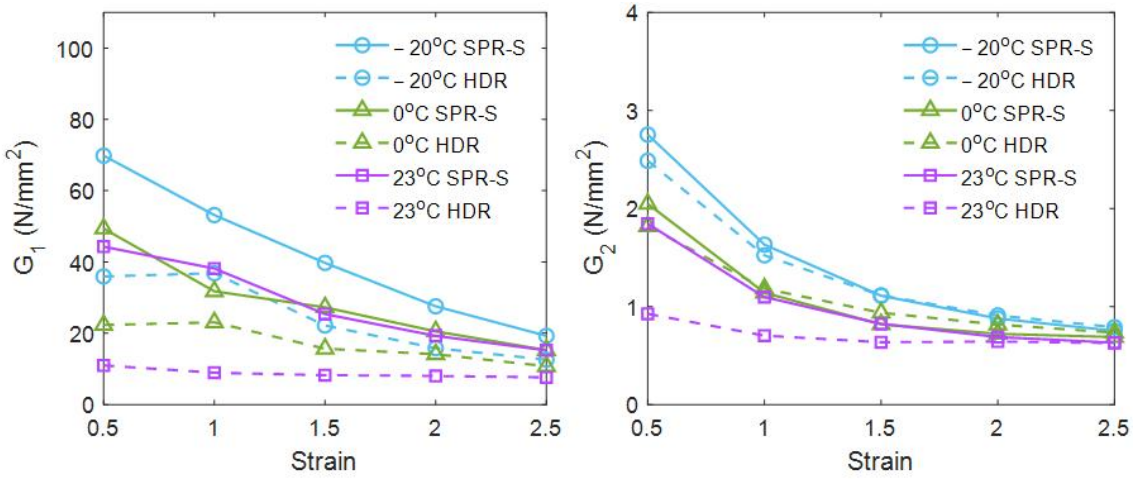

(c) Shear modulus G_1 (d) Shear modulus G_2

Figure 3.5 Comparison of mechanical characteristics between SPR-S bearing and HDR bearing

3.3.4 Measured temperature

The measured temperature of SPR-S bearings in cyclic loading tests SC1, SC2, SC3 is shown in Fig. 3.6. Note that some thermocouples inserted in the lead plugs were broken during the tests, and thus the results of the broken thermocouples are not shown in the figure. Obvious temperature increase can be observed at different cyclic deformations during the tests, especially at higher deformations as the area of hysteresis loops of bearing is larger at higher strain amplitudes. The temperature of the high damping rubber and lead plugs increases under cyclic loading, and decreases during the interval of adjacent cyclic loading with different cyclic deformations due to the heat conduction over the volume of the bearing, especially for the inner center of lead plug (lead3). It can also be observed that the temperature increase is higher in the lead plug than the high damping rubber at each strain amplitude, and the temperature drop rate of the lead plug is also larger than the high damping rubber, as the thermal conductivity of the lead is larger than the rubber. Although there is an obvious

difference in different location of the lead during the loading phase at each strain amplitude, the temperature tends to be same quickly during the rest phase between the adjacent strain amplitudes because of the high thermal conductivity of the lead. Furthermore, the temperature of the cover rubber increased for a while after the test was finished, especially at 23℃, which is considered to be caused by the heat conduction from the inner rubber to the cover rubber.

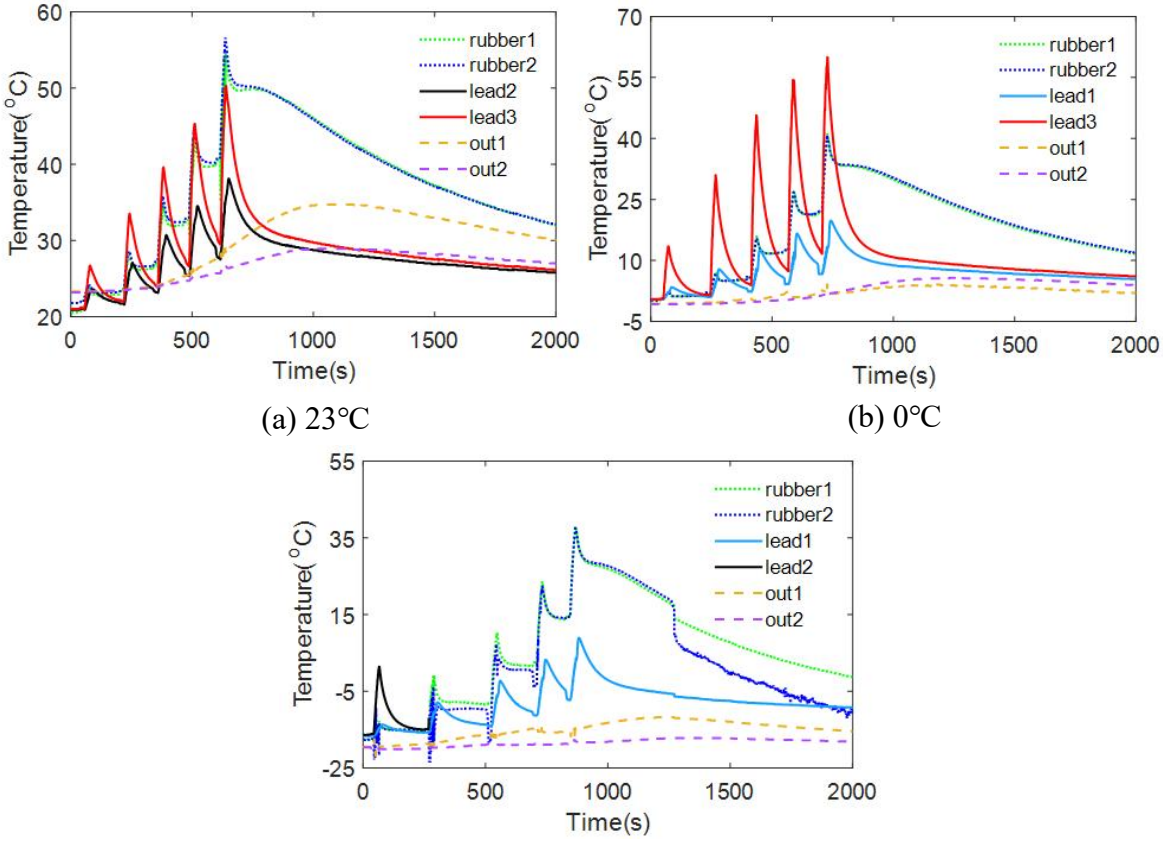

(a) 23℃ (b) 0℃

(c) −20℃

Figure 3.6 Measured temperature of SPR-S bearing in cyclic loading tests

The temperature rise of the high damping rubber and lead plugs at the end of tests for each ambient temperature case is presented in Table 3.2. It is observed that the temperature rise is higher at lower ambient temperatures, thus the self-heating of the rubber materials and lead plugs is more obvious at lower temperatures. The temperature rise of the high damping rubber is higher than that of the lead plug at 23℃, while the temperature rise of the inner center of the lead plug is higher than the high damping rubber at 0℃. The temperature rise at the inner center of lead plug reached 59℃ at the end of the test at ambient temperature 0℃, and the temperature rise at the center of rubber rose 53℃ at the end of test at ambient temperature −20℃. Although the thermocouple of lead3 at −20℃ was broken, it might be predicted that the temperature has risen by at least 70℃ considering the results at 23℃ and 0℃.

Table 3.2 Temperature rise in cyclic loading tests

Ambient temperature	23℃	0℃	−20℃
Center of rubber (rubber1/2)	35	40	53
Side surface of lead plug (lead1)	-	19	25
Upper surface of lead plug (lead2)	17	-	-
Inner center of lead plug (lead3)	29	59	-

3.4 Hybrid simulation results

The input ground motion is same with that described in Fig. 2.15 in the hybrid simulation for this section.

3.4.1 Responses of the SPR-S bearing and pier

The load-displacement hysteresis loops and shear strain time history of the SPR-S bearings obtained in Tests SH1, SH2 and SH3 are shown in terms of stress-strain relationship in Fig. 3.7. It is observed that the stiffness and shear stress are higher at lower ambient temperatures, while the maximum shear strain is smaller at lower temperatures, and the maximum shear strain at −20°C is reduced by a factor of 0.66 compared with the result at 23°C due to the stiffness hardening of the SPR-S bearing at a lower temperature.

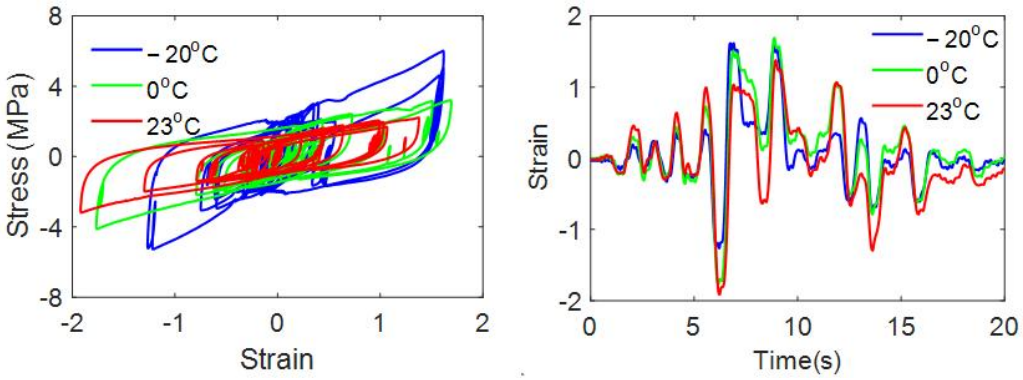

(a) Hysteresis loops (b) Time history

Figure 3.7 Test results of SPR-S bearing responses

The restoring force of the SPR-S bearing is increased due to a low temperature, resulting a larger force transmitted to the bridge piers. The time histories of pier top displacement, velocity and acceleration at room and low temperatures are shown in Fig. 3.8. It is observed that the pier top displacement, velocity and acceleration are higher at lower temperatures as expected, and the maximum pier top displacement at −20°C is increased by a factor of 2.16 compared with the result at 23°C, quantitatively indicating the expected increase in seismic demand at the piers caused by the low ambient temperature.

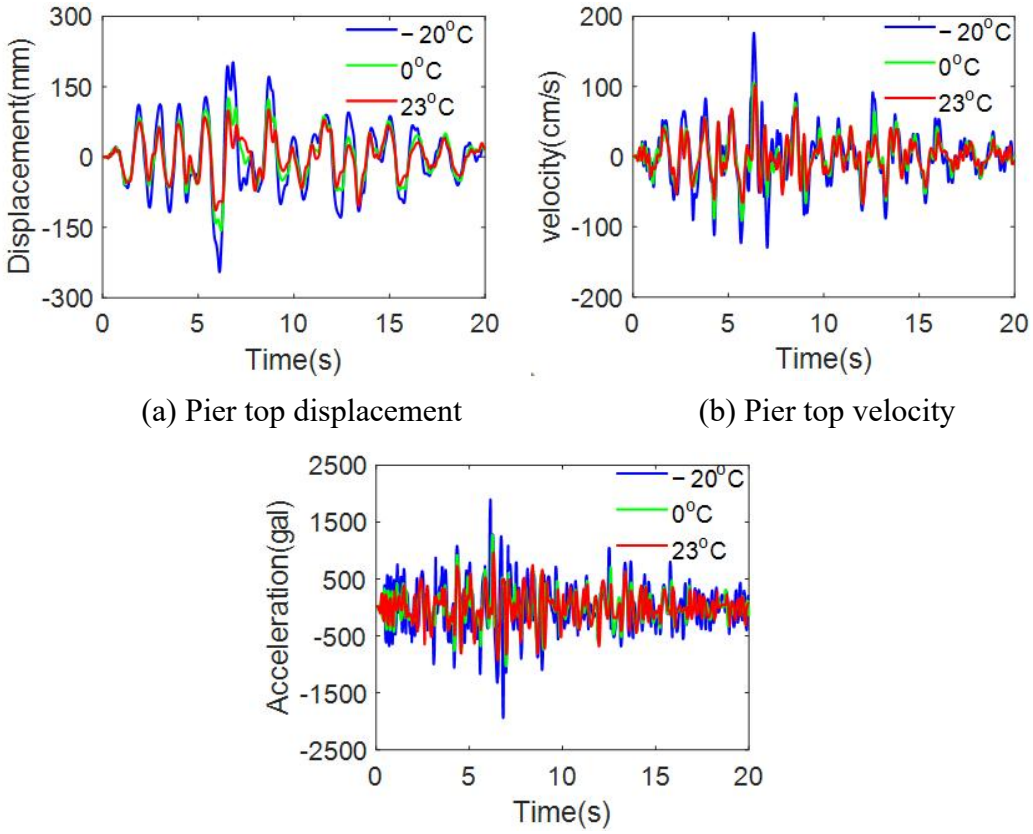

(a) Pier top displacement (b) Pier top velocity

(c) Pier top acceleration

Figure 3.8 Pier top responses

The super-structure displacement, velocity and acceleration obtained in hybrid simulation are shown in Fig. 3.9 for the three ambient temperature cases. The super-structure responses at lower temperatures are greater than those for 23°C as expected.

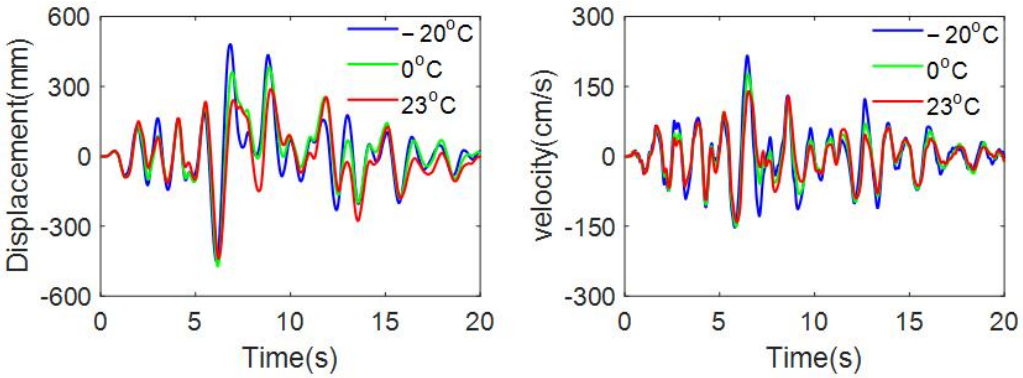

(a) Super-structure displacement (b)Super-structure velocity

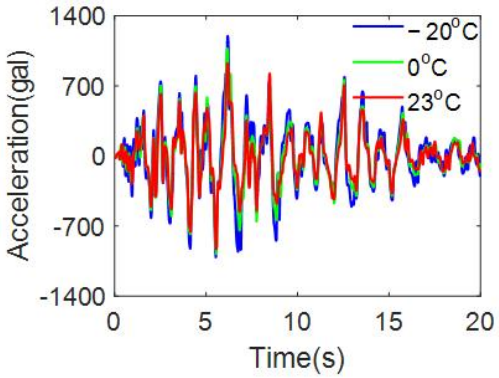

(c) Super-structure acceleration

Figure 3.9 Super-structure response

The seismic response amplification factor due to low temperatures is shown in Table 3.3, m_1 and m_2 represent bridge super-structure and pier, respectively. The maximum strain of the bearing is reduced by a factor of 0.92 at 0°C and 0.66 at −20°C compared with the result at 23°C, showing a quantitative representation of the reduced effectiveness of the SPR-S bearing due to low temperatures. The maximum pier top displacement is increased by a factor of 1.38 at 0°C and 2.16 at −20°C compared with the result at 23°C, implying the quantitative increase of seismic demand of piers due to low temperatures.

Table 3.3 Seismic response amplification factor due to low temperatures

Temperature case	Bearing strain	Bearing stress	m_1 disp.	m_1 vel.	m_1 accle.	m_2 disp.	m_2 vel.	m_2 accle.
0ºC	0.92	1.44	1.32	1.28	1.16	1.38	1.36	1.32
−20ºC	0.66	2.71	1.67	1.55	1.29	2.16	1.94	2.09

3.4.2 Measured temperature

The measured temperature of SPR-S bearings in hybrid simulation SH1, SH2 and SH3 at different ambient temperatures is shown in Fig. 3.10. It is observed that both the high damping rubber and lead plugs generate heat within the duration time of the earthquake as expected. The temperature at the inner center rose more than the side surface and upper surface for the lead plug, thus the heat generation at different parts of the lead plug was different and the core temperature was higher than the surface temperature. The inner center temperature of the lead plug sharply increased during the hybrid simulation and sharply decreased after the hybrid simulation compared with the inner rubber, as the thermal conductivity of the lead is higher than the rubber. Furthermore, the temperature of the cover rubber basically remained at a same value, indicating that the heat did not diffuse from the inner rubber to the cover rubber during the earthquake with a short time.

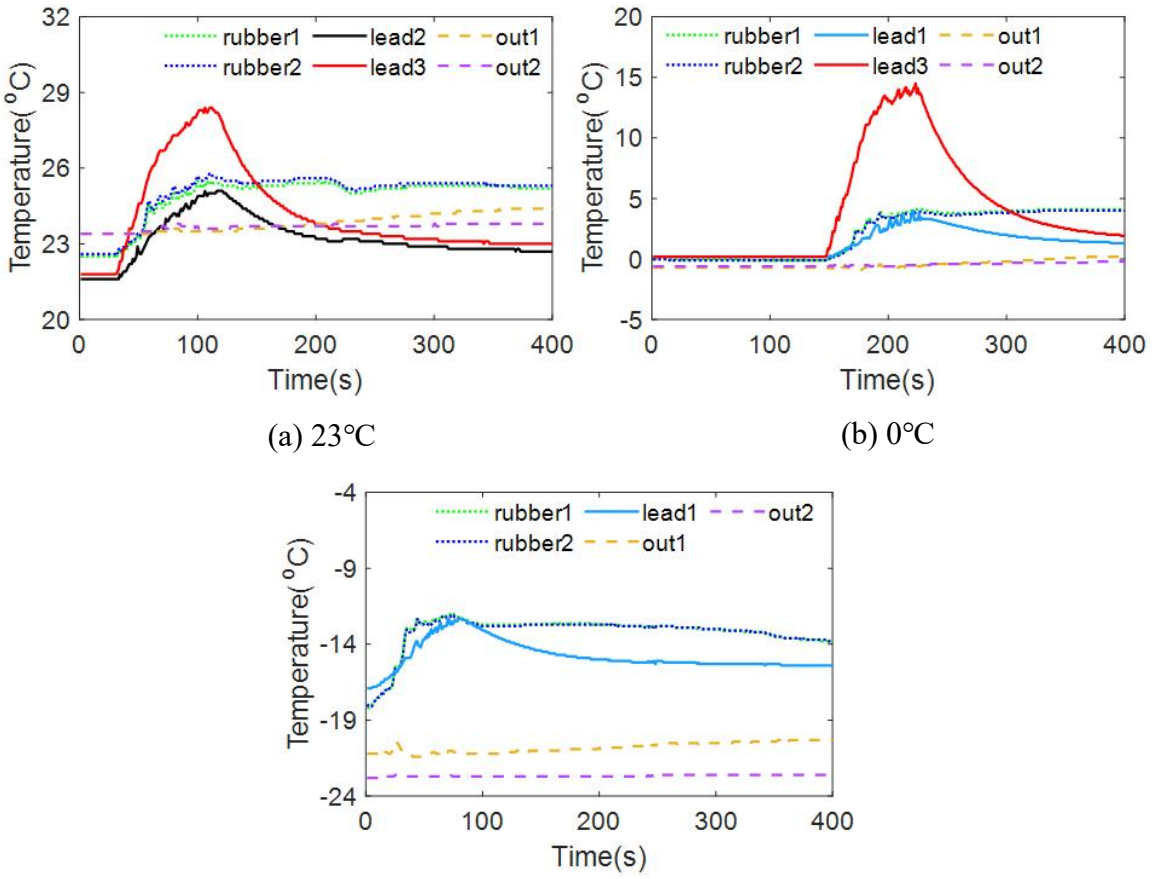

Figure 3.10 Measured temperature of SPR-S bearings in hybrid simulation

The temperature rise of the high damping rubber and lead plugs at the end of the hybrid simulation for each ambient temperature case is presented in Table 3.4. It is observed that the temperature rise in the hybrid simulation is far less than that in the cyclic loading tests, as the cyclic time and cyclic deformation are larger in the cyclic loading tests. The temperature rise at the inner center of the lead plug reached 14.3℃ at the end of ground motion at ambient temperature 0℃, and the temperature rise at the center of rubber rose 6.2℃ at the end of the earthquake at ambient temperature −20℃.

Table 3.4 Temperature rise in hybrid simulation

Ambient temperature	23℃	0℃	−20℃
Center of rubber (rubber1/2)	3.0	4.1	6.2
Side surface of lead plug (lead1)	-	3.8	4.6
Upper surface of lead plug (lead2)	3.5	-	-
Inner center of lead plug (lead3)	6.6	14.3	-

3.4.3 Comparison of seismic response between bridges isolated with SPR-S bearings and HDR bearings

The comparison of hysteresis loops between the SPR-S bearings (obtained in Tests SH1, SH2 and SH3) and the HDR bearings (obtained in Tests H1, H2 and H3) at different ambient temperatures is shown in Fig. 3.11. Although there is not obvious difference between the SPR-S bearings and HDR bearings, the maximum stress of SPR-S bearing is larger than that of the HDR bearing at 0℃ and −20℃, and is slightly smaller than the HDR bearing at 23℃. Meanwhile, the maximum strain of the HDR bearing is slightly larger that that of the SPR-S bearing at each ambient temperature case. The low-temperature condition effect on the strain-stress hysteresis behavior of the SPR-S bearing is smaller than that of the HDR bearing, this may be caused by the higher temperature increase for the lead plugs than the high damping rubber in the SPR-S bearing, the stiffness hardening appears in the initial phase due to a low ambient temperature decreases as the inner temperature of the SPR-S bearing increases under cyclic loading.

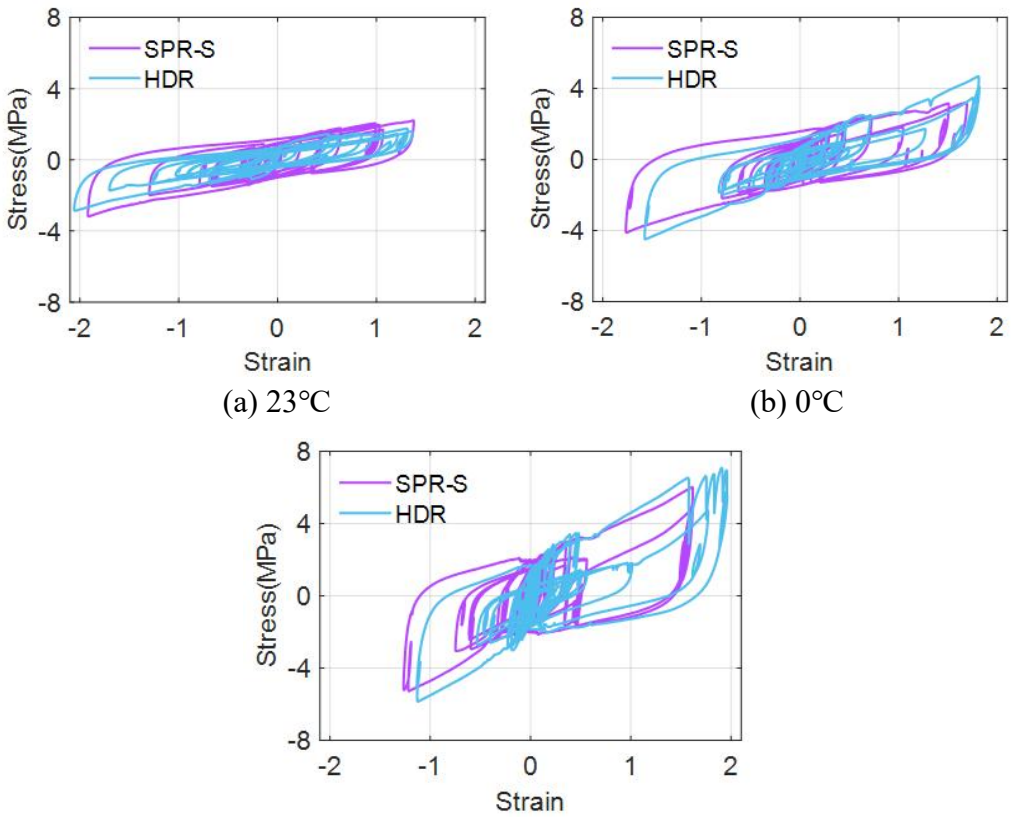

(a) 23℃ (b) 0℃

(c) −20℃

Figure 3.11 Hysteresis loops of SPR-S bearings and HDR bearings at different ambient temperatures

The comparison of strain time histories between the SPR-S bearing and the HDR bearing at different ambient temperatures is shown in Fig. 3.12. It can be seen that the strain response is similar for these two types of bearings in the beginning time, and the difference is more obvious after the maximum strain appears.

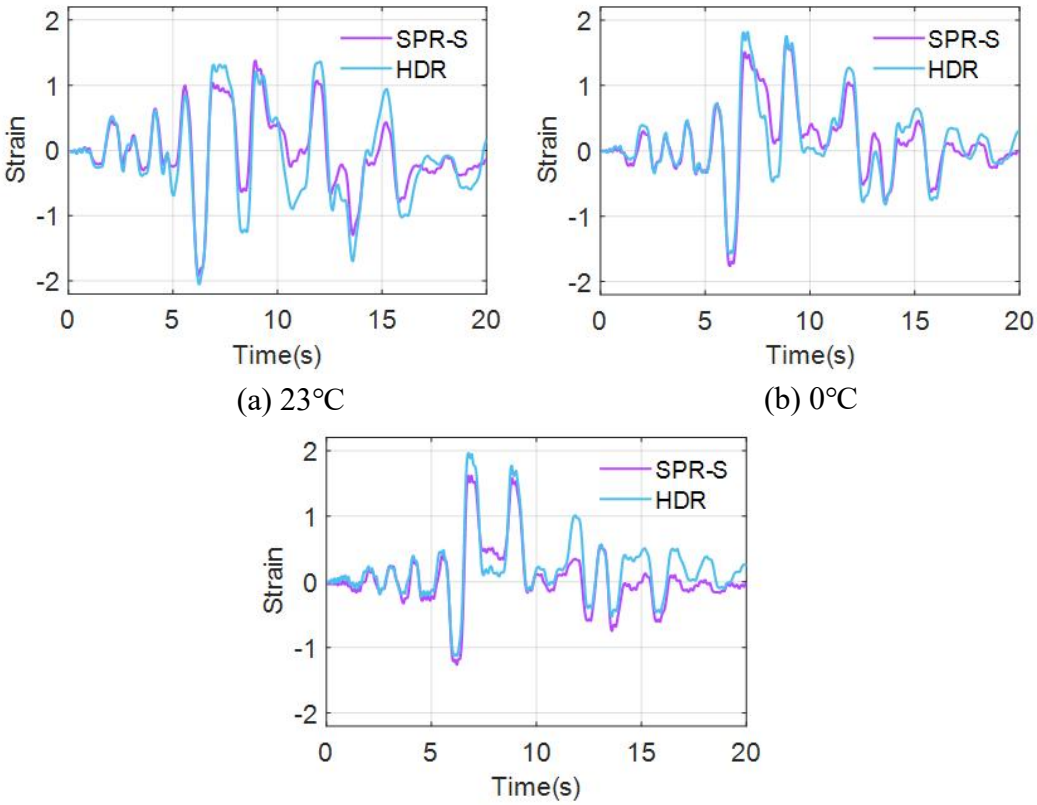

(a) 23℃ (b) 0℃

(c) −20℃

Figure 3.12 Strain time histories of SPR-S bearings and HDR bearings at different ambient temperatures

The comparison of pier top displacement of a bridge isolated with SPR-S bearings and HDR bearings at different ambient temperatures is shown in Fig. 3.13. It can be concluded that the pier top displacement is decreased by using the SPR-S bearings compared with that of the HDR bearings at 0℃ and −20℃, and there is not obvious difference for 23℃, hence, the seismic performance of SPR-S bearings is better than the HDR bearings at lower temperatures.

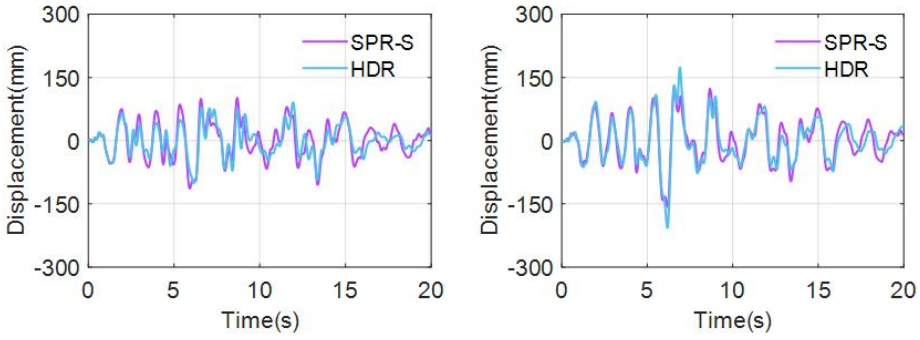

(a) 23℃ (b) 0℃

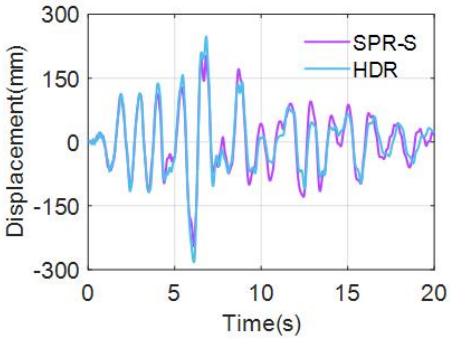

(c) −20℃

Figure 3.13 Pier top displacement of bridge isolated with SPR-S bearings and HDR bearings at different ambient temperatures

The calculated energy dissipation of the SPR-S bearings and HDR bearings at different ambient temperatures is shown in Fig. 3.14. The energy dissipation is calculated by Eq. 2.7. The seismic energy is absorbed and exchanged to heat energy by the SPR-S bearings according to the self-heating of high damping rubber and lead plugs, thus the seismic energy transferred to the substructure could be reduced according to the energy dissipation capacity of the SPR-S bearings, it is observed that the energy dissipation capacity of the SPR-S bearing is enhanced at −20℃ by 43% compared with the result at 23℃, which is favorable under earthquake ground motions. It can be concluded that the energy dissipation of the SPR-S bearing is higher than that of the HDR bearing at 23℃, and is similar with that of the HDR bearing at 0℃, and is smaller than the HDR bearing at −20℃ during the early phase under ground motions.

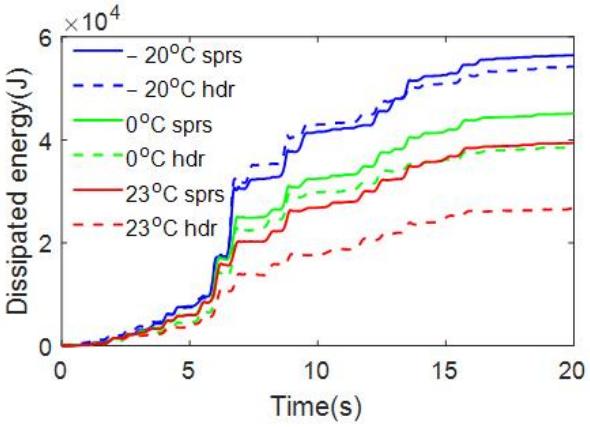

Figure 3.14 Energy dissipation of SPR-S bearings and HDR bearings at different ambient temperatures

3.5 Comparison of numerical and experimental inner temperature of rubber

In this section, the numerical inner temperature is investigated and compared with the inner temperature of rubber in the SPR-S bearing (rubber1 shown in Fig. 3.2) measured in the cyclic loading tests and hybrid simulation, the temperature of the lead plugs and cover rubber is not investigated in this section. The simulation method of the inner temperature for SPR-S bearings is developed based on the method described in chapter 2 for HDR bearings.

The following equation can be obtained according to Eq. 2.11 and Eq. 2.12.

$$\dot{T} = \dot{E}\lambda - Ah\lambda(T - T_a) \tag{3.1}$$

The meaning of the parameters in Eq. 3.1 is same with those expressed in chapter 2, and the only difference is that the parameter λ is determined by

$$\lambda = \frac{1}{m_r C_{pr} + m_s C_{ps} + m_L C_{pL}} \tag{3.2}$$

where the newly added parameters m_L and C_{pL} are the mass and specific heat capacity of the lead, respectively. The density and thermal property of lead are presented in Table 3.5, and the calculated λ is 1.513×10^{-4} for the SPR-S bearing. The details about the calculation of λ can be found in Appendix B.

Table 3.5 Density and thermal property of lead

Density(kg/m^3)	Specific heat capacity(J/(kg·K))
11360	129

Hence, the only unknown parameter for the Eq. 3.1 is the area A, here the $Ah\lambda$ is used as an unknown parameter and will be identified by the measured inner temperature of rubber in the SPR-S bearing obtained in cyclic loading tests SC1, SC2, and SC3.

3.5.1 Comparison of numerical and experimental inner temperature in cyclic loading tests

The measured inner temperature of rubber (rubber1 shown in Fig. 3.2) at different temperatures obtained in the cyclic loading tests is shown in Fig. 3.15. The measured temperature can be divided into two parts: during the tests and after the tests, the displacement and force of the bearing are zero after the test is finished, and the temperature gradually decreases to the ambient temperature after the test, here, the experimental data after the test is used to identify the parameter $Ah\lambda$ in this section.

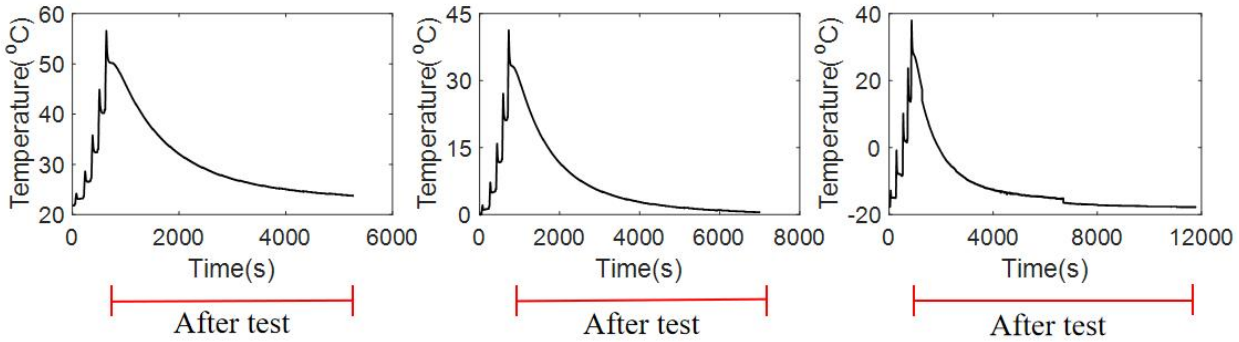

(a) 23℃ (b) 0℃ (c) −20℃

Figure 3.15 Measured inner temperature of rubber in cyclic loading test at different temperatures

Eq. 3.1 can be expressed by Eq. 3.3 after the test is finished as the dissipated energy E calculated by hysteretic force-displacement loops of the bearing is zero. Then we can use the measured temperature obtained after test and Eq. 3.3 to identify the parameter $Ah\lambda$, the KH method described in Appendix C is used for the optimization method.

$$\dot{T} = -Ah\lambda(T - T_a) \tag{3.3}$$

The measured and analytical inner temperatures of rubber using Eq. 3.3 after tests are shown in Fig. 3.16, and the analytical inner temperature is calculated by Eq. 3.3. Good agreement can be observed between the measured and analytical inner temperatures, and the identified parameter $Ah\lambda$ at each ambient temperature is shown in Table 3.6.

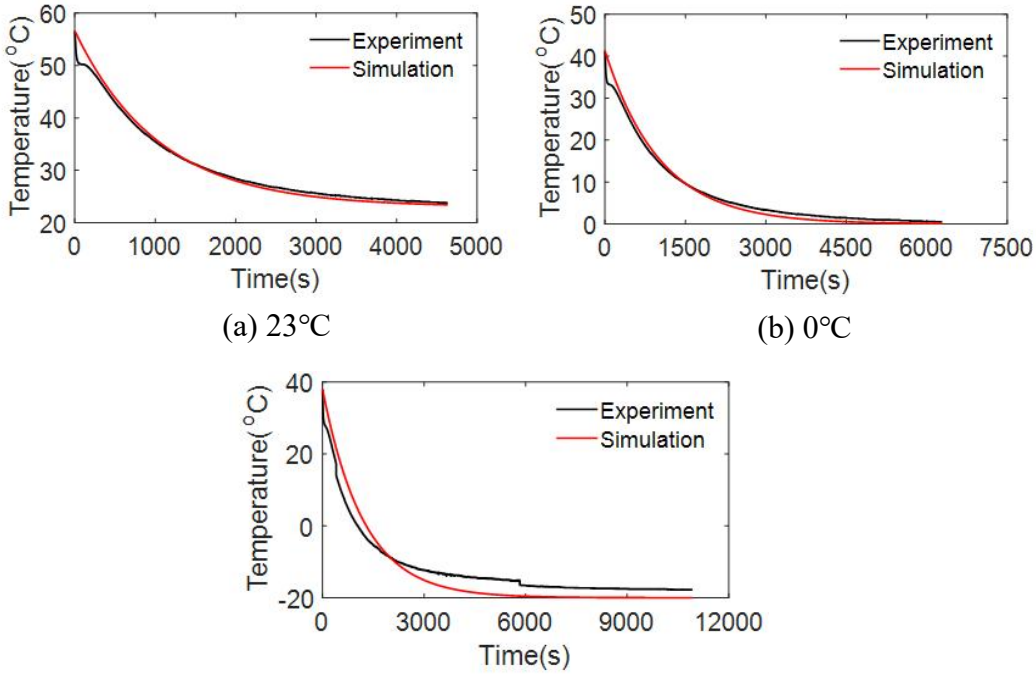

(a) 23℃ (b) 0℃

(c) −20℃

Figure 3.16 Measured and analytical inner temperature of rubber after cyclic loading tests

Table 3.6 Identified parameters

Case	23°C	0°C	−20°C
$Ah\lambda$	9.5×10^{-4}	9.7×10^{-4}	8.2×10^{-4}

Then the identified parameter $Ah\lambda$ is used in Eq. 3.1 to calculate the inner temperature during the cyclic loading test, and the calculated and experimental inner temperature are shown in Fig. 3.17. It can be observed that the calculated temperature increment during the loading phase is similar to that measured by the thermocouple at each strain amplitude. However, the calculated temperature decrement during the rest time between the adjacent strain amplitudes is smaller that measured by thermocouples, hence, the calculated maximum temperature is larger than the measured maximum temperature.

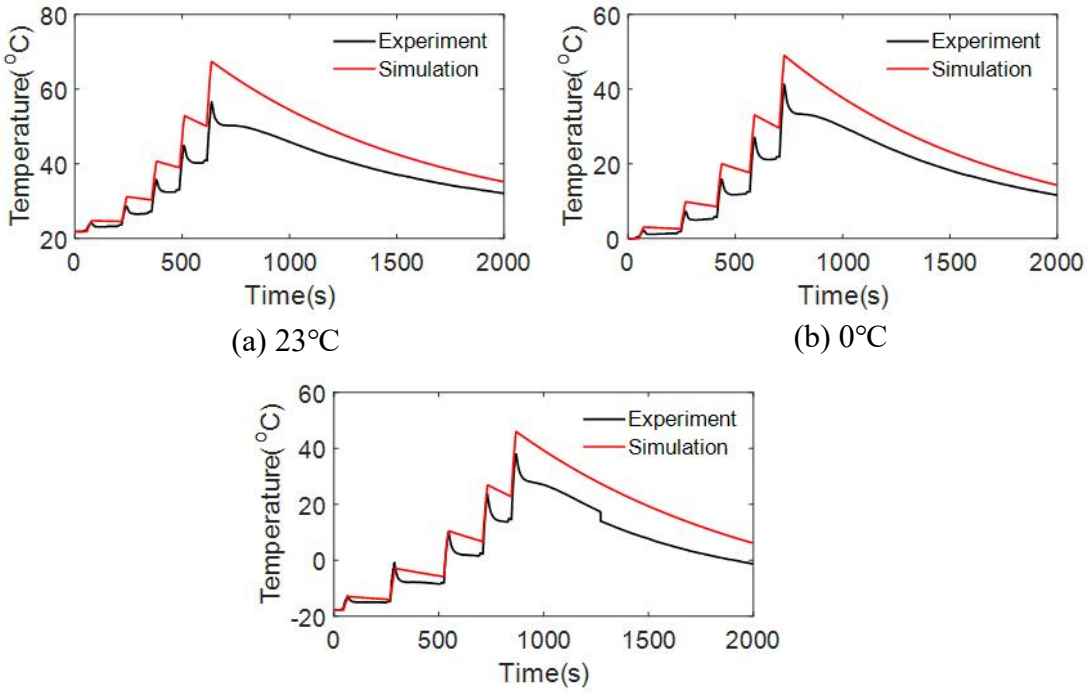

Figure 3.17 Comparison of the experimental and numerical inner temperature of rubber in cyclic loading tests

3.5.2 Comparison of numerical and experimental inner temperature in hybrid simulation

The identified parameter $Ah\lambda$ and Eq. 3.1 are also used to calculate the inner temperature during the hybrid simulation, and the hysteresis displacement-force loops of the SPR-S bearing are used to calculate the temperature. The calculated and experimental inner temperatures are shown in Fig. 3.18. It can be observed that the calculated inner temperature is larger than the experimental inner temperature as expected, as the identified $Ah\lambda$ is smaller than the true value.

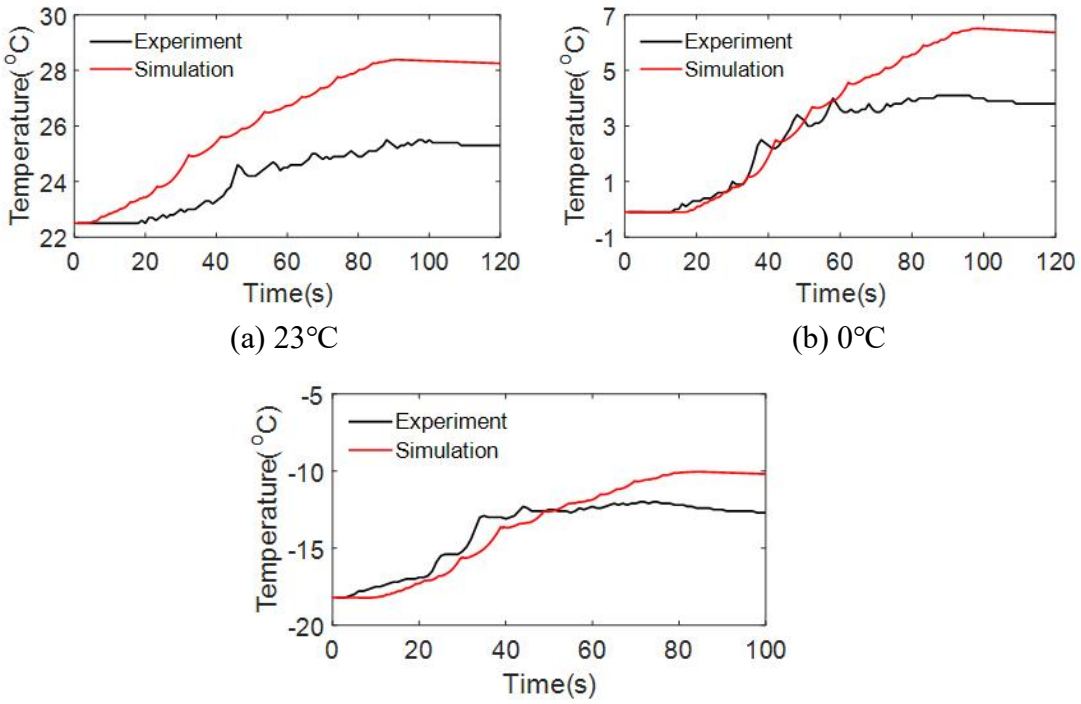

(a) 23℃ (b) 0℃

(c) −20℃

Figure 3.18 Comparison of the experimental and numerical inner temperature of rubber in hybrid simulation

3.6 Hysteresis behavior depending on inner temperature

The shear modulus and equivalent damping ratio vs. inner temperature at different ambient temperatures are shown in Fig. 3.19. The shear modulus and equivalent damping ratio are calculated by Eq. 2.1, Eq. 2.2, Eq. 2.3, Eq. 2.4, respectively. The temperature is measured inner temperature of rubber1 of the SPR-S bearing in cyclic loading. Different color means different ambient temperature case. For each case, the 1st to the 5th data points are calculated from the 1st to the 5th hysteresis loops of the SPR-S bearing in cyclic loading tests at strain level 50%, the 6th to the 10th data points are calculated from the five hysteresis loops at strain level 100%, other data points are also ordered like this, until the 21st to 25th data points are calculated from the five hysteresis loops at strain level 250%.

It can be observed that although the shear modulus decreases as the inner temperature of rubber increases for each ambient temperature case, the difference of shear modulus at different ambient temperature cases when the inner temperature is around 25℃ shows that the inner temperature of rubber is not the only factor that affects the shear modulus, other factors such as the strain amplitude and distribution of temperature over the volume of the bearing may also influence the mechanical characteristics of the bearing. From Eq. 3.19(b), it can be found that the equivalent damping ratio increases as the inner temperature increases at same strain amplitude for each ambient temperature case, and the equivalent damping ratio is less affected by the inner temperature compared with the strain amplitude.

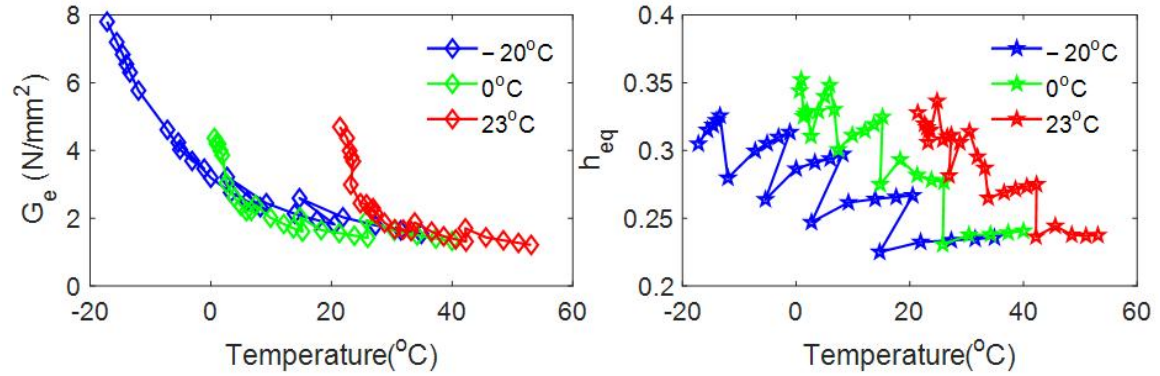

(a) Equivalent shear modulus G_e

(b) Equivalent damping ratio h_{eq}

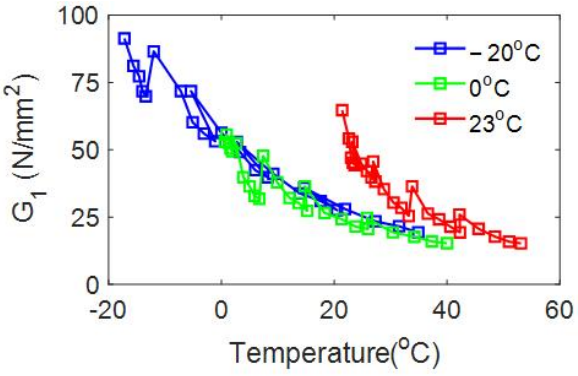

(c) Shear modulus G_1

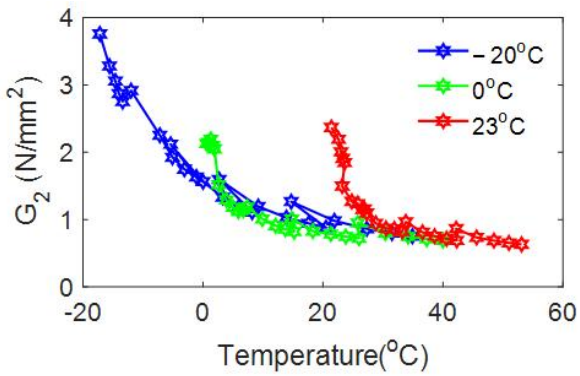

(d) Shear modulus G_2

Figure 3.19 Shear modulus and equivalent damping ratio vs. inner temperature in cyclic loading

3.7 Comparison between experimental and analytical seismic response by bilinear model

3.7.1 Model parameters identification by cyclic loading test

The bilinear model is applied to conduct the seismic analysis of a SPR-S bearings isolated bridge in order to investigate the applicability of the bilinear model. The bilinear model parameters identified from the cyclic loading tests SC1, SC2, SC3 and the corresponding contribution rate calculated by Eq. 2.14 are shown in Table 3.7.

Table 3.7 Identified parameters and contribution rates using bilinear model in cyclic loading tests

Temperature	K_1 (*KN/mm*)	α	q (*KN*)	Contribution rate R
23°C	8.79	0.13	66.53	0.81
0°C	6.39	0.20	62.20	0.73
−20°C	12.65	0.13	96.82	0.74

The comparison of the experimental and numerical hysteresis loops computed by the bilinear model in cyclic loading tests is shown in Fig. 3.20. Since the model parameters are identified respectively for each ambient temperature, the increase in the area of the hysteresis loop at lower temperature is captured in a limited extent.

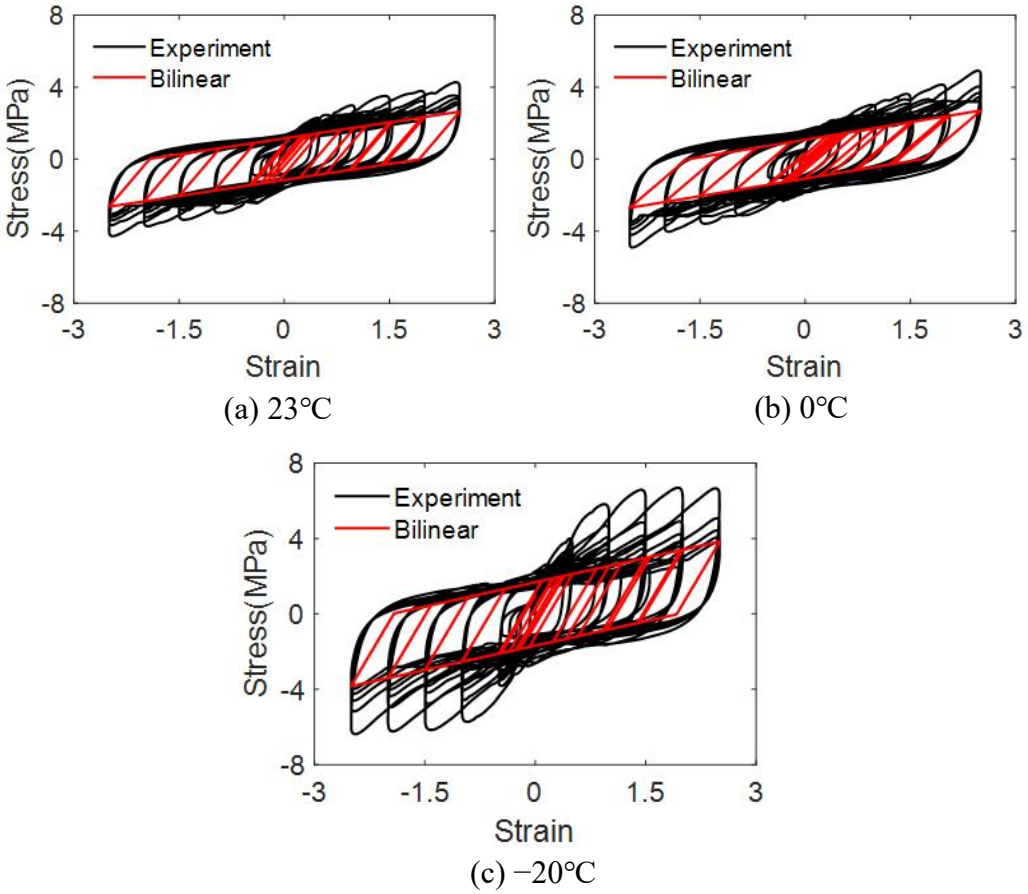

(a) 23℃ (b) 0℃

(c) −20℃

Figure 3.20 Comparison of the experimental and numerical hysteresis loops computed by the bilinear model in cyclic loading tests

3.7.2 Comparison between experimental and analytical results

Then the identified model parameters shown in Table 3.7 are used to conduct the seismic response analyses of the SPR-S bearings isolated bridge. The comparison of experimental (in Tests SH1, SH2 and SH3) and numerical SPR-S bearing hysteresis loops at different ambient temperatures is shown in Fig. 3.21. Although the increased energy dissipation of the SPR-S bearings can be described by the bilinear model at a limited degree, the significant stiffness hardening behavior of the SPR-S bearing at lower temperatures can not be well captured, as the conventional bilinear model is temperature-independent.

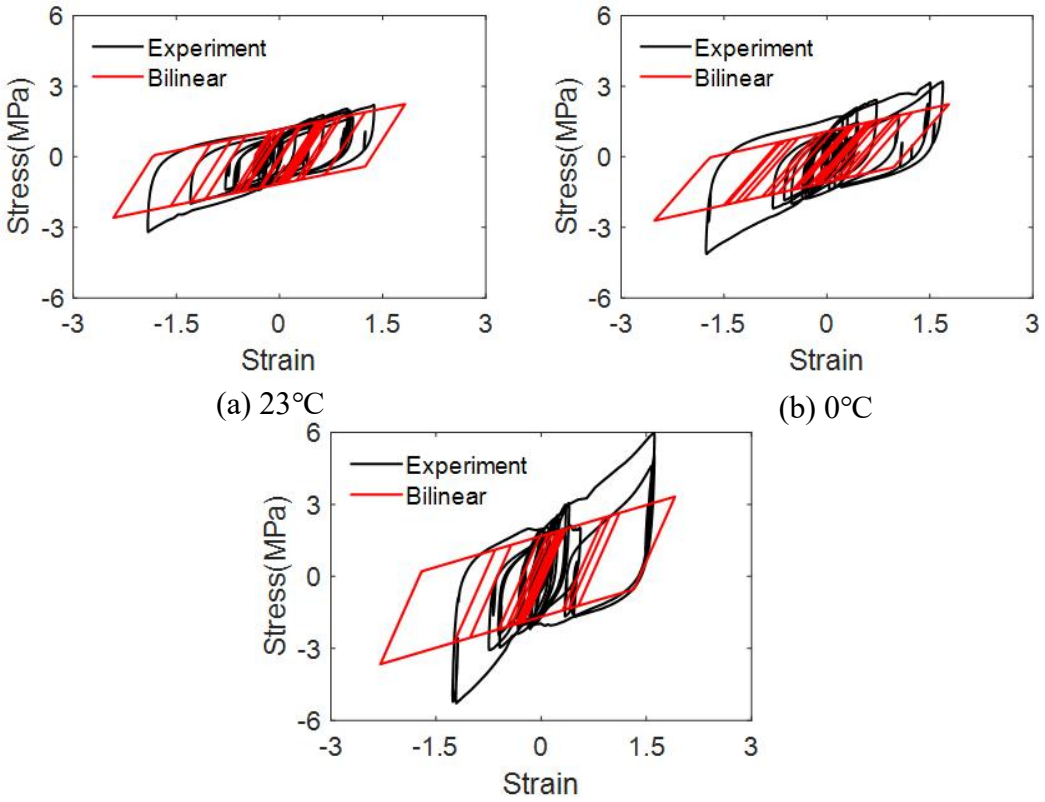

(a) 23℃ (b) 0℃

(c) −20℃

Figure 3.21 Comparison of experimental and numerical SPR-S bearing hysteresis loops

The comparisons of experimental and numerical results in terms of the SPR-S bearing strain pier top displacement and pier top acceleration for different ambient temperatures are shown in Fig. 3.22, Fig. 3.23 and Fig. 3.24, respectively. Although the maximum bearing strain is overestimated in the numerical result as the stiffness of the bearing is underestimated by the bilinear model, especially at −20℃, the numerical pier top displacement shows a similar result with the hybrid simulation, this might be caused by the reduced experimental pier top displacement due to the enhanced energy dissipation capacity of the SPR-S bearings under the ground motion. The maximum pier top acceleration is overestimated by the bilinear model, especially at lower temperatures.

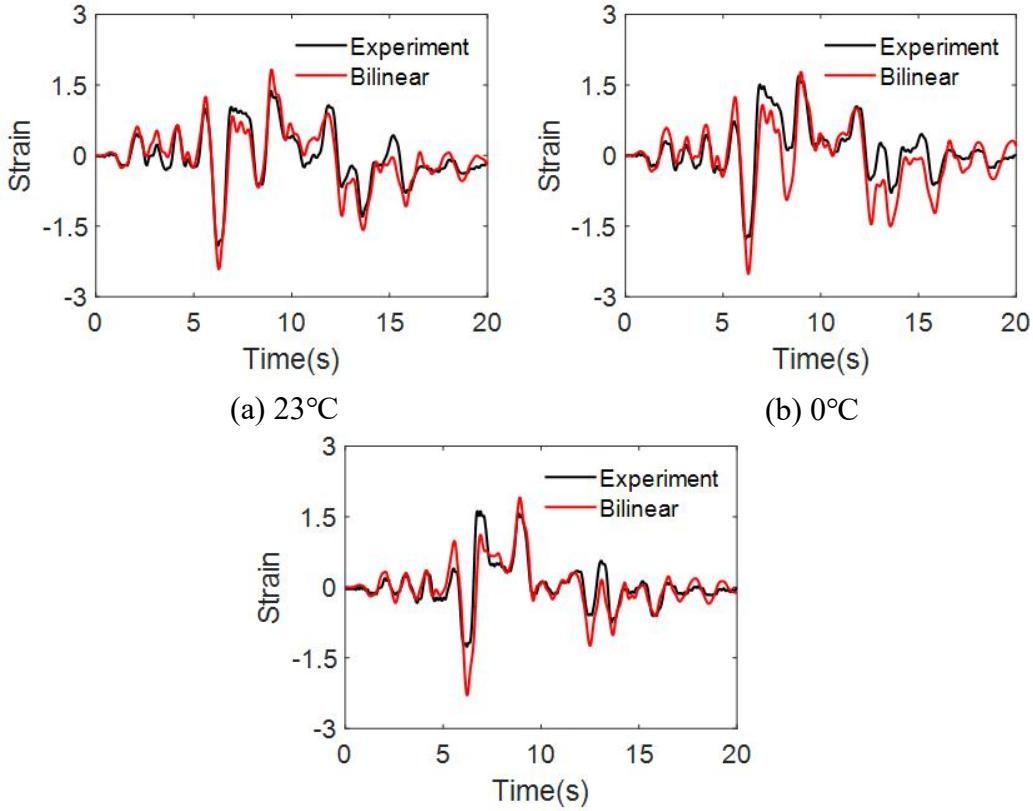

(a) 23℃ (b) 0℃

(c) −20℃

Figure 3.22 Comparison of experimental and numerical SPR-S bearing strain

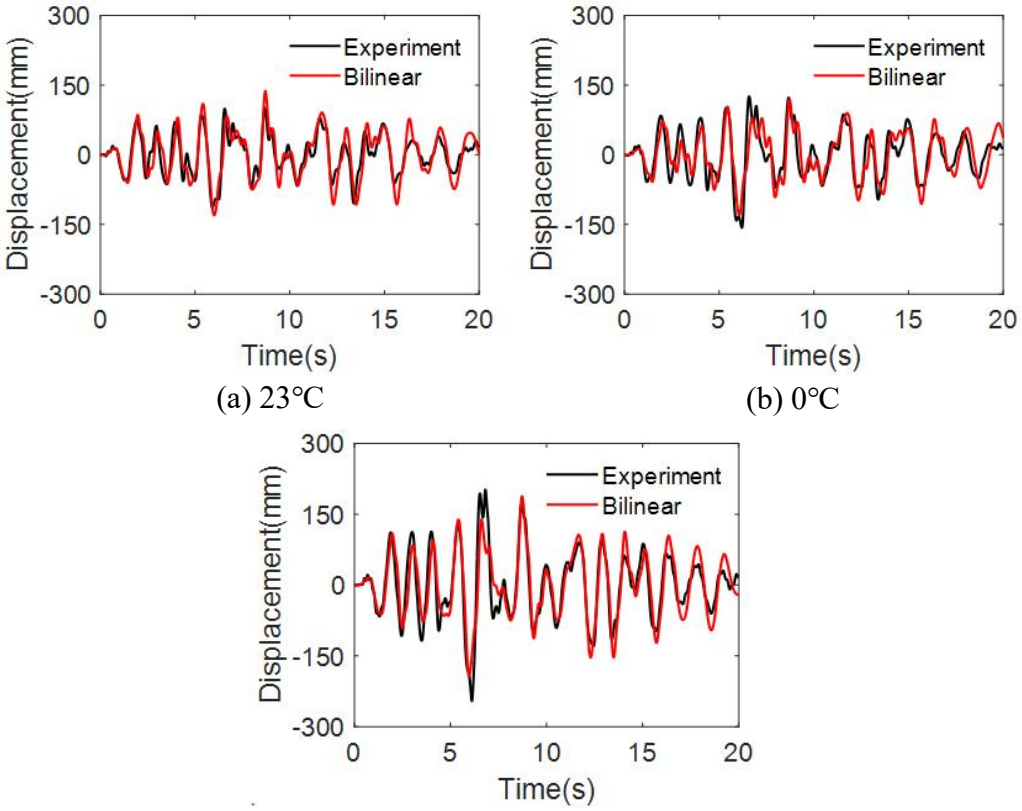

(a) 23℃ (b) 0℃

(c) −20℃

Figure 3.23 Comparison of experimental and numerical pier top displacement

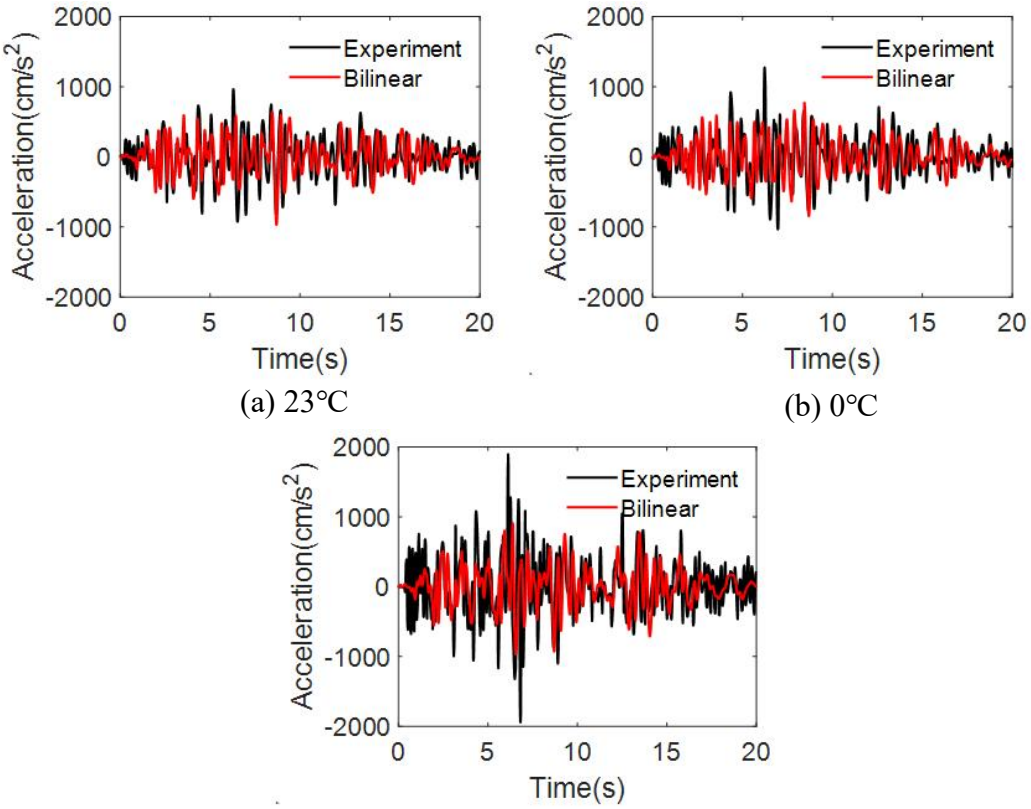

(a) 23℃ (b) 0℃

(c) −20℃

Figure 3.24 Comparison of experimental and numerical pier top acceleration

3.8 Summary

In this chapter, the cyclic shear loading tests and hybrid simulation at ambient temperature of −20℃, 0℃ and 23℃ are carried out to evaluate the low-temperature effect on the seismic performance of the SPR-S bearing and the isolated bridge with SPR-S bearings. The seismic response of the SPR-S bearing in hybrid simulation is compared with that of the HDR bearing in terms of the bearing hysteresis loops, bearing strain and energy dissipation. The formula proposed in chapter 2 is improved and used to calculate the inner temperature of the SPR-S bearing and the estimated temperature is compared with the measured temperature in cyclic loading tests and hybrid simulation. The hysteresis behavior of SPR-S bearings depending on the inner temperature is investigated according to the successfully measured inner temperature in the cyclic loading. Moreover, the seismic response analysis of the SPR-S bearings isolated bridge is conducted by using the bilinear model for the SPR-S bearing, and the analytical results are compared with the hybrid simulation results in terms of the bearing hysteresis loops, bearing strain, pier top displacement and pier top acceleration. The following main conclusions can be obtained according to the results.

(1) In the cyclic shear loading tests, the cyclic behavior of the SPR-S bearing at 23℃ and 0℃ is similar, while the cyclic behavior at −20℃ shows a significant difference with the result at 23℃ and 0℃, as the stiffness hardening and higher energy dissipation are more obviously

observed at −20℃.

(2) The shear modulus and equivalent damping ratio of the SPR-S bearing among different temperatures decrease as the cyclic loading progresses to larger shear strain amplitudes due to the self-heating of high damping rubber and lead plugs.

(3) In the hybrid simulation, the SPR-S bearing stress and pier top displacement are higher at lower ambient temperatures. The maximum shear strain of SPR-S bearings is reduced by a factor of 0.66 and the maximum pier top displacement is increased by a factor of 2.16 at −20°C compared with the test results at 23°C.

(4) The energy dissipation capacity of SPR-S bearings is enhanced at −20℃ by 43% compared with the result at 23℃, which is favorable under ground motions.

(5) The comparison of seismic responses between the SPR-S bearing and HDR bearing shows that the SPR-S bearing is less affected by the low-temperature effect than the HDR bearing, this may be caused by the higher temperature increment for the lead plugs than the high damping rubber, thus, the inner temperature rise of SPR-S bearing is larger than that of the HDR bearing, and the stiffness hardening appears in the initial phase due to a low ambient temperature decreases as the inner temperature of the SPR-S bearing increases under cyclic loading.

(6) The comparison between the numerical and experimental seismic responses of the isolated bridge shows that the maximum bearing strain is overestimated by the bilinear model, especially at −20℃, while the numerical pier top displacement shows a similar result with the hybrid simulation at each ambient temperature.

Chapter 4 Real-time hybrid simulation for seismic performance assessment of HDR bearings at low temperatures

4.1 General

In hybrid simulation H1, H2 and H3, the loading speed was slow and different from the actual condition. Hence, the real-time hybrid simulation was performed and compared with the low loading speed hybrid simulation results in this chapter.

In this chapter, the real-time hybrid simulation is conducted at ambient temperature 23°C, 0°C and −20°C. The real-time hybrid simulation results are compared with those obtained in the pseudo dynamic hybrid simulation with constant slower loading rate described in chapter 2 in terms of the hysteresis loops of the HDR bearing, bearing strain, pier top displacement and pier top acceleration. There are 10 thermocouples installed in the HDR bearing to better understand the inner temperature distribution. The cyclic shear loading tests at ambient temperature 23°C, 0°C and −20°C are also carried out to investigate the mechanical characteristics of the HDR bearing at low temperatures.

4.2 Experimental program

4.2.1 HDR bearing specimen

The dimensions and material properties of HDR bearing specimens used in the cyclic loading tests and real-time hybrid simulation described in this chapter are same with those shown in Table 2.1 in chapter 2. Different from the tests described in chapter 2 with small number of thermocouples in which the most of thermocouples are broken during the test, there are 10 thermocouples installed in the specimen, and many thermocouples are not destroyed in the tests described in this chapter, as the thermocouples are installed in a perpendicular direction to the horizontal shear loading to protect the thermocouples from damage. The thermocouple layout of the HDR bearing specimen is shown in Fig. 4.1, four thermocouples (No1~No4) are installed in the third layer (central layer) and another four thermocouples (No5~No8) are installed in the first layer in the same locations with those in the third layer, two thermocouples (No9~No10) are installed on the outside surface of the rubber at 1/2 and 3/4 of the total height of high damping rubber.

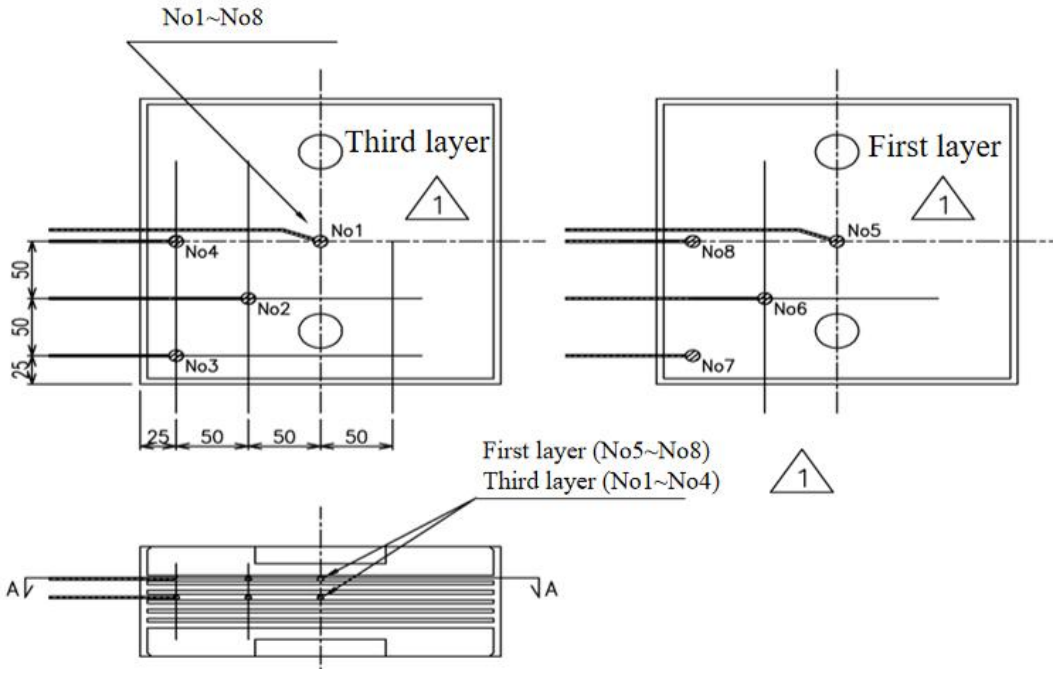

Figure 4.1 Thermocouple layout of HDR bearing specimen

4.2.2 Test cases and test sequence

The test cases for the cyclic loading tests and hybrid simulation are listed in Table 4.1. Three HDR bearing test specimens (No. 8, No. 9, No. 10) were used for the cyclic loading tests C4, C5, C6 and three real-time hybrid simulation tests RH1, RH2, RH3 at three different air temperatures (23℃, 0℃ and −20℃). The tests C4, C5, C6 were conducted using previously unloaded specimens No. 8, No. 9, No. 10, and then those specimens were used in the tests RH1, RH2 and RH3, respectively. Different from the tests C1, C2, C3 in chapter 2, there was a long interval time about 1 hour between the adjacent cycles with different strain amplitudes to make the bearing temperature approach the ambient temperature to eliminate the influence of self-heating of rubber materials in the tests C4, C5, C6. For the test C4, there was not enough time to conduct the cyclic loading at 250% strain amplitude and the test C4 was continued on the next day.

Table 4.1 Test cases

Case No.	Test	Temperature (℃)	Specimen No.	Date	Initial loading	Recovery days
C4	Cyclic loading	−20	8	2022/2/15, 2/16	Yes	Initial loading
RH1	Hybrid simulation	−20	8	2022/2/17	No	1
C5	Cyclic loading	0	9	2022/2/22	Yes	Initial loading
RH2	Hybrid simulation	0	9	2022/2/24	No	2
C6	Cyclic loading	23	10	2021/12/14	Yes	Initial loading
RH3	Hybrid simulation	23	10	2021/12/16	No	2

4.3 Quasi-static cyclic loading test

4.3.1 Cyclic behavior of the HDR bearing at different temperatures

The loading conditions for the HDR bearing in cyclic loading tests C4, C5 and C6 are same with that described in Table 2.5. The shear stress–strain relationships of HDR bearings at different ambient temperatures are shown in Fig. 4.2, the 'Int' denotes the data obtained in the cyclic loading tests C4, C5 and C6 described in this chapter in which there is an interval time about 1 hour between the loading with different strain amplitudes, and the 'Cont' denotes the data obtained in the cyclic loading tests C1, C2 and C3 described in chapter 2 in which there is small interval time about 3 minutes between the loading with different strain amplitudes and the specimen can be treated as loaded continuously. Since the specimens are initially loaded and the inner temperature of the bearing is partly recovered during the rest time between different strain amplitudes in the Int cyclic loading test, the stiffness and the characteristic strength in the cyclic loading tests C4, C5, C6 are larger than those in the cyclic loading tests C1, C2, C3 and the Mullins effect in the cyclic loading tests C4, C5, C6 is more obviously observed.

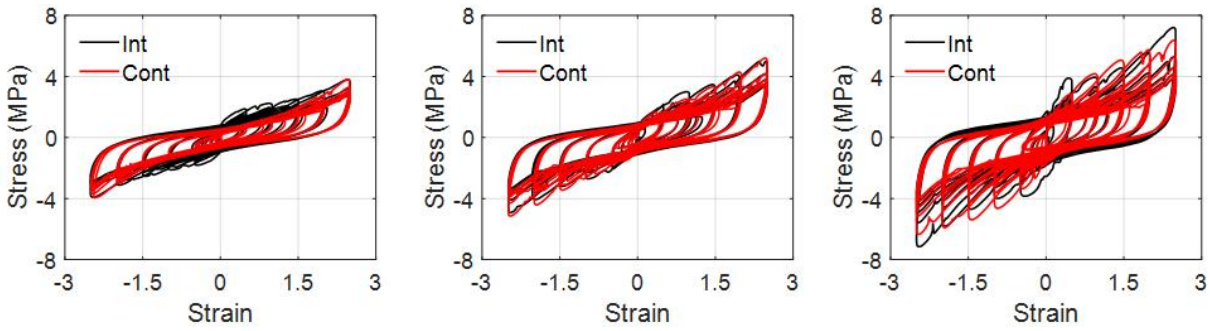

(a) 23℃ (b) 0℃ (c) −20℃

Figure 4.2 Shear stress–strain relationships of HDR bearings at different ambient temperatures

4.3.2 Mechanical characteristics of the HDR bearing

The equivalent shear modulus and equivalent damping ratio of the bearing calculated by Eq. 2.1 and Eq. 2.2 based on the first and fifth hysteresis loops of the bearing in Int cyclic loading tests C4, C5, C6 and Cont cyclic loading tests C1, C2, C3 are compared in this study. The comparison of equivalent shear modulus of the bearing under different cyclic loading tests is shown in Fig. 4.3. It can be seen that the equivalent shear modulus in the Int cyclic loading tests is larger than that in the Cont cyclic loading tests at small strain amplitude, indicating the softening phenomenon of the bearing due to the initial loading effect. Meanwhile, although the bearing temperature almost recovered to the ambient temperature during the rest time between the adjacent cycles with different strain amplitudes in the Int cyclic loading tests, the difference of equivalent shear modulus between Int cyclic loading tests and Cont

cyclic loading tests is smaller at larger strain amplitudes, which is caused by the self-heating of rubber materials under cyclic loading.

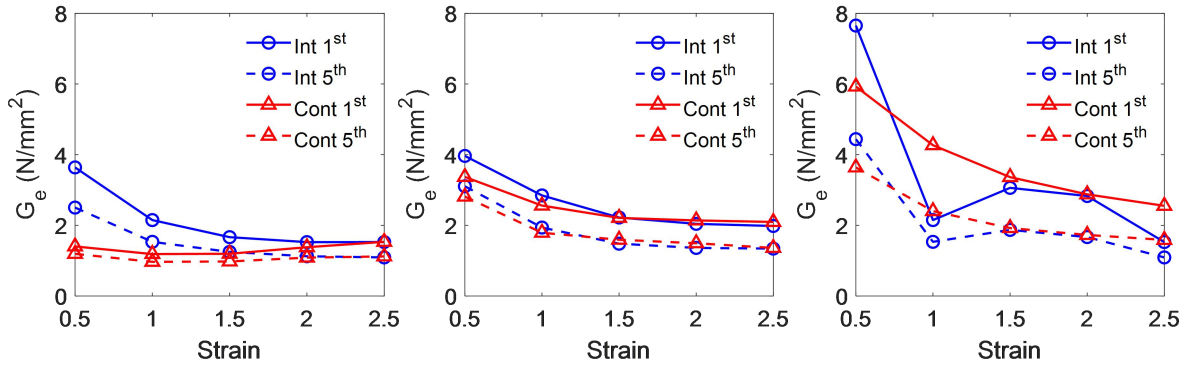

(a) 23℃ (b) 0℃ (c) −20℃

Figure 4.3 Comparison of equivalent shear modulus of the bearing under different cyclic loading tests

The comparison of equivalent damping ratio of the bearing under different cyclic loading tests is shown in Fig. 4.4. It can be found that the difference of damping ratio between the Int cyclic loading tests and Cont cyclic loading tests is smaller at lower ambient temperature, hence, the damping ratio is less affected by the initial loading effect under lower temperatures. In general, the damping ratio in the Int cyclic loading tests is larger than that in the Cont cyclic loading tests, indicating a better seismic performance of the bearing that has not been loaded.

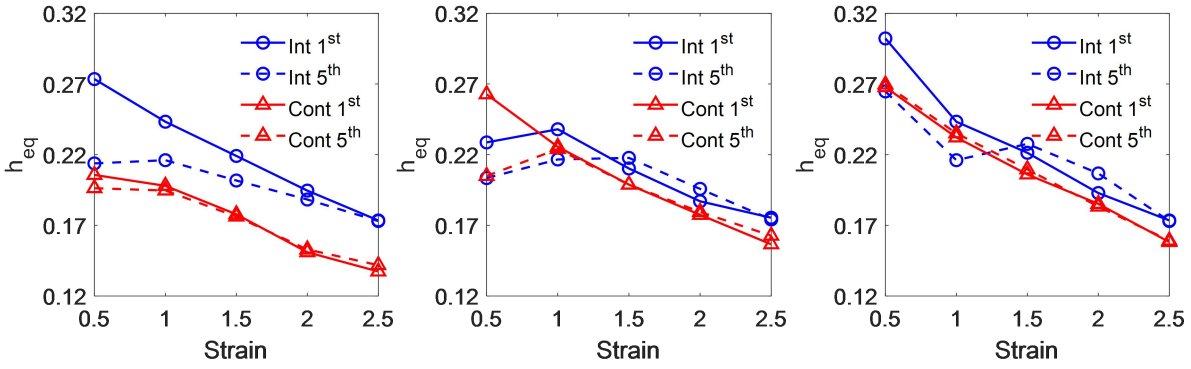

(a) 23℃ (b) 0℃ (c) −20℃

Figure 4.4 Comparison of equivalent damping ratio of the bearing under different cyclic loading tests

4.3.3 Measured temperature

The measured temperature of the bearing in tests C4, C5, C6 is shown in Fig. 4.5, the subtitle of each small figure denotes the umber of the thermocouple shown in Fig. 4.1, the red lines show the results in the third layer of rubber and the black lines show the results in the first layer of rubber, some thermocouples are broken during the cyclic loading tests and the results of the broken thermocouples are not shown in Fig. 4.5. It can be observed that the

temperature for the No 1~No 4 at the third layer of the bearing is higher than that of the No 5~No 8 at the first layer of the bearing, as the third layer is close to the center of the bearing. Meanwhile, the temperature drop rate for the first layer is higher than that of the third layer of the bearing, as the first layer is closer to the outer steel and the thermal conductivity rate is faster. The temperature increment is larger under cyclic loading with larger strain amplitude, as the area of hysteresis loops of the bearing is larger at larger strain amplitude, the maximum temperature increment of the bearing measured by the thermocouple No 1 is 18.2℃, 18.8℃ and 26.3℃ at ambient temperature 23℃, 0℃ and −20℃, respectively. Moreover, the temperature variation of the outside surface (No 9 and No 10) of the bearing is small except for the ambient temperature case 23℃. For the case of −20℃, there was not enough time to conduct the cyclic loading at 250% strain amplitude for one day and the test at 250% strain amplitude was continued on the next day, the measured temperature during the long rest time is eliminated for better view of the temperature history.

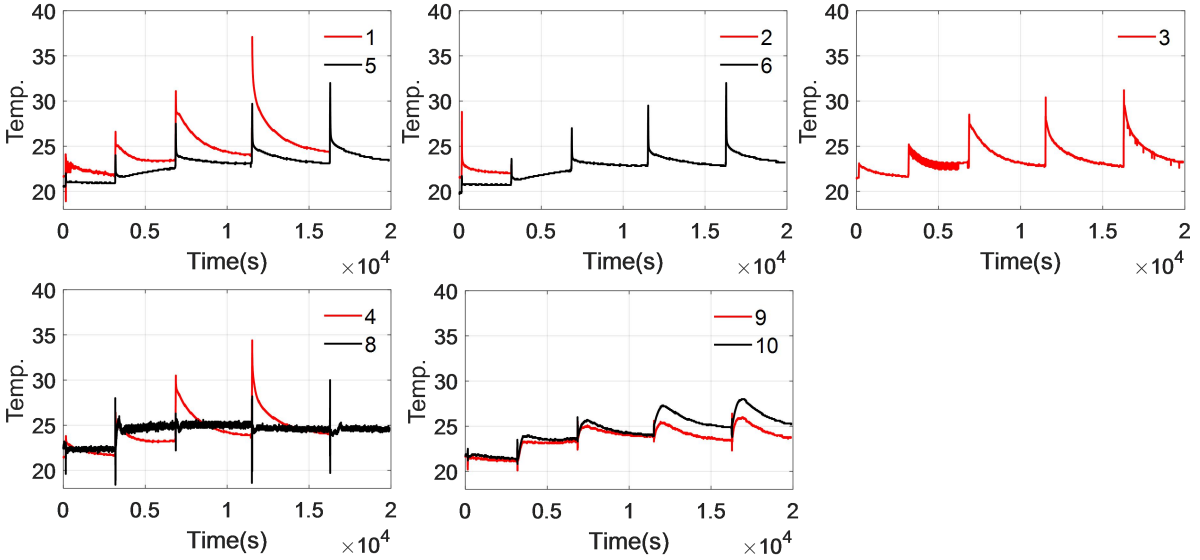

(a) 23℃

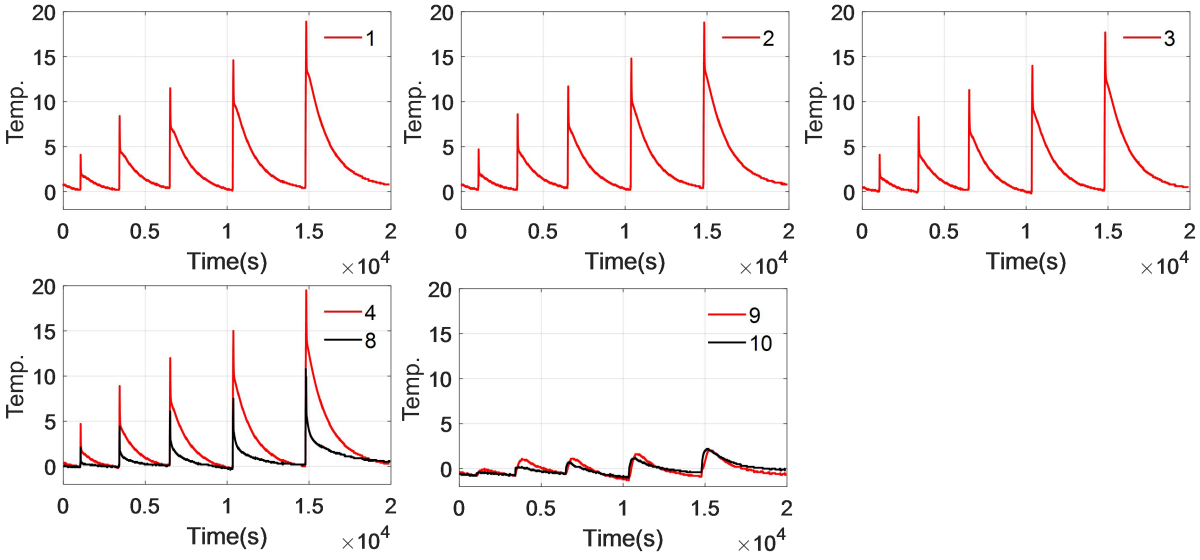

(b) 0℃

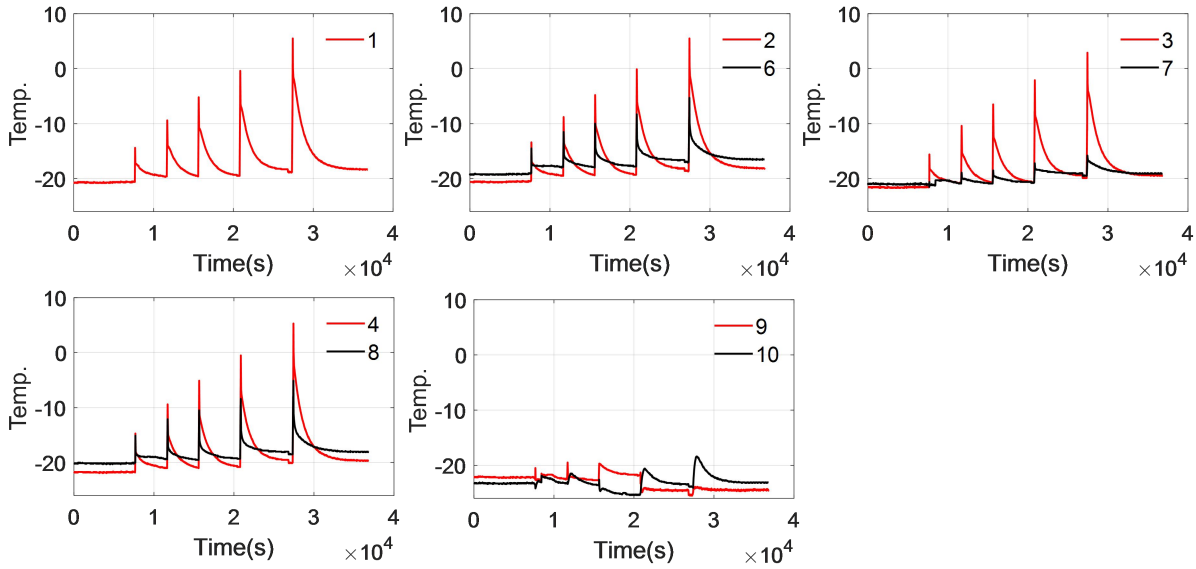

(c) −20℃

Figure 4.5 Measured temperature of the bearing under cyclic loading at different ambient temperatures

4.4 Comparisons of the real-time and pseudo dynamic hybrid simulation results

The results of the pseudo dynamic hybrid simulation with low loading speed are compared with the real-time hybrid simulation results. Since the pseudo dynamic hybrid simulation was conducted twice under each ambient temperature case to investigate the initial loading effect, and all of the specimens are non-initially loaded in the real-time hybrid simulation, the pseudo dynamic hybrid simulation shown in Table 4.2 is chosen to compare with the real-time hybrid simulation. Note that there is some problem in the pseudo dynamic hybrid simulation with non-initial loading at 0℃ (the detail is explained in section 2.5.5), hence, the pseudo dynamic hybrid simulation with initial loading is chosen to compare with the real-time hybrid simulation at 0℃. The input ground motion is same with that described in Fig. 2.15 in the real-time hybrid simulation.

Table 4.2 Pseudo dynamic hybrid simulation chosen to compare with the real-time hybrid simulation

Case No.	Temperature (℃)	Specimen No.	Date	Initial loading	Recovery days
H4	−20	2	2020/01/30	No	43
H2	0	3	2020/01/16	Yes	Initial loading
H6	23	1	2019/11/14	No	1

The similitude law used in the real-time hybrid simulation is shown in Table 4.3, it is set

based on the same strain velocity between the bearing with real size and the 1/6 scaled bearing specimen in the test, and the scale factor is also 6.

Table 4.3 Similitude law for real-time hybrid simulation

Physical parameter	Unit	Scale factor
Strain velocity	1	1
Displacement	m	S
Force	N	S^2
Acceleration	m/s^2	S
Velocity	m/s	S
Time	sec	1

The horizontal loading speed in the pseudo dynamic (Tests H4, H2, H6) and real-time hybrid simulation (Tests RH1, RH2, RH3) at different temperatures is shown in Fig. 4.6 and Fig. 4.7, respectively. In the pseudo dynamic hybrid simulation, the loading speed is controlled to be 10mm/s, and the loading time is around 130s. In the real-time hybrid simulation, the loading speed at each time step is obtained by the absolute value of the displacement increment of the bearing specimen divided by the time interval, the loading time is around 20s which is same with the real ground motion time.

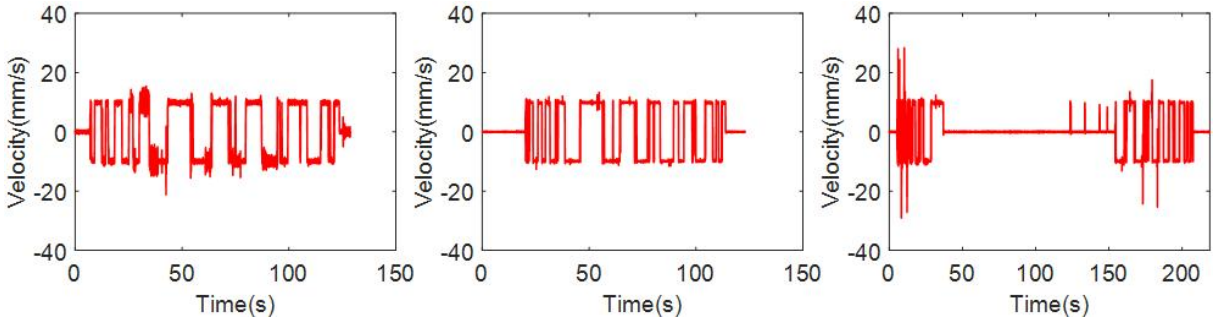

(a) 23℃ (b) 0℃ (c) −20℃

Figure 4.6 Horizontal loading speed in pseudo dynamic hybrid simulation at different temperatures

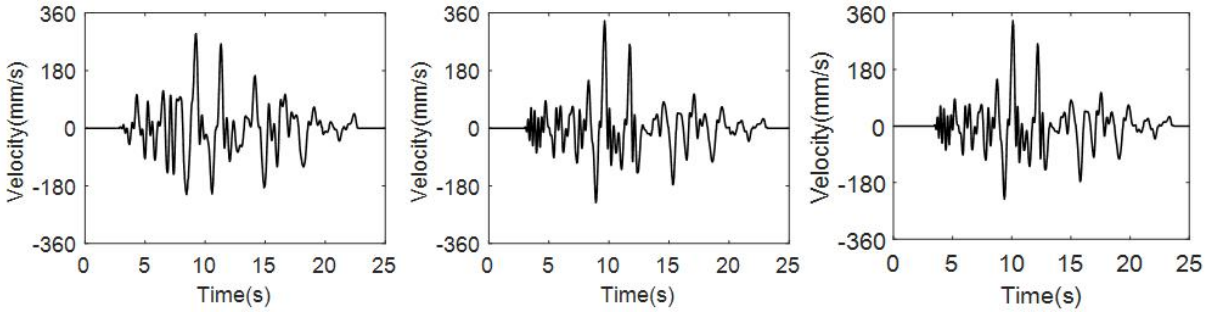

(a) 23℃ (b) 0℃ (c) −20℃

Figure 4.7 Horizontal loading speed in real-time hybrid simulation at different temperatures

4.4.1 Responses of the HDR bearing and pier

The comparison of load-displacement hysteresis loops of the HDR bearing in the real-time and pseudo dynamic hybrid simulation is shown in Fig. 4.8. Different from what we expected, the maximum stress of the bearing is larger in the pseudo dynamic hybrid simulation with lower loading speed at low temperatures, especially at −20℃, and the sharper corners at the maximum strain observed in the pseudo dynamic hybrid simulation at 0℃ and −20℃ can not be seen in the real-time hybrid simulation. Moreover, the initial large stiffness and subsequent stiffness softening observed in the pseudo dynamic hybrid simulation result can not be found in the real-time hybrid simulation at −20℃. The low-temperature effect of HDR bearings is less than we expected under ground motions with higher speed. It might be caused by the higher inner temperature of the bearing due to the smaller energy loss from the bearing to loading system in the real-time hybrid simulation with shorter time, or an island with concentrated higher inner temperature is generated in the intermediate rubber layers and the deformation of the bearing is more concentrated around this island, thus the overall stiffness softening occurs in the real-time hybrid simulation. However, these are only hypothesis, the cause of this phenomenon will be clarified in detail in the future.

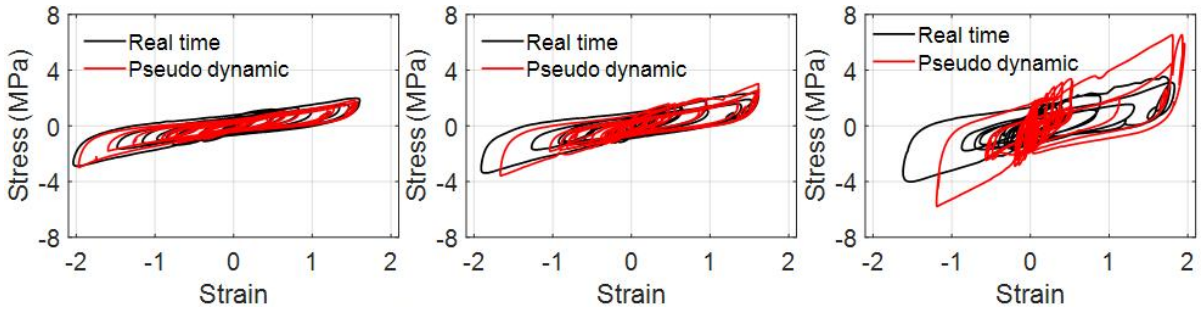

(a) 23℃ (b) 0℃ (c) −20℃

Figure 4.8 Comparison of hysteresis loops of HDR bearing in the real-time and pseudo dynamic hybrid simulation

The comparison of shear strain of HDR bearings in the real-time and pseudo dynamic hybrid simulation is shown in Fig. 4.9. It can be seen that the maximum strain is larger in the real-time hybrid simulation at 23℃ and 0℃, and is larger in pseudo dynamic hybrid simulation at −20℃. Meanwhile, the difference of strain between the real-time and pseudo dynamic hybrid simulation is more obvious at lower ambient temperatures.

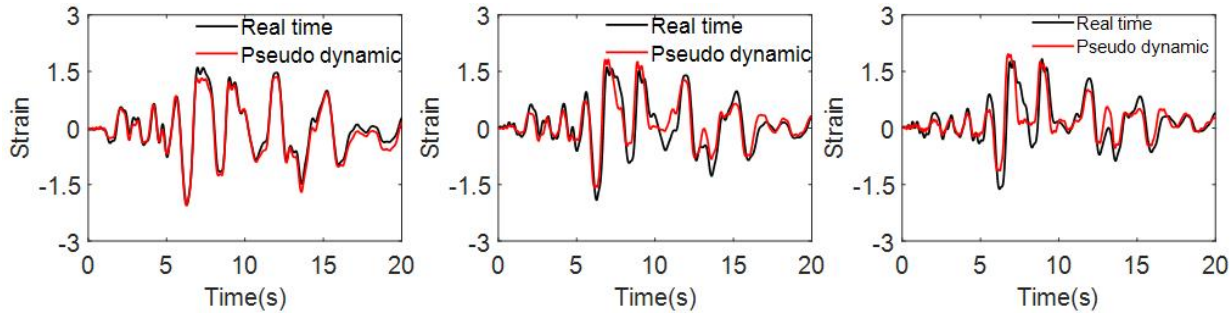

(a) 23℃ (b) 0℃ (c) −20℃

Figure 4.9 Comparison of shear strain of HDR bearings in the real-time and pseudo dynamic hybrid simulation

The comparisons of pier top displacement and pier acceleration are shown in Fig. 4.10 and Fig. 4.11, respectively. It can be seen that the pier responses are larger in pseudo dynamic hybrid simulation, and the difference of pier responses between the real-time and pseudo dynamic hybrid simulation is more obviously observed at lower ambient temperatures.

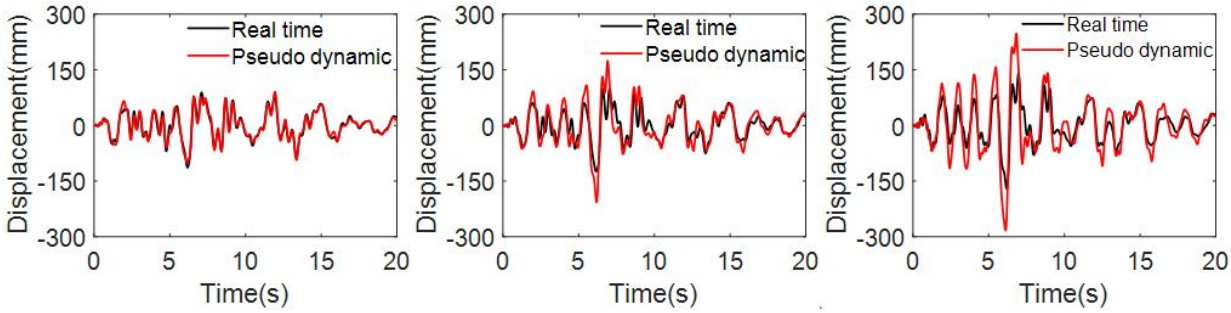

(a) 23℃ (b) 0℃ (c) −20℃

Figure 4.10 Comparison of pier top displacement in the real-time and pseudo dynamic hybrid simulation

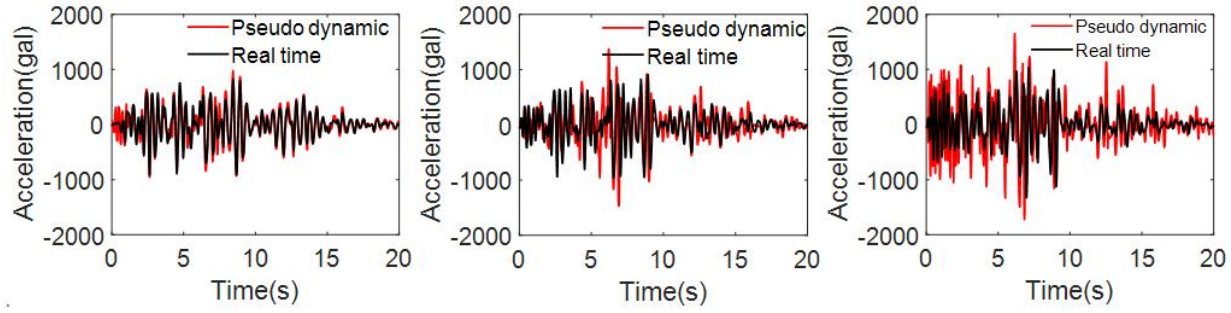

(a) 23℃ (b) 0℃ (c) −20℃

Figure 4.11 Comparison of pier top acceleration in the real-time and pseudo dynamic hybrid simulation

The comparison of actuator command and measured displacements of HDR bearings in Tests RH1, RH2, RH3 in shown in Fig. 4.12. It can be seen that there is a small delay of 0.03s between the actuator command and measured displacements, the measured displacement is 0.03s slower than the actuator command displacement, and the displacement difference between the actuator command and measured values is less than 1.5mm. The real-time hybrid

simulation is successfully conducted in this study, and the occurrence of divergence of the HDR bearing displacement is considered to be prevented by the long period of the HDR bearings isolated bridge according to the stability condition of vibration analysis. It is required that the time increment (it is 0.01s in this study) is smaller than the 1/20 of the period of structure, and the time increment is small enough in this study.

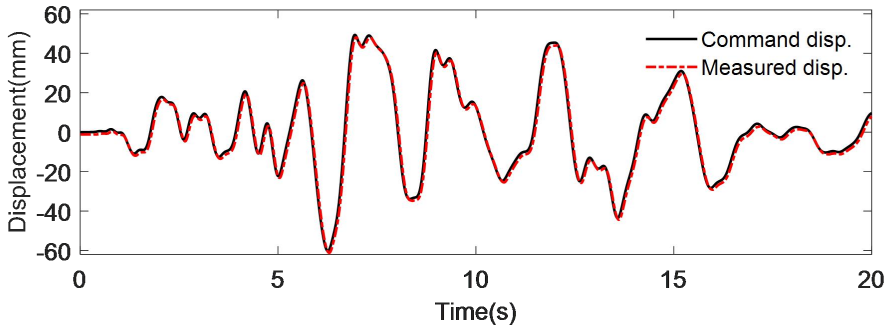

(a) 23℃

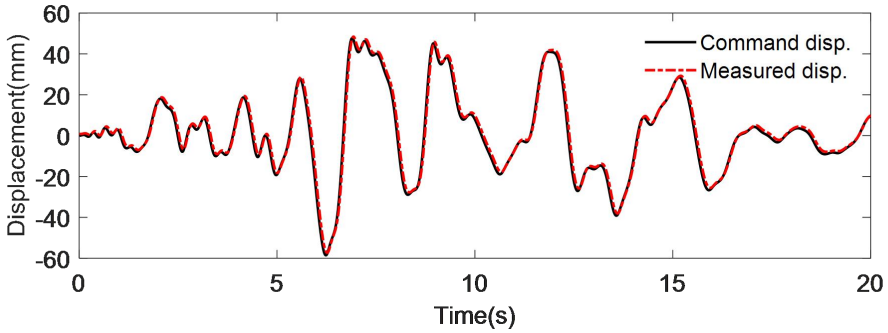

(b) 0℃

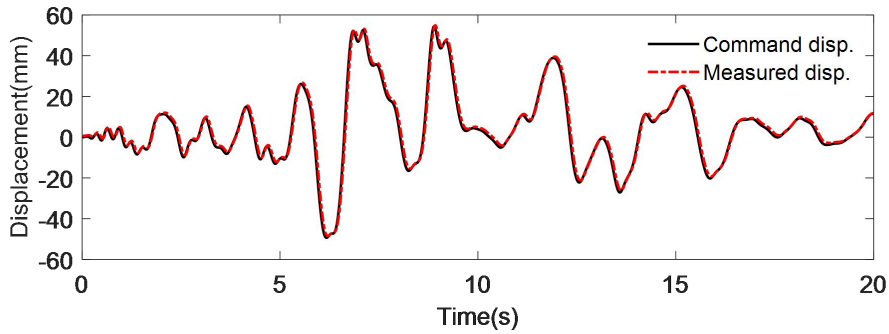

(c) −20℃

Figure 4.12 Comparison of actuator command and measured displacements of HDR bearings in real-time hybrid simulation

4.4.2 Measured temperature

The measured temperature of HDR bearings in Tests RH1, RH2, RH3 at different ambient temperatures is shown in Fig. 4.13. The results shown in left figures with long time are measured by thermocouples during and after the hybrid simulation, and the right figures with shorter time show the enlarge image of left figures during the hybrid simulation. It can be seen that the temperature suddenly increased during the loading phase, and slowly progressed

to a stable value after the test was finished in a long time in each temperature case. The inner temperatures of the bearing at different locations tend to different stable values, indicating the uniformly distributed temperature over the volume of bearing.

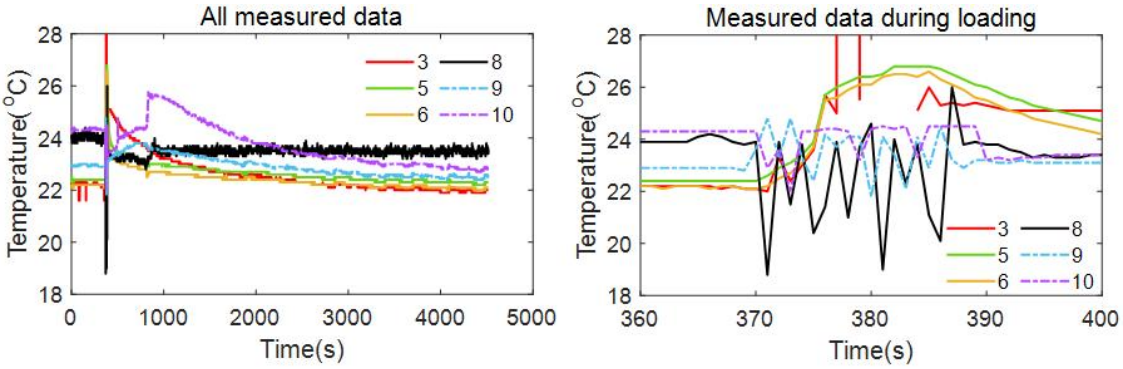

(a) 23℃

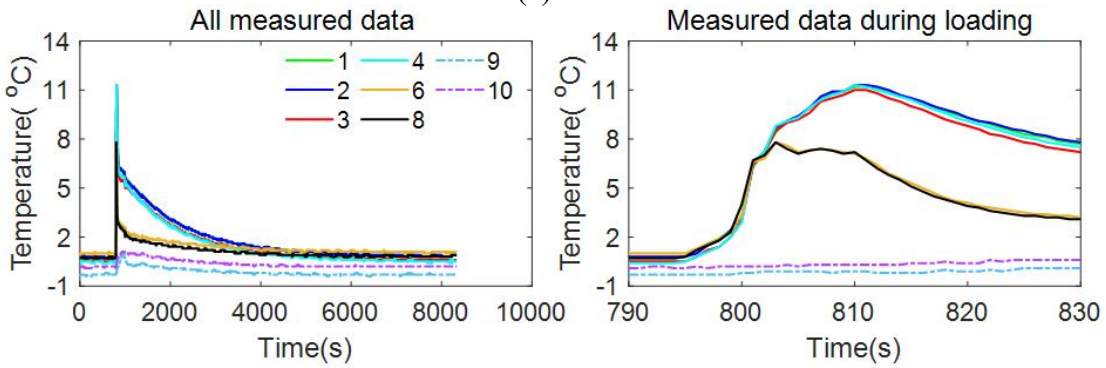

(b) 0℃

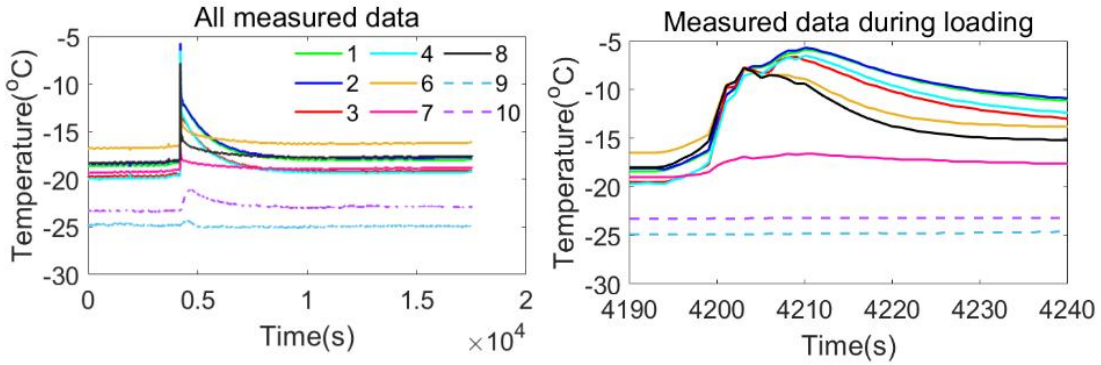

(c) −20℃

Figure 4.13 Measured temperature of HDR bearing in real-time hybrid simulation

The comparison of measured temperature of HDR bearings in pseudo dynamic (Test H4) and real-time (Test RH1) hybrid simulation at −20℃ is shown in Fig. 4.14, the temperatures are measured by the thermocouples (P1 and P2) installed in the central location of bearings in Test H4 and the No 1 thermocouple installed in the third layer of bearings in Test RH1, respectively. Note that the thermocouples located at the third layer of the bearing in the case of 23℃ real-time hybrid simulation and the thermocouples located at the fourth layer of the bearing in the cases of 0℃ pseudo dynamic hybrid simulation were broken, thus, only the result of case −20℃ is compared. It can be seen that the temperature rose 12.5℃ in the real-time hybrid simulation and 10.6℃ in the pseudo dynamic hybrid simulation at −20℃.

The temperature rose is higher in the pseudo dynamic hybrid simulation at the initial phase, then the temperature rose is higher in the real-time hybrid simulation.

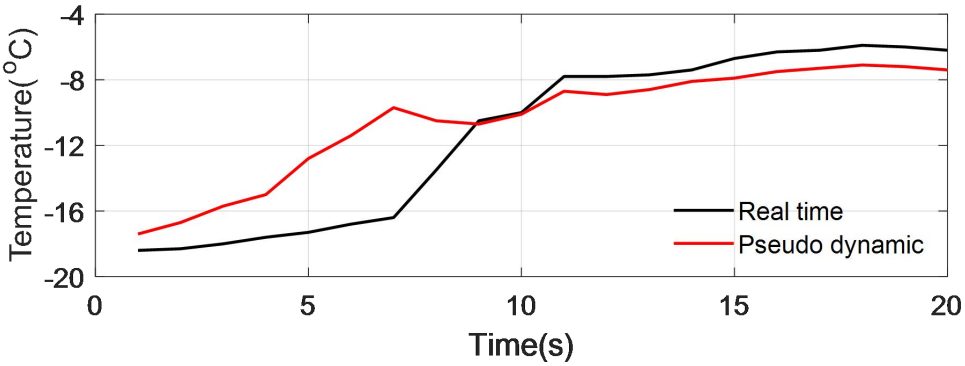

Figure 4.14 Comparison of measured temperature of HDR bearings in real-time and pseudo dynamic hybrid simulation at −20℃

To more obviously show the inner temperature distribution of the bearing, the three-dimensional figures of measured inner temperatures in the real-time hybrid simulation are plotted. The inner temperature at locations that the thermocouples are not installed is predicted by interpolation, and the delaunay triangulation and cubic interpolation algorithm are used as the interpolation methods. Assuming that the temperatures are same at the positions with same distance from the center location at each layer of bearing, then the temperature sample data can be increased according to this symmetry principle. The locations of sample data at the 1st and 3rd layers of the bearing at temperature case −20℃ are shown in Fig. 4.15. The red points denote the locations of measured data and the blue points denote the locations of added symmetry data, there are 12 sample points at the 1st layer and 13 sample points at the 3rd (central) layer as the thermocouple No 5 in the 1st layer was broken during the test. The x-axis and y-axis represent the distance from the center location in the two different orientations, respectively, for example, the coordinate of thermocouple No 3 is (−0.1 m ~ 0.1 m) according to the thermocouple layout of bearing specimen in Fig. 4.1. Note that the loading direction in the tests is the same with the y-axis direction.

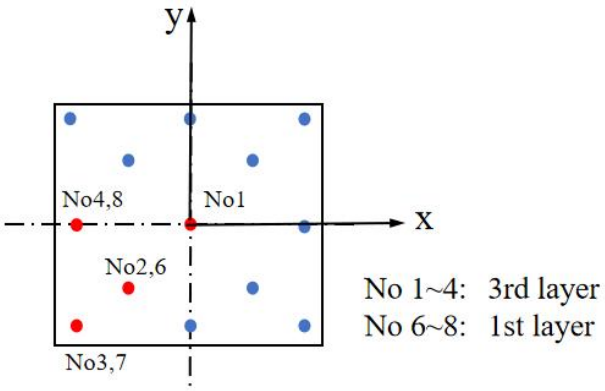

Figure 4.15 Locations of temperature sample data at the 1st and 3rd layers of bearings at −20℃

The plotted temperatures of bearing at the 3rd and 1st layers at −20℃ (in Test RH1) are shown in Fig. 4.16 and Fig. 4.17, respectively. The temperature values shown in the figures

are only typical values obtained during the tests when the inner temperature is near to the maximum value. It can be seen that there is not obvious difference of temperature at different locations at the 3rd layer of bearing, while the temperature values at the edges are much lower than those near the center at the 1st layer of bearing. The temperature distribution shows a shape of 'butterfly' at the 3rd layer and a shape of 'pan' at the 1st layer as there is no measured data in the centre of the 1st layer.

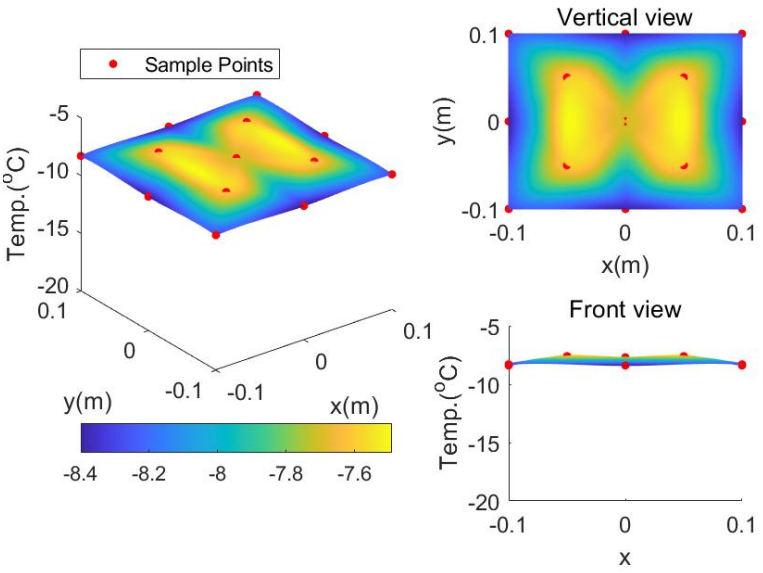

Figure 4.16 Temperature of bearing at the 3rd layer at −20℃

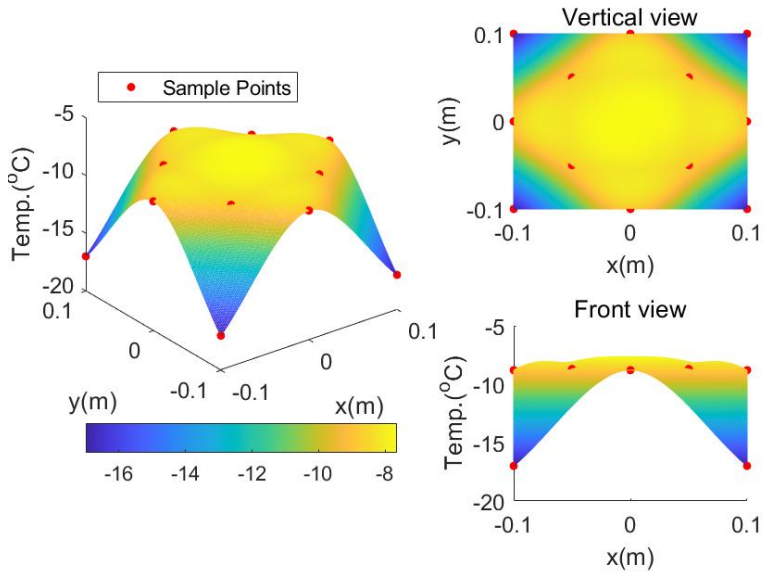

Figure 4.17 Temperature of bearing at the 1st layer at −20℃

The locations of sample data at the 3rd layer of bearing in temperature case 0℃ (in Test RH2) are shown in Fig. 4.18, there are 13 sample points at the 3rd layer. The results at the 1st layer at 0℃ and at the 1st and 3rd layers of bearing at 23℃ are not presented as the measured temperature data is insufficient.

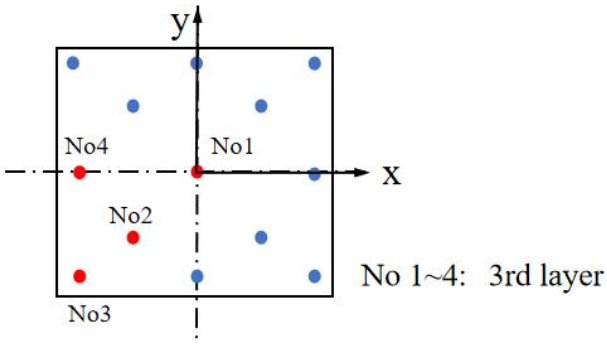

Figure 4.18 Locations of sample data at the 3rd layer of bearing at 0℃

The temperature of the bearing at the 3rd layer at 0℃ is shown in Fig. 4.19. It can be seen that difference of temperature among different locations at the 3rd is also small, and the temperature distribution shows a shape of 'butterfly' which is the same with that shown in Fig. 4.16.

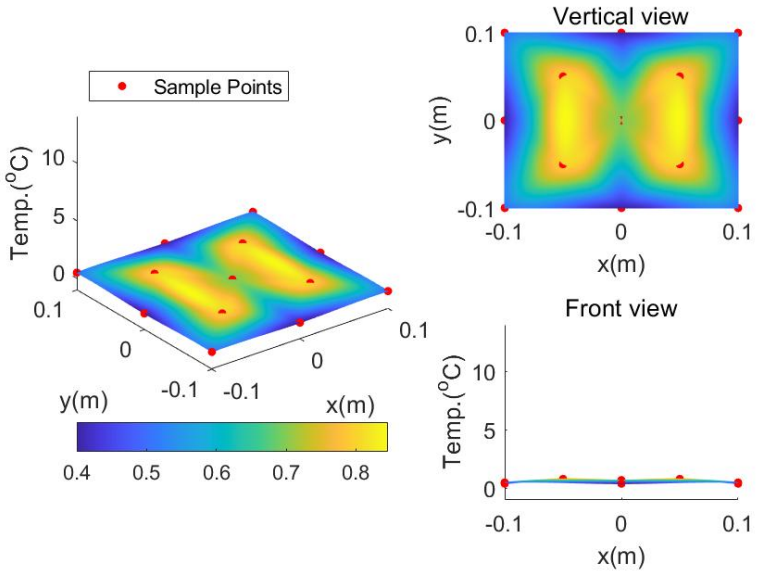

Figure 4.19 Temperature of bearing at the 3rd layer at 0℃

4.4.3 Energy dissipation

The comparison of energy dissipation of the bearing in the pseudo dynamic (Tests H4, H2, H6) and real-time hybrid simulation (Tests RH1, RH2, RH3) is shown in Fig. 4.20. The energy dissipation is calculated by Eq. 2.7. It can be seen that the energy dissipation of the bearing is higher in the pseudo dynamic hybrid simulation at −20℃ and 0℃, as the area of hysteresis loop of the bearing is larger in the pseudo dynamic hybrid simulation at lower temperatures, while the energy dissipation is higher in the real-time hybrid simulation at 23℃. The maximum energy dissipation is reduced by a factor of 0.83 in the real-time hybrid simulation compared with that in the pseudo dynamic hybrid simulation at −20℃.

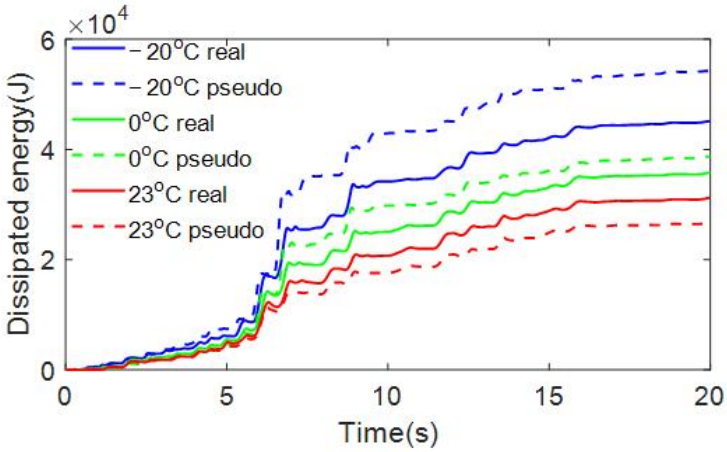

Figure 4.20 Comparison of energy dissipation of the bearing

4.5 Summary

In this chapter, the cyclic shear loading tests and real-time hybrid simulation of the HDR bearings at ambient temperature of −20°C, 0°C and 23°C are carried out to evaluate the low-temperature effect and rate dependence on the seismic performance of HDR bearings, and the experimental results are compared with the results of low loading speed hybrid simulation describe in the chapter 2, the following main conclusions can be obtained according to the results.

(1) In the cyclic loading tests, the equivalent shear modulus of HDR bearing under initial loading is larger than that in the non-initial loading at small strain amplitude, and the difference of equivalent shear modulus caused by the initial loading effect is smaller at larger strain amplitudes, which is considered to be caused by the self-heating of rubber materials under cyclic loading.

(2) The inner temperature is higher at location that is closer to the center of the bearing, and temperature drop rate is quicker at location that is farther from the center of the bearing.

(3) In the hybrid simulation, the maximum stress of the bearing is larger under slower speed loading at lower ambient temperatures, hence, a higher loading speed is not equal to a larger stress for the HDR bearing at low temperatures. Meanwhile, the pier top displacement and pier acceleration are larger under loading with slower speed, and the loading rate effect on the pier responses is more obviously observed at lower ambient temperatures.

(4) For the measured inner temperature in the real-time hybrid simulation, there is not obvious difference of temperature at different locations at the 3rd (central) layer of bearing, while the temperature values at the edges are much lower than those near the center at the 1st layer of bearing at −20°C.

(5) The energy dissipation of the bearing is higher in the pseudo dynamic hybrid simulation at −20°C and 0°C, while the energy dissipation is higher in the real-time hybrid simulation at 23°C. The maximum energy dissipation is reduced by a factor of 0.83 in the real-time hybrid

simulation compared with that in the pseudo dynamic hybrid simulation at −20°C.

Chapter 5 Hysteretic restoring force models of HDR bearings including thermo-mechanical coupled effect

5.1 General

In chapter 2, the bilinear model is used to conduct the seismic response analysis of a HDR bearings isolated bridge, however, the comparison between the experimental and analytical results shows that the bilinear model can only describe the hysteresis behavior of HDR bearings at room temperature, the phenomenon of increased stiffness due to the lower temperature and higher strain amplitude can not be captured by the conventional bilinear model. Furthermore, from the cyclic loading test results described in chapter 2, it can be concluded that the stiffness of HDR bearing decreases as the inner temperature increases caused by the self-heating of rubber materials, hence, it is urgently needed to propose a new constitutive model in which the thermo-mechanical coupled effect is considered to more accurately simulate the seismic performance of the HDR bearings.

In this chapter, two hysteretic restoring force models are developed with consideration of thermo-mechanical coupled effect for HDR bearings, these two models are proposed based on the bilinear model and the modified Park-Wen model [59] in which the temperature dependence is not considered. The developed thermo-mechanical coupled models consist of thermal simulation and seismic response analysis, in the thermal simulation, the instantaneous inner temperature of HDR bearings is estimated by the information of the hysteretic energy dissipation and heat conduction/radiation; in the seismic response analysis, the mechanical properties of the HDR bearing are updated according to the calculated inner temperature at each time step increment, this procedure is repeated until the end of the simulation. The model parameters are identified from the hysteretic shear strain-stress curves of HDR bearings in quasi-static loading tests at three different ambient temperatures. Different with the bilinear model in which the three sets of model parameters are identified to describe the three ambient temperature cases, respectively, only one single set of model parameters is identified to describe all the three ambient temperature cases in the thermo-mechanical coupled model. The accuracy of the improved models is verified by comparing the result of seismic response analysis of a HDR bearings isolated bridge using the proposed models with the experimental result obtained in hybrid simulation in terms of hysteresis loops of the bearing, bearing strain and pier top displacement at room and low ambient temperatures.

5.2 Thermo-mechanical coupled models

5.2.1 Outline of thermo-mechanical coupling model

In the developed nonlinear restoring force model with the thermo-mechanical coupling of HDR bearings, the restoring force at each time is determined by the given displacement sequence, and the inner temperature of the HDR bearing is estimated by the heat transfer mechanisms within the model. Although the inner temperature is not likely to be uniform within the bearing, the inner temperature in this model is defined as a single variable as a representative and indicative measure of the increase of the temperature within the rubber material. The time variation of the inner temperature is computed by a heat transfer/radiation model based on the computed hysteretic energy dissipation and ambient air temperature, and the load determined by the restoring force model is modified by a temperature influence model considering the effect of inner temperature.

The schematic representation of the outline of the nonlinear restoring force model with thermo-mechanical coupling is shown in Fig. 5.1. The model is based on the nonlinear hysteretic restoring force model conventionally used for HDR bearings, and the thermo-mechanical coupling mechanism is represented by introducing the following additional components in the computation in the model: (1) calculation of hysteretic energy dissipation from the displacement and load time histories, (2) the heat transfer/radiation model to compute the inner temperature from the dissipated energy and ambient temperature, (3) temperature influence model that expresses the influence of the inner temperature to the restoring force of the HDR bearing. The description of these model components is followed by the detail of the proposed computation procedure to determine the hysteretic restoring force of HDR considering the thermo-mechanical coupling.

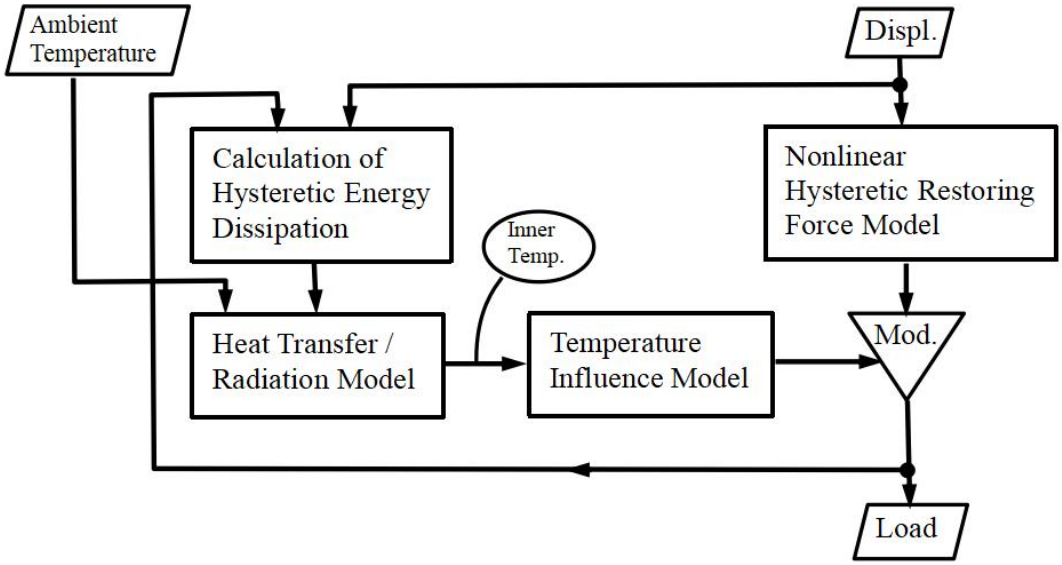

Figure 5.1 Overview of nonlinear restoring force model with thermo-mechanical coupling

5.2.2 Thermo-mechanical coupled bilinear model

The restoring force of the conventional bilinear model can be decomposed to the elastic and elasto-plastic force for simple calculation as shown in Fig 2.28. The decomposed hysteresis loops of bearing for bilinear model at low and room temperatures are shown in Fig 5.2, respectively. It can be found that the elastic restoring force and elasto-plastic force are both affected by the temperature, the stiffness and the area of hysteresis loop increase as the temperature decreases, hence, we can update the elastic stiffness K_1 and characteristic strength q according to the inner temperature of HDR bearing to more accurately simulate the hysteresis behavior of the bearing. The temperature effect on the elastic stiffness and characteristic strength is assumed to be expressed by the exponential function of the inner temperature.

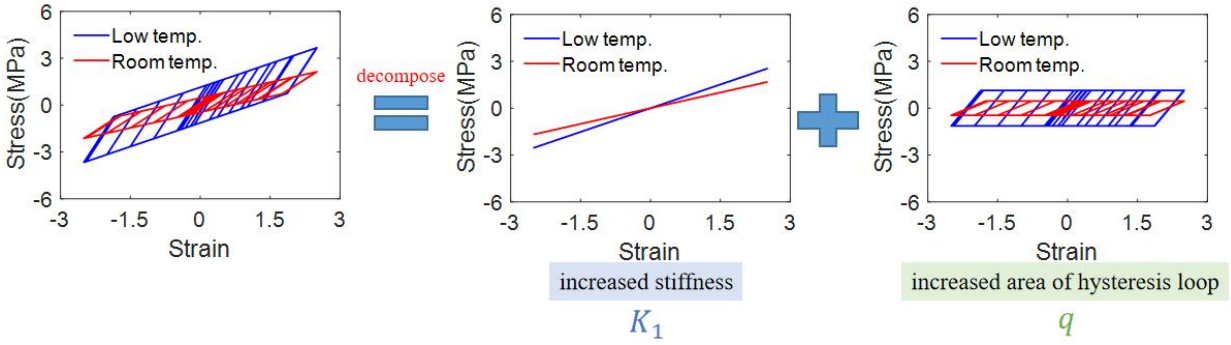

Figure 5.2 Decomposed hysteresis loops of bearing for bilinear model at low and room temperatures

The conventional temperature-independent bilinear model is improved to be a thermo-mechanical coupled bilinear model, hereafter is referred to as the TMC bilinear model. The characteristic strength q and elastic stiffness K_1 are updated by the inner temperature of bearing T calculated by Eq. 2.11, as expressed by

$$q = q_0 e^{m \times \frac{T-23}{100}} \tag{5.1}$$

$$K_1 = K_{1,0} e^{n \times \frac{T-23}{100}} \tag{5.2}$$

where q_0 and $K_{1,0}$ are the initial characteristic strength and elastic stiffness, respectively, m and n are newly introduced constants describing the temperature dependence of mechanical characteristics of the bearing and will be identified from the cyclic loading test results. The application scope of the improved equations is −50°C~50°C, which has a width of 100°C.

The variation of elastic stiffness K_1 and characteristic strength q due to a low temperature T according to Eq. 5.1 and Eq. 5.2 is shown in Fig. 5.3. The elastic stiffness and characteristic strength increase at lower inner temperatures, and the variation rate increases as the inner temperature decreases. When the inner temperature is 23°C, the value of the exponential function factor in Eq. 5.1 and Eq. 5.2 is unity. The problem at room temperature is included as a special case.

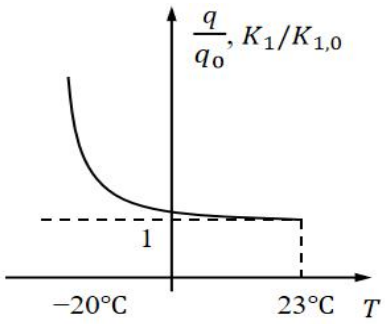

Figure 5.3 Variation of elastic stiffness and characteristic strength due to a low temperature

The hysteresis loops of bearing using TMC bilinear model at different inner temperatures are shown in Fig. 5.4, and the area of hysteresis loop is larger at lower inner temperature of the HDR bearing.

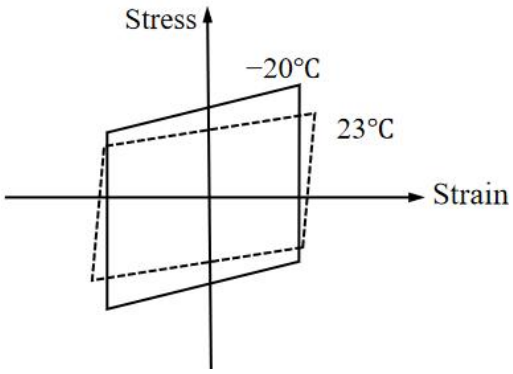

Figure 5.4 Hysteresis loops of the bearing using TMC bilinear model at different inner temperatures

The thermo-mechanical coupled analysis in this study is carried out with the following procedure at each time step: (1) the dissipated energy increment ΔE is calculated by Eq. 2.9 according to the shear displacement increment and shear force increment of bearing; (2) the inner temperature is estimated by Eq. 2.11 based on ΔE; (3) a step of the seismic response analysis is conducted with the restoring force obtained by the modified elastic stiffness and characteristic strength by the calculated inner temperature using Eq. 5.1 and Eq. 5.2. This procedure is repeated until the end of the thermo-mechanical coupled analysis.

5.2.3 Thermo-mechanical coupled modified Park-Wen model

The modified Park-Wen model is a non-linear hysteretic restoring force model showing a good performance to describe the hysteresis behavior of bearings under large deformation with simple mathematical equations and a small number of parameters. However, the temperature dependence of bearing is not considered in this model. Hereafter, the modified Park-Wen model is referred to as the MPW model. The restoring force of the unidirectional MPW model is expressed by

$$F(t) = \alpha K_1 d(t) + \left(1 + b\varepsilon(t)^2\right)(1-\alpha)K_1 Z \tag{5.3}$$

where $\varepsilon(t)$ is the shear strain defined as the displacement $d(t)$ divided by the total rubber layer thickness, α is the post-yield stiffness ratio, K_1 is the elastic stiffness, b is a constant to describe the strain dependence of bearing. $1 + b\varepsilon^2$ is used to express the non-linear behavior of stiffness hardening under large deformation of bearing. The schematic of strain dependence of bearing is shown in Fig. 5.5.

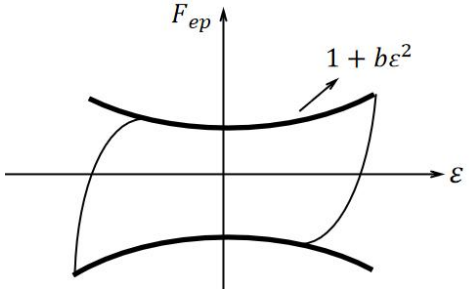

Fig. 5.5 Schematic of strain dependence of bearing

The symbol Z denotes the variable representing the hysteretic component in the restoring force, as expressed by

$$\dot{Z} = \dot{d}(t) - \beta\left|\dot{d}(t)Z\right|Z - \gamma\dot{d}(t)Z^2 \tag{5.4}$$

where β and γ are dimensionless constants for hysteresis curve.

In Eq. 5.3, the restoring force F is expressed by the sum of the elastic component $\alpha K_1 d(t)$ and the elasto-plastic component $(1 + b\varepsilon(t)^2)(1 - \alpha)K_1 Z$ with the hysteresis damping. Let the elastic component be F_e, the elasto-plastic component be F_{ep}. The decomposed hysteresis loops of bearing for MPW model at low and room temperatures are schematically shown in Fig. 5.6. It can be seen that both the elastic stiffness for the elastic component and characteristic strength for the elasto-plastic component are increased at a lower temperature. The temperature effect on the elastic stiffness and characteristic strength is assumed to be expressed by the exponential function of the inner temperature.

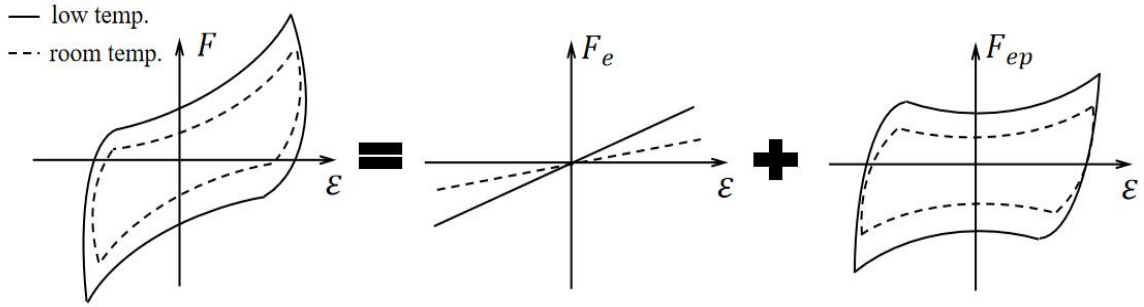

Fig. 5.6 Schematic of decomposed hysteresis loops of bearing for MPW model at low and room temperatures

Using this assumption, the thermo-mechanical coupled modified Park-Wen model, referred to as the TMC MPW model is expressed by

$$F(t) = \alpha K_1 d(t) e^{n\times\frac{T(t)-23}{100}} + \left(1 + b\varepsilon(t)^2\right)(1-\alpha)K_1 Z e^{m\times\frac{T(t)-23}{100}} \tag{5.5}$$

where the newly introduced two parameters n and m are used to describe the inner temperature effect on the elastic stiffness and characteristic strength, respectively. These

parameters are to be identified from the cyclic loading test results.

5.3 Model parameters identification by cyclic loading test results

The model parameters are identified from the displacement-displacement hysteresis loops of HDR bearings obtained in cyclic loading tests C1, C2 and C3. The model parameters are determined by the best fitting of the load-displacement output using an optimization technique [59] maximize the contribution rate R as expressed in Eq. 2.14, and the V is the shear force of the HDR bearing in this section. In order to determine a single set of model parameters to describe the hysteresis behavior of the bearing in the three different ambient temperature cases, the sum of the contribution rates of the three temperature cases is used in the optimization process, hence, the analytical result is closer to the experimental result when the R is closer to 3.

5.3.1 TMC bilinear model and bilinear model

Identified model parameters and the corresponding contribution rates R at each ambient temperature case using the TMC bilinear model and bilinear model are summarized in Table 5.1 and Table 5.2, respectively, as can be seen, m and n are negative, which further demonstrates the strength of HDR reduces due to the self-heating of rubber materials. In addition, the contribution rate is around 0.83 for the TMC bilinear model, and the TMC bilinear model shows better capability in describing the hysteresis behavior of HDR bearing than the conventional bilinear model.

Table 5.1 Identified parameters and contribution rates of the TMC bilinear model

K_1 (kN/mm)	α	q (KN)	m	n	R(−20°C)	R(0°C)	R(23°C)
4.321	0.322	31.208	-1.211	-1.663	0.811	0.839	0.843

Table 5.2 Identified parameters and contribution rates of the bilinear model

K_1 (kN/mm)	α	q (KN)	R(−20°C)	R(0°C)	R(23°C)
4.988	0.300	37.125	0.717	0.831	0.808

The comparison of hysteresis loops of bearing computed by the TMC bilinear model and bilinear model with cyclic loading test results is shown in Fig. 5.7. It can be seen that both the bilinear model and TMC bilinear model are only able to capture the steady-state hysteresis behavior of HDR bearings at room temperature and low-to-moderate shear strain amplitude. The hysteresis loops using bilinear model are same as the model parameter for different ambient temperature cases are same and the temperature dependence is not considered in the bilinear model. Moreover, although the ability in describing the hardening behavior of HDR bearings is improved by the TMC bilinear model, the stiffness hardening phenomenon

observed in the test results at lower temperatures and higher strain levels can not be well described.

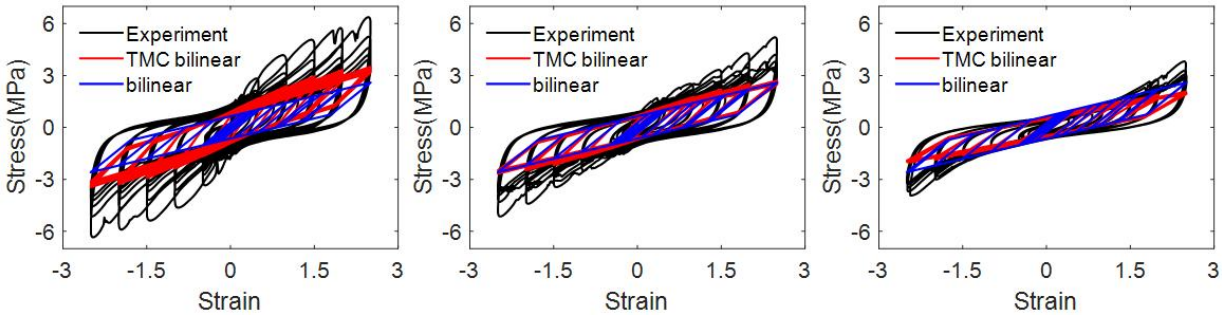

(a) −20℃ (b) 0℃ (c) 23℃

Figure 5.7 Hysteresis loops computed by TMC bilinear model and bilinear model and comparison with cyclic loading test results

5.3.2 TMC MPW model and MPW model

The identified parameters and contribution rates of the TMC MPW model and MPW model are shown in Table 5.3 and Table 5.4, respectively. Note that only one set of parameters is used to describe the hysteresis behavior of bearings for three different ambient temperature cases for both of these two models. It is concluded that the contribution rate of the TMC MPW model is around 0.95, which shows better fit than the MPW model and TMC bilinear model.

Table 5.3 Identified parameters and contribution rates of the TMC MPW model

α	K_1(kN/mm)	β	γ	b	m	n	R(−20°C)	R(0°C)	R(23°C)
0.476	2.811	0.197	-0.192	0.856	-3.077	-1.213	0.938	0.969	0.955

Table 5.4 Identified parameters and contribution rates of the MPW model

α	K_1(kN/mm)	β	γ	b	R(−20°C)	R(0°C)	R(23°C)
0.385	3.582	0.196	-0.192	0.369	0.791	0.937	0.900

The comparison of hysteresis loops of the bearing computed by the TMC MPW model and MPW model with cyclic loading test results is shown in Fig. 5.8. The hysteresis loops using MPW model are same as there is only one set of model parameter for different ambient temperature cases. A good agreement between the experimental and numerical results computed by the TMC MPW model is indicated by this plot. This result demonstrates not only the strain amplitude dependency of the hysteresis behavior is well described by the TMC MPW model, but also the phenomenon of gradually decreased stiffness with increased loading cycles caused by the self-heating of rubber materials. The noticeable discrepancy between the TMC MPW model and the test result is poor representation of the Mullins effect, that is the sharp reduction of the maximum restoring force from the second cycle after the first cycle at each strain amplitude.

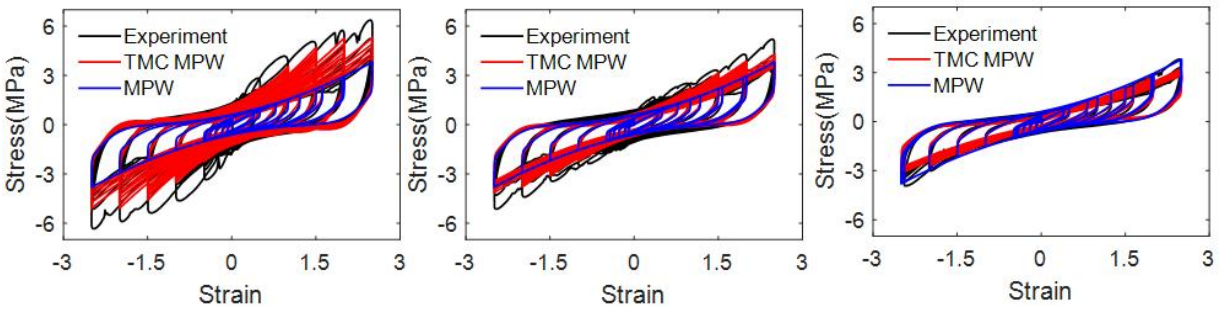

(a) −20℃ (b) 0℃ (c) 23℃

Figure 5.8 Hysteresis loops computed by TMC MPW model and MPW model and comparison with test results

5.4 Models validation by hybrid simulation

The validity of the developed thermo-mechanical coupled models is discussed based on the comparison between the seismic response analysis of the bridge model and the results of Tests H1, H2 and H3. The hypothesized bridge model and input seismic ground motion are the same as expressed in chapter 2.4.

5.4.1 TMC bilinear model and bilinear model

The comparison of hysteresis loops of the bearing computed by the TMC bilinear model and bilinear model with hybrid simulation H1, H2, H3 results is shown in Fig. 5.9. It is observed that the shear strain-stress relationship of HDR bearings computed by the bilinear model is identical at all the three ambient temperatures, as the conventional bilinear model is temperature-independent. In contrast, the TMC bilinear model is able to capture the stiffening occurred at lower ambient temperatures, especially at −20℃. However, a substantial difference is observed between the experimental and numerical result computed by the TMC bilinear model at lower temperatures, indicating that the TMC bilinear model can only describe the temperature dependence of HDR bearings to a limited degree.

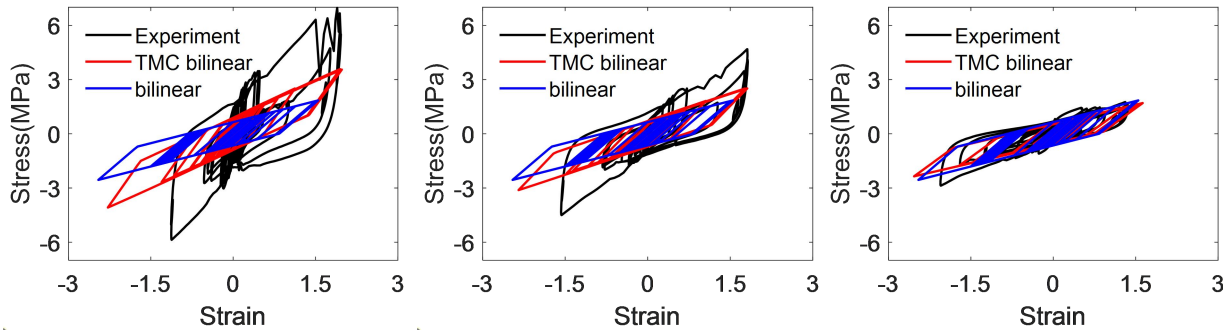

(a) −20℃ (b) 0℃ (c) 23℃

Figure 5.9 Comparison of hysteresis loops of the bearing computed by the TMC bilinear model and bilinear model with hybrid simulation results

The comparisons between numerical results computed by the TMC bilinear model and bilinear model with hybrid simulation results in terms of shear strain of the bearing and pier top displacement in different ambient temperature cases are shown in Fig. 5.10 and Fig. 5.11, respectively. It can be seen that the numerical results show a good agreement with the hybrid simulation results at 23℃. However, an obvious difference is observed at lower ambient temperatures, especially for the maximum shear strain of HDR bearings and pier top displacement at −20℃, indicating that the maximum pier top displacement might be underestimated by the TMC bilinear model and bilinear model at low ambient temperatures.

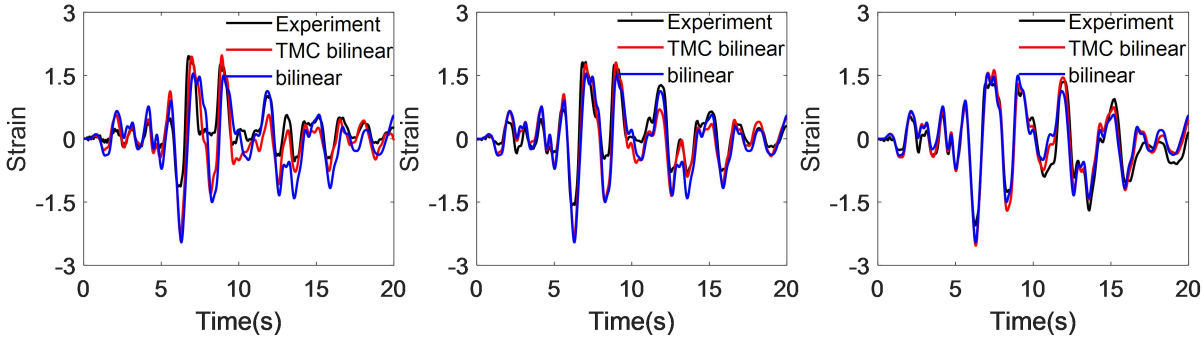

(a) −20℃ (b) 0℃ (c) 23℃

Figure 5.10 Comparison of shear strain of bearing between numerical results computed by the TMC bilinear model and bilinear model with hybrid simulation results

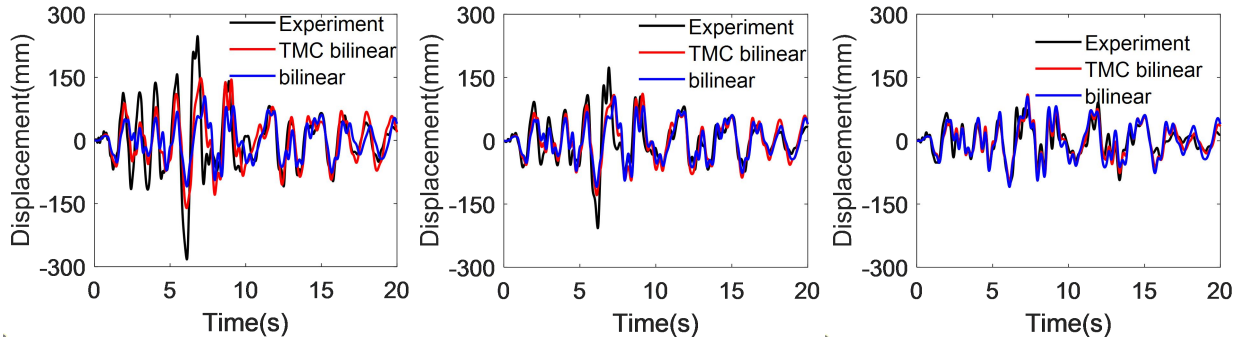

(a) −20℃ (b) 0℃ (c) 23℃

Figure 5.11 Comparison of pier top displacement between numerical results computed by the TMC bilinear model and bilinear model with hybrid simulation results

The inner temperature of the bearing in the seismic response analysis using the TMC bilinear model at different ambient temperatures is shown in Fig. 5.12. Different from the Fig. 2.25, the inner temperature in Fig. 5.12 is calculated based on the numerical hysteresis loops of HDR bearings obtained in the seismic response analysis shown in Fig. 5.9, and the inner temperature in Fig. 2.25 is calculated based on the experimental hysteresis loops obtained in hybrid simulation. It can be seen that the inner temperature increment in Fig. 5.12 is smaller than the result in Fig. 2.25 at −20℃ and 0℃, as the area of numerical hysteresis loops of the bearing is smaller than that measured in hybrid simulation at −20℃ and 0℃, on the other hand, the inner temperature increment in Fig. 5.12 and Fig. 2.25 is almost identical at 23℃, as the area of numerical hysteresis loops is similar with that measured in hybrid simulation at

23°C.

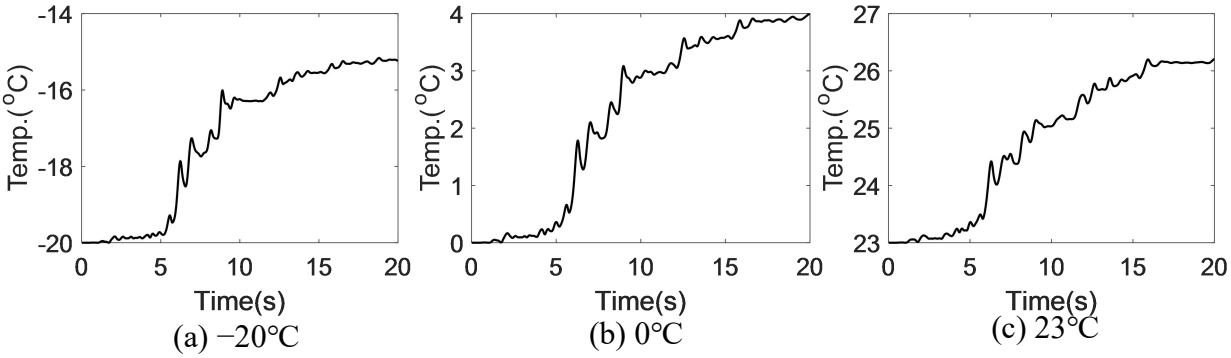

Figure 5.12 Inner temperature of the bearing in the seismic response analysis using TMC bilinear model

5.4.2 TMC MPW model and MPW model

The comparison of hysteresis loops of the bearing computed by the TMC MPW model and MPW model with hybrid simulation H1, H2, H3 results is shown in Fig. 5.13. As shown in Fig. 5.13(a), the hysteretic behavior, as well as the dynamic response to the ground motion, of the HDR bearings at the room temperature of 23°C (Test H3) is well duplicated with the TMC MPW model and MPW model, and accuracy of the assessment of maximum strain and stress under seismic response appears to be adequate. For the case of the ambient temperature of 0°C in Fig. 5.13(b), it can be seen that the simulated seismic response (Test H2) deviates from the one predicted by the MPW model. However, the dynamic response computed by TMC MPW model shows a good match with the result of Test H2, in terms of the assessment of the maximum bearing strain and stress. At the ambient temperature of −20°C Fig. 5.13(c), the remarkable performance of TMC MPW model can be evidently seen in capturing the highly nonlinear behavior including the hardening in the large strain range and the increase of the stress due to a low temperature. Compared with the MPW model, the advantage of TMC MPW model arises from its capability to reflect the effect of both the ambient temperature and the change of inner temperature with only a single set of model parameters.

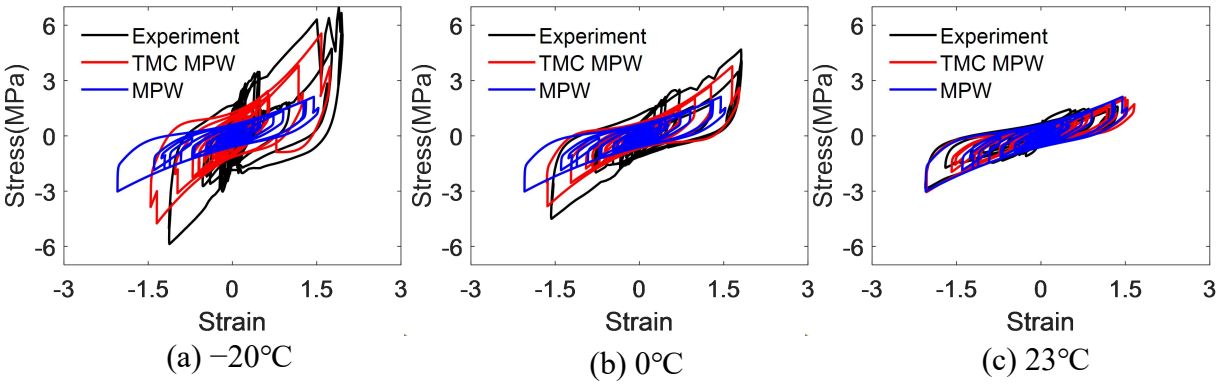

Figure 5.13 Comparison of hysteresis loops of the bearing computed by the TMC MPW model and MPW model with hybrid simulation results

The comparisons between numerical results computed by the TMC MPW model and MPW model with hybrid simulation H1, H2, H3 results in terms of shear strain of the bearing and pier top displacement at different temperatures are shown in Fig. 5.14 and Fig. 5.15, respectively. The advantage of the TMC MPW model showing good agreement with the experimental results at three temperatures can be seen, compared with the MPW model. In particular, the benefit of the TMC MPW model can be clearly demonstrated in the assessment of the pier top displacements at the temperature of −20℃ shown in Fig. 5.15(a).

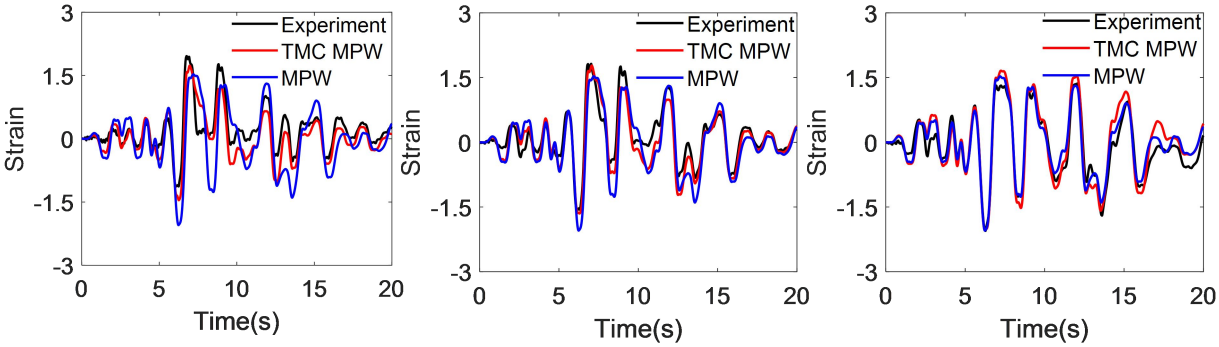

(a) −20℃ (b) 0℃ (c) 23℃

Figure 5.14 Comparison of shear strain of the bearing between numerical results computed by the TMC MPW model and MPW model with hybrid simulation results

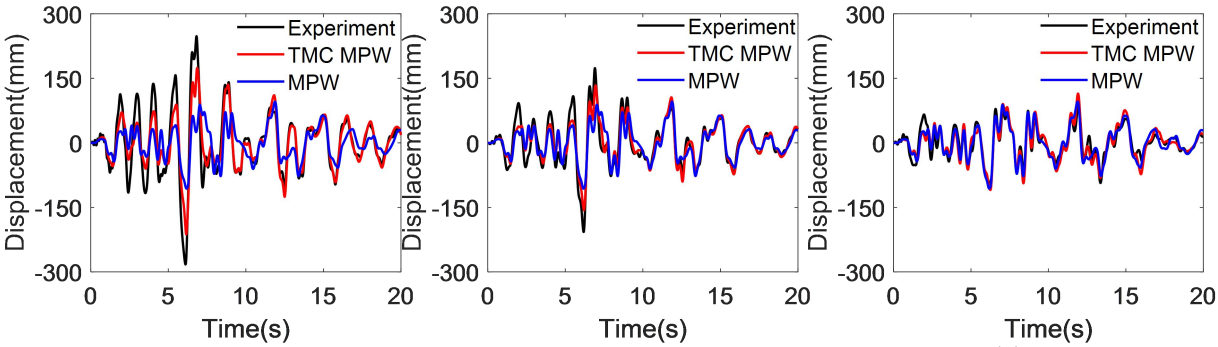

(a) −20℃ (b) 0℃ (c) 23℃

Figure 5.15 Comparison of pier top displacement between numerical results computed by the TMC MPW model and MPW model with hybrid simulation results

The time history plots of the inner temperature of bearings computed by the TMC MPW model in the seismic response analysis are shown in Fig. 5.16. It can be seen that the inner temperature rise under the ambient temperature of −20℃ (Fig. 5.16a) is larger than the cases of 0℃ (Fig. 5.16b) and 23℃ (Fig. 5.16c). It can be explained as a consequence of the increase of energy dissipation of the high damping rubber bearing under lower ambient temperatures, as expressed by TMC MPW model.

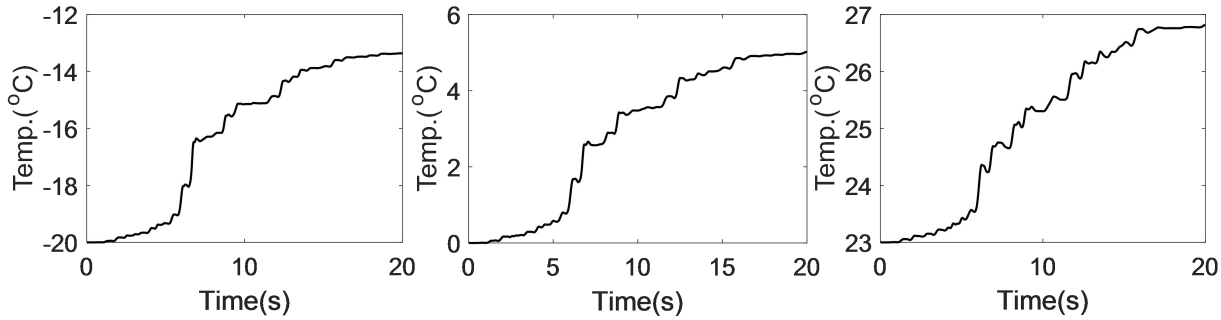

(a) −20°C (b) 0°C (c) 23°C

Figure 5.16 Inner temperature of the bearing in the seismic response analysis using the TMC MPW model

The contribution rates of four models in hybrid simulation at different ambient temperatures are given in Table 5.5, the contribution rate is calculated by the Eq. 2.14, and the bearing shear force is used as the experimental and analytical value. It can be seen that the results of thermo-mechanical coupled models are obviously better than the temperature-independent models at lower ambient temperatures. Furthermore, the TMC MPW model shows to be superior to the TMC bilinear model in expressing the hysteresis behavior of the HDR bearing.

Table 5.5 Contribution rates of models in hybrid simulation

Ambient temperature case	Bilinear	TMC Bilinear	MPW	TMC MPW
−20°C	0.324	0.527	0.369	0.773
0°C	0.630	0.687	0.664	0.861
23°C	0.667	0.766	0.836	0.814

The bearing hysteresis loops computed by the TMC MPW model are also compared with the real-time hybrid simulation RH1, RH2 and RH3 as shown in Fig. 5.17. It can be seen that the real-time hybrid simulation result has a better agreement with the TMC MPW model, which is considered to be due to the similar loading speed conditions. The rate dependence has not been considered in the proposed model and it will be discussed in the future.

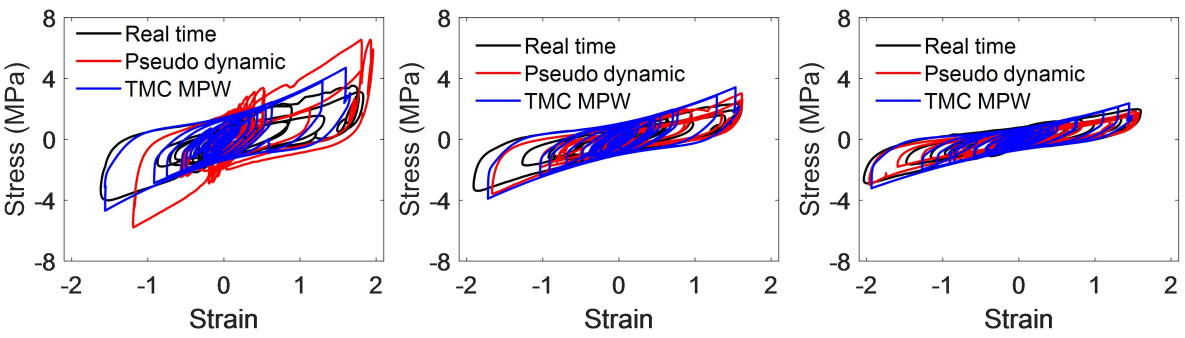

(a) −20°C (b) 0°C (c) 23°C

Figure 5.17 Comparison of TMC MPW model with pseudo dynamic and real-time hybrid simulation: bearing hysteresis loops

5.5 Summary

In this chapter, two thermo-mechanical coupled analytical models, referred to as the TMC bilinear model and TMC MPW model, are proposed to express the hysteresis behavior of HDR bearings at room and low ambient temperatures. The model parameters are identified from the shear strain-stress curves of HDR bearings obtained in cyclic loading tests at ambient temperatures of −20℃, 0℃ and 23℃, and the accuracy of the proposed models is discussed by comparing the result of seismic response analysis of an isolated bridge model using the proposed models with the loading test result using hybrid simulation at the three ambient temperatures. The following main conclusions can be obtained according to the results.

(1) The TMC bilinear model is able to capture the stiffening occurred at lower ambient temperatures, especially at −20℃. However, a substantial difference is observed between the experimental and numerical result computed by the TMC bilinear model at lower temperatures, indicating that the TMC bilinear model can only describe the temperature dependence of HDR bearings to a limited degree.

(2) A good agreement between the cyclic loading test results and TMC MPW model is achieved. Not only the strain amplitude dependency of the hysteresis behavior, but also the phenomenon of gradually decreased stiffness with increased loading cycles caused by the self-heating of rubber materials can be expressed by TMC MPW model.

(3) The high damping rubber bearing's hysteretic behavior as well as the dynamic response to the ground motion obtained by the loading test using the hybrid simulation technique is well duplicated with the proposed TMC MPW model, and accuracy of the assessment of maximum strain and stress under seismic response is adequate for the ambient temperatures of −20℃, 0℃ and 23℃.

(4) The advantage of the TMC MPW model showing good agreement with the experimental results obtained in the hybrid simulation at three temperatures is demonstrated. In particular, the benefit of the TMC MPW model can be clearly demonstrated in the assessment of the increased seismic demand to the bridge piers at lower temperatures.

Chapter 6 Micro scaled physical model for HDR bearings at low temperatures

6.1 General

In chapter 5, a new constitutive model called TMC MPW model in which the thermo-mechanical coupled effect is considered to more accurately simulate the seismic performance of HDR bearings at low temperatures is proposed. However, the phenomenon of sharply decreased stiffness after the first cycle at a certain strain amplitude called the Mullins effect can not be described by the TMC MPW model.

In this chapter, the TMC MPW model is advanced with consideration of the Mullins effect from a micro-mechanical viewpoint, the new model is referred to as the Mullins TMC MPW model. An additional function that changes with the progressed strain history of the bearing is introduced to the TMC MPW model. The parameters of Mullins TMC MPW model are firstly identified by the hysteresis loops of the HDR bearing in the cyclic shear loading tests C1, C2 and C3 that have been described in chapter 2, and the hysteresis loops of HDR bearings in the seismic response analysis of a HDR bearings isolated bridge simplified as 2-degree-of-freedom system using the Mullins TMC MPW model with identified model parameters are compared with those using TMC MPW model and the experimental hysteresis loops of HDR bearing obtained in hybrid simulation. Next, the model parameters are also directly identified from the hybrid simulation results considering the different loading conditions between the cyclic loading tests and ground motion, the seismic response analysis is conducted again using the Mullins TMC MPW model with these identified models, and the accuracy of the Mullins TMC MPW model is verified by comparing the analytical results with the hybrid simulation results in terms of the HDR bearing strain and pier top displacement at different ambient temperatures.

Finally, the verified Mullins TMC MPW model is used to conduct seismic response analysis of the HDR bearings isolated bridge under 18 types of earthquake to investigate the low-temperature effect on the seismic performance of HDR bearings under different ground motions. The pier is assumed to be a linear elastic element for simplicity in hybrid simulation, in this chapter, the clough model is also used for the pier spring to conduct the seismic response analysis of 2-DOF system model for a comparison.

6.2 Mullins TMC MPW model

6.2.1 Concept of Mullins TMC MPW model

The Mullins effect is described as follows: the rubber material of HDR bearing is composed of a large number of polymers, and it is assumed that these polymers move with the deformation of the bearing and the high damping rubber material. A frictional force is generated between two polymers when these two polymers cross, for example, a frictional force is generated between polymer 1 and polymer 2 as shown in Fig. 6.1, no frictional force is generated between polymer 1 and polymer 3 as these two polymers do not cross.

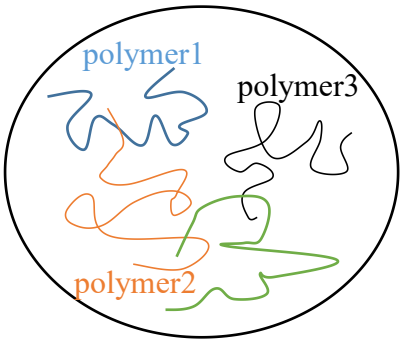

Figure 6.1 Image of moving polymers in HDR bearing

The frictional force between certain two polymers is generated only when the bearing strain is within a certain range, moreover, the frictional force changes with the variation of the bearing strain. The decrease of friction force due to movement of fiber is shown in Fig. 6.2 from a micro view, in Fig. 6.2 (a), the friction force is generated between two polymers when the bearing strain is a certain value and the friction force is strong since these two polymers have not been worn out, then the friction force decreases as the cumulative cross displacement between the two polymers increases with the progressed bearing strain as shown in Fig. 6.2 (b), finally, in Fig. 6.2 (c), the frictional force becomes zero as the polymers are badly worn due to the movement of polymers with the progressed bearing strain. By this way, the phenomenon of sharply decreased stiffness after the first cycle at each bearing strain amplitude called the Mullins effect is described by the changed friction forces of polymers in the rubber.

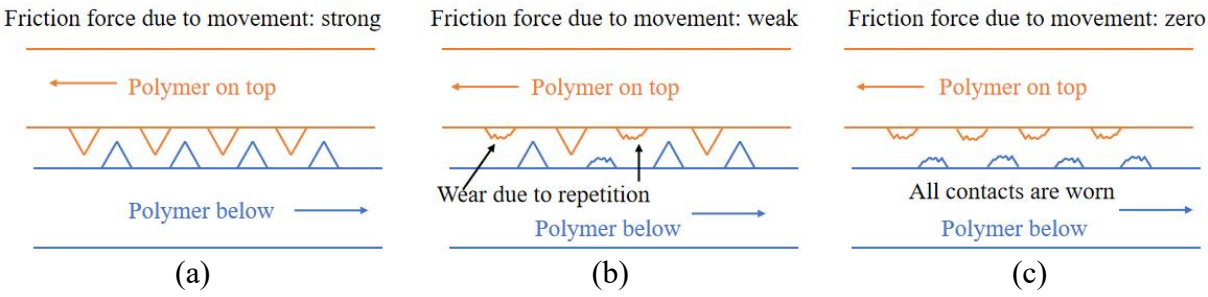

Figure 6.2 The decrease of friction force due to movement of fiber

The possible strain range (for example −3~3) of the bearing is divided to many small strain intervals, and a friction may be generated for each divided small strain interval, the total friction that affects the hysteresis behavior of the bearing is the sum of these different frictions of different small strain intervals, whether the friction of a certain small strain interval is generated dependent on the strain history of the bearing, and this will be described later.

For example, the generated friction of a certain small strain interval due to the movement of the bearing is shown in Fig. 6.3, the S denotes the bearing strain, S_1 and S_2 are the minimum and maximum strains of this certain small strain interval, respectively. Assuming there are two polymers on top and below for this small strain interval [S_1 S_2], respectively. In phase ①, the bearing strain $S < S_1$, these two polymers have not contacted with each other and thus the friction of this small strain interval is 0; in phase ②, $S = S_1$, these two polymers begin to contact with each other and the friction is still 0; in phase ③, $S_1 < S < S_2$, these two polymers contact with each other and the friction is generated; in phase ④, $S > S_2$, these two polymers leave with each other and the friction becomes 0 again. In general, the friction of a small strain interval [S_1 S_2] is generated only when the two polymers intersect, which means the bearing strain S is within the small strain interval [S_1 S_2]. Meanwhile, these two polymers are partially worn due to the generated friction, and the generated friction becomes smaller and smaller as the accumulative strain of this small strain interval increases, note that accumulative strain will increase only when the bearing strain passes through this small strain interval.

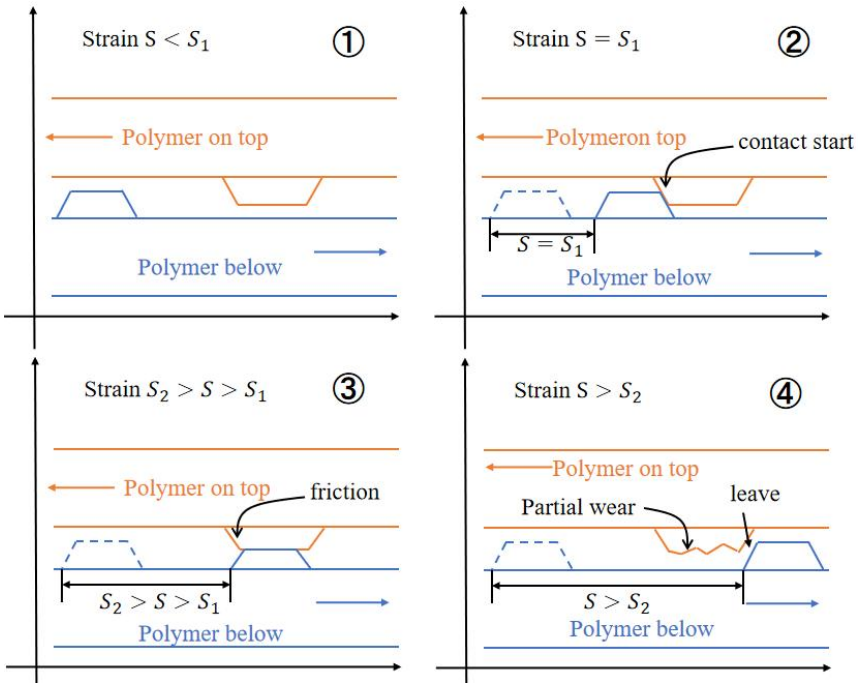

Figure 6.3 Friction of a small strain interval due to the movement of the bearing

6.2.2 Formula of Mullins TMC MPW model

The generated friction force caused by the Mullins effect is considered by adding a new

function V to the TMC MPW model presented in Eq. 5.5 as expressed by

$$F(t)=\alpha K_1 d(t)e^{n\times\frac{T(t)-23}{100}}+\left(1+b\varepsilon(t)^2+V(\varepsilon)\right)(1-\alpha)K_1 Ze^{m\times\frac{T(t)-23}{100}} \tag{6.1}$$

The value of the V is decided by the experienced strain of bearing. The elasto-plastic component of the hysteresis loop of bearing is increased by adding the introduced new function as shown in Fig. 6.4.

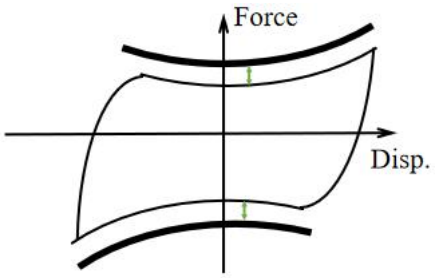

Figure 6.4 Schematic of the effect of added new function on the elasto-plastic component of the hysteresis loop of bearing

Divide the bearing strain interval into many small strain intervals with different strain lengths, for example, the small strain interval S_1 with length of $\Delta\varepsilon$ is one of the divided strain intervals as shown in Fig. 6.5. The bearing strain passed the small strain interval S_1 four times as shown in the figure, and the increment of the cumulative strain of S_1 is $\Delta\varepsilon$ every time the bearing strain passed the small strain interval S_1.

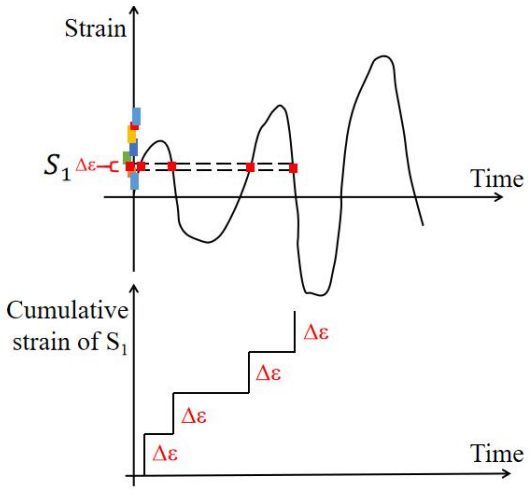

Figure 6.5 Schematic of relationship between bearing strain and cumulative strain of small strain interval

V is expressed by

$$V=\sum_{i=1}^{M} v_i \tag{6.2}$$

where v_i is the coefficient of generated friction force i of small strain interval S_i, and the new function V is the sum of all the v_i, the method of the bearing strain dividing into small

strain intervals will be described later.

The schematic of relationship between v_i and cumulative strain of small strain interval S_i is shown in Fig. 6.6. The v_i decreases as the cumulative strain of small strain interval S_i increases, and the v_i is 0 when the S_i is $4\Delta\varepsilon$, the reason of the four times of the small strain interval length will be described later.

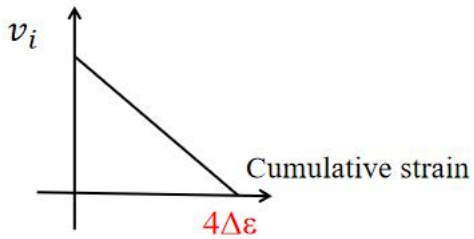

Figure 6.6 Schematic of relationship between v_i and cumulative strain of small strain interval S_i

The reason that why we use the sum function is that different frictions are generated between different polymers for different small strain intervals, the friction of a small strain interval will not be generated when this small strain interval has not been reached by the bearing strain, as the stress-strain behavior of the bearing at the strain amplitude that has not been reached will not be influenced by the Mullins effect, hence, we need to distinguish different small strain intervals to remember the strain history dependence of the Mullins effect.

The coefficient $v_{i,n}$ of small strain interval i at time step n is calculated by

$$v_{i,n} = v_{i,0}(1 - CS_{i,n} / CS_{i,u}) \tag{6.3}$$

where $v_{i,0}$ is the initial value of small strain interval i, $CS_{i,n}$ is the cumulative strain of small strain interval i at time step n, the initial value of $CS_{i,n}$ is 0 and is increased as the bearing strain goes through this small strain interval, note that the bearing strain length that does not cross this strain interval i will not be added to the $CS_{i,n}$. $CS_{i,u}$ is the maximum cumulative strain of small strain interval i. By this way, $v_{i,n}$ decreases as the accumulated strain $CS_{i,n}$ increases, and $v_{i,n}$ completely vanishes when the $CS_{i,n}$ exceeds $CS_{i,u}$, then the gradually decreased stiffness due to the increased strain is described until it disappears.

The $v_{i,n}$ calculated by Eq. 6.3 is shown in Fig. 6.7, it can be seen that $v_{i,n}$ decreases as the cumulative strain $CS_{i,n}$ increases and $v_{i,n}$ becomes 0 after $CS_{i,n}$ is larger than $CS_{i,n}$.

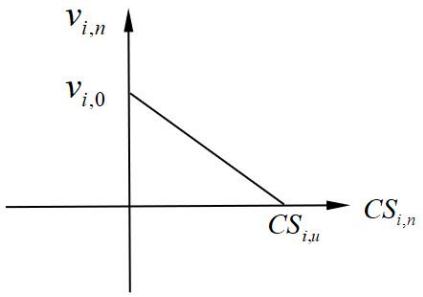

Figure 6.7 Friction $v_{i,n}$ of small strain interval i at time step n

The initial value $v_{i,0}$ is determined by

$$v_{i,0} = p + q \times abs(S_{c,i}) \tag{6.4}$$

in which p and q are constants that will be identified from the hysteresis loops of bearing obtained in cyclic loading tests, $S_{c,i}$ is the central strain of small strain interval i and will be described below. A linear function is used for the initial value of the friction to take into account that $v_{i,0}$ is larger for a small strain interval with higher strain amplitude, as shown in Fig. 6.8.

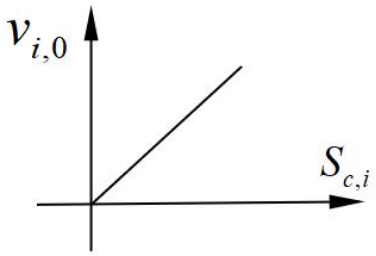

Figure 6.8 The linear relationship between $v_{i,0}$ and $S_{c,i}$

Divide the bearing strain interval [-3 3] into many small strain intervals with different strain lengths, M is the number of divided small strain intervals and is set to be 500 in this study. A moderate value for M=500 is chosen as the calculation time will be too long when the M is too small, and the V will be sharply changed when the M is too large. The bearing strain interval [-3 3] is used considering about the large strain range of seismic isolation bearing under strong ground motions. When the bearing strain is within the range of a certain small strain interval i, the v_i is assumed to be generated in this small strain interval i, otherwise the v_i of this small strain interval i is 0.

The schematic of divided small strain intervals is shown in Fig. 6.9, there is an overlap part between neighboring small strain intervals, hence, the bearing strain may be within many small strain intervals rather than only one small strain interval at each time step, and thus the new function V is the sum of some coefficient of friction forces rather than only one coefficient of friction force, resulting a flatter increase for function V.

Figure 6.9 Schematic of divided small strain intervals

Let the central strain of small strain interval i be $S_{c,i}$, and the distance between the two adjacent centers be d_{se}, d_{se} is set to be constant: d_{se}=(3−(−3))/M=6/M=0.012, $S_{c,i}$ is expressed by

$$S_{c,i} = -3 + d_{se} \times i \tag{6.5}$$

For example, $S_{c,i}$ is -2.988, -2.976, -2.964, ... ,2.976, 2.988. The strain length $d_{s,i}$ of small strain interval i is calculated by

$$d_{s,i} = d_{se} + 0.5 \times f(M,i) \tag{6.6}$$

in which the function $f(M,i)$ denotes the uniform distribution. The adjacent strain intervals may intersect as shown in Fig. 6.10, there is a cross section between the small strain interval i $[S_{1,i}\ S_{2,i}]$ in red color and small strain interval $i+1$ $[S_{1,i+1}\ S_{2,i+1}]$ in blue color. Hence, the bearing strain at time step n may be in several small strain intervals rather than only one small strain interval, then there are several small strain intervals with non-zero friction coefficient v_i, and the function V is not only calculated from only one friction coefficient v_i, resulting a flatter increase for function V.

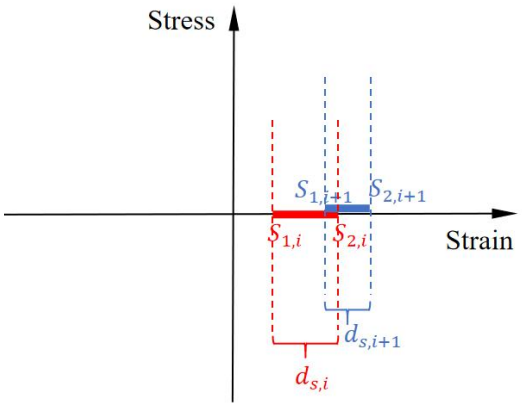

Figure 6.10 Concept of overlapping of two small strain intervals

The quantity of small strain intervals with a specific strain length $d_{s,i}$ is shown in Fig. 6.11, the vertical axis indicates the number of small strain intervals that are in the specific strain length shown in the horizontal axis.

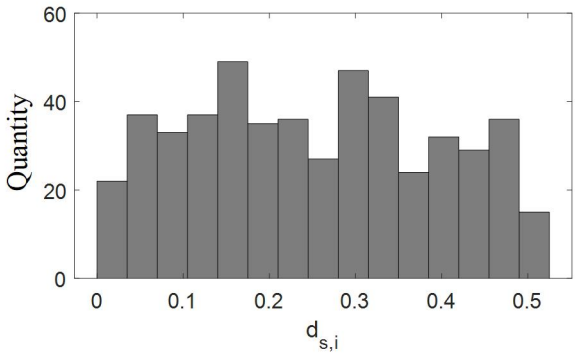

Figure 6.11 Quantity of small strain intervals in a specific strain length

Then the minimum strain $S_{1,i}$ and maximum strain $S_{2,i}$ of small strain interval i $[S_{1,i}\ S_{2,i}]$ can be determined according to the central strain of small strain interval $S_{c,i}$ and the strain length $d_{s,i}$, as expressed by

$$S_{1,i} = S_{c,i} - d_{s,i}/2 \qquad S_{2,i} = S_{c,i} + d_{s,i}/2 \tag{6.7}$$

The cumulative strain $CS_{i,n}$ of small strain interval i at time step n is expressed by

$$CS_{i,n} = CS_{i,n-1} + \Delta CS_{i,n} \tag{6.8}$$

in which $CS_{i,n-1}$ is the cumulative strain of small strain interval i at time step n-1, and $\Delta CS_{i,n}$ is the increased cumulative strain.

The details of calculated increased cumulative strain $\Delta CS_{i,n}$ of small strain interval i at time step n are shown in Table 6.1. S_n and S_{n-1} denote the bearing strain at time n and time n-1, respectively, $S_{1,i}$ and $S_{2,i}$ are the minimum and maximum strain of a small strain interval i, respectively, the crossed strain length between orange strain zone [S_{n-1} S_n] and blue strain zone [$S_{1,i}$ $S_{2,i}$] is $\Delta CS_{i,n}$, which is the strain length that bearing strain passes through the small strain interval i. There are 8 cases to calculate $\Delta CS_{i,n}$ considering about the cases of relative position of S_{n-1}, S_n, $S_{1,i}$ and $S_{2,i}$, the value of $\Delta CS_{i,n}$ for each case is presented in Table 6.1. $\Delta CS_{i,n}$ for case 1 is shown in Fig. 6.12 for an example.

Table 6.1 Increased cumulative strain of small strain interval i at time step n

Case	Relative position of S_{n-1}, S_n, $S_{1,i}$ and $S_{2,i}$						$\Delta CS_{i,n}$
1	S_{n-1}	$S_{1,i}$	S_n		$S_{2,i}$		S_n-$S_{1,i}$
2	S_{n-1}	$S_{1,i}$			$S_{2,i}$	S_n	$S_{2,i}$-$S_{1,i}$
3		$S_{1,i}$	S_{n-1}	S_n	$S_{2,i}$		S_n-S_{n-1}
4		$S_{1,i}$	S_{n-1}		$S_{2,i}$	S_n	$S_{2,i}$-S_{n-1}
5	S_n	$S_{1,i}$	S_{n-1}		$S_{2,i}$		S_{n-1}-$S_{1,i}$
6	S_n	$S_{1,i}$			$S_{2,i}$	S_{n-1}	$S_{2,i}$-$S_{1,i}$
7		$S_{1,i}$	S_n	S_{n-1}	$S_{2,i}$		S_{n-1}-S_n
8		$S_{1,i}$	S_n		$S_{2,i}$	S_{n-1}	$S_{2,i}$-S_n

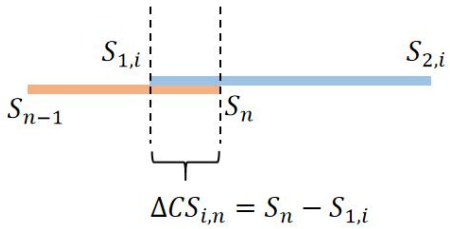

Figure 6.12 Increased cumulative strain of small strain interval i at time step n

The maximum cumulative strain $CS_{i,u}$ for small strain interval i is set to be 4 times of the small strain interval length $d_{s,i}$, as expressed by

$$CS_{i,u} = 4 \times d_{s,i} \tag{6.9}$$

Hence, the friction of small strain interval i becomes 0 after the bearing strain passed through this small strain interval for 4 times, as shown in Fig. 6.13, and thus the phenomenon of sharply decreased stiffness after the first cycle at each strain amplitude called the Mullins effect can be described.

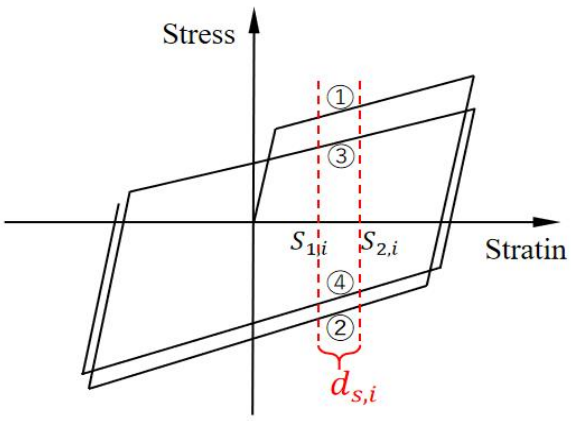

Figure 6.13 Bearing strain passed through small strain interval *i* for 4 times

6.3 Model parameters identification by cyclic loading tests

The model parameters are identified from the displacement-force hysteresis loops of HDR bearings obtained in cyclic loading tests C1, C2 and C3.

The original model parameters and calculated contribution rates using Mullins TMC MPW model are presented in Table 6.2, Eq. 2.14 is used to calculate the contribution rate, *V* is the force of the bearing. Note that the parameters shown in Table 6.2 are original parameters that have not been identified from the test results.

Table 6.2 Original model parameters and contribution rates using Mullins TMC MPW model in cyclic loading tests

α	K_1(kN/mm)	β	γ	b	m	n	p	q	R(23°C)	R(0°C)	R(−20°C)
0.382	3.782	0.201	-0.192	0.694	-2.710	-1.246	0.010	0.027	0.939	0.971	0.943

The comparison of the experimental and numerical hysteresis loops computed by the Mullins TMC MPW model using the original parameters presented in Table 6.2 in cyclic loading tests is shown in Fig. 6.14. It is observed that the phenomenon of stress softening between the first and second cycles is better described by the Mullins TMC MPW model compared with the result using the TMC MPW model shown in Fig. 5.8.

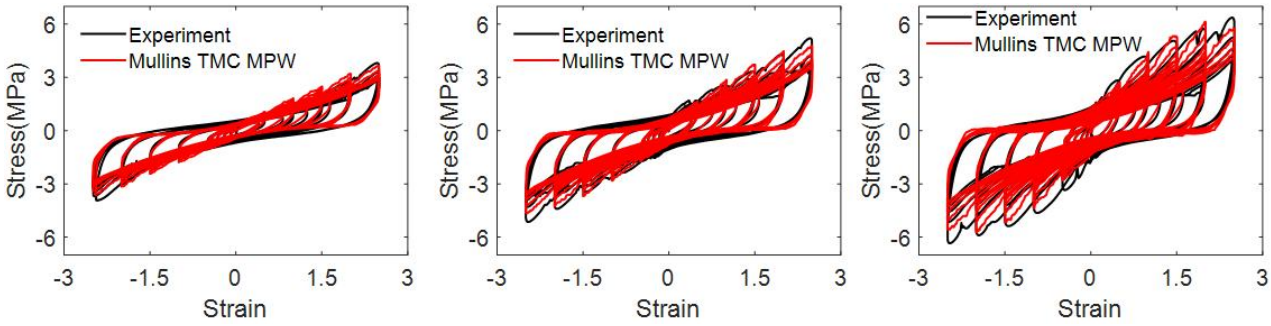

(a) 23°C (b) 0°C (c) −20°C

Figure 6.14 Comparison of the experimental and numerical hysteresis loops computed by the Mullins TMC MPW model using the original parameters in cyclic loading tests

The model parameters are then identified based on the original parameters using the hysteresis loops of HDR bearings in cyclic loading tests C1, C2 and C3 by the KH method (the details of KH method can be found in Appendix C), the identified parameters and contribution rates using Mullins TMC MPW model are presented in Table 6.3. It can be seen that the contribution rate for each ambient temperature case in Table 6.3 is higher than that in the Table 6.2.

Table 6.3 Identified parameters and contribution rates using Mullins TMC MPW model in cyclic loading tests

α	K_1(kN/mm)	β	γ	b	m	n	p	q	R(23°C)	R(0°C)	R(−20°C)
0.383	3.404	0.201	-0.192	0.700	-2.439	-1.371	0.010	0.027	0.951	0.971	0.945

The comparison of the experimental and numerical hysteresis loops computed by the Mullins TMC MPW model using the identified parameters in cyclic loading tests C1, C2 and C3 is shown in Fig. 6.15. It is observed that although the contribution rates are increased after the identification, the Mullins TMC MPW model using the identified parameters shows the worse ability to describe the phenomenon of stress softening at the first and second cycles compared with the result using the original parameters shown in Fig. 6.14, this may be caused by the calculation formula of contribution rate in the KH method, since all the hysteresis loops are used to calculate the contribution rate and the hysteresis loops are mainly concentrated in the third circle, the hysteresis loops using the Mullins TMC MPW model with identified parameters tend to concentrate in the third circle in order to obtain a higher contribution rate.

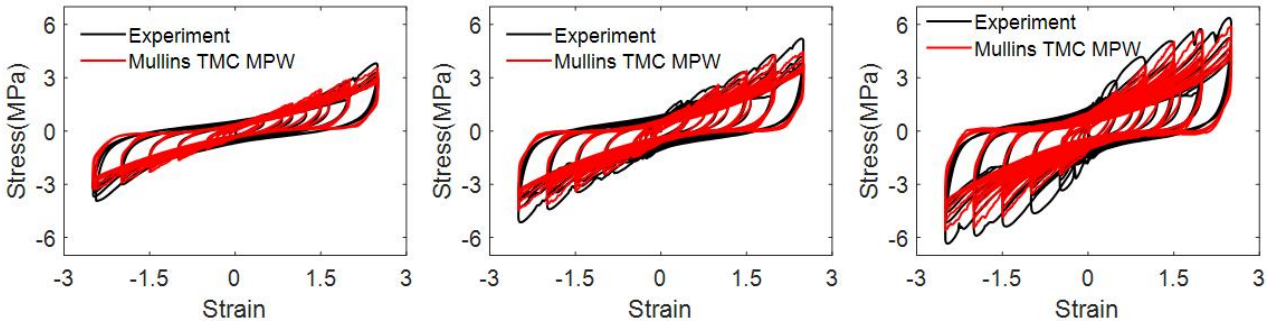

(a) 23℃ (b) 0℃ (c) −20℃

Figure 6.15 Comparison of the experimental and numerical hysteresis loops computed by the Mullins TMC MPW model using the identified parameters in cyclic loading tests

6.4 Seismic response analysis and comparison with hybrid simulation results

The seismic response of the isolated bridge is conducted using the Mullins TMC MPW model and TMC MPW model with the parameters identified from the cyclic loading tests, respectively, and the obtained hysteresis loops of HDR bearing are compared with the results of Tests H1, H2, H3, as shown in Fig. 6.16. It is observed that the maximum shear stress is still underestimated, and the hardening behavior of HDR bearings at small amplitudes can not be captured very well at −20°C by the Mullins TMC MPW model.

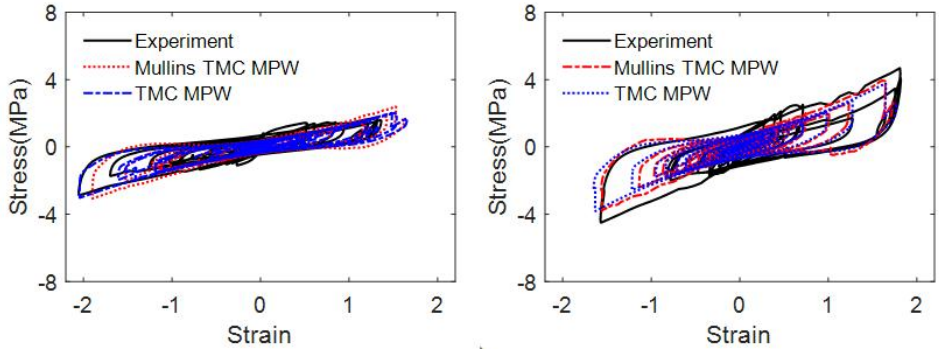

(a) 23℃ (b) 0℃

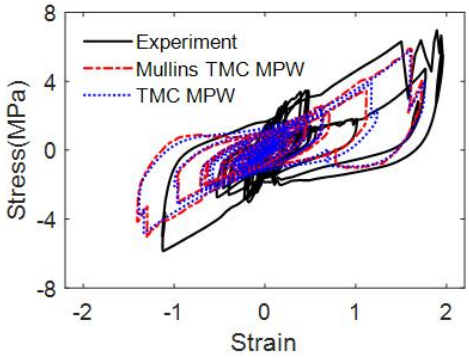

(c) −20℃

Figure 6.16 Comparison of the experimental and numerical hysteresis loops of HDR bearing using the Mullins TMC MPW model and TMC MPW model with the parameters identified from the cyclic loading tests

As for the reason of this phenomenon, in the cyclic loading tests, the HDR bearings were cycled with increased or constant strain amplitudes, the maximum loading speed was 23.55mm/s at strain amplitude 50% and was 117.75mm/s at strain amplitude 250%. In the hybrid simulation, the HDR bearings were loaded with an arbitrary earthquake ground motion, and the loading speed was 10mm/s. Considering the loading condition of cyclic loading is different from those for the ground motion and the loading rate dependence of the hysteresis behavior of HDR bearing, the model parameters are then directly identified by the hysteresis loops of HDR bearing obtained in the hybrid simulation results. The identified parameters and contribution rates using Mullins TMC MPW model in hybrid simulation are summarized in Table 6.4.

Table 6.4 Identified parameters and contribution rates using Mullins TMC MPW model in hybrid simulation

α	K_1(kN/mm)	β	γ	b	m	n	p	q	R(23°C)	R(0°C)	R(−20°C)
0.328	3.775	0.201	-0.192	0.314	-2.924	-2.213	0.026	0.023	0.932	0.941	0.850

The comparison of the experimental and numerical hysteresis loops of HDR bearings using the Mullins TMC MPW model and TMC MPW model in hybrid simulation is shown in Fig. 6.17, the parameters shown in Table 6.4 are used for the Mullins TMC MPW model and the parameters shown in Table 5.3 are used for the TMC MPW model. It is observed that the hysteresis behavior of HDR bearing is better described by the Mullins TMC MPW model compared with the TMC MPW model at 0 ℃ and − 20 ℃, as the stress softening phenomenon is more obvious at lower temperatures. The hardening behavior of HDR bearings at small strain amplitudes and the maximum stress at larger strain amplitudes are well captured by the Mullins TMC MPW model, hence, the capability of the Mullins TMC MPW model in predicting the hysteresis behaviour of HDR with consideration of the Mullins effect and inner temperature dependence is validated.

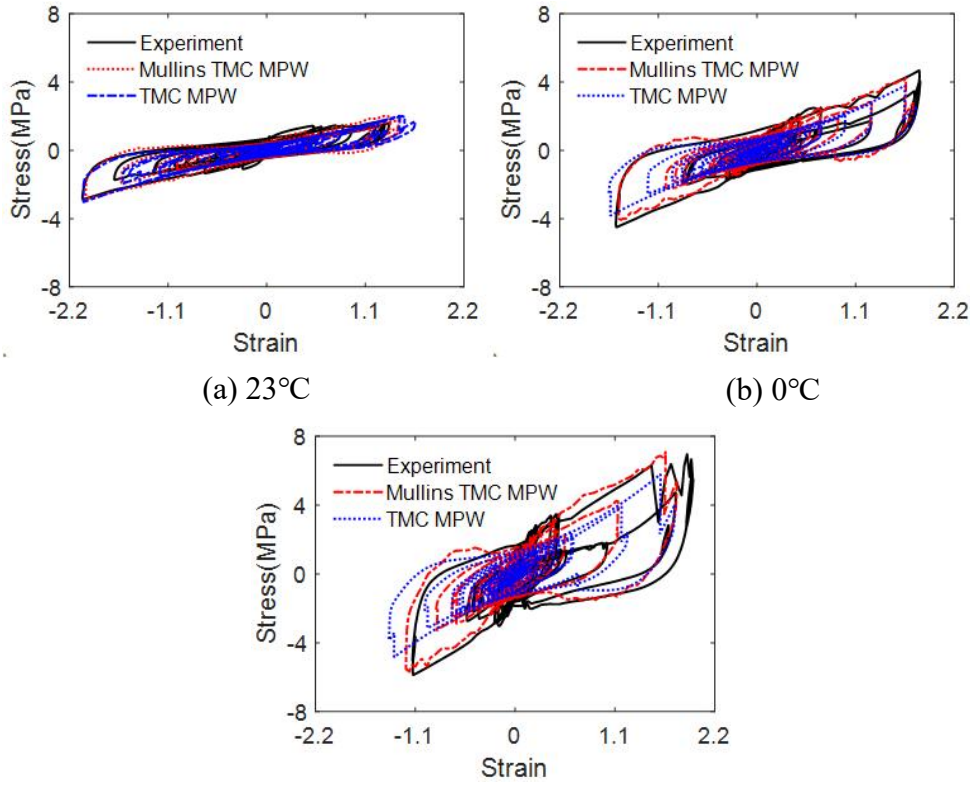

(a) 23℃ (b) 0℃

(c) −20℃

Figure 6.17 Comparison of the experimental and numerical hysteresis loops of HDR bearing using the Mullins TMC MPW model and TMC MPW model in hybrid simulation

The comparisons of the experimental and numerical results in terms of the bearing strain and pier top displacement using the Mullins TMC MPW model and TMC MPW model in hybrid simulation H1, H2 and H3 are shown in Fig. 6.18 and Fig. 6.19, respectively. No obvious difference is observed for the HDR bearing strain by using the two different models, while the initial part of the pier top displacement is better predicted by the Mullins TMC MPW model at −20℃ and 0℃, since the Mullins effect influences the initial part of the seismic response of structures, especially at lower temperatures. Hence, the advanced model provides a better description of the seismic response of HDR bearings isolated bridge at lower temperatures.

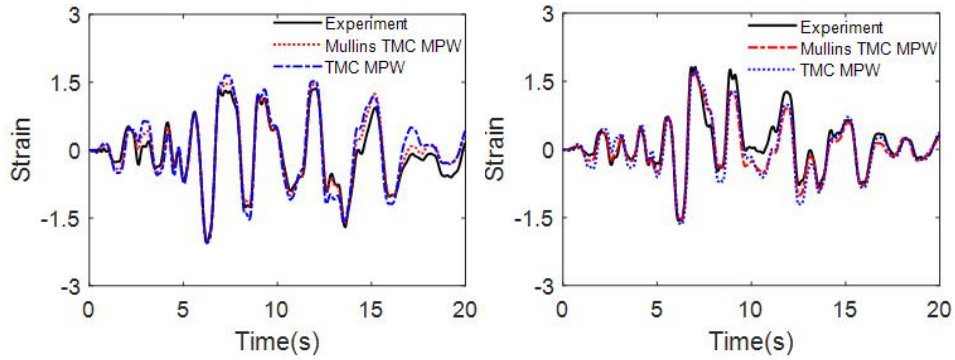

(a) 23℃ (b) 0℃

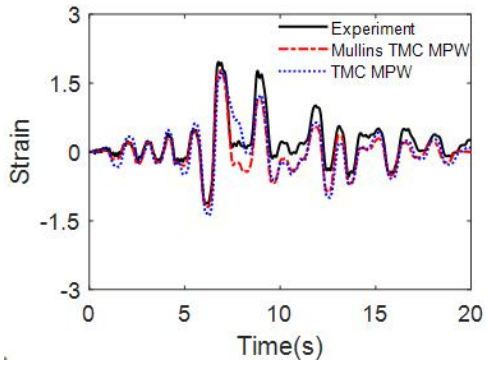

(c) −20℃

Figure 6.18 Comparison of the experimental and numerical bearing strain using the Mullins TMC MPW model and TMC MPW model in hybrid simulation

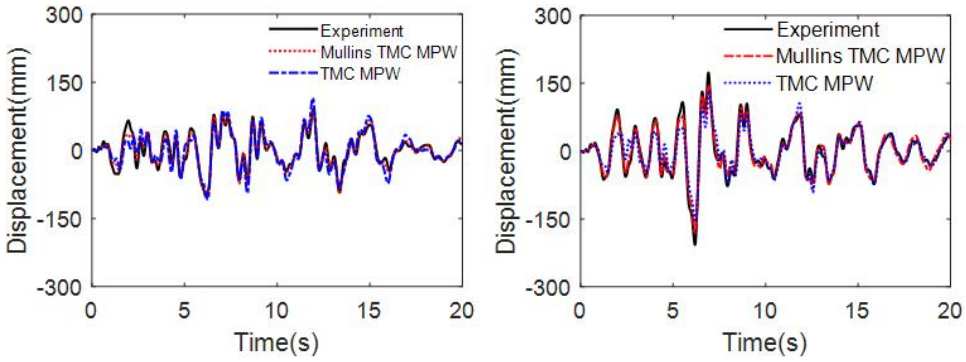

(a) 23℃ (b) 0℃

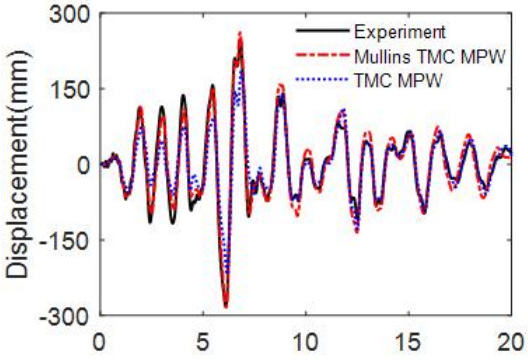

(c) −20℃

Figure 6.19 Comparison of the experimental and numerical pier top displacement using the Mullins TMC MPW model and TMC MPW model in hybrid simulation

The inner temperature of HDR bearings obtained in the seismic response analysis using the Mullins TMC MPW model and TMC MPW model is shown in Fig. 6.20. The inner temperature increment using the Mullins TMC MPW model is higher than that by the TMC MPW model, especially at lower temperatures, it can be explained as a consequence of the increase of energy dissipation of the high damping rubber bearing under lower ambient temperatures, as expressed by the Mullins TMC MPW model.

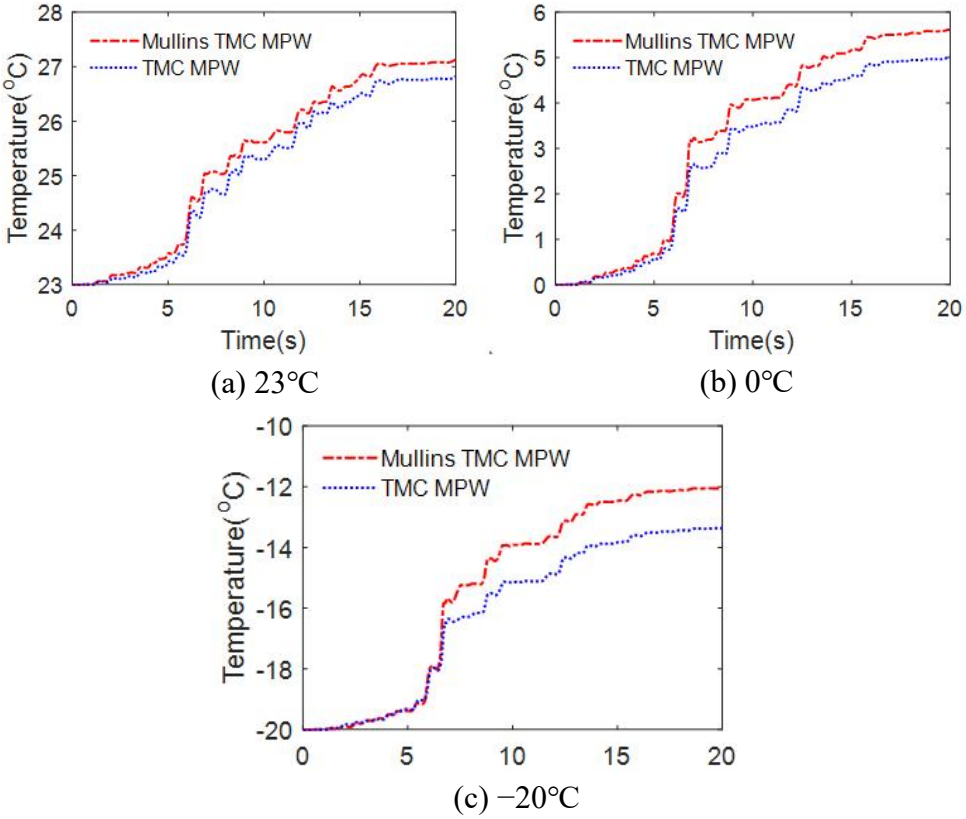

Figure 6.20 Inner temperature of HDR bearings obtained in the seismic response analysis using the Mullins TMC MPW model and TMC MPW model

6.5 Seismic response analysis using Mullins TMC MPW model under different ground motions

The verified Mullins TMC MPW model is then used to conduct seismic response analysis of the HDR bearings isolated bridge under 18 types of ground motions to investigate the low-temperature effect on the seismic performance of HDR bearings under different ground motions. 18 types of ground motions as specified in the Design Specification of Highway Bridges (Japan Road Association, 2017) are applied as the input earthquakes, only level 2 accelerograms are used in this study. These 18 types of ground motions are numbered as shown in Table 6.5. For example, the type I, ground type-I accelerogram 1 is numbered as 1, type I, ground type-II accelerogram 2 is numbered as 5. The maximum acceleration of type II is larger than that of the type I, and the duration time of type II is smaller than that of the type I. Moreover, the ground is harder for the type I ground, hence, the natural period of the type I ground is shorter.

Table 6.5 The number of 18 types of ground motions

1	2	3	4	5	6	7	8	9
I-I-1	I-I-2	I-I-3	I-II-1	I-II-2	I-II-3	I-III-1	I-III-2	I-III-3
10	11	12	13	14	15	16	17	18
II-I-1	II-I-2	II-I-3	II-II-1	II-II-2	II-II-3	II-III-1	II-III-2	II-III-3

In order to simulate the real loading condition for HDR bearing, the analytical case 3 presented in Table 2.11 is applied in this section, in which the area A is the sum of upper and lower surface areas of the bearing considering about the actual environment for isolated bearings. The hysteresis loops of HDR bearings obtained in the seismic response analysis of the isolated bridge at different ambient temperatures under 18 types of ground motions are shown in Fig. 6.21. The Mullins TMC MPW model is used for HDR bearing and linear model is used for pier spring. The title of each small figure denotes the ambient temperature case and the input ground motion number.

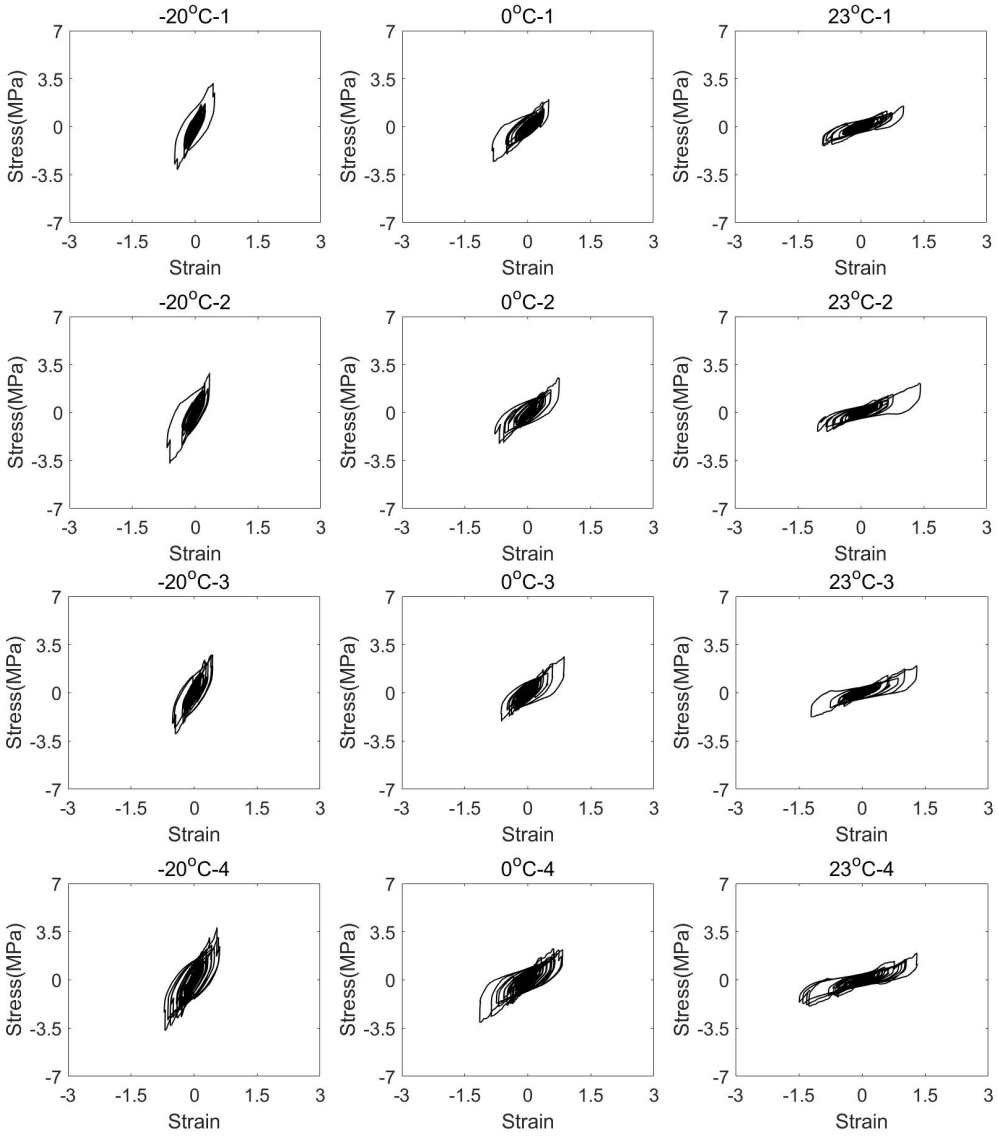

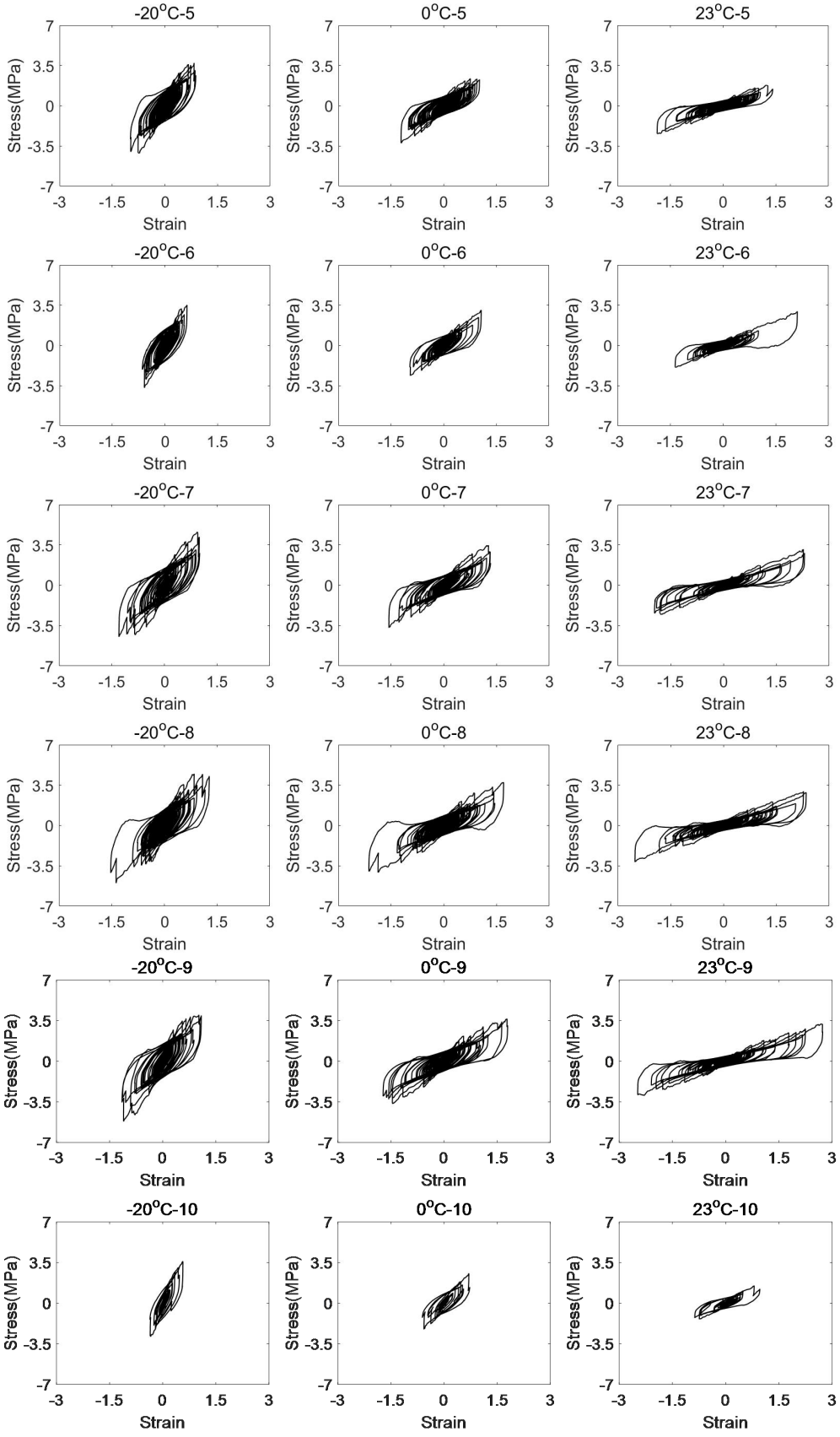
-20°C-5
0°C-5
23°C-5
-20°C-6
0°C-6
23°C-6
-20°C-7
0°C-7
23°C-7
-20°C-8
0°C-8
23°C-8
-20°C-9
0°C-9
23°C-9
-20°C-10
0°C-10
23°C-10
Stress(MPa)
Strain
7
3.5
0
-3.5
-7
-3
-1.5
0
1.5
3

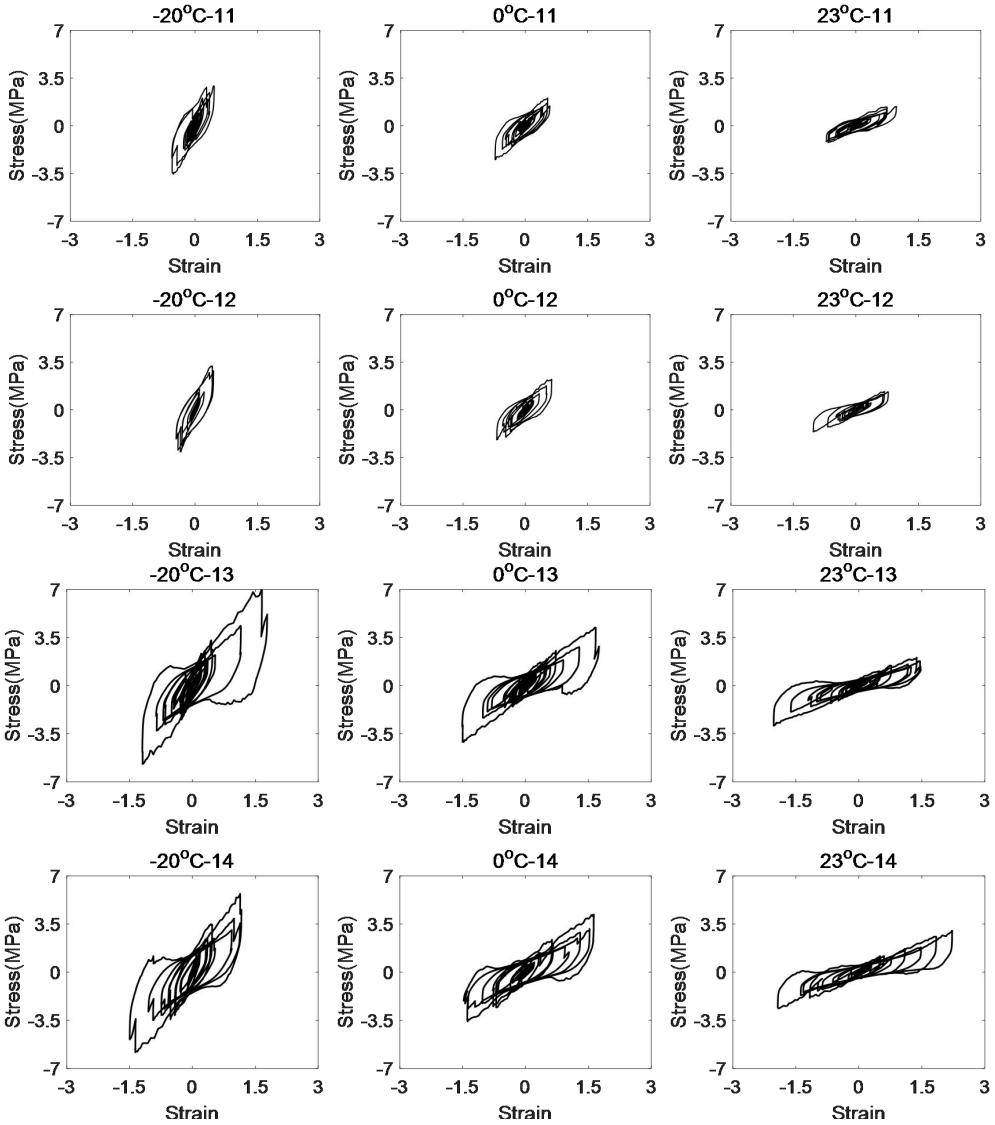
-20°C-11
0°C-11
23°C-11
-20°C-12
0°C-12
23°C-12
-20°C-13
0°C-13
23°C-13
-20°C-14
0°C-14
23°C-14
Stress(MPa)
Strain
7
3.5
0
-3.5
-7
-3
-1.5
0
1.5
3

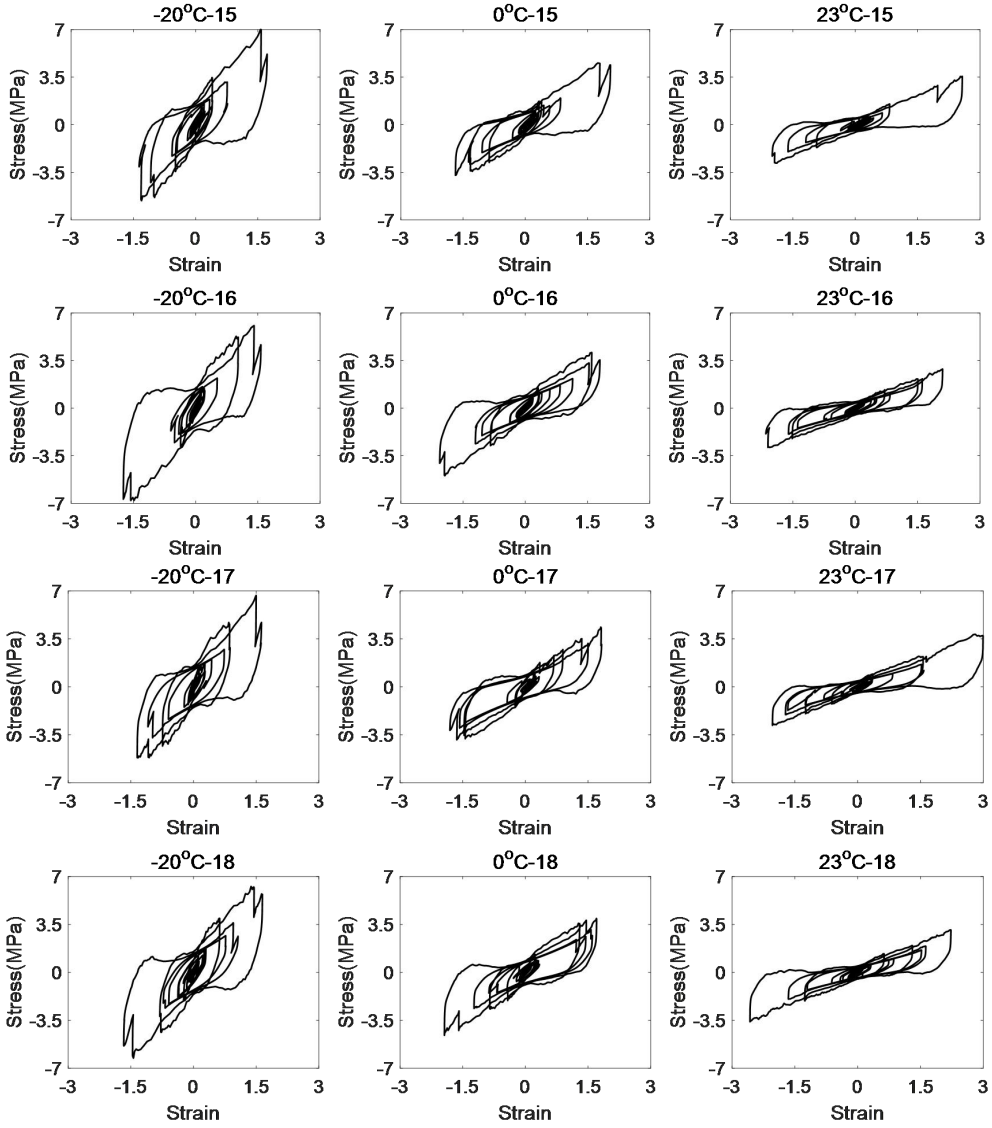

Figure 6.21 Hysteresis loops of HDR bearings at different temperatures under 18 types of ground motions

The maximum absolute strain of HDR bearings at different temperatures under 18 types of ground motions is shown in Fig. 6.22. In Fig. 6.22(a), the horizontal axis denotes the maximum absolute bearing strain at ambient temperature of 23℃ under each ground motion, and the vertical axis denotes the maximum absolute bearing strain at −20℃ or 0℃ under each ground motion. It can be seen that the maximum absolute bearing strain at −20℃/0℃ is smaller than that at 23℃ under each ground motion, as the stiffness of HDR bearing increases at a lower temperature. In Fig. 6.22(b), the horizontal axis denotes the number of the input 18 types of ground motions as given in Table 6.5, and the vertical axis denotes the maximum bearing strain ratio which is calculated as the maximum absolute bearing strain at −20℃ or 0℃ divided by the maximum absolute bearing strain at 23℃, a quantitative decrease in the maximum absolute bearing strain due to a low temperature can be seen from Fig. 6.22(b). In general, maximum absolute bearing strain ratio is smaller under wave from umber 1 to 9, hence, the HDR bearing is more affected by the low temperatures under type-I ground motion with a lower maximum acceleration, it is assumed that the hysteresis area of bearing is larger under stronger ground motion, and thus the energy absorbed by the bearing

is greater at lower temperatures.

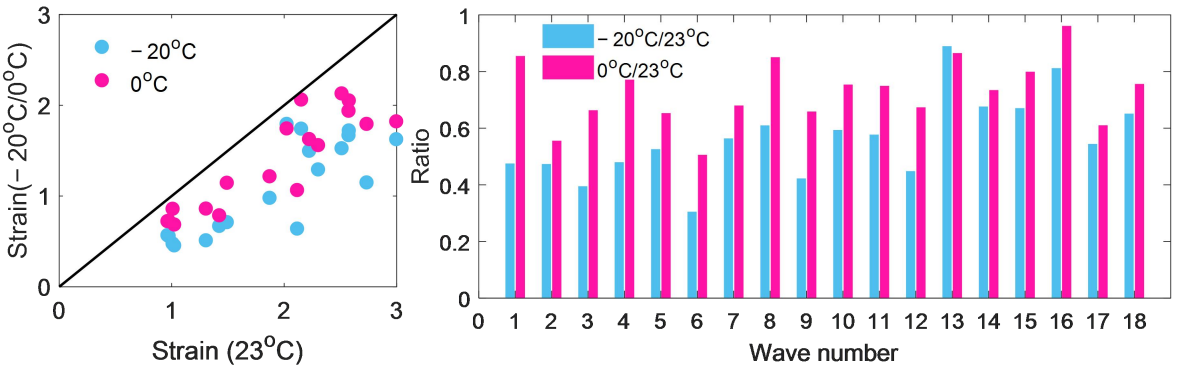

(a) Maximum bearing strain (b) Maximum bearing strain ratio

Figure 6.22 Maximum absolute strain of HDR bearings at different temperatures under 18 types of ground motions

The maximum absolute pier top displacement at different temperatures under 18 types of ground motions is shown in Fig. 6.23. In Fig. 6.23(a), the horizontal axis denotes the maximum absolute pier top displacement at 23°C under each ground motion, and the vertical axis denotes the maximum absolute pier top displacement at −20°C or 0°C under each ground motion. It can be seen that the maximum absolute pier top displacement at −20°C/0°C is almost larger than that at 23°C under each ground motion, as the force transmitted from the bearing is larger at a lower temperature. In Fig. 6.23(b), the horizontal axis denotes the number of the input 18 types of ground motions, and the vertical axis denotes the maximum absolute pier top displacement ratio which is calculated as the maximum absolute pier top displacement at −20°C or 0°C divided by the maximum absolute pier top displacement at 23°C, a quantitative increase in the maximum absolute pier top displacement due to a low temperature can be seen from this figure. The maximum absolute pier top displacement is increased by a factor of 2.69 at −20°C compared with that at 23°C under wave 16.

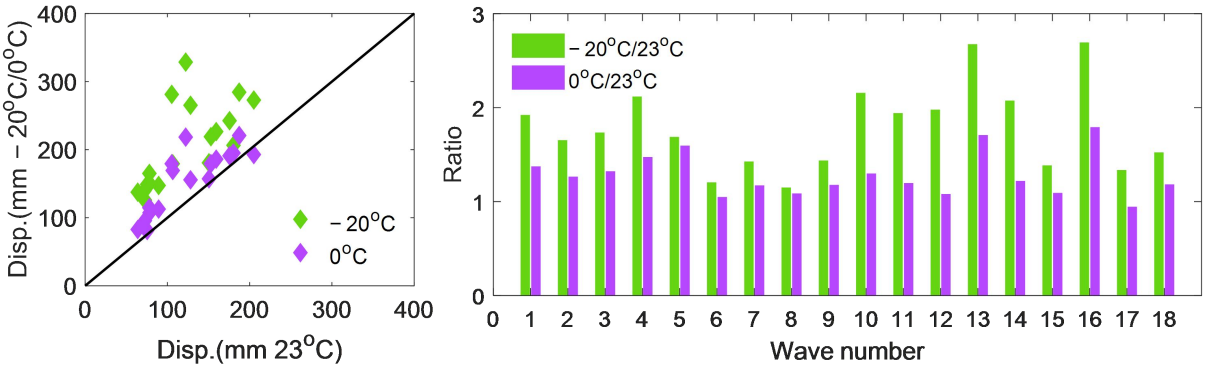

(a) Maximum pier top displacement (b) Maximum pier top displacement ratio

Figure 6.23 Maximum absolute pier top displacement at different temperatures under 18 types of ground motions

Then the 95% and 99% confidence intervals of maximum absolute bearing strain ratio and maximum absolute pier top displacement ratio are established. The 95% confidence interval

is defined as: if the estimated 95% confidence interval is [a, b], then there is a 95% confidence interval that the mean of the sample is between a and b, and the probability of an error is 5%.

The 95% confidence interval [a, b] is defined as

$$a = mean - 1.96 \times ST$$
$$b = mean + 1.96 \times ST \tag{6.10}$$

In which *mean* denotes mean value of the sample data, *ST* denotes the standard deviation of the sample data. The 99% confidence interval [a, b] is defined as

$$a = mean - 2.58 \times ST$$
$$b = mean + 2.58 \times ST \tag{6.11}$$

The confidence intervals of maximum absolute bearing strain ratio under 18 types of ground motions are shown in Fig. 6.24, the maximum absolute bearing strain ratio calculated by experimental results is also shown in the figure. The ratio calculated as the maximum absolute bearing strain at −20℃ divided by the maximum absolute bearing strain at 23℃ is shown in Fig. 6.24(a), the mean value of simulation results under 18 types of ground motions is 0.56, the 99% upper limit of confidence is 0.93, and the 95% upper limit of confidence is 0.84, while the experimental maximum absolute bearing strain ratio is 0.96 under wave 13. The ratio calculated as the maximum absolute bearing strain at 0℃ divided by the maximum absolute bearing strain at 23℃ is shown in Fig. 6.24(b), the mean value of simulation results is 0.73, the 99% upper limit of confidence is 1.02, and the 95% upper limit of confidence is 0.95, while the experimental maximum absolute bearing strain ratio is 0.89 under wave 13.

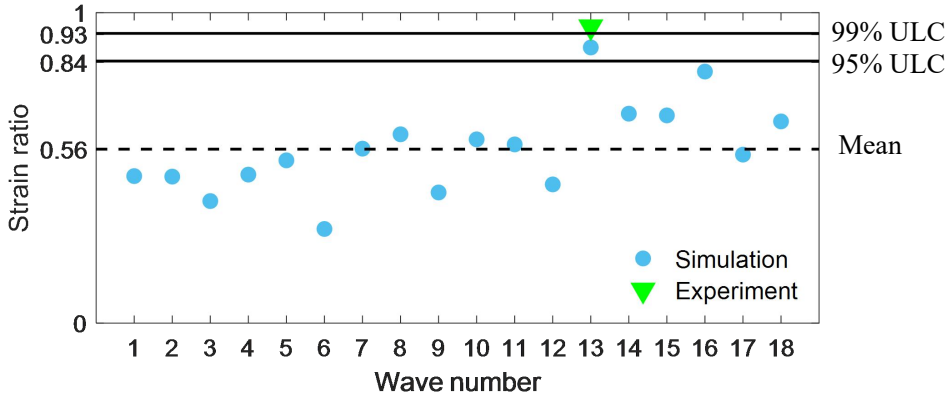

(a) −20℃/23℃

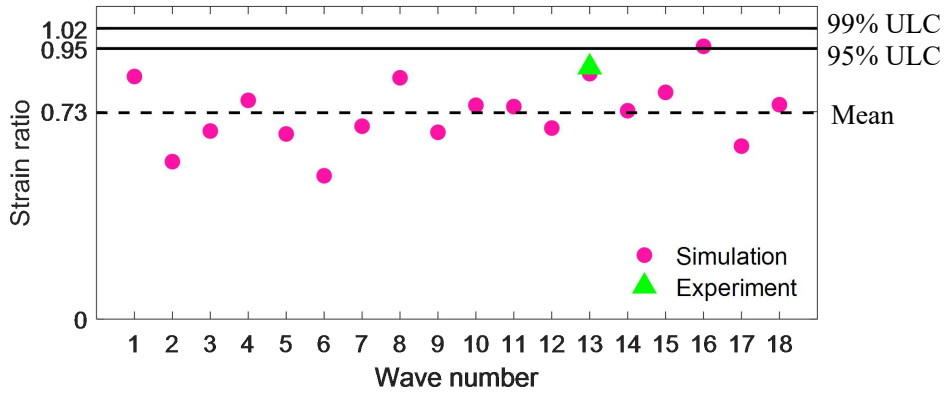

(b) 0℃/23℃

Figure 6.24 Confidence intervals of maximum absolute bearing strain ratio under 18 types of ground motions

The confidence intervals of maximum absolute pier top displacement ratio under 18 types of ground motions are shown in Fig. 6.25. The ratio calculated as the maximum absolute pier top displacement at −20℃ divided by the maximum absolute pier top displacement at 23℃ is shown in Fig. 6.25(a), the mean value of simulation results is 1.78, the 99% upper limit of confidence is 2.94, and the 95% upper limit of confidence is 2.67, while the experimental maximum absolute pier top displacement ratio is 2.82 under wave 13. The ratio calculated as the maximum absolute pier top displacement at 0℃ divided by the maximum absolute pier top displacement at 23℃ is shown in Fig. 6.25(b), the mean value of simulation results is 1.28, the 99% upper limit of confidence is 1.87, and the 95% upper limit of confidence is 1.73, while the experimental maximum absolute pier top displacement is 2.06 under wave 13.

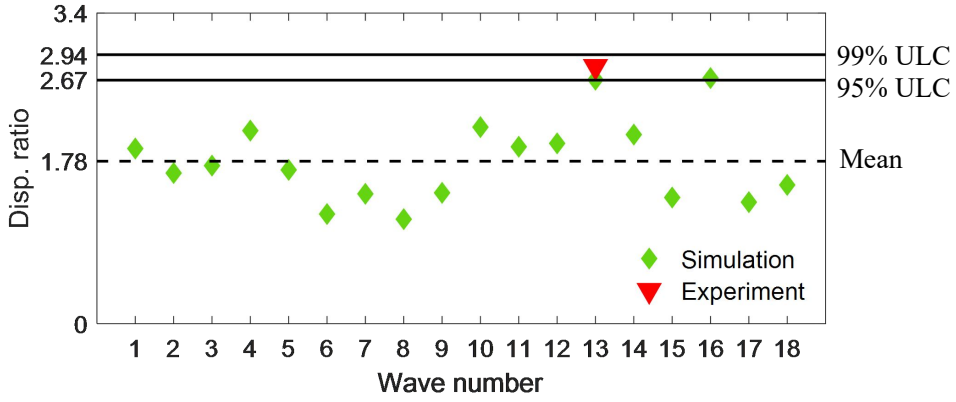

(a) −20℃/23℃

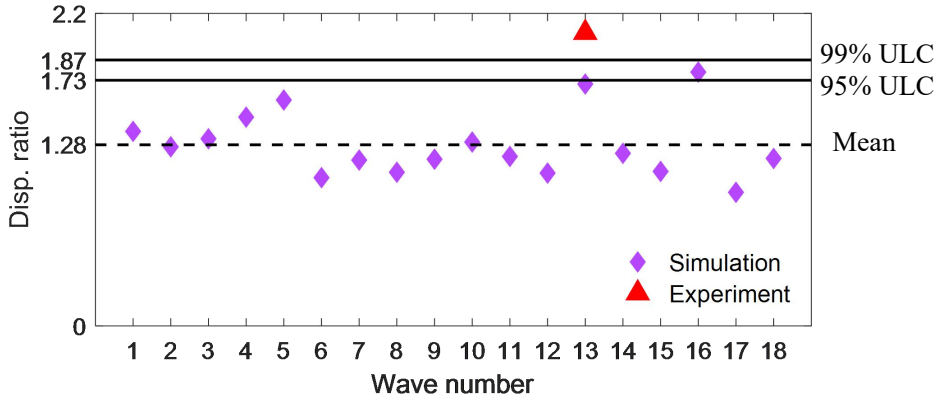

(b) 0℃/23℃

Figure 6.25 Confidence intervals of maximum absolute pier top displacement ratio under 18 types of ground motions

The pier spring is assumed to be linear elastic for simple calculation during the hybrid simulation, in this section, the clough model is also used for the pier spring to conduct the seismic response analysis of 2-DOF system model shown in Fig. 2.15 under level 2, type II, ground type-II accelerogram 1 ground motion. The elastic stiffness K_1 of the clough model is set to be same with the stiffness in the linear model, the post-yield stiffness ratio α is 0.05, and the yield force F_0 is calculated by

$$F_0 = (G_{\text{super-structure}} + G_{\text{pier}}) \times a_y \tag{6.12}$$

in which a_y is set to be 0.5, $G_{\text{super-structure}}$ and G_{pier} are the mass of the super-structure and pier, respectively.

The seismic response of the isolated bridge using linear model and clough model for the piers and comparison with the experimental results in hybrid simulation are shown in Fig 6.26, the Mullins TMC MPW model and the model parameters shown in Table 6.4 are used for HDR bearings. The first to the third row are the results at −20℃, 0℃ and 23℃, respectively, the first to the fourth column are the results of the bearing strain-stress hysteresis loop, bearing strain time history, pier top displacement-force hysteresis loop, pier top displacement time history, respectively. Note that the pier top displacement is divided by the yield displacement, and pier force is divided by the yield force for figures in the third column, and the pier displacement is divided by the yield displacement for figures in the fourth column. It can be seen that the area of hysteresis loops and strain of the bearing are decreased, and the pier displacement and force are increased by using the clough model for piers at −20℃, it is assumed that the seismic energy is partly dissipated by the inelastic pier and thus the seismic response of the bearing decreases. Moreover, there is not obvious difference for the seismic response at 0℃ and 23℃, as the piers behavior almost linearly at 0℃ and 23℃.

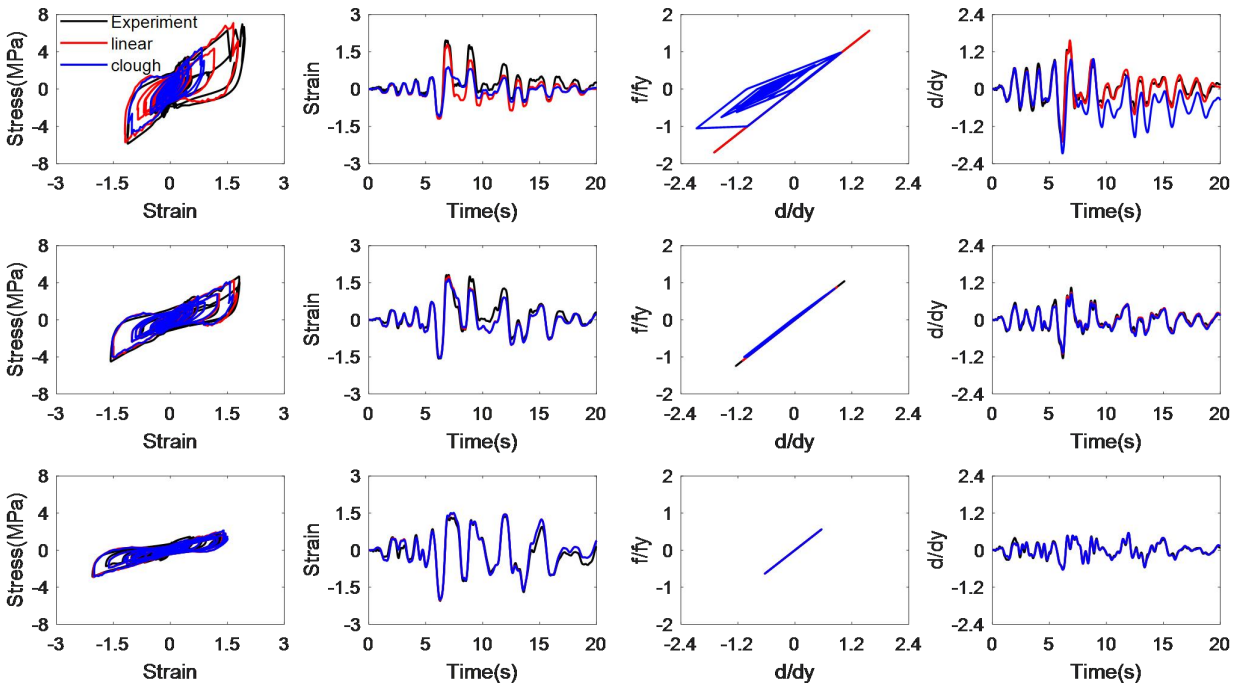

Figure 6.26 Seismic response of isolated bridge using linear model and clough model and comparison with the experimental results in hybrid simulation

6.6 Summary

In this chapter, a thermal-mechanical coupled hysteretic restoring force model with consideration of Mullins effect, referred to as the Mullins TMC MPW model, is proposed to predict the hysteresis behavior of HDR bearings. The Mullins TMC MPW model is developed based on the previously proposed TMC MPW model by adding a new function that changes with the progressed strain history from a micro-mechanical viewpoint. Moreover, the verified Mullins TMC MPW model is used to conduct seismic response analysis of a HDR bearings isolated bridge under 18 types of earthquake, the following main conclusions can be obtained according to the results.

(1) The comparisons of experimental and analytical dynamic response of a HDR bearings isolated bridge in terms of the HDR bearing strain and pier top displacement confirm the advanced performance of the Mullins TMC MPW model compared with the TMC MPW model in predicting the hysteresis behavior of the HDR bearing at lower temperatures.

(2) The HDR bearing is more affected by the low-temperature conditions under type-I ground motion with a lower maximum acceleration.

(3) The statistical data of maximum absolute pier top displacement at different temperatures under 18 types of ground motions shows that the maximum absolute pier top displacement is increased by a factor of 2.69 at −20℃ compared with that at 23℃ under type II, ground type-III accelerogram 1 ground motion.

(4) The area of hysteresis loops and strain of bearings decrease when the seismic energy is partly dissipated by the inelastic piers at −20℃.

Chapter 7 Conclusions

In the application of High Damping Rubber (HDR) bearings and spring confined Pb high damping rubber bearings (SPR-S bearings) as seismic isolation for bridges in cold regions, there are concerns about the low-temperature effect on the hysteresis performance of HDR bearings and SPR-S bearings and the resulting deterioration in bridge performance under strong ground motions. The stiffness of the HDR bearing and SPR-S bearing significantly increase at lower ambient temperature, and the stiffness reduces as the inner temperature of the bearing increases due to the self-heating of rubber materials and lead plugs under repeated cyclic loading, resulting in a complicated thermo-mechanical coupled hysteresis behavior which is not expressed by the currently available restoring force models of HDR bearings and SPR-S bearings.

The aim of this study is to investigate the low-temperature effect on the seismic performance of the HDR bearings and SPR-S bearings.

In Chapter 2, the quasi-static cyclic loading tests and hybrid simulation of HDR bearings are conducted at there different ambient temperatures (−20℃, 0℃, 23℃) to investigate the seismic performance of the HDR bearings. A formula to calculate the inner temperature of the HDR bearing is developed, the calculated inner temperature is compared with the measured temperature in cyclic loading tests and hybrid simulation, and the hysteresis behavior of HDR bearing depending on the calculated inner temperature and strain amplitude is investigated. Moreover, the bilinear model is used to conduct the seismic response analysis of the HDR bearings isolated bridge, and the analytical results are compared with the experimental results in hybrid simulation. The following main conclusions can be drawn.

(1) Under cyclic loading, the shear modulus and damping ratio of the bearing increase as the ambient temperature decreases. The differences in stiffness at different temperatures become smaller at larger strain amplitudes which is considered to be caused by the self-heating of rubber materials.

(2) In the hybrid simulation, the stiffness and peak stress of the HDR bearings increase, as well as the pier top displacement, for lower ambient temperatures. The maximum strain of the bearing is reduced by a factor of 0.77 at 0°C and 0.55 at −20°C compared with the result at 23°C, the maximum pier top displacement is increased by a factor of 2.06 at 0°C and 2.82 at −20°C compared with the result at 23°C. This test result is a clear quantitative demonstration of the anticipated increase in seismic demand on the bridge at low temperatures.

(3) The maximum deformation primarily occurs on the pier at low temperatures, which may arise from the changed structural modal shape in the response due to hardening of the rubber bearings at low temperatures.

(4) The actual inner temperature change of HDR bearing due to the self-heating effect is

obtained successfully under random loading in hybrid simulation, this is considered to be important data for evaluating the hysteretic restoring force characteristics of HDR bearings under low-temperature environment. Moreover, a lower initial ambient temperature corresponds to a larger temperature rise during the earthquake ground motion.

(5) The equivalent damping ratio is less affected by inner temperature compared to the shear modulus at low temperatures.

(6) Regarding the effect of initial loading, there is no significant difference in seismic response between initial loading and non-initial loading at 23°C and −20°C.

(7) A comparison between experimental and analytical results shows that the bilinear model can only be used at room temperature. Thus, a new constitutive model is needed to more accurately simulate the seismic performance of HDR bearings at low temperatures.

In Chapter 3, the cyclic shear loading tests and hybrid simulation at ambient temperature of −20ºC, 0ºC and 23ºC are carried out to evaluate the low-temperature effect on the seismic performance of the SPR-S bearing and the isolated bridge with SPR-S bearings. The seismic response of the SPR-S bearing in hybrid simulation is compared with that of the HDR bearing. A formula is proposed to calculate the inner temperature of SPR-S bearing and the estimated temperature is compared with the measured temperature in cyclic loading test and hybrid simulation. The hysteresis behavior of SPR-S bearing depending on the inner temperature is investigated according to the successfully measured inner temperature of SPR-S bearing in the cyclic loading. Moreover, the seismic response analysis of the SPR-S bearings isolated bridge is conducted by using the bilinear model, and the analytical results are compared with the hybrid simulation results. The following main conclusions can be drawn.

(1) In the cyclic shear loading tests, the cyclic behavior of the SPR-S bearing at 23℃ and 0℃ is similar, while the cyclic behavior at −20℃ shows a significant difference with the result at 23℃ and 0℃, as the stiffness hardening and higher energy dissipation are more obviously observed at −20℃.

(2) The shear modulus and equivalent damping ratio of the SPR-S bearing among different temperatures decrease as the cyclic loading progresses to larger shear strain amplitudes due to the self-heating of high damping rubber and lead plugs.

(3) In the hybrid simulation, the SPR-S bearing stress and pier top displacement are higher at lower ambient temperatures. The maximum shear strain of SPR-S bearing is reduced by a factor of 0.66 and the maximum pier top displacement is increased by a factor of 2.16 at −20°C compared with the test results at 23°C.

(4) The energy dissipation capacity of SPR-S bearing is enhanced at −20℃ by 43% compared with the result at 23℃, which is favorable during the ground motion.

(5) The comparison of seismic responses between the SPR-S bearing and HDR bearing shows that the SPR-S bearing is less affected by the low-temperature effect than the HDR bearing, this may be caused by the higher temperature increment for the lead plugs than the high damping rubber, thus, the inner temperature rise of SPR-S bearing is larger than that of

the HDR bearing, and the stiffness hardening appears in the initial phase due to the low ambient temperature decreases as the inner temperature of the SPR-S bearing increases under cyclic loading.

(6) The comparison between the numerical and experimental seismic responses of the isolated bridge shows that the maximum bearing strain is overestimated by the bilinear model, especially at −20℃, while the numerical pier top displacement shows a similar result with the hybrid simulation at each ambient temperature.

In Chapter 4, the cyclic shear loading tests and real-time hybrid simulation at ambient temperature of −20ºC, 0ºC and 23ºC are carried out to evaluate the low-temperature effect and rate dependence on the seismic performance of the HDR bearing and the isolated bridge with HDR bearings, and the experimental results are compared with those describe in the chapter 2. The following main conclusions can be drawn.

(1) In the cyclic loading test, the equivalent shear modulus of HDR bearing under initial loading is larger than that in the non-initial loading at small strain amplitude, and the difference of equivalent shear modulus caused by the initial loading effect is smaller at larger strain amplitudes, which is caused by the self-heating of HDR under cyclic loading.

(2) The inner temperature of the bearing is higher at position that is closer to the center of the bearing, and temperature drop rate is quicker at position that is farther from the center of the bearing.

(3) In the hybrid simulation, the maximum stress of the bearing is larger under loading with slower speed which is different from what we thought, especially at lower ambient temperatures, hence, a higher loading speed is not equal to a larger stress for the HDR bearing at low temperatures. Meanwhile, the pier top displacement and pier acceleration are larger under loading with slower speed, and the loading rate effect on the pier responses is more obvious at lower ambient temperatures.

(4) Although the loading time and loading rate are different between the real-time and pseudo dynamic hybrid simulation, there is not much difference between the inner temperature at the central of the bearing. As for the measured inner temperature in the real-time hybrid simulation, there is not obvious difference of temperature at different positions at the 3rd (central) layer of the bearing, while the temperature values at the edges are much lower than those near the center at the 1st layer of the bearing at ambient temperature case −20℃.

(5) The energy dissipation of the bearing is higher in the pseudo dynamic hybrid simulation at −20℃ and 0℃, while the energy dissipation is higher in the real-time hybrid simulation at 23℃.

In Chapter 5, In this chapter, two thermo-mechanical coupled analytical models, referred to as the TMC bilinear model and TMC MPW model, are proposed to express the hysteresis behavior of HDR bearings at room and low ambient temperatures. The model parameters are identified from the shear strain-stress curves of HDR bearings obtained in cyclic loading tests at ambient temperatures of −20℃, 0℃ and 23℃, and the accuracy of the proposed models is discussed by comparing the result of seismic response analysis of an isolated bridge model

using the proposed models with the loading test result using hybrid simulation at the three ambient temperatures. The following main conclusions can be obtained according to the results.

(1) The TMC bilinear model is able to capture the stiffening occurred at lower ambient temperatures, especially at −20℃. However, a substantial difference is observed between the experimental and numerical result computed by the TMC bilinear model at lower temperatures, indicating that the TMC bilinear model can only describe the temperature dependence of HDR bearings to a limited degree.

(2) A good agreement between the cyclic loading test results and TMC MPW model is achieved. Not only the strain amplitude dependency of the hysteresis behavior, but also the phenomenon of gradually decreased stiffness with increased loading cycles caused by the self-heating of rubber materials can be expressed by TMC MPW model.

(3) The high damping rubber bearing's hysteretic behavior as well as the dynamic response to the ground motion obtained by the loading test using the hybrid simulation technique is well duplicated with the proposed TMC MPW model, and accuracy of the assessment of maximum strain and stress under seismic response is adequate for the ambient temperatures of −20℃, 0℃ and 23℃.

(4) The advantage of the TMC MPW model showing good agreement with the experimental results obtained in the hybrid simulation at three temperatures is demonstrated. In particular, the benefit of the TMC MPW model can be clearly demonstrated in the assessment of the increased seismic demand to the bridge piers at lower temperatures.

In Chapter 6, a thermal-mechanical coupled hysteretic restoring force model with consideration of Mullins effect, referred to as the Mullins TMC MPW model, is proposed to predict the hysteresis behavior of HDR bearings. The Mullins TMC MPW model is developed based on the previously proposed TMC MPW model by adding a new function that changes with the progressed strain history from a micro-mechanical viewpoint. Moreover, the verified Mullins TMC MPW model is used to conduct seismic response analysis of a HDR bearings isolated bridge under 18 types of earthquake, the following main conclusions can be obtained according to the results.

(1) The comparisons of experimental and analytical dynamic response of a HDR bearings isolated bridge in terms of the HDR bearing strain and pier top displacement confirm the advanced performance of the Mullins TMC MPW model compared with the TMC MPW model in predicting the hysteresis behavior of the HDR bearing at lower temperatures.

(2) The HDR bearing is more affected by the low-temperature conditions under type-I ground motion with a lower maximum acceleration.

(3) The statistical data of maximum absolute pier top displacement at different temperatures under 18 types of ground motions shows that the maximum absolute pier top displacement is increased by a factor of 2.69 at −20℃ compared with that at 23℃ under type II, ground type-III accelerogram 1 ground motion.

(4) The area of hysteresis loops and strain of bearings decrease when the seismic energy is

partly dissipated by the inelastic piers at −20℃.

In addition, there are still many topics need to be explored in the future such as:

(1) The models proposed in this study only account for the temperature dependence, Mullins effect and strain amplitude dependence, a new model that also accounts for the loading rate dependence of the HDR bearing is needed.

(2) It is necessary to conduct the real-time hybrid simulation under different ground motions to obtain more information about the seismic response of the isolated bridge with rubber bearings at low temperatures.

(3) The application of the proposed models to the design practice of isolated bridges at low temperatures is still need to be explored.

(4) The inner temperature of the bearing is considered to be uniformly distributed over the volume of HDR in this study, a more accurate model for calculating the uneven distribution of inner temperature is indispensable.

References

[1] Skinner RI, Robinson WH, McVerry GH. An Introduction to Seismic Isolation. John Wiley and Sons, Chichester, U.K., 1993.
[2] Kelly JM. Earthquake-resistant design with rubber. 1993.
[3] Itoh Y, Gu HS. Prediction of aging characteristics in natural rubber bearings used in bridges. Journal of Bridge Engineering, 2009; 14(2): 122-128.
[4] Gu HS, Itoh Y. Ageing behaviour of natural rubber and high damping rubber materials used in bridge rubber bearings. Advances in Structural Engineering, 2010; 13(6): 1105-1113.
[5] Arafat A, Gimenez JL, Himeno T, Yoshihara S, Nuruzzaman ASM. High damping rubber isolators: application to bridges in Bangladesh. IABSE-JSCE Conference on Advances in Bridge Engineering-IV, Bangladesh, 2020.
[6] Turkington DH, Carr AJ, Cooke N, Moss, PJ. Seismic design of bridges on lead-rubber bearings. Journal of Structural Engineering, 1989; 115(12): 3000-3016.
[7] Gimenez JL, Himeno T. Seismic isolation of bridges using rubber bearings with high energy dissipation capacity. 20th ASEP International Convention: " Structural Engineering: Getting Smarter to New and Future Challenges", 2021.
[8] Shinohara M, Enomoto T, Inoue T, Hoshikuma J, Okada S, Nishi H, Takahashi Y. Researches on properties of laminated elastomeric bearings under cyclic loading. Journal of Structural Engineering, A, 2016; Vol. 61A. (in Japanese)
[9] Yabana S, Matsuda A. Mechanical properties of laminated rubber bearings for three-dimensional seismic isolation. 12th World Conference on Earthquake Engineering, Auckland, New Zealand, Paper; 2000.
[10] Abe M, Yoshida J, Fujino Y. Multiaxial behaviors of laminated rubber bearings and their modeling. I: Experimental study. Journal of Structural Engineering, 2004; 130(8): 1119-32.
[11] Aiken ID, Kelly JM, Clark PW, Tamura K, Kikuchi M, Itoh T. Experimental studies of the mechanical characteristics of three types of seismic isolation bearings. Proceedings, Tenth World Conference on Earthquake Engineering, Madrid, Spain; 1992.
[12] Kikuchi M, Aiken ID. An analytical hysteresis model for elastomeric seismic isolation bearings. Earthquake Engineering and Structural Dynamics, 1997; 26(2): 215-31.
[13] Dung NA, Sang NV. Dynamic performance of highway bridges: low temperature effect and modeling effect of high damping rubber bearings. Modern Mechanics and Applications: Springer, 2022; 476-88.
[14] Mullins L. Softening of rubber by deformation. Rubber Chemistry and Technology, 1969; 42(1): 339-362.
[15] Jankowski R. Nonlinear rate dependent model of high damping rubber bearing. Bulletin of Earthquake Engineering, 2003; 1(3): 397-403.
[16] Ryan KL, Kelly JM, Chopra AK. Nonlinear model for lead–rubber bearings including axial-load effects. Journal of Engineering Mechanics, 2005; 131(12): 1270-8.

[17] Oliveto ND, Markou AA, Athanasiou A. Modeling of high damping rubber bearings under bidirectional shear loading. Soil Dynamics and Earthquake Engineering, 2019; 118: 179-90.
[18] Okui Y, Nakamura K, Sato T, Imai T. Seismic response of isolated bridge with high damping rubber bearings: Self-heating effect at subzero temperatures. Steel Construction, 2019; 12(1): 2-9.
[19] Takaoka E, Takenaka Y, Kondo A, Hikita M, Kitamura H. Heat-mechanics interaction behavior of laminated rubber bearings under large and cyclic lateral deformation. Proceedings of the 14th Conference on Earthquake Engineering, Beijing, China, 2008.
[20] Cardone D, Gesualdi G. Experimental evaluation of the mechanical behavior of elastomeric materials for seismic applications at different air temperatures. International Journal of Mechanical Sciences, 2012; 64(1): 127-43.
[21] Mendez-Galindo C, Moor G, Rodriguez-Bahena J, Nieto-Higuera J, Bailles B, Rassy S. Dynamic performance of lead rubber bearings at low temperature. 16th World Conference Earthquake Engineering, 2017.
[22] ISO 22762-2:2018. Elastomeric seismic-protection isolators. Part 2: Applications for bridges-Specifications.
[23] Japan road association (JRA). Bearing support design guide for highway bridges. Japan, 2012. (in Japanese)
[24] Govindjee S, Simo J. A micro-mechanically based continuum damage model for carbon black-filled rubbers incorporating Mullins' effect. Journal of the Mechanics and Physics of Solids, 1991; 39(1): 87-112.
[25] Kasai S, Sato K. Research on evaluation method for quality assurance of durability of rubber bearings. 2019. (in Japanese)
[26] Plagge J, Klüppel M. Mullins effect revisited: Relaxation, recovery and high-strain damage. Materials Today Communications, 2019; 20: 100588.
[27] Koo G-H, Ohtori Y. Loading rate effects of high damping seismic isolation rubber bearing on earthquake responses. KSME International Journal, 1998; 12(1): 58-66.
[28] Imai T, Bhuiyan A, Razzaq M, Mitamura H. Experimental studies of rate-dependent mechanical behavior of laminated rubber bearings. Joint Conference Proceedings of 7th International Conference on Urban Earthquake Engineering and 5th International Conference on Earthquake Engineering, 2010; 1921-28.
[29] Zhang R, Li A. Experimental study on loading-rate dependent behavior of scaled high performance rubber bearings. Construction and Building Materials, 2021; 279: 122507.
[30] Dall'Asta A, Ragni L. Experimental tests and analytical model of high damping rubber dissipating devices. Engineering Structures, 2006; 28(13): 1874-84.
[31] Nguyen D, Dang J, Okui Y, Amin A, Okada S, Imai T. An improved rheology model for the description of the rate-dependent cyclic behavior of high damping rubber bearings. Soil Dynamics and Earthquake Engineering, 2015; 77: 416-31.
[32] Yuan Y, Wei W, Tan P, Igarashi A, Zhu H, Iemura H. A rate - dependent constitutive model of high damping rubber bearings: modeling and experimental verification. Earthquake Engineering and Structural Dynamics, 2016; 45(11): 1875-92.
[33] Tsai C, Chiang TC, Chen BJ, Lin S, dynamics s. An advanced analytical model for high damping rubber bearings. Earthquake Engineering and Structural Dynamics, 2003; 32(9):

1373-87.
[34] Igarashi A, Iemura H, Yoshida M, Taya F. Hybrid simulation for seismic performance assessment of a cable-stayed bridge retrofitted with laminated high damping rubber dampers. 15th World Conference on Earthquake Engineering, 2012.
[35] Mishra HK, Igarashi A, Ji D, Matsushima H. Pseudo-dynamic testing for seismic performance assessment of buildings with seismic isolation system using scrap tire rubber pad isolators. Journal of Civil Engineering and Architecture, 2014; 8(1): 73.
[36] Takanashi K, Udagawa K, Seki M, Okada T, Tanaka H. Non-linear earthquake response analysis of structures by a computer-actuator on-line system. Transactions of the Architectural Institute of Japan, 1975; 229: 77–83.
[37] Mahin SA, Shing PB. Pseudodynamic method for seismic testing. Journal of Structural Engineering, ASCE, 1985; 111(7): 1482–1501.
[38] Nakashima M, Akazawa T, Igarashi H. Pseudo-dynamic testing using conventional testing devices. Earthquake Engineering and Structural Dynamics 1995; 24: 1409–1422.
[39] Shing PB, Nakashima M, Bursi OS. Application of pseudodynamic test method to structural research. Earthquake Spectra, 1996; 12(1): 29–56.
[40] Mosqueda G, Ahmadizadeh M. Iterative implicit integration procedure for hybrid simulation of large nonlinear structures. Earthquake Engineering and Structural Dynamics, 2011; 40: 945–960.
[41] Jung RY, Shing PB. Performance evaluation of a real-time pseudo dynamic test system. Earthquake Engineering and Structural Dynamics, 2006; 25(4): 333–55.
[42] Jung RY, Shing PB, Stauffer E, Thoen Bradford. Performance of a real-time pseudo dynamic test system considering nonlinear structural response. Earthquake Engineering and Structural Dynamics, 2007; 36(12): 1785–809.
[43] Chang SY. Explicit pseudo dynamic algorithm with unconditional stability. Journal of Engineering Mechanics, 2002; 128(9): 935-947.
[44] Lamarche CP, Bonelli A, Bursi OS, Tremblay R. A Rosenbrock-W method for real-time dynamic substructuring and pseudo-dynamic testing. Earthquake Engineering and Structural Dynamics, 2009; 38(9): 1071–92.
[45] Chen C, Ricles JM. Development of direct integration algorithms for structural dynamics using discrete control theory. Journal of Engineering Mechanics, 2008; 134(8): 676-683.
[46] Igarashi A, Sanchez-Flores F, Iemura H, Fujii K, Toyooka A. Real-time hybrid testing of laminated rubber dampers for seismic retrofit of bridges. Proceedings of the 3rd International Conference on Advances in Experimental Structural Engineering, San Francisco, USA, 2009.
[47] Nakashima M, Kato H, Takaoka E. Development of real-time pseudo dynamic testing. Earthquake Engineering and Structural Dynamics, 1992; 21(1): 79-92.
[48] Yuan Y, Wei W, Igarashi A, Tan P, Iemura H, Zhu H. Experimental and analytical studies of seismic response of highway bridges isolated by rate-dependent rubber bearings. Engineering Structures, 2017; 150: 288-99.
[49] Wallace MI, Sieber J, Neild SA, Wagg DJ, Krauskopf B. Stability analysis of real time dynamic substructuring using delay differential equation models. Earthquake Engineering and Structural Dynamics, 2005; 34(15): 1817–32.
[50] Mercan O, Ricles JM. Stability and accuracy analysis of outer loop dynamics in

real-time pseudodynamic testing of SDOF systems. Earthquake Engineering and Structural Dynamics, 2007; 36(11): 1523–43.
[51] Chen C, Ricles JM. Stability analysis of SDOF real-time hybrid testing systems with explicit integration algorithms and actuator delay using. Earthquake Engineering and Structural Dynamics, 2008; 37(4): 597–613.
[52] Jung RY, Shing PB. Performance evaluation of a real-time pseudodynamic test system. Earthquake Engineering and Structural Dynamics, 2006; 25(4): 333–55.
[53] Jung RY, Shing PB, Stauffer E, Thoen Bradford. Performance of a real-time pseudodynamic test system considering nonlinear structural response. Earthquake Engineering and Structural Dynamics, 2007; 36(12): 1785–809.
[54] Horiuchi T, Inoue M, Konno T, Namita Y. Real-time hybrid experimental system with actuator delay compensation and its application to a piping system with energy absorber. Earthquake Engineering and Structural Dynamics, 1999; 28(10): 1121–41.
[55] Horiuchi T, Konno T. A new method for compensating actuator delay in real – time hybrid experiments. Philosophical Transactions of the Royal Society of London. Series A: Mathematical, Physical and Engineering Sciences, 2001; 359(1786): 1893-1909.
[56] Chen C. Development and numerical simulation of hybrid effective force testing method. Ph.D. dissertation, Department of Civil and Environmental Engineering. Bethlehem, PA: Lehigh University, 2007.
[57] Wen YK. Method for random vibration of hysteretic systems. Journal of the Engineering Mechanics Division, 1976; 102(2): 249-63.
[58] Park Y, Wen Y, Ang AHS. Random vibration of hysteretic systems under bi-directional ground motions. Earthquake Engineering and Structural Dynamics, 1986; 14(4): 543-57.
[59] Dang J, Igarashi A, Murakoshi Y. Development of hysteretic model for high-damping rubber bearings under bi-directional and large strain domain loading. Japan Society of Civil Engineers, 2016; 72(1): 250-62. (in Japanese)
[60] Yoshida J, Abe M, Fujino Y. Constitutive model of high-damping rubber materials. Journal of Engineering Mechanics, 2004, 130(2): 129-141. (in Japanese)
[61] Bhuiyan A, Okui Y, Mitamura H, Imai T. A rheology model of high damping rubber bearings for seismic analysis: Identification of nonlinear viscosity. International Journal of Solids and Structures, 2009; 46(7-8): 1778-92.
[62] Kalpakidis IV, Constantinou MC. Effects of heating on the behavior of lead-rubber bearings. I: Theory. Journal of Structural Engineering, 2009; 135(12): 1440-9.
[63] Kalpakidis IV, Constantinou MC, Whittaker AS. Modeling strength degradation in lead–rubber bearings under earthquake shaking. Earthquake Engineering and Structural Dynamics, 2010; 39(13): 1533-49.
[64] Kondo A, Takenaka Y, Takaoka E, Hikita M, Hyodo Y, Kitamura H. Response analysis method considering heat-mechanics interaction behavior of lead rubber bearings. Journal of Structural and Construction Engineering, 2018; 83(753): 1595-605.
[65] Hwang J, Wu J, Pan TC, Yang G. A mathematical hysteretic model for elastomeric isolation bearings. Earthquake Engineering and Structural Dynamics, 2002; 31(4): 771-89.
[66] Nguyen D, Dang J, Okui Y, Amin A, Okada S, Imai T. An improved rheology model for the description of the rate-dependent cyclic behavior of high damping rubber bearings. Soil Dynamics and Earthquake Engineering, 2015; 77: 416-31.

[67] Hwang J, Hsu T. A fractional derivative model to include effect of ambient temperature on HDR bearings. Engineering structures, 2001; 23(5): 484-90.
[68] Kikuchi M, Ishii K. Thermal-mechanical coupled behavior of elastomeric isolation bearings under cyclic loadings. 15th European Conference on Earthquake Engineering Thessaloniki, Greece, 2018.
[69] Naito N, Mazda T, Uno H, Kawakami M. Seismic performance evaluation of LRB considering Mullins effect and hardening. JSCE Journal of Earthquake Engineering, 2017; 73(4): 499-510. (in Japanese)
[70] Dall'Asta A, Ragni L. Experimental tests and analytical model of high damping rubber dissipating devices. Engineering Structures, 2006; 28(13): 1874-84.
[71] Tubaldi E, Ragni L, Dall'Asta A, Ahmadi H, Muhr A. Stress softening behaviour of HDNR bearings: modelling and influence on the seismic response of isolated structures. Earthquake Engineering and Structural Dynamics, 2017; 46(12): 2033-54.
[72] December 2011 Seismic Isolation/Vibration Control Design Manual for Road Bridges. Civil Engineering Research Center, 2011; 6-32-6-37. (in Japanese)
[73] Hughes TJR, Liu WK. Implicit-explicit finite elements in transient analysis: implementation and numerical examples. Journal of Applied Mechanics, Transactions ASME, 1978; 45(2): 375-378.
[74] Yuan Y, Iemura H, Igarashi A, Aoki T, Yamamoto Y. Investigation of seismic performance of high damping rubber bearing for isolated bridges using real-time substructure hybrid loading test method. JSCE, Doboku Gakkai Ronbunshuu A, 2007; 63(1): 265-276.

Appendix A Algorithm for hybrid simulation

In this study, the Newmark's β method is applied as the step-by-step time integration scheme for the 2-DOF system of the isolated bridge. A value of 1/6 for coefficient β and a time increment Δt of 0.01s are used. At each time step, the predicted displacement of the bearing was calculated and then imposed on the bearing specimen, and the restoring force of the bearing specimen was measured to correct the displacement, velocity and acceleration of the bridge for the next time step integration. This steps were repeated until the end of the test. The details about the algorithm are described as follows. [1]

The 2-DOF system of the isolated bridge is shown in Fig. A1.where m_1 and m_2 are the mass of the super-structure and pier, respectively, d and u are absolute displacement and relative displacement of mass, respectively.

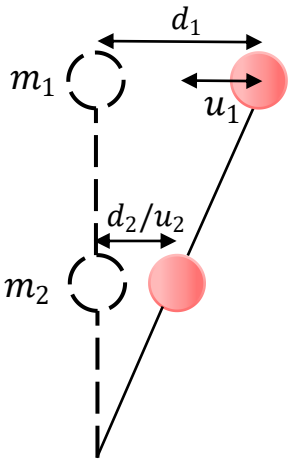

Figure A1 2-DOF system of the isolated bridge

The restoring force r_1 and r_2 of mass points of the 2-DOF system can be calculated by

$$r_1 = f_1 = k_1 u_1 = k_1(d_1 - d_2) = k_1 d_1 - k_1 d_2 \tag{A1}$$

$$r_2 = f_2 - f_1 = k_2 u_2 - k_1 k_1 = k_2 d_2 - k_1(d_1 - d_2) = -k_1 d_1 + (k_1 + k_2) d_2 \tag{A2}$$

where f is the spring force, k is the stiffness of spring.

The restoring force r can also be determined by

$$r_1 = \mathrm{m}_1(a_g - a_1) \tag{A3}$$

$$\mathrm{r}_2 = m_2(a_g - a_2) \tag{A4}$$

where a_g is the ground acceleration, a_1 and a_2 are acceleration of mass points of the 2-DOF system, respectively.

By substituting the Eqs. A3 and A4 into Eqs. A1 and A2, the matrix of the restoring force is obtained as

$$\{\mathrm{r}\} = [\mathrm{K}]\{\mathrm{d}\} = \begin{bmatrix} \mathrm{m}_1 & 0 \\ 0 & \mathrm{m}_2 \end{bmatrix} \begin{Bmatrix} a_g - a_1 \\ a_g - a_2 \end{Bmatrix} = [\mathrm{M}]\{\mathrm{a_g}\} - [\mathrm{M}]\{\mathrm{a}\} \tag{A5}$$

By considering about the structural damping matrix [C], the Eq. A5 of motion of the 2-DOF system is expressed in

$$[\mathrm{M}]\{\mathrm{a}\} + [\mathrm{C}]\{\mathrm{v}\} + [\mathrm{K}]\{\mathrm{d}\} = [\mathrm{M}]\{\mathrm{a_g}\} \tag{A6}$$

where the mass matrix and stiffness matrix are expressed in

$$[\mathrm{M}] = \begin{bmatrix} \mathrm{m}_1 & 0 \\ 0 & \mathrm{m}_2 \end{bmatrix} \quad [\mathrm{K}] = \begin{bmatrix} \mathrm{K}_1 & -\mathrm{K}_1 \\ -\mathrm{K}_1 & \mathrm{K}_1 + \mathrm{K}_2 \end{bmatrix} \tag{A7}$$

Then the equation of motion at time steps n+1 and n are expressed by Eqs. A8 and A9, respectively.

$$Ma_{n+1} + Cv_{n+1} + Kd_{n+1} = Ma_{gn+1} \tag{A8}$$

$$Ma_n + Cv_n + Kd_n = Ma_{\mathrm{gn}} \tag{A9}$$

Subtracting the Eq. A8 by Eq. A9, obtained as

$$M\Delta a_{n+1} + C\Delta v_{n+1} + K\Delta d_{n+1} = M\Delta a_{\mathrm{gn}+1} \tag{A10}$$

Assuming that the acceleration varies linearly during the small time interval Δt, as shown in Fig. A2.

Appendix

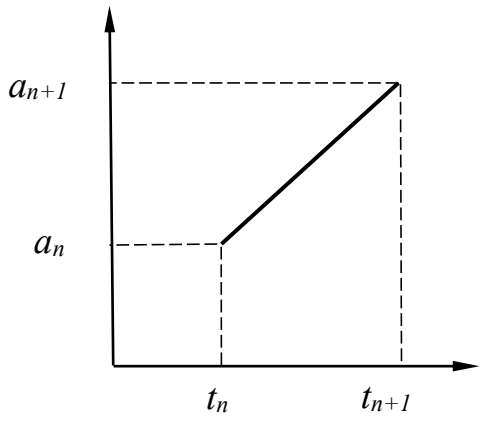

Figure A2 Linear variation of acceleration

The acceleration, velocity and displacement in $t_n \le t \le t_{n+1}$ are then expressed as Eqs. A11, A12 and A13, respectively.

$$a(t) = a_n + \frac{\Delta a_{n+1}}{\Delta t} t \tag{A11}$$

$$v(t) = \int a dt + v_n = a_n t + \frac{\Delta a_{n+1}}{2\Delta t} t^2 + v_n \tag{A12}$$

$$\mathrm{d(t)} = \int v dt + d_n = d_n + v_n \Delta t + \frac{a_n t^2}{2} + \frac{1}{6} \frac{\Delta a_{n+1}}{\Delta t} \Delta t^3 \tag{A13}$$

The incremental velocity and displacement at t_{n+1} are obtained by putting $t=t_n+\Delta t$ in Eqs. A12 and A13, as expressed by

$$\Delta \mathrm{v}_{\mathrm{n+1}} = \mathrm{v}_{\mathrm{n+1}} - \mathrm{v}_{\mathrm{n}} = a_n \Delta t + \frac{1}{2} \Delta a_{n+1} \Delta t \tag{A14}$$

$$\Delta \mathrm{d}_{\mathrm{n+1}} = d_{n+1} - d_n = v_n \Delta t + \frac{1}{2} a_n \Delta t^2 + \frac{1}{6} \Delta a_{n+1} \Delta t^2 \tag{A15}$$

Substituting Eqs. A14 and A15 into Eq. A10

$$(M + \frac{1}{2}\Delta t C + \frac{1}{6}\Delta t^2 K)\Delta a_{n+1} = M \Delta a_{gn+1} - (\Delta t C + \frac{1}{2}\Delta t^2 K) a_n - \Delta t K v_n \tag{A16}$$

Express the $\hat{M}$, A_a, A_v in Eqs. A17, A18 and A19, and substitute these equations into Eq. A16, Eq. A20 can be obtained.

$$\hat{M} = M + \frac{1}{2}\Delta t C + \frac{1}{6}\Delta t^2 K \tag{A17}$$

$$A_a = \Delta t C + \frac{1}{2}\Delta t^2 K \tag{A18}$$

$$A_v = \Delta t K \tag{A19}$$

Solving Eq. A20 with respect to the predicted acceleration increment $\Delta \tilde{a}_{n+1}$, the Eq. A21 is

obtained.

$$\hat{M}\Delta a_{n+1} = M\Delta a_{gn+1} - A_a a_n - A_v v_n = \Delta\hat{F} \tag{A20}$$

$$\Delta\widetilde{a}_{n+1} = \frac{\Delta\hat{F}}{\hat{M}} \tag{A21}$$

The Eq. A21 is then used to predict the acceleration, velocity and displacement at time t_{n+1}, which are obtained as

$$\widetilde{a}_{n+1} = a_n + \Delta\widetilde{a}_{n+1} \tag{A22}$$

$$\widetilde{v}_{n+1} = v_n + a_n\Delta t + \frac{1}{2}\Delta\widetilde{a}_{n+1}\Delta t \tag{A23}$$

$$\widetilde{\mathrm{d}}_{n+1} = d_n + v_n\Delta t + \frac{1}{2}a_n\Delta t^2 + \frac{1}{6}\Delta\widetilde{a}_{n+1}\Delta t^2 \tag{A24}$$

The acceleration, velocity, and displacement obtained from above are estimated values, the estimated displacement was divided by 6 (scale factor, the specimen is 1/6 scaled and there exits a similitude law for the test) and then imposed on the bearing specimen in the hybrid simulation. It is noted that these estimated values are approximations and need to be corrected, the procedure used to correct the values are expressed as follows.

The relationship between measured, predicted and true value of force at time step t_{n+1} is shown in Fig. A3.

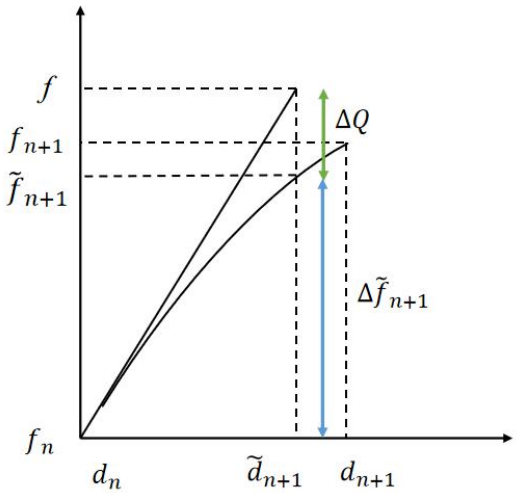

Figure A3 Measured and true force

where the $\tilde{f}_{n+1}$ is the measured force in hybrid simulation, f_{n+1} is the true force, f is the predicted force based on the initial elastic stiffness, $\tilde{d}_{n+1}$ is the measured displacement, $d_{n+1}$is the true displacement. The increments of the displacement and force are defined by

$$\Delta f_{n+1} = f_{n+1} - f_n \tag{A25}$$

$$\Delta \tilde{f}_{n+1} = \tilde{f}_{n+1} - f_n \tag{A26}$$

$$\Delta d_{n+1} = d_{n+1} - d_n \tag{A27}$$

$$\Delta \tilde{d}_{n+1} = \tilde{d}_{n+1} - \tilde{d}_n \tag{A28}$$

$$f_{n+1} = \tilde{f}_{n+1} + K(d_{n+1} - \tilde{d}_{n+1}) \tag{A29}$$

The measured force $\tilde{f}_{n+1}$ is used to evaluate the correction of force ΔQ, which is the difference between predicted force and the measured force, and is expressed as

$$\Delta Q = \tilde{f}_{n+1} - (f_n + K\Delta \tilde{d}_{n+1}) = \Delta \tilde{f}_{n+1} - K\Delta \tilde{d}_{n+1} \tag{A30}$$

Then the force increment at time step $n+1$ is obtained in Eq. A31 by substituting the equations described above. Considering about the similitude law, the measured restoring force of specimen was multiplied by 36 for the real size of the bearing in the seismic response analysis.

$$\begin{aligned} \Delta f_{n+1} &= f_{n+1} - f_n \\ &= \tilde{f}_{n+1} - f_n + K(d_{n+1} - \tilde{d}_{n+1}) \\ &= \Delta \tilde{f}_{n+1} + K(d_{n+1} - d_n - \tilde{d}_{n+1} + d_n) \\ &= \Delta \tilde{f}_{n+1} + K\Delta d_{n+1} - K\Delta \tilde{d}_{n+1} \\ &= \Delta Q + K\Delta d_{n+1} \end{aligned} \tag{A31}$$

Therefore, Eq. A10 is modified as Eq. A32, and Δa_{n+1} is changed and expressed in Eq. A33.

$$M\Delta a_{n+1} + C\Delta v_{n+1} + K\Delta d_{n+1} + \Delta Q = M\Delta a_{gn+1} \tag{A32}$$

$$\Delta a_{n+1} = \frac{\Delta \hat{F}}{\hat{M}} - \frac{\Delta Q}{\hat{M}} \tag{A33}$$

From the above, the corrected acceleration increment is obtained from

$$\Delta a^*_{n+1} = \Delta a_{n+1} - \Delta \tilde{a}_{n+1} = -\frac{\Delta Q}{\hat{M}} \tag{A34}$$

Thus the corrected acceleration, velocity and displacement at time t_{n+1} are shown in

$$a_{n+1} = \tilde{a}_{n+1} + \Delta a^*_{n+1} \tag{A35}$$

$$v_{n+1} = \tilde{v}_{n+1} + \frac{1}{2}\Delta a^*_{n+1}\Delta t \tag{A36}$$

$$d_{n+1} = \tilde{d}_{n+1} + \frac{1}{6}\Delta a^*_{n+1}\Delta t^2 \tag{A37}$$

The displacement, velocity and acceleration of the structure for the next time step *n+1* are corrected by the measured restoring force of the specimen at time step *n*, this steps are repeated until the end of the test.

References

[1] 高減衰ゴム支承の低温時地震挙動に関するハイブリッド実験, 柴野祐介,卒業論文,2020 年.

Appendix B Calculation of parameters in the temperature simulation of the bearing

B.1 HDR bearing

Let the cross-sectional length of HDR bearing specimen be L, L=240mm, the total rubber layer thickness be t_r, t_r=30mm, the total steel thickness be t_s, t_s=16mm.

Then the volume of total rubber layer V_r is expressed as:

$$V_r = L \times L \times t_r = 0.24 \times 0.24 \times 0.03 = 0.001728m^3$$

The volume of total steel layer V_s is expressed as:

$$V_s = L \times L \times t_s = 0.24 \times 0.24 \times 0.016 = 0.0009216m^3$$

The mass of total rubber layer m_r is expressed as:

$$m_r = V_r \times \rho_r = 0.001728 \times 1146 = 1.98kg$$

The mass of total rubber layer m_s is expressed as:

$$m_s = V_s \times \rho_s = 0.0009216 \times 7740 = 7.13kg$$

The constant λ is calculated by:

$$\lambda = \frac{1}{m_r C_{pr} + m_s C_{ps}} = 1.536 \times 10^{-4}$$

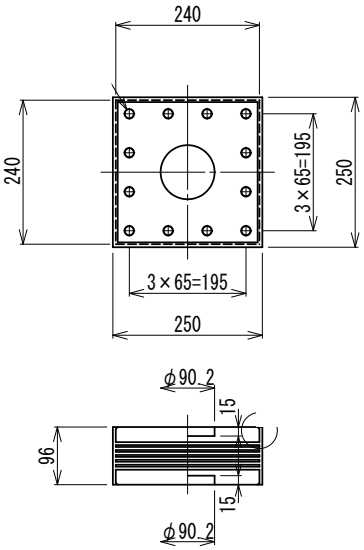

The diameter of the shear key d_s is 90.2mm, the height of he shear key h_s is 15mm, the side area of the shear key A is determined by:

$$A = \pi \times d_s \times h_s = 0.0042\text{m}^2$$

In the natural environment, A is assumed to be the sum of upper and lower surface areas of the bearing specimen as expressed by:

$$A = L \times L \times 2 = 0.1152\text{m}^2$$

B.2 SPR-S bearing

Let the diameter of lead plug be d_L, d_L=34.5 mm, the height of lead plug be h_L, h_L=96 mm.

The cross-sectional area of rubber layer A_r and steel layer A_s is expressed as:

$A_r = A_s = L \times L = 0.0576m^2$

The cross-sectional area of four lead plugs A_L is:

$$A_L = 4 \times \pi \times (\frac{d_L}{2})^2 = 0.0037m^2$$

Then the volume of total rubber layer V_r is expressed by:

$V_r = (A_r - A_L) \times t_r = 0.0016m^3$

The volume of total steel layer V_s is expressed by:

$V_s = (A_s - A_L) \times t_s = 8.618 \times 10^{-4}m^3$

The volume of total lead plugs V_L is expressed by:

$V_L = A_L \times h_L = 3.552 \times 10^{-4}m^3$

The mass of total rubber layer m_r is expressed by:

$m_r = V_r \times \rho_r = 1.8517kg$

The mass of total steel layer m_s is expressed by:

$m_s = V_s \times \rho_s = 6.6701kg$

The mass of total lead plugs m_L is expressed by:

$m_L = V_L \times \rho_L = 4.0351kg$

The constant λ is calculated by:

$$\lambda = \frac{1}{m_r C_{pr} + m_s C_{ps} + m_L C_{pL}} = 1.513 \times 10^{-4}$$

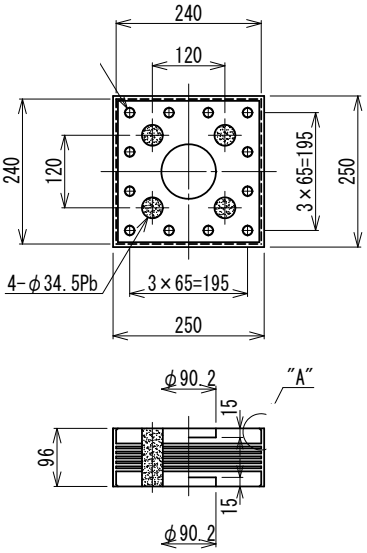

Appendix C Optimization calculation approach: KH method

KH method is one of the optimization method proposed by Kuroda [1-2]. It is very useful to get the model parameters in the nonlinear restoring force simulation of rubber bearings without the need to build derivative of the objective function. In this study, the model parameters are identified from the hysteresis loops of rubber bearings in the quasi-static cyclic loading tests by the KH method.

The accuracy of the simulation with the model parameters compared with the experimental data is defined by a correlation coefficient parameter R^2:

$$\mathrm{R}^2 = 1 - \frac{\sum (\mathrm{f_{e,i}} - \mathrm{f_{a,i}})^2}{\sum (\mathrm{f_{e,i}} - \overline{\mathrm{f}}_\mathrm{e})^2} \tag{B1}$$

where the $f_{e,i}$ is the experimental restoring force, $\overline{f_e}$ is the mean value of the f_e, and f_a is the analytical restoring force calculated by simulation model based on the experimental displacement.

The accuracy of the simulation is higher as the R^2 is larger. Let the model parameters be the $\{S_i\}$(i=1, 2, ... , N), and the N is the number of the model parameters, for example, the N is 3 for bilinear model. For one set of model parameters $\{S_i\}$, one value of R^2 can be calculated by Eq. B1, the parameters $\{S\}$ that maximize the R^2 is defined as the identified parameters.

The flowchart of the KH method is shown in Fig. B1. [3] The procedure begins with the input initial model parameters $\{S_i\}$, and the initial value of R^2 can be calculated based on the experimental displacement and experimental restoring force of rubber bearing. The model parameters $\{\mathrm{S_i}\}$ will be updated to obtain the best simulation with a highest R^2 during the procedure. Firstly, the ith parameter S_i is increased and decreased to S_i^+ and S_i^-, respectively. The D_i is the searching step length for the ith parameter, D_i is initially set to be 0.1 for each model parameter as shown in Table B1, and it will be changed during the procedure. Then the corresponding R^{2+} and R^{2-} are calculated according to the S_i^+ and S_i^-, respectively. Next, the value of the R^{2+}, R^{2-} and R^2 are compared, if the maximum value is the R^{2+}, S_i is updated to S_i^+; if the maximum value is the R^{2-}, S_i is updated to S_i^-; for these two conditions, it means that the S_i is far from the model parameter that we need, hence, the D_i is increased using the step length increasing ratio C_i, if the maximum value is the R^2, S_i is not changed, it means that the S_i is near to the model parameter that we need, hence, the D_i is reduced using the step length decreasing ratio C_r. These procedure will be repeated for each model parameters, and the convergence is achieved when each searching step length D_i is smaller than the error tolerance ε.

Appendix

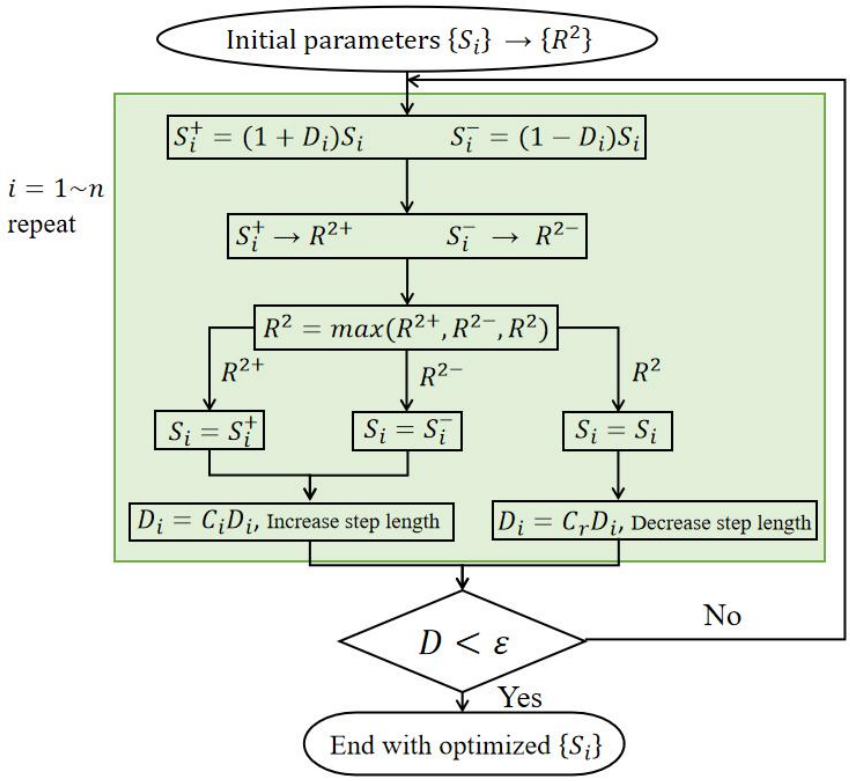

Figure B1 Flowchart of the KH method

The initial parameters set is shown in Table 1, D_i is updated during the procedure, C_i, C_r and ε are constants [3].

Table 1 Initial parameters set

D_i	C_i	C_r	ε
0.1	3	0.3	10^{-4}

References

[1] Kuroda H. Visual basic engineering calculation program. CQ Press, Tokyo, 2001; 69–74.
[2] Kuroda H. Visual basic numerical analysis program. CQ Press, Tokyo, 2002; 233–235.
[3] Dang J, Yuan H, Igarashi A. Multiple-spring model for square-section steel bridge columns under bidirectional seismic load. Journal of Structural Engineering, 2017; 143(5): 04017005.

Acknowledgment

Time flies like an arrow, I had a happy and meaningful time in Kyoto University and learned a lot in the past three years. I would like to express my sincere gratitude to all those who have helped me a lot during the past three years. Without their support and encouragement, I can not finish this dissertation.

First and foremost, my hearty thanks go to my supervisor, Prof. Akira Igarashi, who has given me insightful suggestions on the researches and taught me how to give a better presentation. His patient instruction and constructive suggestions are beneficial to me a lot. Thank you for your being with me and letting me see the charm of scientific research.

I would like to extend my deep gratitude to Prof. Kunitomo Sugiura and Prof. Chul-Woo Kim, for their insightful comments and support during my study.

My sincere thanks also go to the Assistant Professor Ji Dang (Saitama University), he provided me with abundant suggestions and priceless criticisms for my research work.

I am truly thankful to Dr. Takehiko Himeno (Kawakin Core-Tech Co., Ltd.), Manager Yuki Hamada (Kawakin Core-Tech Co., Ltd.) and Technical Advisor Yoshifumi Uno (Office U-Tech) for the experimental technical support, critical comments and invaluable suggestions. The experiments in this dissertation were conducted by using the laboratory facilities and bearing specimens provided by Kawakin Core-Tech Co., Ltd., I indeed gratefully thank you for the precious experimental data.

I would like to express my sincere gratitude to Associate Professor Nozomu Yoneyama, the secretary Miho Mori and all the members of laboratory for their kind support, patience and fantastic research environment.

I am greatly indebted to China Scholarship Council (CSC) for providing financial support through my doctor course.

Also, I own my deep thanks to my friends, Xinhao He, Yu Lin, Katrina Montes (Saitama University), Jian Zhou, Jie Shen, Siyi He, Haodong Bai and Yongxia Ren, thank you for giving suggestions when I have problems in the researches, thank you for being with me and letting me have a happy time in Japan.

Finally, I am also grateful to my family members for their spiritual support and encouragement in my life.

August, 2022

Yuqing Tan